Spectroscopic Studies On Nanomaterials For Solar Energy Harvesting Application

THESIS

SUBMITTED FOR THE DEGREE OF

DOCTOR OF PHILOSOPHY (SCIENCE)

BY

PRASENJIT KAR

DEPARTMENT OF CHEMISTRY

UNIVERSITY OF CALCUTTA

2017

To My Family

Acknowledgements

First of all I would like to express my deepest gratitude to Professor Samir Kumar Pal for giving me the opportunity to carry out my research work under his constant guidance, support and encouragement. His in-depth knowledge on multidisciplinary field of science has been extremely beneficial for me and of immense help as well. I appreciate his key ideas for motivating my research work in real world application. I am especially grateful for his constant availability, great interest and innumerous helpful discussions for my work. He has provided me with many opportunities to gain scientific experience, allowing me to explore new areas of research, interact and collaborate with talented researchers from a number of different national and international institutes.

Special recognition is given to Dr. Srabanti Ghosh, CGCRI, India for share her valuable ideas and for reviewing my works.

I would like to thank Prof. Peter Lemmens of TU Braunschweig, Germany, Prof. Omar F. Mohammed of KAUST, KSA, Dr. Hynd Remita of Université Paris-Sud, France, and Prof. Suddhasatwa Basu of IIT Delhi, India for fruitful collaborations.

I am also thankful to all those faculty members and the staffs of S. N. Bose National Centre for Basic Sciences for their sincere cooperation and help.

I am extremely thankful to Council of Scientific and Industrial Research (CSIR), Government of India, for providing the financial support through Junior Research Fellowship (JRF) for first two years and then through Senior Research Fellowship (SRF) for following years. I gratefully acknowledge S. N. Bose National Centre for Basic Sciences for providing the research facilities and Department of Science and Technology (DST), India for projects.

I would like to acknowledge all my seniors and colleagues for assisting me in research. Specially, I have to thank Dr. Samim Sardar for introducing me to the experimental techniques and for helping of my research work. A special thank to Nabarunda and Probir for helping me from many technical difficulties during my works. I would like to thank Susobhanda and Priya for helping me in solvation dynamics study. I am also thankful to Tuhin for his kind support in TOC and also in scientific discussion. I am grateful to Dr. Siddhi Chaudhuri for helping me in dialysis. I am also thankful to Damayanti and Tuhin for their assistance in formatting and proof-reading my thesis. I would like to acknowledge all my seniors (Dr. Soumik Sarkar, Dr. Subrata Batabyal, Dr. Nirmal Goswami, Dr. Ranajay Saha, Dr. Surajit Rakshit, Dr. Anupam Giri, Dr. Soma Banerjee, Dr. Prasanna Kumar Mondal, Dr. Shreyasi Dutta, Dr. Siddhi Chaudhuri, Dr. Samim Sardar, Susobhan Choudhury and Dr. Nabarun Polley) and my other colleagues

(Damayanti, Priya, Probir, Tuhin, Aniruddha, Jayita, Ramesh, Animeshda and Poulomi) for providing me a homely and cheerful environment. I am, especially, thankful to Probir who shared glorious moments over a long period of time, supported my work annoyances, and also for the good moments of fun! I also want to thank all my friends for the good times I shared with them.

Finally, I would like to express my gratitude to my family who supports me through thick and thin, with loves and affections. I want them to know that I love them cordially. Without their sacrifices, moral supports and blessings the thesis would not have taken its shape.

Dated:
Department of Chemical, Biological
and Macromolecular Sciences,
S. N. Bose National Centre for Basic Sciences,
Salt Lake, Kolkata 700106, India
(Prasenjit Kar)

CONTENTS

Chapter 3: Instrumentation and Sample Preparation

Chapter 1

Introduction

1.1. Nanomaterials:

Nanoscience and nanotechnology is a broad and interdisciplinary area of research and development activity that has been exceptionally growing worldwide in the past few years. Nanoscale materials are defined as a set of substances where at least one dimension is less than approximately 100 nanometers. Nanomaterials have unique properties that are significantly different compare to their bulk counterparts [1, 2]. The property changes due to their small grain sizes, the large percentage of their atoms in large grain boundary environments and the interaction between the grains. The unique properties of these various types of nanomaterials give them novel electrical, catalytic, magnetic, mechanical, thermal and spectroscopic features that are highly desirable for applications in catalysis, biomedicines and environmental sectors [2-4]. Nanomaterials exist with great chemical diversity in the form of nanoparticles, nanowires, nanotubes, quantum dots, nanoporous solids, 2-D arrays (of nanoparticles) etc.

1.2. Classification of Nanomaterials:

Depending on the dimension in which the size effect on the resultant property becomes apparent, the nanomaterials can be classified as zero dimensional, one dimensional, two dimensional, three dimensional nanostructures.

1.2.1. Zero dimensional (0-D): These nanomaterials have nano-dimensions in all the three directions. Metallic nanoparticles including gold and silver nanoparticles and semiconductor such as quantam dots are the perfect example of this kind of nanoparticles. Most of these nanoparticles are spherical in size and the diameter of these particles will be in the1-50 nm range (Figure 1.1).

1.2.2. One dimensional (1-D): In these nanostructures, one dimension of the nanostructure will be outside the nanometer range. These include nanowires, nanorods, and nanotubes. These materials are long (several micrometer in length), but with diameter of only a few nanometer (Figure 1.1). Nanowire and nanotubes of metals, oxides and other materials are few examples of these kind of materials.

1.2.3. Two dimensional (2-D): In this type of nanomaterials, two dimensions are outside the nanometer range. Two-dimensional nanomaterials include nanofilms, nanolayers, and nanocoatings. The area of the nanofilms can be large (several square micrometer), but the thickness is always in nano scale range (Figure 1.1).

1.2.4. Three dimensional (3-D): This types of nanomaterials are not confined to the nanoscale in any dimension (Figure 1.1). These include bulk materials composed of the individual blocks which are in the nanometer scale (1-100 nm).
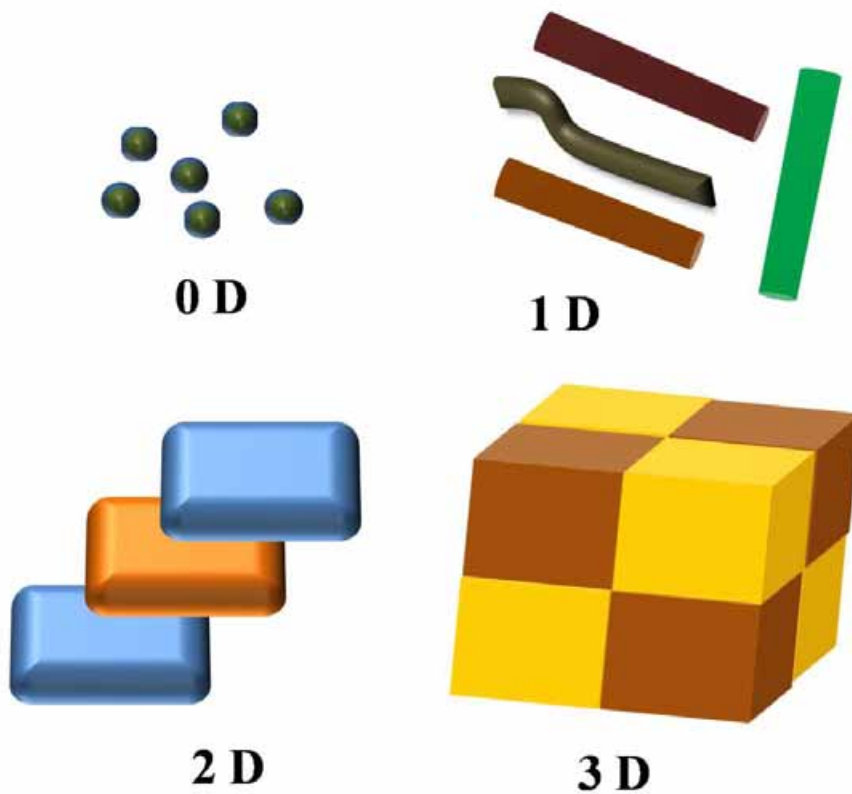
Figure 1.1. *Classification of nanomaterials.*

1.3. Synthesis of Nanomaterials:

The great appeal of diverse synthetic approaches to novel nanomaterials of facilitates the capability to create nanoscale building blocks of diverse chemical composition. The synthetic routes of nanomaterials can be divided into two main categories:

1.3.1. Top-Down Approach: It starts with a large structure and proceeds to make it smaller through successive cuttings (Figure 1.2). Different kinds of lithographic techniques, cutting (such as electron beam, photo ion beam or X-ray lithography cutting), etching, grinding, ball milling and sol gel technique are the example of top-down approach [5, 6]. The top-down method is currently in use to manufacture computer chips as well as other day to day products. However, the techniques suffer from the need to remove large amounts of material. Physical limits of the technique are also a problem.
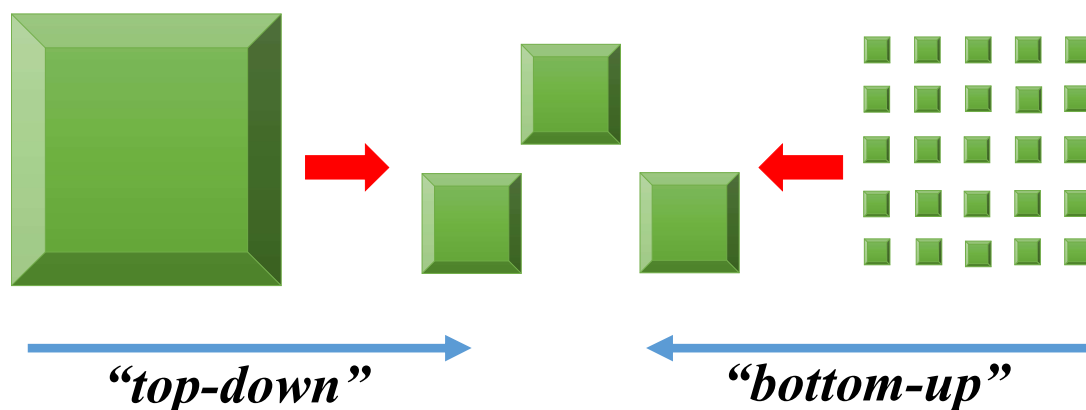
Figure 1.2. Approaches for the synthesis of nanomaterials.

1.3.2. Bottom-Up Approach: It can be accessed from a molecularly dispersed system whereby the size of a dissolved species is increased continuously until the nanometer regime is reached. In general, it refers to the build-up of a material from the bottom (Figure 1.2): atom-by-atom, molecule-by-molecule, or cluster-by-cluster [6, 7]. Colloidal dispersion is a good example of bottom-up approach in the synthesis of nanoparticles. This approach allows smaller geometries of the nanomaterials compare to top-down approach. It is more economical than top-down approach as it does not waste material for etching. However, controlling various parameters for monodispersed nanomaterails preparation is difficult.

1.4. Scope of the Spectroscopic Studies On Nanomaterials For Solar Energy Harvesting Application:

In light of steadily increasing global energy demands, the impending scarcity of easily recoverable fossil fuels and growing concerns about CO_2 emissions, identifying and exploiting renewable energy sources is an increasingly urgent endeavor [8-10]. Solar energy is by far the

3

most abundant and widely available sustainable energy source. Therefore, solar energy harvesting refers to the set of processes by which solar light is captured by different materials and is converted into a usable form. The different kinds of nanomaterials have been extensively used in order to harvest solar light [11-13]. Nanomaterials for tailor made applications, one of the most fascinating and useful aspect is their optical properties. The unique optical properties of nanomaterials strongly depend on parameters such as size, shape, surface properties, and other variables including doping and interaction with the surrounding environment or other nanostructures [14-17]. Thus it is very much essential to study optical properties of nanomaterials since for probing different charge carrier dynamics in nanomaterials with different spectroscopy tools. The importance of spectroscopic studies of nanomaterials lies in various fields of science like solar cell, photocatalysis, photoelectrochemistry, photodynamic therapy and biomedical applications [13, 18-21].

Ultrafast photoinduced electron transfer is a fundamental process occurring in a wide range of nanostructured materials used in enhanced solar energy conversation [22, 23]. A detail understanding of this fundamental mechanism and dynamics of these ultrafast charge transfer processes is important for the future development and design of efficient systems for sustainable solar energy conversion. In particular, the electron injection dynamics of different wide bandgap semiconductors has been of much interest in the last decades [24-26]. The slower dynamic response is, therefore, often related to the limited performance of nanomaterials, but its physical origin is still not fully understood.

The key focus of this thesis is to synthesize of applied nanomaterials and also to explore excited-state dynamics of nanomaterials, which is important from both fundamental and application perspectives, such as, energy-harvesting devices, photocatalysis, dye sensitized solar cell application. In one of our studies, we have synthesized Pd nanostructures, which exhibit pronounced electrocatalytic activity for ethanol oxidation in alkaline solution. We have also investigated formation of Pd nanostructures in the confined region of hexagonal mesophases with the help of water relaxation dynamics study using solvation probe. Formation of Mn_2O_3 nanoballs via microwave assisted hydrothermal method exhibit bifunctional activity towards oxygen reduction and oxygen evolution reaction. Extending our work in this direction, we have also synthesized reduced grapheme oxide supported hierarchical manganese oxide, which act as efficient electrocatalytic activity toward reduction and evolution of oxygen. In another study, we

have synthesized protoporphyrin-IX-zinc oxide (PP-ZnO) nanohybrids for applications in photocatalytic devices. The modulation of photocatalytic activity of PP-ZnO nanohybrid in presence of water soluble metal iron(III) and copper(II) ions also investigated. We have used time-resolved fluorescence and transient absorption techniques to study the ultrafast dynamical events that are key to photocatalytic activities. In another work, we have also explored the crucial role of ultrafast dynamics of a good light harvesting nanohybrid (Cu)PP-TiO$_2$, as it is efficient for photocatalytic application but inefficient for photovoltaic application. In another study, we have reported a facile approach for the in situ synthesis of Au-reduced graphene oxide (Au-RGO) nanohybrids by photochemical reduction technique, which demonstrate excellent adsorption capacities and recyclability for a broad range of dyes. Picosecond resolved fluorescence technique unravels the excited state dynamical processes of dye molecules adsorbed on the Au-RGO surface.

In another work, Bi-Bi$_2$O$_2$CO$_3$ heterojunctions were fabricated by in-situ decoration of Bi nanoparticles on Bi$_2$O$_2$CO$_3$ nanosheets via a simple hydrothermal synthesis approach. Detailed ultrafast electronic spectroscopy reveals that the in-situ decoration of Bi nanoparticles on Bi$_2$O$_2$CO$_3$ nanosheets exhibit a dramatically enhanced electron–hole pair separation rate, resulting in an extraordinarily high photocatalytic activity for the degradation of a model organic dye, methylene blue (MB), under visible light illumination. In another study, we demonstrate that the interaction of a small organic ligand (citrate) with one of the oxide varieties (Mn$_2$O$_3$) induces completely new optical properties and functionalities (photocatalysis). New optical properties of the surface engineered nanomaterials have been explained by details ultrafast spectroscopy studies. In another work, we have compared the effect of Au with Al nanoparticles as the former have strong SPR band (peak 560 nm) at the emission (~600 nm) of the model dye protoporphyrin IX (PP) in the proximity of mesoporous TiO$_2$ nanoparticles in a model dye sensitized solar cell (DSSC). Picosecond resolved emission spectroscopy on the model dye reveal an ultrafast component consistent with photoinduced electron transfer (PET) from the dye to TiO$_2$ matrix in the presence of Au nanoparticles.

The experimental tools used for studying the dynamical processes involve such as, solvation dynamics, fluorescence anisotropy, picosecond-resolved carrier relaxation dynamics, femtosecond-resolved transient absorption spectroscopy, photoinduced electron transfer (PET), Förster resonance energy transfer (FRET) and nanosurface energy transfer (NSET). Koutecky-

Levich equation to determine the electron transfer numbers per oxygen molecule involved in oxygen reduction reaction (ORR). Langmuir−Hinshelwood (L−H) model is used for surface catalysis. The different experimental techniques employed for the structural and functional characterization of the light harvesting materials include steady-state UV-VIS absorption and fluorescence, thermogravimetric analysis (TGA), Fourier transform infrared spectroscopy (FTIR), Raman scattering, powder X-ray diffraction (XRD), Field Emission scanning electron microscopy (FESEM), high-resolution transmission electron microscopy (HRTEM) and X-ray photoelectron spectroscopy (XPS), zeta potential, inductively coupled plasma mass spectrometry (ICP-MS), BET surface area analyzer. The electrochemical measurements were conducted by using cyclic voltammetry (CV). Rotating disk electrode (RDE) experiments were performed to determine oxygen reduction reaction (ORR) and oxygen evolution reaction (OER). Hydrothermal technique and microwave-assisted hydrothermal technique employed for the synthesis of nanomaterials. The DSSCs were fabricated and characterized by using photocurrent−voltage (J−V) measurements and photovoltage decay measurements.

1.5. Objective:

Solar energy harvesting is of increased interest as an abundant renewable energy due to the excessive amounts of available energy that fall on the earth's surface in the form of light every day [13, 27, 28]. The different kinds of nanomaterials have been extensively used in order to harvest light. Such kind of energy harvesters have been evaluated for photocatalysis, dye removal, energy production [27, 29-32]. Thus, need for renewable energy is motivating the discovery of new materials for designing next generation energy conversion devices. Therefore, the key objective of this thesis is to synthesis of applied nanomaterails and spectroscopy studies on light harvesting nanomaterials to alter excited deactivation pathways in order design efficient light harvesting nanomaterials for potential real world application.

The development of advanced materials and processes is a central issue which contributes to the ultimate goal to accelerate the implementation of novel nanomaterials-based technology providing clean and affordable energy [12, 33-36]. Semiconductor based nanomaterials such as TiO_2, ZnO have been widely used in energy production and waste water purification [37-40]. A number of other semiconductors like Mn_3O_4, Fe_2O_3, ZnS etc were investigated to replicate and extend this work to meet energy demand and for waste water purification [41-44]. In this direction, we have synthesized Pd nanostructures in the confined region of hexagonal

mesophases and also studied the ethanol oxidation reaction (EOR) using as prepared Pd nanostructures as the anode material [45]. In another work, a facile and effective microwave-assisted route has been developed to synthesize structurally uniform and electrochemically active pure and transition metal doped manganese oxides nanoballs (Mn_2O_3 NBs), which exhibit bifunctional catalytic activity for oxygen reduction and oxygen evolution reaction [46]. Very recently, a facile and effective hydrothermal route has been developed to synthesize hierarchical with controllable structures of manganese oxides (Mn_2O_3) and reduced graphene oxides supported Mn_2O_3 composites and explored the electrocatalytic activity toward reduction and evolution of oxygen [47].

In practical application, semiconductor based light harvesting nanomaterials has its limitation since its use only 4% light of total solar spectrum. In order to harvest visible light of solar spectra for enhanced solar energy conversation, several methods has been utilized like doping of nanomaterial with several metal and nonmetal, noble metal deposition, narrow bad gap semiconductor coupling, conducting polymer sensitization and dye sensitization [48-51]. Organic based porphyrin dyes are promising dye over inorganic based dyes because of their environmental friendliness and non-toxicity. Spectroscopic studies on harvesting nanomaterials are crucial to alter excited state deactivation pathways in order design efficient light harvesting materials for potential real world application. In the above context, we have addressed how impact of metal ions in porphyrin-based applied materials influence visible-light photocatalysis using ultrafast spectroscopy [52]. Extending our research in this direction, we have also observed that a good light harvesting nanohybrid (Cu)PP-TiO_2 exhibit efficient photocatalytic activity but inefficient photovoltaic efficiency [53]. Time-resolved fluorescence technique has been applied to study the ultrafast dynamic events that are key to photocatalytic and photovoltaic activities. Recently, graphene consisting of single layer of carbon atoms with a honeycomb two-dimensional (2D) lattice crystal structure has been recognized as a promising material in various fields, such as solar energy harvesting, drug delivery, nanoelectronics, sensors, H_2 production and water purification [54, 55]. We have also developed a facile approach for the synthesis of Au-RGO nanohybrid via the photochemical reduction technique [56]. The nanohybrid have extensively used for dye removal from waste water and the detail ultrafast spectroscopy has been employed to investigate the proximity of the dye after adsorption.

7

Bismuth containing nanomaterials recently received increasing attention with respect to environmental applications because of their low cost, high stability and nontoxicity [57-60]. In this direction, Bi-$Bi_2O_2CO_3$ heterojunction were fabricated by in-situ decoration of Bi nanoparticles on $Bi_2O_2CO_3$ nanosheet [61]. We also observed that the heterojunction exhibited high photocatalytic activity which is useful for real world application. Our recent attention towards manganese oxide nanomaterials is due to their emerging use in biomedical, photocatalysis, super capacitor applications and also because this material is relatively inexpensive, non-toxic, and naturally abundant [62, 63]. We have addressed surface functionalization of Mn_2O_3 with biologically compatible citrate ligand act as a promising material for solar energy harvesting application [64].

The mechanistic pathways for the enhancement of the efficiency of a dye sensitized solar cell (DSSC) using plasmonic nanoparticles have attracted lots of attention in contemporary literature [65-68]. Here, we have shown the direct experimental evidence of dipolar coupling between electronic transition of a dye in a DSSC and plasmonic resonance of a metal nanoparticle in active electrode on the overall efficiency of the DSSC [69].

1.6. Summary of the Work Done:

1.6.1. Synthesis and Characterization of Various Applied Nanomaterials:

1.6.1.1. Facile Synthesis of Pd Nanostructures in Hexagonal Mesophases as a Promising Electrocatalyst for Ethanol Oxidation [45]:

One of the significant challenges for the commercialization of direct ethanol fuel cells (DEFCs) is the preparation of active, robust, and low-cost catalysts. In this work, a facile and reproducible method is demonstrated for the synthesis of Pd assembled nanostructures in a hexagonal mesophase formed by a quaternary system (Pd-doped water, surfactant, oil, and cosurfactant) *via* photoirradiation. The formation of Pd nanostructures in the confined region of hexagonal mesophases was further supported by water relaxation dynamics study using a solvation probe. The mesophases can be doped with high concentrations of a palladium salt (0.1 M) without any disturbance to the structure of the mesophases which results in a high yield and facilitates the clean synthesis of Pd nanostructures without using any toxic chemicals. Electrochemical measurement confirms that the as-prepared catalysts exhibit significant electrocatalytic activity for ethanol oxidation in alkaline solution. Additionally, we present an alternative strategy using reduced graphene oxide nanosheets in combination with nafion (a proton conducting phase) as a

support, revealing the pronounced impact on dramatically enhanced electrocatalytic activity and stability of Pd nanostructures compared to nafion alone. This unique combination allowed the effective dispersion of the Pd nanostructures that is responsible for the enhancement of the catalytic activity. Our approach paves the way towards the rational design of practically relevant catalysts with both the enhanced activity and durability for fuel cell applications.

1.6.1.2. Microwave-Assisted Synthesis of Porous Mn_2O_3 Nanoballs as Bifunctional Electrocatalyst for Oxygen Reduction and Evolution Reaction [46]:

Technological hurdles that still prevent the commercialization of fuel cell technologies necessitate designing low-cost, efficient and non-precious metals. These could serve as alternatives to high-cost Pt based materials. Herein, a facile and effective microwave-assisted route has been developed to synthesize structurally uniform and electrochemically active pure and transition metal-doped manganese oxide nanoballs (Mn_2O_3 NBs) for fuel cell applications. The average diameter of pure and doped Mn_2O_3 NBs was found to be ~610 nm and ~650 nm, respectively, as estimated using transmission electron microscopy (TEM). The nanoparticles possess a good degree of crystallinity as evedent from the lattice fringes in high-resolution transmission electron microscopy (HRTEM). The cubic crystal phase was ascertained using X-ray diffraction (XRD). The energy dispersive spectroscopic (EDS) elemental mapping confirms the formation of copper-doped Mn_2O_3 NBs. The experimental parameter using trioctylphosphine oxide (TOPO) as the chelating agent to control the nanostructure growth has been adequately addressed using scanning electron microscopy (SEM). The solid NBs were formed by the self-assembly of very small Mn_2O_3 nanoparticles as evident from the SEM image. Moreover, the concentration of TOPO was found to be the key factor whose subtle variation can effectively control the size of the as-prepared Mn_2O_3 NBs. The cyclic voltammetry and galvanostatic charge/discharge studies demonstrated enhanced electrochemical performance for copper doped Mn_2O_3 NBs which is supported by a 5.2 times higher electrochemically active surface area (EASA) in comparison with pure Mn_2O_3 NBs. Electrochemical investigations indicate that both pure and copper doped Mn_2O_3 NBs exhibit a bifunctional catalytic activity toward the four-electron electrochemical reduction as well the evolution of oxygen in alkaline media. Copper doping in Mn_2O_3 NBs revealed its pronounced impact on the electrocatalytic activity with a high current density for the electrochemical oxygen reduction and evolution reaction. The synthetic

approach provides a general platform for fabricating well-defined porous metal oxide nanostructures with prospective applications as low-cost catalysts for alkaline fuel cells.

1.6.1.3. Reduced Graphene Oxide Supported Hierarchical Flower like Manganese Oxide as Efficient Electrocatalysts toward Reduction and Evolution of Oxygen [47]:

The slow kinetics of the electrochemical oxygen reduction reaction (ORR) is a major bottleneck for the development of alkaline fuel cells. Herein, a facile and effective hydrothermal route has been developed to synthesize hierarchical with controllable structures of manganese oxides (Mn_2O_3) and reduced graphene oxides supported Mn_2O_3 composites. The hierarchal metal oxides were formed by self-assembly of very small Mn_2O_3 nanoparticles as evident from transmission electron microscopy. The nature of chelating agents has found to be the key factor whose subtle variation can effectively control the morphology of the Mn_2O_3. Electrochemical investigations indicate that the both pure and supported Mn_2O_3 demonstrate bifunctional catalytic activity toward the four-electron electrochemical reduction of oxygen and evolution reaction in alkaline media. Due to the 3D assembled hierarchical architecture of Mn_2O_3 composed of rose- and petal-like nano-particle arrays and the interconnection of reduced graphene oxides (rGO) network, as well as the synergetic effects of rGO as a support, revealing the pronounce impact on the electrocatalytic activity the Mn_2O_3 composites with high current density and excellent durability as cathode material which is comparable with other electrocatalysts. The synthetic approach provides a general platform for fabricating well-defined pure and supported metal oxides with prospective applications as low-cost catalysts for alkaline fuel cells.

1.6.2. Electronic Spectroscopic Studies on Light Harvesting Nanomaterials:

1.6.2.1. Impact of Metal Ions in Porphyrin-Based Applied Materials for Visible-Light Photocatalysis: Key Information from Ultrafast Electronic Spectroscopy [52]:

Protoporphyrin IX-Zinc Oxide (PP-ZnO) nanohybrids have been synthesized for applications in photocatalytic devices. High-resolution transmission electron microscopy (HRTEM), X-ray diffraction (XRD), and steady-state infrared, absorption, and emission spectroscopies have been used to analyze the structural details and optical properties of these nanohybrids. Time-resolved fluorescence and transient absorption techniques have been applied to study the ultrafast dynamic events that are key to photocatalytic activities. The photocatalytic efficiency under visible-light irradiation in the presence of naturally abundant iron (III) and copper (II) ions has been found to be significantly retarded in the former case, but enhanced in the latter case. More

importantly, femtosecond (fs) transient absorption data have clearly demonstrated that the residence of photoexcited electrons from the sensitizer PP in the centrally located iron moiety hinders ground-state bleach recovery of the sensitizer, affecting the overall photocatalytic rate of the nanohybrid. The presence of copper (II) ions, on the other hand, offers additional stability against photobleaching and eventually enhances the efficiency of photocatalysis. In addition, we have also explored the role of UV light in the efficiency of photocatalysis and have rationalized our observations from femtosecond- to picosecond-resolved studies.

1.6.2.2. Can a Light Harvesting Material be Always Common in Photocatalytic and Photovoltaic Applications? [53]:

Nanomaterials and nanohybrids hold promising potency to enhance the performance of photovoltaic as well as photocatalysis efficiency by improving both light trapping and photo-carrier collection. In the present study, we have synthesized Protoporphyrin IX-Titanium dioxide (PP-TiO_2) nanohybrid as a model light harvesting nanohybrid for potential applications in photovoltaics and photocatalytic devices. We observed that the light harvesting nanohybrid shows efficient photocatalytic activity when copper (II) ion is centrally located within the porphyrin moiety. In contrast, presence of copper (II) ion within the porphyrin moiety decreases photovoltaic efficiencies. High-resolution transmission electron microscopy (HRTEM), X-ray diffraction (XRD), and steady-state absorption and emission spectroscopies have been used to analyze the structural details and optical properties of this nanohybrid. Time-resolved fluorescence technique has been applied to study the ultrafast dynamics which is key to photocatalytic and photovoltaic activities. The reason behind the outstanding photocatalytic performance of the nanohybrid after copper metalation, is found to be additional stability against photobleaching while enhanced back electron transfer after copper metalation decreases its photovoltaic efficiency.

1.6.2.3. Facile Synthesis of Reduced Graphene Oxide–Gold Nanohybrid for Potential Use in Industrial Waste-Water Treatment [56]:

Here, we report a facile approach, by the photochemical reduction technique, for in situ synthesis of Au-reduced graphene oxide (Au-RGO) nanohybrids, which demonstrate excellent adsorption capacities and recyclability for a broad range of dyes. High-resolution transmission electron microscopy (HRTEM), X-ray diffraction (XRD), X-ray photoelectron spectroscopy (XPS) data confirm the successful synthesis of Au-RGO nanohybrids. The effect of several experimental

parameters (temperature and pH) variation can effectively control the dye adsorption capability. Furthermore, kinetic adsorption data reveal that the adsorption process follows a pseudo second-order model. The negative value of Gibbs free energy (ΔG^0) confirms spontaneity while the positive enthalpy (ΔH^0) indicates the endothermic nature of the adsorption process. Picosecond resolved fluorescence technique unravels the excited state dynamical processes of dye molecules adsorbed on the Au-RGO surface. Time resolved fluorescence quenching of Rh123 after adsorption on Au-RGO nanohybrids indicates efficient energy transfer from Rh123 to Au nanoparticles. A prototype device has been fabricated using Au-RGO nanohybrids on a syringe filter (pore size: 0.220 µm) and the experimental data indicate efficient removal of dyes from waste water with high recyclability. The application of this nanohybrid may lead to the development of an efficient reusable adsorbent in portable water purification.

1.6.3. Spectroscopic Studies on Light Harvesting Nanomaterials for Solar Light Photocatalysis Application:

1.6.3.1. In-Situ Hydrothermal Synthesis of Bi–Bi$_2$O$_2$CO$_3$ Heterojunction Photocatalyst with Enhanced Visible Light Photocatalytic Activity [61]:

Bismuth containing nanomaterials recently received increasing attention with respect to environmental applications because of their low cost, high stability and nontoxicity. In this work, Bi-Bi$_2$O$_2$CO$_3$ heterojunctions were fabricated by in-situ decoration of Bi nanoparticles on Bi$_2$O$_2$CO$_3$ nanosheets *via* a simple hydrothermal synthesis approach. X-ray diffraction (XRD), scanning electron microscopy (SEM), transmission electron microscopy (TEM) and high-resolution transmission electron microscopy (HRTEM) were used to confirm the morphology of the nanosheet-like heterostructure of the Bi-Bi$_2$O$_2$CO$_3$ composite. Detailed ultrafast electronic spectroscopy reveals that the in-situ decoration of Bi nanoparticles on Bi$_2$O$_2$CO$_3$ nanosheets exhibit a dramatically enhanced electron–hole pair separation rate, which results in an extraordinarily high photocatalytic activity for the degradation of a model organic dye, methylene blue (MB) under visible light illumination. Cycling experiments revealed a good photochemical stability of the Bi-Bi$_2$O$_2$CO$_3$ heterojunction under repeated irradiation. Photocurrent measurements further indicated that the heterojunction incredibly enhanced the charge generation and suppress the charge recombination of photogenerated electron-hole pairs.

1.6.3.2. Nano Surface Engineering of Mn$_2$O$_3$ for Potential Light-Harvesting Application [64]:

Manganese oxides are well known applied materials including their use as efficient catalysts for various environmental applications. Multiple oxidation states and their change due to various experimental conditions are concluded to be responsible for their multifaceted functionality. Here, we demonstrate that the interaction of a small organic ligand with one of the oxide varieties induces completely new optical properties and functionalities (photocatalysis). We have synthesized Mn$_2$O$_3$ microspheres via a hydrothermal route and characterized them using scanning electron microscopy (SEM), X-ray diffraction (XRD) and elemental mapping (EDAX). When the microspheres are allowed to interact with the biologically important small ligand citrate, nanometer-sized surface functionalized Mn$_2$O$_3$ (NPs) are formed. Raman and Fourier transformed infrared spectroscopy confirm the covalent attachment of the citrate ligand to the dangling bond of Mn at the material surface. While cyclic voltammetry (CV) and X-ray photoelectron spectroscopy (XPS) analysis confirm multiple surface charge states after the citrate functionalization of the Mn$_2$O$_3$ NPs, new optical properties of the surface engineered nanomaterials in terms of absorption and emission emerge consequently. The engineered material offers a novel photocatalysis functionality to the model water contaminant methylene blue (MB). The effect of doping other metal ions including Fe^{3+} and Cu^{2+} on the optical and catalytic properties is also investigated. In order to prepare a prototype for potential environmental application of water decontamination, we have synthesized and duly functionalized the material on the extended surface of a stainless steel metal mesh (size 2 cm × 1.5 cm, pore size 150 μm × 200 μm). We demonstrate that the functionalized mesh always works as a "physical" filter of suspended particulates. However, it works as a "chemical" filter (photocatalyst) for the potential water soluble contaminant (MB) in the presence of solar light.

1.6.4. Spectroscopic Studies on Light Harvesting Nanomaterials for Enhanced Solar Photovoltaic Application:

Direct Observation of Electronic Transition-Plasmon Coupling for Enhanced Electron Injection in Dye-Sensitized Solar Cells [69]:

We illustrate experimental evidence of the effect of surface plasmon resonance (SPR) of a noble metal on the ultrafast-electron injection efficiencies of a sensitizing dye in proximity of a wide band gap semiconductor. We have compared the effect of Au with Al nanoparticles as the former

have a strong SPR band (peak 560 nm) at the emission (~600 nm) of the model dye protoporphyrin IX (PP) in the proximity of mesoporous TiO_2 nanoparticles in a model dye sensitized solar cell (DSSC). We have used detailed electron microscopic procedures for the characterization of Au/Al nanoparticle-embedded TiO_2, the host of PP. Picosecond resolved emission spectroscopy on the model dye reveals an ultrafast component consistent with photoinduced electron transfer (PET) from the dye to the TiO_2 matrix in the presence of Au nanoparticles. In order to investigate the dipolar separation of PP from the Au nanoparticle surface, we have employed a Förster Resonance Energy Transfer (FRET) strategy in the PP-Au nanoparticle system in the absence of TiO_2. Although the time scale of FRET and PET were found to be similar, the plasmon induced enhanced electron transfer in the case of Au nanoparticles is found to be clear from various device parameters of the plasmonic solar cell (DSSC) designed from the materials. We have also fabricated a DSSC with the developed materials consisting of Al-Au nanoparticles with N719 dye as sensitizer. The fabricated DSSC exhibits a much higher power conversion efficiency of (7.1 ± 0.1) % compared to that with TiO_2 alone (5.63 ± 0.13) %. The outstanding performance of DSSC based on plasmonic nanoparticles was attributed to the plasmonic coupling and scattering effect for enhanced electron injection efficiencies.

1.7. Plan of Thesis:

The plan of the thesis is as follows:

Chapter 1: This chapter gives a brief introduction to the scope and motivation behind the thesis work. A brief summary of the work done is also included in this chapter.

Chapter 2: This chapter provides a brief overview of the steady-state and dynamical tools, the structural aspects of dyes and fluorescent probes used in the experiments.

Chapter 3: Details of instrumentation, data analysis and experimental procedures have been discussed in this chapter.

Chapter 4: In this chapter, we have described different processes for the synthesis of nanomaterials. A facile and reproducible method is demonstrated for the synthesis of Pd assembled nanostructures in a hexagonal mesophase, which further supported by water relaxation dynamics study using a solvation probe. Electrochemical measurement confirms that the as-prepared catalysts exhibit significant electrocatalytic activity for ethanol oxidation in alkaline solution. We have also included microwave-assisted synthesis of porous Mn_2O_3

nanoballs in this chapter. We also observed that as synthesized Mn_2O_3 nanoball exhibit bifunctional catalytic activity towards oxygen reduction and evolution reaction. A facile and effective hydrothermal route has been developed to synthesize hierarchical with controllable structures of manganese oxides (Mn_2O_3) and reduced graphene oxides supported Mn_2O_3 composites. Electrochemical investigations indicate that the both pure and supported Mn_2O_3 demonstrate bifunctional catalytic activity towards oxygen reduction and evolution reaction in alkaline media.

Chapter 5: In this chapter, we have explored key ultrafast dynamical event of light harvesting nanomaterials. Time-resolved fluorescence and transient absorption techniques have been used to study the ultrafast dynamic events in porphyrin based applied materials that are key to photocatalytic activities. We have also explored the crucial role of ultrafast dynamics in (Cu)PP-TiO_2, as it is efficient for photocatalytic application but inefficient photovoltaic application. In another study, we have employed picosecond resolved fluorescence technique to study the excited state dynamical processes of dye molecules adsorbed on the Au-RGO surface.

Chapter 6: In this chapter, we have considered detailed ultrafast electronic spectroscopy to reveal that in-situ decoration of Bi nanoparticles on $Bi_2O_2CO_3$ nanosheets exhibits an extraordinarily high photocatalytic activity for the degradation of a model organic dye, methylene blue (MB) under visible light illumination. Generation of new optical properties (absorption and emission) and functionality (photocatalysis) after citrate functionalization of Mn_2O_3 has also been described in this chapter.

Chapter 7: In this chapter, we have fabricated DSSCs with plasmonic nanoparticles (Al and Au) which exhibit much higher power conversation efficiencies in compared to their counterparts. Steady state and picosecond resolved photoluminescence of the model dye protoporphyrin IX (PP) has also been discussed in this chapter in order to explain improved photovoltaic efficiencies.

References

[1] B. Wu, Y. Kuang, X. Zhang, J. Chen, Noble metal nanoparticles/carbon nanotubes nanohybrids: Synthesis and applications, *Nano Today* 6 (2011) 75-90.

[2] X. Chen, S. S. Mao, Titanium Dioxide Nanomaterials: Synthesis, Properties, Modifications, and Applications, *Chem. Rev.* 107 (2007) 2891-2959.

[3] A.-H. Lu, E. L. Salabas, F. Schüth, Magnetic Nanoparticles: Synthesis, Protection, Functionalization, and Application, *Angew. Chem.* 46 (2007) 1222-1244.

[4] J. Gao, H. Gu, B. Xu, Multifunctional Magnetic Nanoparticles: Design, Synthesis, and Biomedical Applications, *Acc. Chem. Res.* 42 (2009) 1097-1107.

[5] R. Ghosh Chaudhuri, S. Paria, Core/Shell Nanoparticles: Classes, Properties, Synthesis Mechanisms, Characterization, and Applications, *Chem. Rev.* 112 (2012) 2373-2433.

[6] X. Wang, J. Zhuang, Q. Peng, Y. Li, A general strategy for nanocrystal synthesis, *Nature* 437 (2005) 121-124.

[7] W. K. Choi, T. H. Liew, H. G. Chew, F. Zheng, C. V. Thompson, Y. Wang, M. H. Hong, X. D. Wang, L. Li, J. Yun, A Combined Top-Down and Bottom-Up Approach for Precise Placement of Metal Nanoparticles on Silicon, *Small* 4 (2008) 330-333.

[8] G. Liu, N. Hoivik, K. Wang, H. Jakobsen, Engineering TiO_2 Nanomaterials for CO_2 Conversion/Solar Fuels, *Sol. Energ. Mat. Sol. Cells* 105 (2012) 53-68.

[9] J. A. Turner, A Realizable Renewable Energy Future, *Science* 285 (1999) 687-689.

[10] M. Mikkelsen, M. Jorgensen, F. C. Krebs, The Teraton Challenge. A Review of Fixation and Transformation of Carbon Dioxide, *Energy Environ. Sci.* 3 (2010) 43-81.

[11] M. J. Bierman, S. Jin, Potential Applications of Hierarchical Branching Nanowires in Solar Energy Conversion, *Energy Environ. Sci.* 2 (2009) 1050-1059.

[12] A. S. Arico, P. Bruce, B. Scrosati, J.-M. Tarascon, W. van Schalkwijk, Nanostructured Materials for Advanced Energy Conversion and Storage Devices, *Nat. Mater.* 4 (2005) 366-377.

[13] P. V. Kamat, Meeting the Clean Energy Demand: Nanostructure Architectures for Solar Energy Conversion, *J. Phys. Chem. C* 111 (2007) 2834-2860.

[14] P. C. Ray, Size and Shape Dependent Second Order Nonlinear Optical Properties of Nanomaterials and Their Application in Biological and Chemical Sensing, *Chem. Rev.* 110 (2010) 5332-5365.

[15] C. Burda, X. Chen, R. Narayanan, M. A. El-Sayed, Chemistry and Properties of Nanocrystals of Different Shapes, *Chem. Rev.* 105 (2005) 1025-1102.

[16] K. L. Kelly, E. Coronado, L. L. Zhao, G. C. Schatz, The Optical Properties of Metal Nanoparticles: The Influence of Size, Shape, and Dielectric Environment, *J. Phys. Chem. B* 107 (2003) 668-677.

[17] Y. S. Wang, P. J. Thomas, P. O'Brien, Optical Properties of ZnO Nanocrystals Doped with Cd, Mg, Mn, and Fe Ions, *J. Phys. Chem. B* 110 (2006) 21412-21415.

[18] S. Sarkar, A. Makhal, T. Bora, K. Lakhsman, A. Singha, J. Dutta, S. K. Pal, Hematoporphyrin–ZnO Nanohybrids: Twin Applications in Efficient Visible-Light Photocatalysis and Dye-Sensitized Solar Cells, *ACS Appl. Mater. Interfaces* 4 (2012) 7027-7035.

[19] D. Wang, B. Fei, L. V. Halig, X. Qin, Z. Hu, H. Xu, Y. A. Wang, Z. Chen, S. Kim, D. M. Shin, Z. Chen, Targeted Iron-Oxide Nanoparticle for Photodynamic Therapy and Imaging of Head and Neck Cancer, *ACS Nano* 8 (2014) 6620-6632.

[20] D. Wang, T. Hu, L. Hu, B. Yu, Y. Xia, F. Zhou, W. Liu, Microstructured Arrays of TiO_2 Nanotubes for Improved Photo-Electrocatalysis and Mechanical Stability, *Adv. Funct. Mater.* 19 (2009) 1930-1938.

[21] S. Jung, K. Yong, Fabrication of CuO-ZnO Nanowires on A Stainless Steel Mesh for Highly Efficient Photocatalytic Applications, *Chem. Commun.* 47 (2011) 2643-2645.

[22] M. Borgwardt, M. Wilke, T. Kampen, S. Mähl, M. Xiao, L. Spiccia, K. M. Lange, I. Y. Kiyan, E. F. Aziz, Charge Transfer Dynamics at Dye-Sensitized ZnO and TiO_2 Interfaces Studied by Ultrafast XUV Photoelectron Spectroscopy, *Sci. Rep.* 6 (2016) 24422.

[23] A. Hagfeldt, G. Boschloo, L. Sun, L. Kloo, H. Pettersson, Dye-Sensitized Solar Cells, *Chem. Rev.* 110 (2010) 6595-6663.

[24] P. Tiwana, P. Docampo, M. B. Johnston, H. J. Snaith, L. M. Herz, Electron Mobility and Injection Dynamics in Mesoporous ZnO, SnO_2, and TiO_2 Films Used in Dye-Sensitized Solar Cells, *ACS Nano* 5 (2011) 5158-5166.

[25] R. L. Milot, G. F. Moore, R. H. Crabtree, G. W. Brudvig, C. A. Schmuttenmaer, Electron Injection Dynamics from Photoexcited Porphyrin Dyes into SnO_2 and TiO_2 Nanoparticles, *J. Phys. Chem. C* 117 (2013) 21662-21670.

[26] S. Ardo, G. J. Meyer, Photodriven Heterogeneous Charge Transfer with Transition-Metal Compounds Anchored to TiO$_2$ Semiconductor Surfaces, *Chem. Soc. Rev.* 38 (2009) 115-164.

[27] M. Grätzel, Solar Energy Conversion by Dye-Sensitized Photovoltaic Cells, *Inorg. Chem.* 44 (2005) 6841-6851.

[28] C. X. Guo, G. H. Guai, C. M. Li, Graphene Based Materials: Enhancing Solar Energy Harvesting, *Adv. Energy Mater.* 1 (2011) 448-452.

[29] S. G. Kumar, L. G. Devi, Review on Modified TiO$_2$ Photocatalysis under UV/Visible Light: Selected Results and Related Mechanisms on Interfacial Charge Carrier Transfer Dynamics, *J. Phys. Chem. A* 115 (2011) 13211-13241.

[30] B. J. Hansen, Y. Liu, R. Yang, Z. L. Wang, Hybrid Nanogenerator for Concurrently Harvesting Biomechanical and Biochemical Energy, *ACS Nano* 4 (2010) 3647-3652.

[31] K. Kabra, R. Chaudhary, R. L. Sawhney, Treatment of Hazardous Organic and Inorganic Compounds through Aqueous-Phase Photocatalysis: A Review, *Ind. Eng. Chem. Res.* 43 (2004) 7683-7696.

[32] W. Guo, X. Xue, S. Wang, C. Lin, Z. L. Wang, An Integrated Power Pack of Dye-Sensitized Solar Cell and Li Battery Based on Double-Sided TiO$_2$ Nanotube Arrays, *Nano Lett.* 12 (2012) 2520-2523.

[33] Q. Zhang, E. Uchaker, S. L. Candelaria, G. Cao, Nanomaterials for Energy Conversion and Storage, *Chem. Soc. Rev.* 42 (2013) 3127-3171.

[34] M. Ni, M. K. H. Leung, D. Y. C. Leung, K. Sumathy, A Review and Recent Developments in Photocatalytic Water-Splitting Using for Hydrogen Production, *Renew. Sustainable Energy Rev.* 11 (2007) 401-425.

[35] Y. Chen, M. Chen, J. Shi, J. Yang, Y. Fan, Pd Nanoparticles on Co Nanofilms as Composite Electrocatalysts for Ethanol Oxidation in Alkaline Solution, *Int. J. Hydrogen Energy* 41 (2016) 17112-17117.

[36] J. Qian, P. Liu, Y. Xiao, Y. Jiang, Y. Cao, X. Ai, H. Yang, TiO$_2$-Coated Multilayered SnO$_2$ Hollow Microspheres for Dye-Sensitized Solar Cells, *Adv. Mater.* 21 (2009) 3663-3667.

[37] A. Fujishima, Electrochemical photolysis of water at a semiconductor electrode, *Nature* 238 (1972) 37-38.

[38] R. Dholam, N. Patel, M. Adami, A. Miotello, Hydrogen Production by Photocatalytic Water-Splitting using Cr- or Fe-doped TiO_2 Composite Thin Films Photocatalyst, *Int. J. Hydrogen Energy* 34 (2009) 5337-5346.

[39] C. Lin, Y. Song, L. Cao, S. Chen, Oxygen Reduction Catalyzed by Au–TiO_2 Nanocomposites in Alkaline Media, *ACS Appl. Mater. Interfaces* 5 (2013) 13305-13311.

[40] A. Burke, S. Ito, H. Snaith, U. Bach, J. Kwiatkowski, M. Grätzel, The Function of a TiO_2 Compact Layer in Dye-Sensitized Solar Cells Incorporating "Planar" Organic Dyes, *Nano Lett.* 8 (2008) 977-981.

[41] Y. Zhang, N. Zhang, Z.-R. Tang, Y.-J. Xu, Graphene Transforms Wide Band Gap ZnS to a Visible Light Photocatalyst. The New Role of Graphene as a Macromolecular Photosensitizer, *ACS Nano* 6 (2012) 9777-9789.

[42] M. Mishra, D.-M. Chun, α-Fe_2O_3 As a Photocatalytic Material: A Review, *Appl. Catal., A.* 498 (2015) 126-141.

[43] S. K. Maji, N. Mukherjee, A. Mondal, B. Adhikary, Synthesis, Characterization and Photocatalytic Activity of α-Fe_2O_3 Nanoparticles, *Polyhedron* 33 (2012) 145-149.

[44] K. M. Lee, C. W. Lai, K. S. Ngai, J. C. Juan, Recent Developments of Zinc Oxide Based Photocatalyst in Water Treatment Technology: A review, *Water Res.* 88 (2016) 428-448.

[45] S. Ghosh, H. Remita, P. Kar, S. Choudhury, S. Sardar, P. Beaunier, P. S. Roy, S. K. Bhattacharya, S. K. Pal, Facile Synthesis of Pd Nanostructures in Hexagonal Mesophases as a Promising Electrocatalyst for Ethanol Oxidation, *J. Mater. Chem. A* 3 (2015) 9517-9527.

[46] S. Ghosh, P. Kar, N. Bhandary, S. Basu, S. Sardar, T. Maiyalagan, D. Majumdar, S. K. Bhattacharya, A. Bhaumik, P. Lemmens, S. K. Pal, Microwave-Assisted Synthesis of Porous Mn_2O_3 Nanoballs as Bifunctional Electrocatalyst for Oxygen Reduction and Evolution Reaction, *Catal. Sci. Technol.* 6 (2016) 1417-1429.

[47] S. Ghosh, P. Kar, N. Bhandary, S. Basu, T. Maiyalagan, S. Sardar, S. K. Pal, Reduced Graphene Oxide Supported Hierarchical Flower like Manganese Oxide as Efficient Electrocatalysts toward Reduction and Evolution of Oxygen, *Int. J. Hydrogen Energy* 42 (2017) 4111-4122.

[48] R. Georgekutty, M. K. Seery, S. C. Pillai, A Highly Efficient Ag-ZnO Photocatalyst: Synthesis, Properties, and Mechanism, *J. Phys. Chem. C* 112 (2008) 13563-13570.

[49] Y. Jiang, Y. Sun, H. Liu, F. Zhu, H. Yin, Solar Photocatalytic Decolorization of C.I. Basic Blue 41 in an Aqueous Suspension of TiO_2–ZnO, *Dyes Pigm.* 78 (2008) 77-83.

[50] C. Wu, L. Shen, Y.-C. Zhang, Q. Huang, Solvothermal Synthesis of Cr-Doped ZnO Nanowires with Visible Light-Driven Photocatalytic Activity, *Mater. Lett.* 65 (2011) 1794-1796.

[51] M. A. Henderson, A Surface Science Perspective on Photocatalysis, *Surf. Sci. Rep.* 66 (2011) 185-297.

[52] P. Kar, S. Sardar, E. Alarousu, J. Sun, Z. S. Seddigi, S. A. Ahmed, E. Y. Danish, O. F. Mohammed, S. K. Pal, Impact of Metal Ions in Porphyrin-Based Applied Materials for Visible-Light Photocatalysis: Key Information from Ultrafast Electronic Spectroscopy, *Chem. Eur. J.* 20 (2014) 10475-10483.

[53] P. Kar, T. K. Maji, J. Patwari, S. K. Pal, Can a Light Harvesting Material be Always Common in Photocatalytic and Photovoltaic Applications?, *Mater. Chem. Phys.,* 200 (2017) 70-77.

[54] D. Chen, H. Feng, J. Li, Graphene Oxide: Preparation, Functionalization, and Electrochemical Applications, *Chem. Rev.* 112 (2012) 6027-6053.

[55] A. K. Geim, K. S. Novoselov, The Rise of Graphene, *Nat. Mater.* 6 (2007) 183-191.

[56] P. Kar, S. Sardar, B. Liu, M. Sreemany, P. Lemmens, S. Ghosh, S. K. Pal, Facile Synthesis of Reduced Graphene Oxide–Gold Nanohybrid for Potential Use in Industrial Waste-Water Treatment, *Sci. Tech. Adv. Mater.* 17 (2016) 375-386.

[57] A. Hameed, T. Montini, V. Gombac, P. Fornasiero, Surface Phases and Photocatalytic Activity Correlation of Bi_2O_3/Bi_2O_{4-x} Nanocomposite, *J. Am. Chem. Soc.* 130 (2008) 9658-9659.

[58] S. Xiao, Y. Li, J. Hu, H. Li, X. Zhang, L. Liu, J. Lian, One-Step Synthesis of Nanostructured Bi-$Bi_2O_2CO_3$-ZnO Composites with Enhanced Photocatalytic Performance, *CrystEngComm* 17 (2015) 3809-3819.

[59] H.-Y. Jiang, J. Liu, K. Cheng, W. Sun, J. Lin, Enhanced Visible Light Photocatalysis of Bi_2O_3 upon Fluorination, *J. Phys. Chem. C* 117 (2013) 20029-20036.

[60] T. W. Kim, K.-S. Choi, Nanoporous $BiVO_4$ Photoanodes with Dual-Layer Oxygen Evolution Catalysts for Solar Water Splitting, *Science* 343 (2014) 990-994.

[61] P. Kar, T. K. Maji, R. Nandi, P. Lemmens, S. K. Pal, In-Situ Hydrothermal Synthesis of Bi–$Bi_2O_2CO_3$ Heterojunction Photocatalyst with Enhanced Visible Light Photocatalytic Activity, *Nano-Micro Lett.* 9 (2016) 18.

[62] P. Li, C. Nan, Z. Wei, J. Lu, Q. Peng, Y. Li, Mn_3O_4 Nanocrystals: Facile Synthesis, Controlled Assembly, and Application, *Chem. Mater.* 22 (2010) 4232-4236.

[63] T. Kim, E. Momin, J. Choi, K. Yuan, H. Zaidi, J. Kim, M. Park, N. Lee, M. T. McMahon, A. Quinones-Hinojosa, J. W. M. Bulte, T. Hyeon, A. A. Gilad, Mesoporous Silica-Coated Hollow Manganese Oxide Nanoparticles as Positive T1 Contrast Agents for Labeling and MRI Tracking of Adipose-Derived Mesenchymal Stem Cells, *J. Am. Chem. Soc.* 133 (2011) 2955-2961.

[64] P. Kar, S. Sardar, S. Ghosh, M. R. Parida, B. Liu, O. F. Mohammed, P. Lemmens, S. K. Pal, Nano Surface Engineering of Mn_2O_3 for Potential Light-Harvesting Application, *J. Mater. Chem. C* 3 (2015) 8200-8211.

[65] J. Villanueva-Cab, J. L. Montaño-Priede, U. Pal, Effects of Plasmonic Nanoparticle Incorporation on Electrodynamics and Photovoltaic Performance of Dye Sensitized Solar Cells, *J. Phys. Chem. C* 120 (2016) 10129-10136.

[66] H. Choi, W. T. Chen, P. V. Kamat, Know Thy Nano Neighbor. Plasmonic versus Electron Charging Effects of Metal Nanoparticles in Dye-Sensitized Solar Cells, *ACS Nano* 6 (2012) 4418-4427.

[67] M. D. Brown, T. Suteewong, R. S. S. Kumar, V. D'Innocenzo, A. Petrozza, M. M. Lee, U. Wiesner, H. J. Snaith, Plasmonic Dye-Sensitized Solar Cells Using Core−Shell Metal−Insulator Nanoparticles, *Nano Lett.* 11 (2011) 438-445.

[68] M. K. Gangishetty, K. E. Lee, R. W. J. Scott, T. L. Kelly, Plasmonic Enhancement of Dye Sensitized Solar Cells in the Red-to-near-Infrared Region using Triangular Core–Shell $Ag@SiO_2$ Nanoparticles, *ACS Appl. Mater. Interfaces* 5 (2013) 11044-11051.

[69] P. Kar, T. K. Maji, P. K. Sarkar, S. Sardar, S. K. Pal, Direct Observation of Electronic Transition-Plasmon Coupling for Enhanced Electron Injection in Dye-Sensitized Solar Cells, *RSC Adv.* 6 (2016) 98753-98760.

Chapter 2

An Overview of Steady-State and Dynamical
Tools and Systems

In order to investigate the ultrafast processes involved in the light harvesting nanomaterials, different steady-state and dynamical tools have been employed. These include solvation dynamics, fluorescence anisotropy, photoinduced electron transfer (PET), Förster resonance energy transfer (FRET) and nanosurface energy transfer (NSET). Koutecky-Levich equation has been used to determine the electron transfer numbers per oxygen molecule involved in oxygen reduction reaction (ORR). Langmuir−Hinshelwood (L−H) model for surface catalysis, photocurrent−voltage ($I−V$) characterization, photovoltage decay measurement of photovoltaic solar cells. In this chapter, we have included a brief discussion about the above mentioned tools. Overviews of the various systems, probes and solar cell dyes used in the studies have also been provided.

2.1. Steady-State and Dynamical Tools:

2.1.1. Solvation Dynamics:

2.1.1.1. Theory: Solvation dynamics refer to the process of reorganization of solvent dipoles around a dipole created instantaneously or an electron/proton injected suddenly in a polar liquid. In order to understand the meaning and scope of solvation dynamics, let us first visualize the physical essence of the dynamical processes involved for a solute molecule in a polar solvent [1-3]. A change in the probe (solute) is made at time t = 0, by an excitation pulse, which leads to the creation of a dipole. This dipole gives rise to an instantaneous electric field on the solvent molecules. The interaction of permanent dipoles of the solvent with the instantaneously created electric field, shifts the free energy minimum of the solvent to a non-zero value of the polarization. The solvent motion is crucial (Figure 2.1). Since the probe is excited instantaneously (a Franck-Condon transition as far as the nuclear degrees of freedom are

concerned), the solvent molecules at t = 0 find themselves in a relatively high-energy configuration. Subsequently, the solvent molecules begin to move and rearrange themselves to reach their new equilibrium positions (Figure 2.2). The nuclear motion involved can be broadly classified into rotational and translational motions.

When the solvent is bulk water, rotational motion would also include hindered rotation and libration, while translation would include the intermolecular vibration due to the extensive hydrogen bonding. The two specific motions, libration and intermolecular vibration, are relatively high in frequency and are expected to play a dominant role in the initial part of solvation [4]. The molecular motions involved are shown schematically in
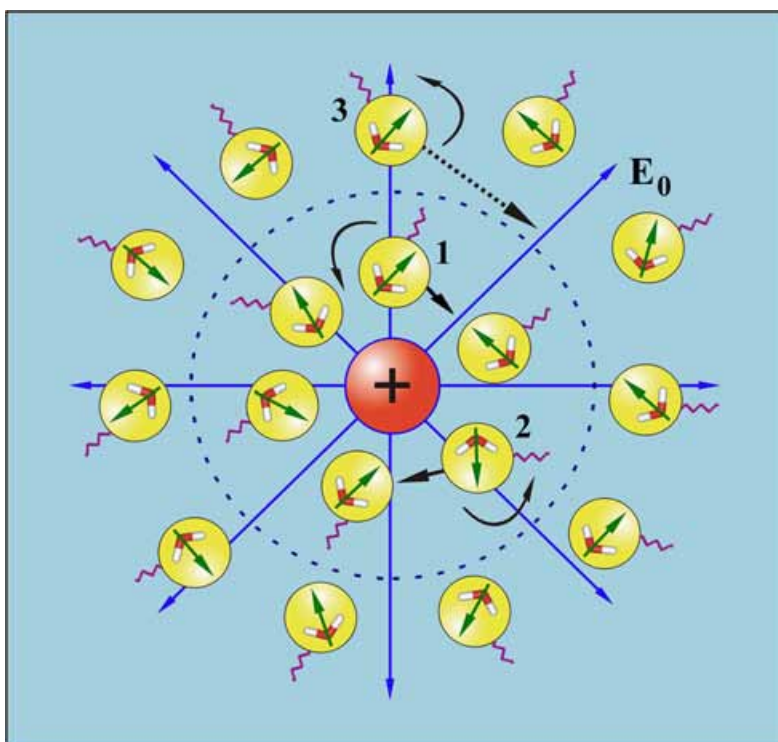
Figure 2.1. *Schematic illustration of solvation of an ion (or dipole) by water. The neighbouring molecules (numbered 1 and 2) can either rotate or translate to attain the minimum energy configuration. On the other hand, distant water molecule 3 can only rotate to attain minimum energy configuration. The field is shown as E_0. The springs connected to the molecules are meant to denote hydrogen bonding.*

Figure 2.1, and in Figure 2.3, we show a typical solvation time correlation function. For clarity, we approximate the motions responsible for the decay in different regions.

A simple way to address the dynamics of polar solvation is to start with the following expression for the solvation energy, $E_{solv}(t)$ [5],

$$E_{solv}(t) = -\frac{1}{2}\int dr\, E_0(r)\cdot P(r,t) \qquad (2.1)$$

where $E_0(r)$ is the instantaneously created, position-dependent electric field from the ion or the dipole of the solute and $P(r,t)$ is the position and time-dependent polarization.
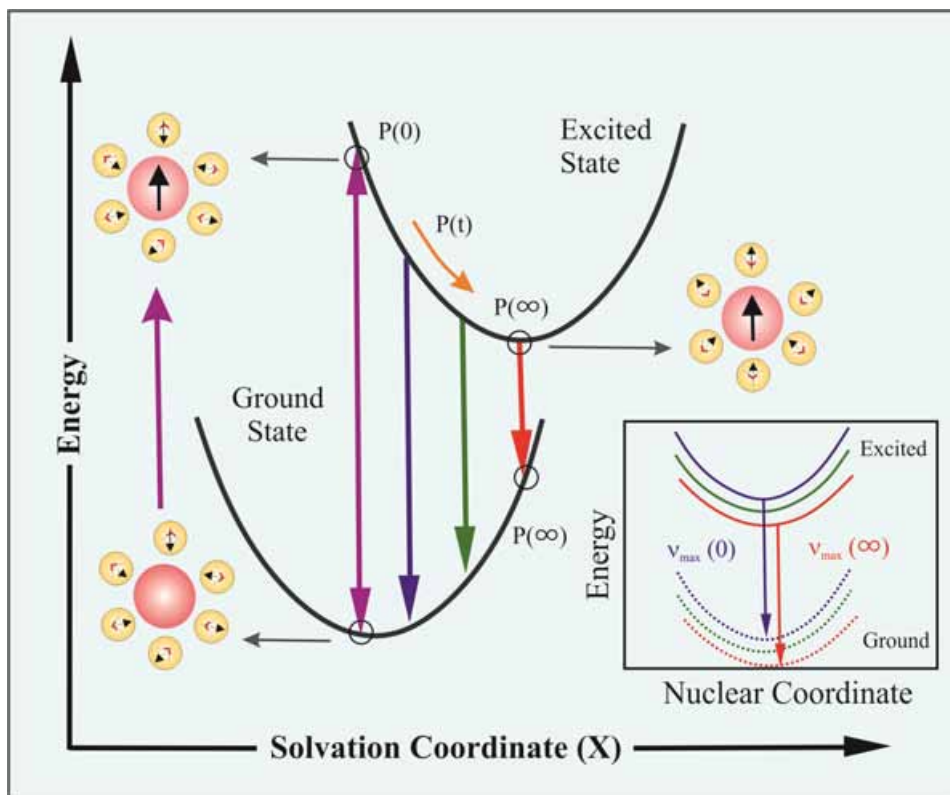
Figure 2.2. Schematic representation of the potential energy surfaces involved in solvation dynamics showing the water orientational motions along the solvation coordinate together with instantaneous polarization P. In the inset we show the change in the potential energy along the intramolecular nuclear coordinate. As solvation proceeds the energy of the solute comes down giving rise to a red shift in the fluorescence spectrum. Note the instantaneous P, e.g., P(∞), on the two connected potentials.

The latter is defined by the following expression,

$$P(r,t) = \int d\Omega\, \mu(\Omega)\, \rho\,(r,\Omega,t) \qquad (2.2)$$

where $\mu(\Omega)$ is the dipole moment vector of a molecule at position r, and $\rho\,(r,\Omega,t)$ is the position, orientation and time-dependent density. Therefore, the time dependence of the solvation energy is determined by the time dependence of polarization that is in turn determined by the time dependence of the density. If the perturbation due to the probe on dynamics of bulk water is

negligible, then the time dependence of polarization is dictated by the natural dynamics of the liquid.

The theoretical analysis of the time-dependent density is usually carried out using a molecular hydrodynamic approach that is based on the basic conservation (density,
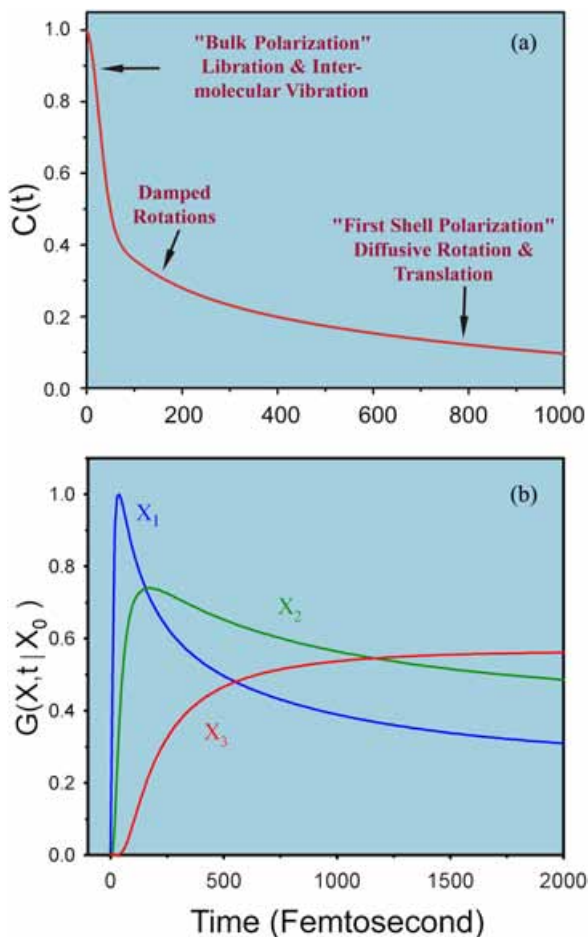
Figure 2.3. *(a) A typical solvation time correlation function for water is shown here. The time correlation function exhibits three distinct regions: The initial ultrafast decay, an intermediate decay of about 200 fs and the last slow decay with time constant of 1 ps. The physical origin of each region is indicated on the plot itself; see text. (b) Green's function $G(X, t|X_0)$ for population relaxation along the solvation coordinate (X) is plotted against time in femtosecond. In G, X_0 is the initial position at t = 0. This Figure shows the position and time dependence of the population fluorescence intensity. At early times (when the population is at X_1) there is ultrafast rise followed by an ultrafast decay. At intermediate times (when the population is at X_2) there is a rise followed by a slow decay as shown by the green line. At long times when the population is nearly relaxed (position X_3, red line) we see only a rise.*

momentum and energy) laws and includes the effects of intermolecular (both spatial and orientational) correlations. The latter provides the free energy surface on which solvation proceeds. The equation of motion of the density involves both orientational and translational

25

motions of the solvent molecules. The details of the theoretical development are reported in literature [1]; here we shall present a simple physical picture of the observed biphasic solvation dynamics.

Within linear response theory, the solvation correlation function is directly related to the solvation energy as,

$$C(t) = \frac{\langle \delta E(0) \cdot \delta E(t) \rangle}{\langle \delta E^2 \rangle} = \frac{\langle E(t) \rangle - \langle E(\infty) \rangle}{\langle E(0) \rangle - \langle E(\infty) \rangle} \qquad (2.3)$$

where δE is the fluctuation of solvation energy from the average, equilibrium value. Note that the equality in equation (2.3) indicates the direct relation for the average of the fluctuations over the equilibrium distribution (left) and the non-equilibrium function (right) which relates to observables; without $\langle E(\infty) \rangle$ the correspondence is clear, and $\langle E(\infty) \rangle$ is rigorously the result of the equilibrium term in the numerator and for normalization in the denominator.

The ultrafast component in the solvation time correlation function (see Figure 2.3a), originates from the initial relaxation in the steep collective solvation potential. The collective potential is steep because it involves the total polarization of the system [1, 3]. This initial relaxation couples mainly to the hindered rotation (i.e., libration) and the hindered translation (i.e., the intermolecular vibration), which are the available high frequency modes of the solvent; neither long amplitude rotation nor molecular translation are relevant here. The last part in the decay of the solvation correlation function involves larger amplitude rotational and translational motions of the nearest neighbour molecules in the first solvation shell. In the intermediate time, one gets contributions from the moderately damped rotational motions of water molecules. In a sense, with the above description one recovers the famous Onsager's "inverse snow-ball" picture of solvation [6]. The slowest time constant is ~1 ps, which is determined by the individual rotational and translational motions of the molecules in the "first solvation shell" nearly close to the probe. The femtosecond component is dominated by the high frequency hindered rotational and translational (vibration) polarization [7].

Figure 2.2 shows a schematic of the solvation potential and the orientational motions for the water molecules involved. From the shape of the potential, it can be seen that the transient behavior for the population during solvation should be a decay function on the blue edge of the spectrum and a rise function on the red edge. These wavelength-dependent features can be

explained nicely within a generalized model of relaxation in which a Gaussian wave packet relaxes on a harmonic surface. The relaxation is non-exponential and a Green's function can describe the approach of the wave packet along the solvation coordinate, X, to its equilibrium value. For the general non-Markovian case it is given by [8],

$$G(X,t|X_0) = \frac{1}{\sqrt{2\pi\langle X^2\rangle[1-C^2(t)]}} \exp\left[-\frac{[X-X_0 C(t)]^2}{2\langle X^2\rangle[1-C^2(t)]}\right] \qquad (2.4)$$

where $\langle X^2\rangle$ is the equilibrium mean square fluctuation of the polarization coordinate in the excited state surface, C(t) is the solvation correlation function described in equation (2.3) and X_0 is the initial value of the packet on the solvation coordinate. Equation (2.4) describes the motion of the wave packet (polarization density) beginning at t = 0 (X_0) as a delta function and according to the solvation time correlation function. As t→∞, C(t)→0 and we recover the standard Gaussian distribution. Initially, (t→0), the exponential is large, so the decay is ultrafast, but at long times, the relaxation slows down, ultimately to appear as a rise. In Figure 2.3b, we present calculations of G(X, t | X_0) at different positions along the solvation coordinate giving decays at X_1 and X_2, but with different time constants, and a rise at X_3, as demonstrated experimentally.

2.1.1.2. Experimental Methods: In order to study solvation stabilization of a probe in an environment, a number of fluorescence transients are taken at different wavelengths across the emission spectrum of the probe. As described earlier, blue and red ends of the emission spectrum are expected to show decay and rise, respectively in the transients. The observed fluorescence transients are fitted by using a nonlinear least square fitting procedure to a function

$$\left(X(t) = \int_0^t E(t')R(t-t')dt'\right) \qquad (2.5)$$

comprising of convolution of the instrument response function (IRF) (E(t)) with a sum of exponentials

$$\left(R(t) = A + \sum_{i=1}^{N} B_i \exp\left(-t/\tau_i\right)\right) \qquad (2.6)$$

with pre-exponential factors (B_i), characteristic lifetimes (τ_i) and a background (A). Relative concentration in a multi-exponential decay is finally expressed as;

$$\alpha_n = \frac{B_n}{\sum\limits_{i=1}^{N} B_i}. \tag{2.7}$$

The relative contribution of a particular decay component (f_n) in the total fluorescence is defined as,

$$f_n = \frac{\tau_n B_n}{\sum\limits_{i=1}^{N} B_i \tau_i} \times 100. \tag{2.8}$$

The quality of the curve fitting is evaluated by reduced chi-square (0.9-1.1) and residual data. The purpose of the fitting is to obtain the decays in an analytical form suitable for further data analysis.

To construct time resolved emission spectra (TRES) we follow the technique described in references [9]. As described above, the emission intensity decays are analyzed in terms of the multi-exponential model,

$$I(\lambda, t) = \sum\limits_{i=1}^{N} \alpha_i(\lambda) \exp(-t/\tau_i(\lambda)) \tag{2.9}$$

where $\alpha_i(\lambda)$ are the pre-exponential factors, with $\Sigma \alpha_i(\lambda) = 1.0$. In this analysis we compute a new set of intensity decays, which are normalized so that the time-integrated intensity at each wavelength is equal to the steady-state intensity at that wavelength. Considering $F(\lambda)$ to be the steady-state emission spectrum, we calculate a set of $H(\lambda)$ values using,

$$H(\lambda) = \frac{F(\lambda)}{\int\limits_{0}^{\infty} I(\lambda, t) dt} \tag{2.10}$$

which for multiexponential analysis becomes,

$$H(\lambda) = \frac{F(\lambda)}{\sum\limits_{i} \alpha_i(\lambda) \tau_i(\lambda)} \tag{2.11}$$

Then, the appropriately normalized intensity decay functions are given by,

$$I'(\lambda, t) = H(\lambda) I(\lambda, t) = \sum\limits_{i=1}^{N} \alpha'_i(\lambda) \exp\left(-t/\tau_i(\lambda)\right) \tag{2.12}$$

where $\alpha'_i(\lambda) = H(\lambda) \alpha_i(\lambda)$. The values of $I'(\lambda,t)$ are used to calculate the intensity at any wavelength and time, and thus the TRES. The values of the emission maxima and spectral width

are determined by nonlinear least-square fitting of the spectral shape of the TRES. The spectral shape is assumed to follow a lognormal line shape ,

$$I(\bar{v}) = I_0 \exp\left\{-\left[\ln 2\left(\frac{\ln(\alpha+1)}{b}\right)^2\right]\right\}$$ (2.13)

with $\alpha = \frac{2b(\bar{v} - \overline{v_{max}})}{\Delta} - 1$ where I_0 is amplitude, $\bar{v}_{max}$ is the wavenumber of the emission maximum and spectral width is given by, $\Gamma = \Delta \frac{\sinh(b)}{b}$. The terms b and Δ are asymmetry and width parameters, respectively and equation (2-9) reduces to a Gaussian function for $b = 0$.

The time-dependent fluorescence Stokes shifts, as estimated from TRES are used to construct the normalized spectral shift correlation function or the solvent correlation function C(t) and is defined as,

$$C(t) = \frac{\bar{v}(t) - \bar{v}(\infty)}{\bar{v}(0) - \bar{v}(\infty)}$$ (2.14)

where, $\bar{v}(0)$, $\bar{v}(t)$ and $\bar{v}(\infty)$ are the emission maxima (in cm^{-1}) of the TRES at time zero, t and infinity, respectively. The $\bar{v}(\infty)$ value is considered to be the emission frequency beyond which insignificant or no spectral shift is observed. The C(t) function represents the temporal response of the solvent relaxation process, as occurs around the probe following its photoexcitation and the associated change in the dipole moment.

In order to further investigate possible heterogeneity in the positional distribution of fluoroprobes at the interfaces of biomimicking self-assemblies, we follow time-resolved area normalized emission spectroscopy (TRANES), which is a well-established technique [10] and is a modified version of TRES. TRANES were constructed by normalizing the area of each spectrum in TRES such that the area of the spectrum at time t is equal to the area of the spectrum at t = 0. A useful feature of this method is the presence of an isoemissive point in the spectra involve emission from two species, which are kinetically coupled either irreversibly or reversibly or not coupled at all.

2.1.2. Fluorescence Anisotropy: Anisotropy is defined as the extent of polarization of the emission from a fluorophore. Anisotropy measurements are commonly used in biochemical

applications of fluorescence. It provides information about the size and shape of proteins or the rigidity of various molecular environments. Anisotropy measurements have also been used to measure protein-protein associations, fluidity of membranes and for immunoassays of numerous substances. These measurements are based on the principle of photoselective excitation of those fluorophore molecules whose absorption transition dipoles are parallel to the electric vector of polarized excitation light. In an isotropic solution, fluorophores are oriented randomly. However, upon selective excitation, partially oriented population of fluorophores with polarized fluorescence emission results. The relative angle between the absorption and emission transition dipole moments determines the maximum measured anisotropy (r_0). The fluorescence anisotropy (r) and polarization (P) are defined by,

$$r = \frac{I_{II} - I_{\perp}}{I_{II} + 2I_{\perp}} \qquad (2.15)$$

$$\text{and} \quad P = \frac{I_{II} - I_{\perp}}{I_{II} + I_{\perp}} \qquad (2.16)$$

where I_{II} and $I_{\perp}$ are the fluorescence intensities of vertically and horizontally polarized emission when the fluorophore is excited with vertically polarized light. Polarization and anisotropy are interrelated as,

$$r = \frac{2P}{3 - P} \qquad (2.17)$$

$$\text{and} \quad P = \frac{3r}{2 + r} \qquad (2.18)$$

Although polarization and anisotropy provides the same information, anisotropy is preferred since the latter is normalized by total fluorescence intensity ($I_T = I_{II} + 2I_{\perp}$) and in case of multiple emissive species anisotropy is additive while polarization is not. Several phenomena, including rotational diffusion and energy transfer, can decrease the measured anisotropy to values lower than maximum theoretical values. Following a pulsed excitation the fluorescence anisotropy, r(t) of a sphere is given by,

$$r(t) = r_0 \exp\left(-t/\tau_{rot}\right) \qquad (2.19)$$

where r_0 is the anisotropy at time t = 0 and τ_{rot} is the rotational correlation time of the sphere.

2.1.2.1. Theory: For a radiating dipole the intensity of light emitted is proportional to the square of the projection of the electric field of the radiating dipole onto the transmission axis of the polarizer. The intensity of parallel and perpendicular projections are given by,

$$I_{\text{II}}(\theta, \psi) = \cos^2 \theta \tag{2.20}$$

$$I_{\perp}(\theta, \psi) = \sin^2 \theta \sin^2 \psi \tag{2.21}$$

where θ and ψ are the orientational angles of a single fluorophore relative to the z and y-axis, respectively (Figure 2.4a). In solution, fluorophores remain in random distribution and the anisotropy is calculated by excitation photoselection. Upon photoexcitation by polarized light, the molecules having absorption transition moments aligned parallel to the electric vector of the polarized light have the highest probability of absorption. For the excitation polarization along z-axis, all molecules having an angle ψ with respect to the y-axis will be excited. The population will be symmetrically distributed about the z-axis. For experimentally accessible molecules, the value of ψ will be in the range from 0 to 2π with equal probability. Thus, the ψ dependency can be eliminated.

$$\left\langle \sin^2 \psi \right\rangle = \frac{\displaystyle\int_0^{2\pi} \sin^2 \psi \, d\psi}{\displaystyle\int_0^{2\pi} d\psi} = \frac{1}{2} \tag{2.22}$$

$$\text{and } I_{\text{II}}(\theta) = \cos^2 \theta \tag{2.23}$$

$$I_{\perp}(\theta) = \frac{1}{2} \sin^2 \theta \tag{2.24}$$

Consider a collection of molecules oriented relative to the z-axis with probability $f(\theta)$. Then, measured fluorescence intensities for this collection after photoexcitation are,

$$I_{\text{II}} = \int_0^{\pi/2} f(\theta) \cos^2 \theta \, d\theta = k \left\langle \cos^2 \theta \right\rangle \tag{2.25}$$

$$I_{\perp} = \frac{1}{2} \int_0^{\pi/2} f(\theta) \sin^2 \theta \, d\theta = \frac{k}{2} \left\langle \sin^2 \theta \right\rangle \tag{2.26}$$
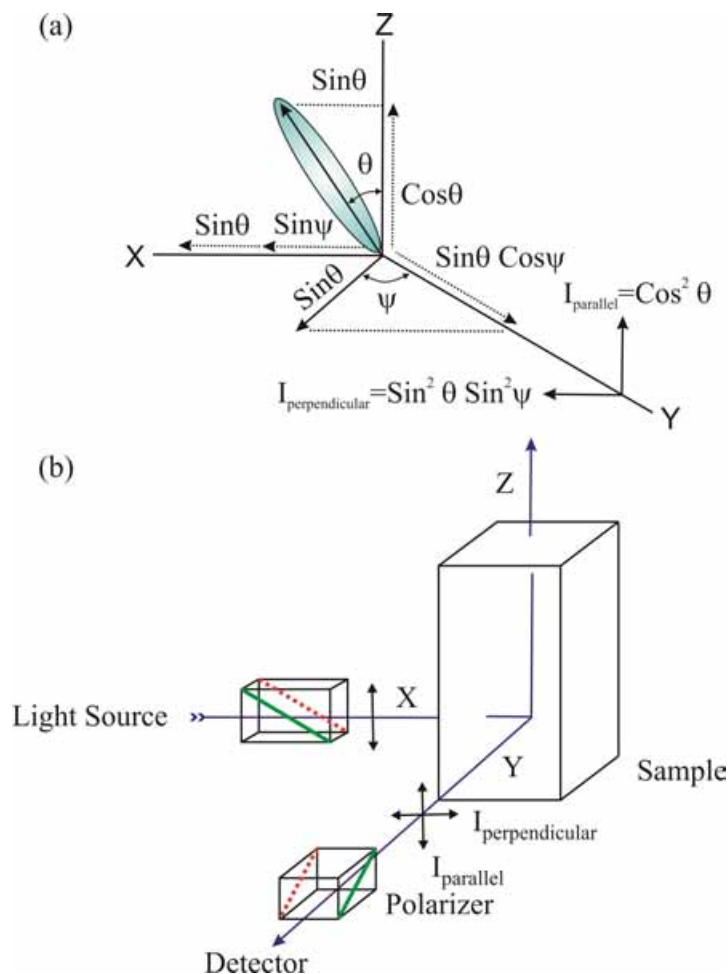
Figure 2.4. *(a) Emission intensity of a single fluorophore (blue ellipsoid) in a coordinate system. (b) Schematic representation of the measurement of fluorescence anisotropy.*

where $f(\theta)d\theta$ is the probability that a fluorophore is oriented between θ and $\theta+d\theta$ and is given by,

$$f(\theta)d\theta = \cos^2\theta \sin\theta d\theta \qquad (2.27)$$

k is the instrumental constant. Thus, the anisotropy (r) is defined as,

$$r = \frac{3\langle \cos^2\theta \rangle - 1}{2} \qquad (2.28)$$

when $\theta = 54.7°$ i.e. when $\cos^2\theta = 1/3$, the complete loss of anisotropy occurs. Thus, the fluorescence taken at $\theta = 54.7°$ with respect to the excitation polarization is expected to be free from the effect of anisotropy and is known as magic angle emission. For collinear absorption and emission dipoles, the value of $\langle \cos^2\theta \rangle$ is given by the following equation,

$$\left\langle \cos^2 \theta \right\rangle = \frac{\int\limits_0^{\pi/2} \cos^2 \theta f(\theta) d\theta}{\int\limits_0^{\pi/2} f(\theta) d\theta} \tag{2.29}$$

Substituting equation (2.27) in equation (2.29) one can get the value of $<\cos^2\theta> = 3/5$ and anisotropy value to be 0.4 (from equation (2.28)). This is the maximum value of anisotropy obtained when the absorption and emission dipoles are collinear and when no other depolarization process takes place. However, for most fluorophore, the value of anisotropy is less than 0.4 and it is dependent on the excitation wavelength. It is demonstrated that as the displacement of the absorption and emission dipole occurs by an angle γ relative to each other, it causes further loss of anisotropy (reduction by a factor 2/5) [11] from the value obtained from equation (2.28). Thus, the value of fundamental anisotropy, r_0 is given by,

$$r_0 = \frac{2}{5}\left(\frac{3\cos^2 \gamma - 1}{2} \right) \tag{2.30}$$

For any fluorophore randomly distributed in solution, with one-photon excitation, the value of r_0 varies from -0.20 to 0.40 for γ values varying from 90° to 0°.

2.1.2.2. Experimental Methods: For time resolved anisotropy (r(t)) measurements (Figure 2.4b), emission polarization is adjusted to be parallel and perpendicular to that of the excitation polarization. Spencer and Weber [12] have derived the relevant equations for the time dependence of $I_{II}(t)$ (equation (2.31)) and $I_{\perp}(t)$ (equation (2.32)) for single rotational and fluorescence relaxation times, τ_{rot} and τ_f, respectively,

$$I_{II}(t) = \exp(-t/\tau_f)(1 + 2r_0 \exp(-t/\tau_{rot})) \tag{2.31}$$

$$I_{\perp}(t) = \exp(-t/\tau_f)(1 - r_0 \exp(-t/\tau_{rot})) \tag{2.32}$$

The total fluorescence is given by,

$$F(t) = I_{II}(t) + 2I_{\perp}(t) = 3\exp(-t/\tau_f) = F_0 \exp(-t/\tau_f) \tag{2.33}$$

The time dependent anisotropy, r(t) is given by,

$$r(t) = \frac{I_{II}(t) - I_{\perp}(t)}{I_{II}(t) + 2I_{\perp}(t)} = r_0 \exp(-t/\tau_{rot}) \tag{2.34}$$

33

F(t) depends upon τ_f and r(t) depends upon τ_{rot} so that these two lifetimes can be separated. This separation is not possible in steady-state measurements. It should be noted that the degree of polarization (P) is not independent of τ_f and is therefore not as useful quantity as r. For reliable measurement of r(t), three limiting cases can be considered.

(a) If $\tau_f < \tau_{rot}$, the fluorescence decays before the anisotropy decays, and hence only r_0 can be measured.

(b) If $\tau_{rot} < \tau_f$, in contrast to steady-state measurements, τ_{rot} can be measured in principle. The equations (2.31) and (2.32) show that the decay of the parallel and perpendicular components depends only upon τ_{rot}. The only experimental disadvantage of this case is that those photons emitted after the period of a few times τ_{rot} can not contribute to the determination of τ_{rot}, but provided the signal-to-noise ratio is favorable, this need not be of great concern.

(c) If $\tau_{rot} \approx \tau_f$, then it becomes the ideal situation since almost all photons are counted within the time (equal to several rotational relaxation times) in which r(t) shows measurable changes.

For systems with multiple rotational correlation times, r(t) is given by,

$$r(t) = r_0 \sum_i \beta_i e^{-t/\tau_i} \tag{2.35}$$

where $\sum_i \beta_i = 1$. It should be noted that the instrument monitoring the fluorescence, particularly the spectral dispersion element, responds differently to different polarizations of light, thus emerging the need for a correction factor. For example, the use of diffraction gratings can yield intensities of emission, which depend strongly upon orientation with respect to the plane of the grating. It is inevitably necessary when using such instruments to correct for the anisotropy in response. This instrumental anisotropy is usually termed as G-factor (grating factor) and is defined as the ratio of the transmission efficiency for vertically polarized light to that for horizontally polarized light ($G = I_{II}/I_{\perp}$). Hence, values of fluorescence anisotropy, r(t) corrected for instrumental response, would be given by [11],

$$r(t) = \frac{I_{II}(t) - GI_{\perp}(t)}{I_{II}(t) + 2GI_{\perp}(t)} \tag{2.36}$$

The G-factor at a given wavelength can be determined by exciting the sample with horizontally polarized excitation beam and collecting the two polarized fluorescence decays, one parallel and other perpendicular to the horizontally polarized excitation beam. G-factor can also be determined following longtime tail matching technique . If $\tau_{rot} < \tau_f$, it can be seen that the curves for $I_{\parallel}(t)$ and $I_{\perp}(t)$ should become identical. If in any experiment they are not, it can usually be assumed that this is due to a non-unitary G-factor. Hence normalizing the two decay curves on the tail of the decay eliminates the G-factor in the anisotropy measurement.

2.1.3. Photoinduced Electron Transfer (PET): PET can be described most simply as the movement of an electron, caused by the absorption of light, from an electron-rich species (a donor D) to an electron deficient species (an acceptor A), as shown in equation 2.37.

$$D + A \rightarrow D^+ + A^- \tag{2.37}$$

The first law of photochemistry tells us that a photoinduced process must be initiated by the absorption of light. In PET, the absorbing species can either be a donor, the acceptor, or a ground-state complex between the donor and acceptor, often referred to as a charge transfer complex. These possibilities are shown in equations 2.38−2.40.

$$D \xrightarrow{h\upsilon} D^* + A \longrightarrow D^+ + A^- \tag{2.38}$$

$$A \xrightarrow{h\upsilon} A^* + D \longrightarrow D^+ + A^- \tag{2.39}$$

$$(D \cdots A) \xrightarrow{h\upsilon} (D \cdots A)^* \longrightarrow D^+ + A^- \tag{2.40}$$
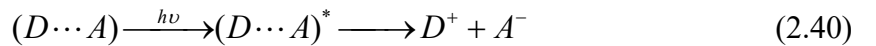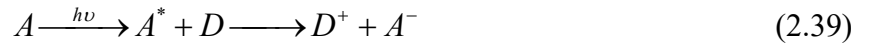
Transports of charges or excitons are commonly seen fundamental processes in many optoelectronic devices as well as biological systems. The creation, diffusion, and annihilation for excitons and the mobility of charges are some of the key processes in many devices that interconvert electric and light energies [13, 14]. PET is an important process in many biochemical systems, such as those in respiration and photosynthesis [15]. To gain a deep understanding for these systems, it is important to describe the rates of these processes with a few empirically derived parameters [16]. Therefore, it has become increasingly important to develop computational techniques that allow us to calculate the rate of charge or energy transport. In our systems the apparent rate constants, k_{nr}, were determined for the nonradiative processes by comparing the lifetimes of donor in the absence (τ_0) and in the presence (τ) of an acceptor, using equation 2.41 [17].

$$k_{nr} = 1/\langle \tau \rangle - 1/\langle \tau_0 \rangle \qquad (2.41)$$

2.1.4. Förster Resonance Energy Transfer (FRET): FRET is an electrodynamic phenomenon involving the nonradiative transfer of the excited state energy from the donor dipole (D) to an acceptor dipole (A) in the ground-state (Figure 2.5a). FRET has been widely used in fluorescence applications including medical diagnostics, DNA analysis and optical imaging. Since, FRET can measure the size of a protein molecule or the thickness of a membrane, it is also known as "spectroscopic ruler" [18]. FRET is very often used to measure the distance between two sites on a macromolecule. Basically, FRET is of two types: (a) homomolecular FRET and (b) heteromolecular FRET. In the former case, the same fluorophore acts both as energy donor and acceptor, while in the latter case two different molecules act as donor and acceptor.

Each donor−acceptor (D−A) pair participating in FRET is characterized by a distance known as Förster distance (R_0) i.e., the D−A separation at which energy transfer is 50% efficient. The R_0 value ranges from 20 to 60 Å. The rate of resonance energy transfer (k_T) from donor to an acceptor is given by,

$$k_T = \frac{1}{\tau_D}\left(\frac{R_0}{r}\right)^6 \qquad (2.42)$$

where, τ_D is the lifetime of the donor in the absence of the acceptor and r is the donor to acceptor (D−A) distance. The rate of transfer of donor energy depends upon the extent of overlap of the emission spectrum of the donor with the absorption spectrum of the acceptor ($J(\lambda)$), the quantum yield of the donor (Q_D), the relative orientation of the donor and acceptor transition dipoles (κ^2) and the distance between the donor and acceptor molecules (r) (Figure 2.5b). In order to estimate FRET efficiency of the donor and hence to determine distances between D−A pairs, the methodology described below is followed [11]. R_0 is given by,

$$R_0 = 0.211\left[\kappa^2 n^{-4} Q_D J(\lambda)\right]^{1/6} \text{ (in Å)} \qquad (2.43)$$

where, n is the refractive index of the medium, Q_D is the quantum yield of the donor and $J(\lambda)$ is the overlap integral. κ^2 is defined as,

$$\kappa^2 = \left(\cos\theta_T - 3\cos\theta_D\cos\theta_A\right)^2 = \left(\sin\theta_D\sin\theta_A\cos\varphi - 2\cos\theta_D\cos\theta_A\right)^2 \qquad (2.44)$$

36

where, θ_T is the angle between the emission transition dipole of the donor and the
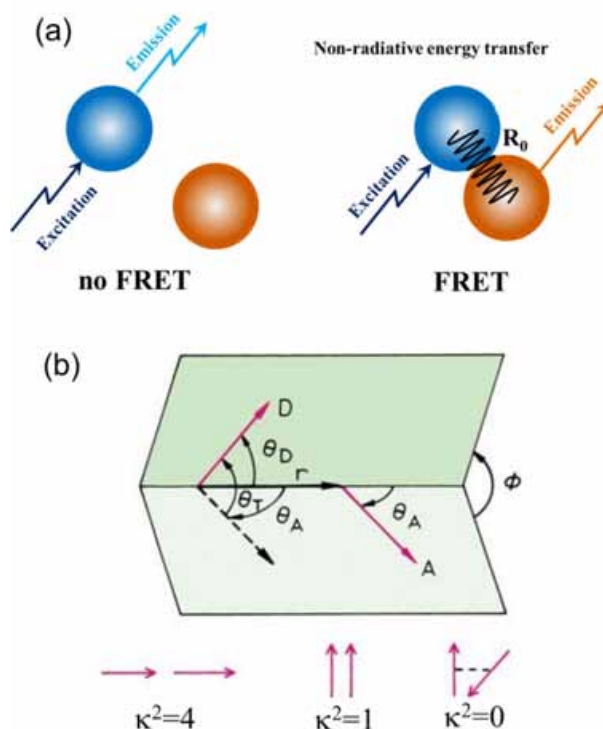
Figure 2.5. *(a) Schematic illustration of the Förster resonance energy transfer (FRET) process. (b) Dependence of the orientation factor κ^2 on the directions of the emission and absorption dipoles of the donor and acceptor, respectively.*

absorption transition dipole of the acceptor, θ_D and θ_A are the angles between these dipoles and the vector joining the donor and acceptor and φ is angle between the planes of the donor and acceptor (Figure 2.5b). κ^2 value can vary from 0 to 4. For collinear and parallel transition dipoles, $\kappa^2 = 4$; for parallel dipoles, $\kappa^2 = 1$; and for perpendicularly oriented dipoles, $\kappa^2 = 0$. For donor and acceptors that randomize by rotational diffusion prior to energy transfer, the magnitude of κ^2 is assumed to be 2/3. $J(\lambda)$, the overlap integral, which expresses the degree of spectral overlap between the donor emission and the acceptor absorption, is given by,

$$J(\lambda) = \frac{\int\limits_0^\infty F_D(\lambda)\varepsilon_A(\lambda)\lambda^4 d\lambda}{\int\limits_0^\infty F_D(\lambda)d\lambda} \tag{2.45}$$

where, $F_D(\lambda)$ is the fluorescence intensity of the donor in the wavelength range of λ to $\lambda+d\lambda$ and it is dimensionless. $\varepsilon_A(\lambda)$ is the extinction coefficient (in $M^{-1}\,cm^{-1}$) of the acceptor at λ. If λ is in nm, then $J(\lambda)$ is in units of $M^{-1}\,cm^{-1}\,nm^4$.

Once the value of R_0 is known, the efficiency of energy transfer can be calculated. The efficiency of energy transfer (E) is the fraction of photons absorbed by the donor which are transferred to the acceptor and is defined as,

$$E = \frac{k_T(r)}{\tau_D^{-1} + k_T(r)} \tag{2.46}$$

or,
$$E = \frac{R_0^6}{r^6 + R_0^6} \tag{2.47}$$

The transfer efficiency is measured by using the relative fluorescence intensity of donor, in the absence (F_D) and presence (F_{DA}) of the acceptor as,

$$E = 1 - \frac{F_{DA}}{F_D} \tag{2.48a}$$

For D−A systems decaying with multiexponential lifetimes, E is calculated from the amplitude weighted lifetimes $\langle \tau \rangle = \sum_i \alpha_i \tau_i$ of the donor in absence (τ_D) and presence (τ_{DA}) of the acceptor as,

$$E = 1 - \frac{\tau_{DA}}{\tau_D} \tag{2.48b}$$

The D−A distance can be measured using equations (2.47), (2.48a−b). The distances measured using equations 2.48a−b are revealed as R^S (steady-state measurement) and R^{TR} (time-resolved measurement), respectively.

2.1.5. Nanosurface Energy Transfer (NSET): The D−A separations can also be calculated using another prevailing technique, NSET [19, 20], in which the energy transfer efficiency depends on the inverse of the fourth power of the D−A separation [21]. The NSET technique is based on the model of Persson and Lang [20], which is concerned with the momentum and energy conservation in the dipole-induced formation of electron−hole pairs. Here the rate of energy transfer is calculated by performing a Fermi golden rule calculation for an excited-state material depopulating with the simultaneous scattering of an electron in the nearby metal to

above the Fermi level. The Persson model states that the damping rate to a surface of a noble metal may be calculated by,

$$k_{NSET} = 0.3 \times \left(\frac{\mu^2 \omega}{\hbar \omega_F k_F d^4} \right) \tag{2.49}$$

which can be expressed in more measurable parameters through the use of the Einstein A_{21} coefficient,

$$A_{21} = \frac{\omega^3}{3\varepsilon_0 \hbar \pi c^3} |\mu|^2 \tag{2.50}$$

To give the following rate of energy transfer in accordance with Coulomb's law ($1/4\pi\varepsilon_0$):

$$k_{NSET} = 0.225 \frac{c^3 \Phi_D}{\omega^2 \omega_F k_F d^4 \tau_D} \tag{2.51}$$

where, c is the speed of light, Φ_D is the quantum yield of the donor, ω is the angular frequency for the donor, ω_F is the angular frequency for acceptor, d is the D−A separation, μ is the dipole moment, τ_D is the average lifetime of the donor, and k_F is the Fermi wave-vector [22, 23]. In our studies, we used k_{NSET} as,

$$k_{NSET} = \frac{1}{\tau_{donor-acceptor}} - \frac{1}{\tau_{donor}} \tag{2.52}$$

where, $\tau_{donor-acceptor}$ is the average lifetime of the D−A system [24].

2.1.6. Data Analysis of Time-Resolved Fluorescence Transients: Curve fitting of the time-resolved fluorescence transients were carried out using a nonlinear least square fitting procedure to a function $(X(t) = \int_0^t E(t')R(t-t')dt')$ comprised of convolution of the IRF ($E(t)$) with a sum of exponentials $(R(t) = A + \sum_{i=1}^{N} B_i e^{-t/\tau_i})$ with pre-exponential factors (B_i), characteristic lifetimes (τ_i) and a background (A). Relative concentration in a multiexponential decay is expressed as, $c_n = \frac{B_n}{\sum_{i=1}^{N} B_i} \times 100$. The average lifetime (amplitude-weighted) of a multiexponential decay is expressed as,

$$\tau_{av} = \sum_{i=1}^{N} c_i \tau_i \tag{2.53}$$

2.1.7. Koutecky-Levich Equation: Oxygen can be directly reduced to water with the concomitant consumption of four electrons per O_2 molecule (equation 2.54). Alternatively, oxygen can be reduced indirectly, forming H_2O_2 as an intermediate and only two electrons per O_2 molecule are consumed (equation 2.55):

$$O_2 + 2H_2O + 4e^- \rightarrow H_2O + 4OH^- \tag{2.54}$$

$$O_2 + 2H_2O + 2e^- \rightarrow H_2O_2 + 2OH^- \tag{2.55}$$
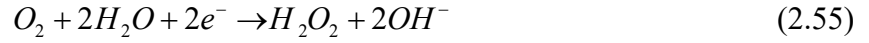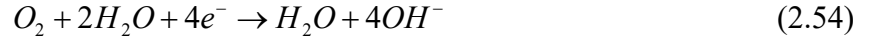
The overall electron transfer numbers per oxygen molecule involved in the typical ORR process were calculated from the slopes of the Koutecky-Levich plots using the following equation [25, 26]:

$$\frac{1}{j} = \frac{1}{j_L} + \frac{1}{j_L} = \frac{1}{B\omega^{\frac{1}{2}}} + \frac{1}{j_k} \tag{2.56}$$

$$B = 0.62nFC_0(D_0)^{\frac{2}{3}}\gamma^{-\frac{1}{6}} \tag{2.57}$$

$$j_k = nFkC_0 \tag{2.58}$$

where, j (mA/cm^2) is the measured current density, j_K and j_L (mA/cm^2) are the kinetic- and diffusion-limiting current densities, ω is the electrode rotating speed in rpm, n is the the number of electrons transferred per oxygen molecule, F is the Faraday constant (F = 96485 C mol^{-1}), C_0 is the bulk concentration of O_2 (1.2 × 10^{-6} mol cm^{-3}), D_0 is diffusion coefficient of O_2 (1.9 × 10^{-5} cm^2 s^{-1}), ν is the kinematic viscosity of the electrolyte (0.01 cm^2 s^{-1}), and k is the electron transfer rate constant, respectively [26].

2.1.8. Langmuir−Hinshelwood (L−H) Model: In the Langmuir−Hinshelwood (L−H) treatment of heterogeneous surface reactions, the rate of the photochemical degradation can be expressed in general terms for both the oxidant (e.g., O_2) and the reductant (e.g., CHCl$_3$) as follows:

$$-\frac{d[\text{Re}d]}{dt} = -\frac{d[Ox]}{dt} = k_d\theta_{\text{Re}d}\theta_{Ox} \tag{2.59}$$

where, k_d is the photodegradation rate constant, θ_{Red} represents the fraction of the electron-donating reductant (e.g., chloroform) sorbed to the surface, and θ_{Ox} represents the corresponding fraction of the electron-accepting oxidant (e.g., oxygen) sorbed to the surface. This treatment is subjected to the assumptions that sorption of both the oxidant and the reductant is a rapid equilibrium process in both the forward and reverse directions and that the rate-determining step

of the reaction involves both species present in a monolayer at the solid-liquid interface. The Langmuir adsorption coefficient, K, for sorption of each reactant is assumed to be readily determined from a classical Langmuir sorption isotherm. In this case, the surface concentration of the reactants is related to their corresponding activities or concentrations in the bulk aqueous phase as follows:

$$R_0 = \frac{dC_0}{dt} = \frac{k_{L-H} K C_0}{1 + K C_0} \qquad (2.60)$$

where, C_0 is the initial concentration of substrate, k_{L-H} is the Langmuir–Hinshelwood (L–H) rate constant, and R_0 is the rate of reaction. If the initial concentration of the solution is sufficiently low ($K C_0 \ll 1$), the equation 2.60 can be simplified to an apparent first-order equation:

$$R_0 = k_{L-H} K C_0 = k_{app} C_0 \qquad (2.61)$$

where, k_{app} is the apparent first-order rate constant. If the initial concentration of the solution is sufficiently high ($K C_0 \gg 1$), the equation 2.60 can be simplified to a zero-order rate equation:

$$R_0 = k_{L-H} \qquad (2.62)$$

The L−H model appears to be a promising tool that has a number of applications in semiconductor photocatalysis such as dye degradation, air purification, water disinfection, hazardous waste remediation and water purification. In addition, the basic research that underlies the application of this potential tool is forging a better understanding of the complex heterogeneous photochemistry of metal oxide systems in multiphasic environments.

2.1.9. Dye-Sensitized Solar Cells (DSSCs): DSSCs [27-29] are potentially inexpensive alternatives to traditional semiconductor solar cells. The essential components of a DSSC are semiconductor metal oxides attached to sensitizing dyes (mostly, ruthenium) and an electrolyte medium (iodine-based). A schematic of the interior of a DSSC showing the principle of how the device operates is shown in Figure 2.6. The typical basic configuration is as follows: at the heart of the device is the metal oxide layer (mostly ZnO/TiO_2), which is deposited on a fluorinated tin oxide (FTO) coated glass substrate. Attached to the surface of the nanocrystalline film is a monolayer of the charge transfer dyes/QDs. Photoexcitation of the latter results in the injection of an electron into the conduction band of the oxide, leaving the dye in its oxidized state. The dye is restored to its ground state by electron transfer from the electrolyte, usually an organic
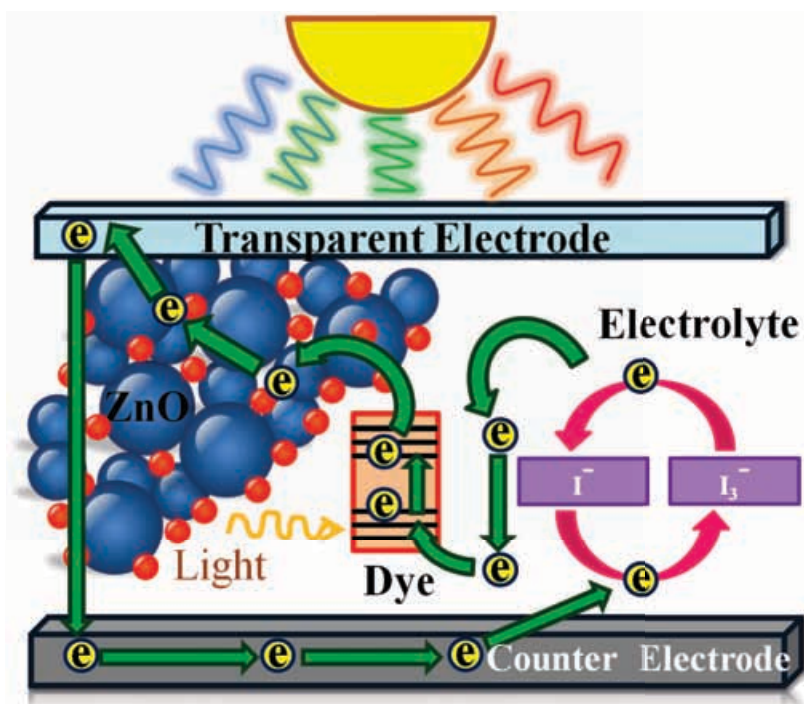
Figure 2.6. *Schematic representation of a ZnO nanoparticle-based DSSC showing different charge migration processes.*

solvent containing the iodide/triiodide (I^-/I_3^-) redox system. The regeneration of the sensitizer by iodide intercepts the recapturing of the conduction band electron by the oxidized dye. The I_3^- ions formed by oxidation of I^- diffuse a short distance (<50 µm) through the electrolyte to the cathode, which is coated with a thin layer of platinum catalyst, where the regenerative cycle is completed by electron transfer to reduce I_3^- to I^-. In order to quantitatively measure the efficacy of a DSSC, photocurrent−voltage (*I−V or J−V*) measurements under simulated sunlight and incident photon-to-current conversion efficiency (IPCE) under monochromatic light are important.

2.1.10. Photocurrent−Voltage (*I−V*) Measurements: A DSSC can be represented by an equivalent electric circuit shown in Figure 2.7, where, I_{ph} is the photocurrent, I_D the diode current, R_S is the series resistance (describes the resistances of the materials) and R_{sh} the shunt resistance.
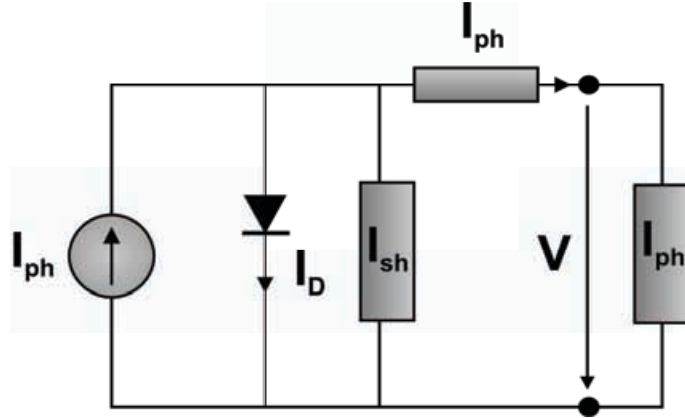
Figure 2.7. *Equivalent electric circuit of a DSSC.*

The semiconductor−metal interface is modelled as a Schottky diode. The equation of such a diode is:

$$I_D = I_S \left[\exp\left(\frac{V + I.R_S}{\eta.V_{th}} \right) - 1 \right] \tag{2.63}$$

where, I_S is the saturation current, the ideality factor (typically varies from 1 to 2.4), and V_{th} is the thermal voltage:

$$V_{th} = \frac{k_B.T}{q} \tag{2.64}$$

The equation for the equivalent electric circuit in Figure 2.7 is:

$$I = I_{ph} - I_S \left[\exp\left(\frac{V + I.R_S}{\eta.V_{th}} \right) - 1 \right] - \frac{V + I.R_S}{R_{sh}} \tag{2.65}$$

During the current−voltage measurements the following parameter will be determined:

A. Short-Circuit Current (I_{SC} or J_{SC}): The current equals the short-circuit current when the applied bias potential is zero:

$$I = I_{ph} - I_S \left[\exp\left(\frac{V + I.R_S}{\eta.V_{th}} \right) - 1 \right] \tag{2.66}$$

B. Open-Circuit Voltage (V_{OC}): When no current is flowing through the cell the potential equals the open-circuit potential, using equation 2.66 one can find:

$$V_{OC} = \eta.V_{th} \ln\left(\frac{I_{ph}}{I_c} + 1 \right) \tag{2.67}$$

43

C. Maximum Power Output (P_{max}): The power delivered from a solar cell at a certain potential equals the product of the current at this potential times the potential:

$$P(V) = I(V).V \qquad (2.68)$$

To obtain a graphic representation of the power one has to vary the potential between V_{OC} and 0. The point where the power is maximum (P_{max}) corresponds to the peak power point (PPP) for the $I-V$ curve. These are the optimal current and potential conditions (I_m, V_m) for the operating cell.
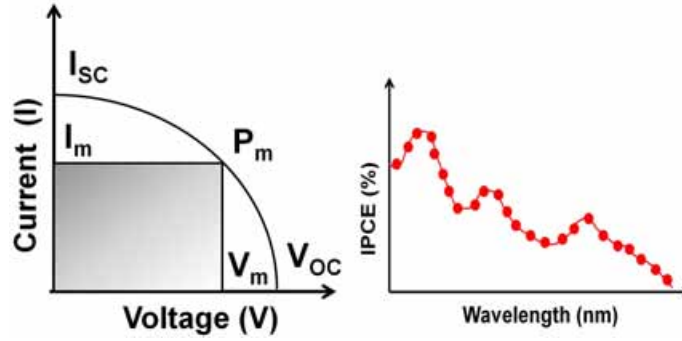
Figure 2.8. *Schematic representation of conventional I−V characteristic diagram (left). Typical IPCE characteristic diagram of a DSSC (right).*

D. Fill Factor (*FF*): The *FF* quantifies the quality of the solar cell, which is the ratio of actual power output ($V_m \times I_m$) versus its 'dummy' power output ($V_{OC} \times I_{SC}$) of a solar cell, as shown in equation 2.69:

$$FF = \frac{V_m I_m}{V_{OC} I_{SC}} \qquad (2.69)$$

The *FF* lies between 0.7 and 0.85 for an efficient DSSC. These values are influenced by the values of the series and the shunt resistances. To obtain high *FF* values the shunt resistance has to be as small as possible and the series resistance as high as possible.

E. Photo-conversion Efficiency (*η*): The overall photo-conversion efficiency is given by the following equation:

$$\eta = \frac{V_m I_m}{P_{in}} = \frac{V_{OC} I_{SC} FF}{P_{in}} \qquad (2.70)$$

It expresses the ratio of produced power and the incoming power (P_{in}). The experimental conditions have been fixed worldwide, in order to compare results coming from different places. An approximated power density value of 100 mW/cm^2, at air mass 1.5 global (AM 1.5 G)

condition has been set for the incident solar radiation, and the temperature of the cell should be 25 °C. The AM is the ratio of the path-length of incoming sunlight through the atmosphere when the sun is at an angle to the zenith, and the path-length when the Sun is at the zenith.

2.1.11. Photovoltage Decay Measurement: The open circuit voltage of a DSSC generated under illumination is equivalent to the separation between the quasi-Fermi level of electrons in the TiO_2 film and the rest potential of the counter electrode, which remains in equilibrium with the redox couple. The forward electron injection from sensitizer to TiO_2 is terminated upon stopping the illumination, thus discharging of electrons occurs through the back electron transfer or recombination with the oxidized electrolytes. The open circuit voltage decay reflects the timescales for the recombination processes.

2.2. Systems:

2.2.1. Molecular Probes: In this section we will discuss about the different probe molecules that have been used in the course of study.

2.2.1.1. Methylene Blue (MB): MB is a heterocyclic aromatic chemical compound with molecular formula: $C_{16}H_{18}ClN_3S$. It has many uses in a range of different fields. At room-temperature it appears as a solid and is odourless and a dark green powder, which yields a blue solution when dissolved in water. They are widely used as model water contaminant [30]. Its structure is given in Figure 2.9. When dissolved in water, the UV-visible spectrum of MB showed three absorption maxima. The first band was observed at 246 nm and then 291 nm and more intensely 663 nm. The absorption maxima wavelength of MB (λ_{max} = 663 nm) was used for the analysis during decolorization of MB dye.

2.2.1.2. Eosin: Eosin, a heterocyclic dye containing bromine atoms is used in the fields of dyeing, printing, leather, and fluorescent pigment, etc. The removal of these non-biodegradable organic chemicals from the environment is a crucial ecological problem [31]. At room-temperature it appears as a red crystalline powder, designated by the formula $C_{20}H_8O_5Br_4$. Its structure is given in Figure 2.9. Eosin has strong absorption at λ_{max} = 510 nm which was used for the analysis during decolorization of Eosin dye.
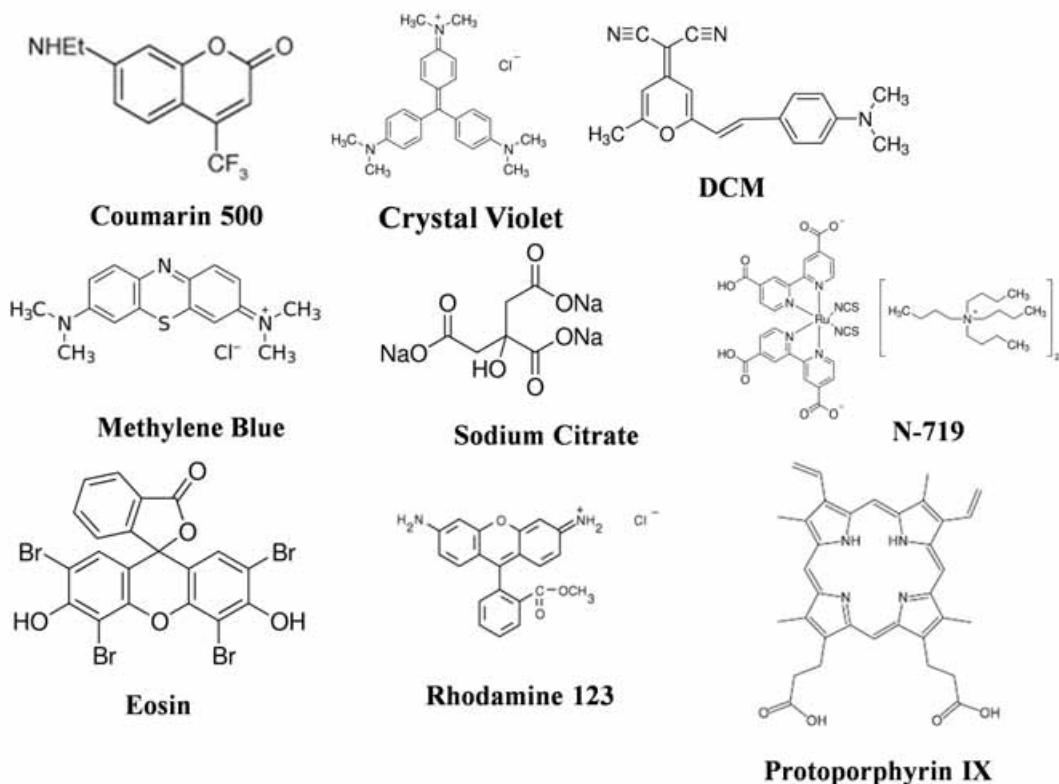
Figure 2.9. Schematic representation of the molecular probes used.

2.2.1.3. Crystal Violet (CV): CV is a triarylmethane dye (Figure 2.9), with molecular formula: $C_{25}N_3H_{30}Cl$. This cationic Dye in waste water has carcinogenic, mutagenic and allergenic properties [32]. Thus removal of ionic dyes from waste water has become an environmental challenge. When dissolved in water, the CV has a blue-violet colour with an absorbance maximum at 590 nm and an extinction coefficient of, 87,000 $M^{-1}cm^{-1}$ at 590 nm.

2.2.1.4. Rhodamine 123 (Rh123): Rh123 is a cationic dye (Figure 2.9), with molecular formula: $C_{21}H_{17}ClN_2O_3$. This kind of dye is wasted during fabrication processes and directly discharges to water causing a pollution of the environment. Rh123 have absorption maxima at 505 nm is used for the removal of Rh123. It also exhibit strong fluorescence around 560 nm, with fluorescence quantum yield is 0.89 [33]. Rh123 have been successfully used to probe electron transfer dynamics after adsorption of dyes on Au-RGO surface.

2.2.1.5. Coumarin 500 (C500): The derivatives of 1,2-benzopyrone, commonly known as the coumarin dyes, are the well-known laser dyes for the blue-green region [34]. The 7-aminocoumarin dyes are usually very strongly fluorescent, with their fluorescence quantum

46

yields often close to unity. C500 is an ideal system for studying water relaxation dynamics of hexagonal mesophases. Coumarin is found naturally in many edible plants such as strawberries, black currants, apricots, and cherries.

2.2.1.6. 4-(dicyanomethylene)-2-methyl-6-(p-dimethylaminostyryl)-4H-pyran (DCM): The laser dye DCM (Figure 2.9), is completely insoluble in water, and has selective binding affinity to micelle [35] vesicle [36] surfaces. The dye is completely hydrophobic (nonpolar) in the ground state. However, photoexcitation increases dipole moment of the probe making it polar and hence increases its hydrophilicity in the excited state. In order to study water relaxation dynamics of hexagonal mesophases we have used DCM as a solvation probe. The molar extinction coefficient value of DCM in methanol is 42,000 M^{-1} cm^{-1} at 468.5 nm and the emission peak is at 630 nm [37].

2.2.1.7. 3,7,12,17-Tetramethyl-8,13-divinyl-2,18-porphinedipropionic acid (Protoporphyrin IX, PP): PP is an important precursor to biologically essential prosthetic groups such as heme, cytochrome c, and chlorophylls. PPIX exhibits an intense Soret band absorption at 406 nm (S_0-S_2 transition), together with four weaker Q-bands at 506, 542, 577, and 630 nm (S_0-S_1 transition) [38]. PP is a very well-known photosensitizer (PS) for photodynamic therapies, energy harvesting application [39, 40].

2.2.1.8. Di-tetrabutylammonium cis-bis(isothiocyanato)bis(2,2′-bipyridyl-4,4′-dicarboxylato)ruthenium(II) (N719): Metal complexes, in particular the Ru(II) complexes, have been investigated intensively for DSSC application because of their broad absorption spectra, large value of extinction coefficient (1.4×10^4 M^{-1} cm^{-1}) [41], and favorable photovoltaic properties. N719 (Figure 2.9) consists of a central Ru(II) ion with ancillary ligands having four anchoring groups (COOH). Light absorption in the visible part of the solar spectrum is due to a metal to ligand charge transfer (MLCT) process. The central metal ion is therefore a crucial part of the overall properties of the complexes. Ancillary ligands (bipyridines) can be tuned by different substituents (alkyl, aryl, heterocycle, etc.) to change the photophysical and electrochemical properties and thus improve the photovoltaic performance. Anchoring groups are employed to link the dye with the semiconductor and facilitate the injection of the excited electron into the conduction band of the semiconductor. One can modify any part of the complex to tune the energy levels of the MLCT states and to optimize electron injection and dye regeneration kinetics.

References

[1] B. Bagchi, R. Biswas, Polar and Nonpolar Solvation Dynamics, Ion Diffusion, and Vibrational Relaxation: Role of Biphasic Solvent Response in Chemical Dynamics, *Adv. Chem. Phys* 109 (1999) 207-433.

[2] G. R. Fleming, M. Cho, Chromophore-Solvent Dynamics, *Ann. Rev. Phys. Chem.* 47 (1996) 109-134.

[3] B. Bagchi, Dynamics of Solvation and Charge Transfer Reactions in Dipolar Liquids, *Ann. Rev. Phys. Chem.* 40 (1989) 115-141.

[4] R. Jimenez, G. R. Fleming, P. Kumar, M. Maroncelli, Femtosecond Solvation Dynamics of Water, *Nature* 369 (1994) 471-473.

[5] S. K. Pal, J. Peon, B. Bagchi, A. H. Zewail, Biological Water: Femtosecond Dynamics of Macromolecular Hydration, *J. Phys. Chem. B* 106 (2002) 12376-12395.

[6] J. Jortner, A. Gaathon, Effects of Phase Density on the Ionization Process and Electron Localization in Fluids, *Can. J. Chem.* 55 (1977) 1801-1819.

[7] R. M. Stratt, M. Maroncelli, Nonreactive Dynamics in Solution: The Emerging Molecular View of Solvation Dynamics and Vibrational Relaxation, *J. Phys. Chem.* 100 (1996) 12981-12996.

[8] J. T. Hynes, Outer-sphere electron transfer reactions and frequency-dependent friction, *J. Phys. Chem.* 90 (1986) 3701–3706.

[9] M. L. Horng, J. A. Gardecki, A. Papazyan, M. Maroncelli, Subpicosecond Measurements of Polar Solvation Dynamics: Coumarin 153 Revisited, *J. Phys. Chem.* 99 (1995) 17311-17337.

[10] A. S. R. Koti, M. M. G. Krishna, N. Periasamy, Time-Resolved Area-Normalized Emission Spectroscopy (TRANES): A Novel Method for Confirming Emission from Two Excited States, *J. Phys. Chem. A* 105 (2001) 1767-1771.

[11] J. R. Lackowicz, Principles of Fluorescence Spectroscopy, *Plenum, New York,* (1983).

[12] R. D. Spencer, G. Weber, Measurements of Subnanosecond Fluorescence Lifetimes with a Cross-Correlation Phase Fluorometer, *Ann. N. Y. Acad. Sci* 158 (1969) 361-376.

[13] H. Spanggaard, F. C. Krebs, A Brief History of the Development of Organic and Polymeric Photovoltaics, *Sol. Energ. Mat. Sol. Cells* 83 (2004) 125-146.

[14]   Y. Shirota, H. Kageyama, Charge Carrier Transporting Molecular Materials and Their Applications in Devices, *Chem. Rev.* 107 (2007) 953-1010.

[15]   G. McLendon, R. Hake, Interprotein Electron Transfer, *Chem. Rev.* 92 (1992) 481-490.

[16]   V. M. Kenkre, J. D. Andersen, D. H. Dunlap, C. B. Duke, Unified Theory of the Mobilities of Photoinjected Electrons in Naphthalene, *Phys. Rev. Lett.* 62 (1989) 1165-1168.

[17]   J. H. Bang, P. V. Kamat, Quantum Dot Sensitized Solar Cells. A Tale of Two Semiconductor Nanocrystals: CdSe and CdTe, *ACS Nano* 3 (2009) 1467-1476.

[18]   L. Stryer, Fluorescence Energy Transfer as a Spectroscopic Ruler, *Annu. Rev. Biochem.* 47 (1978) 819-846.

[19]   M. Montalti, N. Zaccheroni, L. Prodi, N. O'Reilly, S. L. James, Enhanced Sensitized NIR Luminescence from Gold Nanoparticles via Energy Transfer from Surface-Bound Fluorophores, *J. Am. Chem. Soc.* 129 (2007) 2418-2419.

[20]   B. Persson, N. Lang, Electron-Hole-Pair Quenching of Excited States Near a Metal, *Phys. Rev. B* 26 (1982) 5409.

[21]   J. Gersten, A. Nitzan, Spectroscopic Properties of Molecules Interacting with Small Dielectric Particles, *J. Chem. Phys.* 75 (1981) 1139-1152.

[22]   T. L. Jennings, M. P. Singh, G. F. Strouse, Fluorescent Lifetime Quenching near d = 1.5 nm Gold Nanoparticles: Probing NSET Validity, *J. Am. Chem. Soc.* 128 (2006) 5462-5467.

[23]   M. A. H. Muhammed, A. K. Shaw, S. K. Pal, T. Pradeep, Quantum Clusters of Gold Exhibiting FRET, *J. Phys. Chem. C* 112 (2008) 14324-14330.

[24]   A. Makhal, S. Sarkar, S. K. Pal, H. Yan, D. Wulferding, F. Cetin, P. Lemmens, Ultrafast Excited State Deactivation of Doped Porous Anodic Alumina Membranes, *Nanotechnology* 23 (2012) 305705.

[25]   F. H. B. Lima, M. L. Calegaro, E. A. Ticianelli, Electrocatalytic Activity of Manganese Oxides Prepared by Thermal Decomposition for Oxygen Reduction, *Electrochim. Acta* 52 (2007) 3732-3738.

[26]   U. A. Paulus, T. J. Schmidt, H. A. Gasteiger, R. J. Behm, Oxygen Reduction on a High-Surface Area Pt/Vulcan Carbon Catalyst: a Thin-Film Rotating Ring-Disk Electrode Study, *J. Electroanal. Chem.* 495 (2001) 134-145.

[27] B. O'Regan, M. Gratzel, A Low-Cost, High-Efficiency Solar Cell Based on Dye-Sensitized Colloidal TiO$_2$ Films, *Nature* 353 (1991) 737-740.

[28] M. Grätzel, Photoelectrochemical Cells, *Nature* 414 (2001) 338-344.

[29] M. Grätzel, Conversion of Sunlight to Electric Power by Nanocrystalline Dye-Sensitized Solar Cells, *J. Photochem. Photobiol. A* 164 (2004) 3-14.

[30] N. Xu, Z. Shi, Y. Fan, J. Dong, J. Shi, M. Z. C. Hu, Effects of Particle Size of TiO$_2$ on Photocatalytic Degradation of Methylene Blue in Aqueous Suspensions, *Ind. Eng. Chem. Res.* 38 (1999) 373-379.

[31] S. Chatterjee, S. Chatterjee, B. P. Chatterjee, A. R. Das, A. K. Guha, Adsorption of a Model Anionic Dye, Eosin Y, from Aqueous Solution by Chitosan Hydrobeads, *J. Colloid Interface Sci.* 288 (2005) 30-35.

[32] R. Ahmad, Studies on Adsorption of Crystal Violet Dye from Aqueous Solution onto Coniferous Pinus Bark Powder (CPBP), *J. Hazard. Mater.* 171 (2009) 767-773.

[33] X.-F. Zhang, Y. Zhang, L. Liu, Fluorescence Lifetimes and Quantum Yields of Ten Rhodamine Derivatives: Structural Effect on Emission Mechanism in Different Solvents, *J. Lumin.* 145 (2014) 448-453.

[34] S. Nad, H. Pal, Photophysical Properties of Coumarin-500 (C500): Unusual Behavior in Nonpolar Solvents, *J. Phys. Chem. A.* 107 (2003) 501-507.

[35] S. K. Pal, D. Sukul, D. Mandal, S. Sen, K. Bhattacharyya, Solvation Dynamics of DCM in Micelles, *Chem. Phys. Lett.* 327 (2000) 91-96.

[36] S. K. Pal, D. Sukul, D. Mandal, K. Bhattacharyya, Solvation Dynamics of DCM in Lipid, *J. Phys. Chem. B* 104 (2000) 4529-4531.

[37] M. Meyer, J. C. Mialocq, B. Perly, Photoinduced Intramolecular Charge Transfer and Trans-Cis Isomerization of the DCM Styrene Dye: Picosecond and Nanosecond Laser Spectroscopy, High-Performance Liquid Chromatography, and Nuclear Magnetic Resonance Studies, *J. Phys. Chem.* 94 (1990) 98-104.

[38] E. Balasubramaniam, P. Natarajan, Photophysical Properties of Protoporphyrin IX and Thionine Covalently Attached to Macromolecules, *J. Photochem. Photobiol. A* 103 (1997) 201-211.

[39] H. Ding, B. D. Sumer, C. W. Kessinger, Y. Dong, G. Huang, D. A. Boothman, J. Gao, Nanoscopic Micelle Delivery Improves the Photophysical Properties and Efficacy of Photodynamic Therapy of Protoporphyrin IX, *J. Control. Release* 151 (2011) 271-277.

[40] A. Kathiravan, V. Raghavendra, R. Ashok Kumar, P. Ramamurthy, Protoporphyrin IX on TiO$_2$ Electrode: A Spectroscopic and Photovoltaic Investigation, *Dyes Pigm.* 96 (2013) 196-203.

[41] M. K. Nazeeruddin, F. De Angelis, S. Fantacci, A. Selloni, G. Viscardi, P. Liska, S. Ito, B. Takeru, M. Grätzel, Combined Experimental and DFT-TDDFT Computational Study of Photoelectrochemical Cell Ruthenium Sensitizers, *J. Am. Chem. Soc.* 127 (2005) 16835-16847.

Chapter 3

Instrumentation and Sample Preparation

In this chapter the details of instrumental setup and sample preparation techniques used in our studies have been described.

3.1. Instrumental Setups:

3.1.1. Steady-state UV-Vis Absorption and Emission Measurement: Steady-state UV-Vis absorption and emission spectra of the probe molecules were measured with Shimadzu
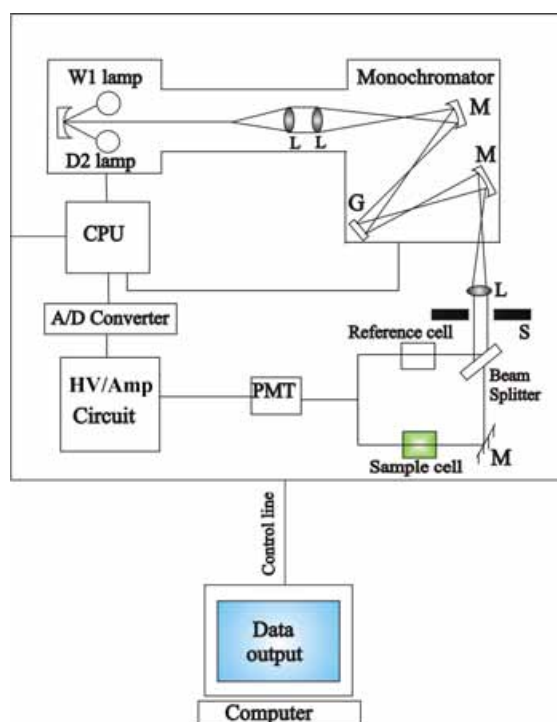
Figure 3.1. *Schematic ray diagram of an absorption spectrophotometer. Tungsten halogen (W1) and Deuterium lamps (D2) are used as light sources in the visible and UV regions, respectively. M, G, L, S, PMT designate mirror, grating, lens, shutter and photomultiplier tube, respectively. CPU, A/D converter and HV/Amp indicate central processing unit, analog to digital converter and High-voltage/Amplifier circuit, respectively.*
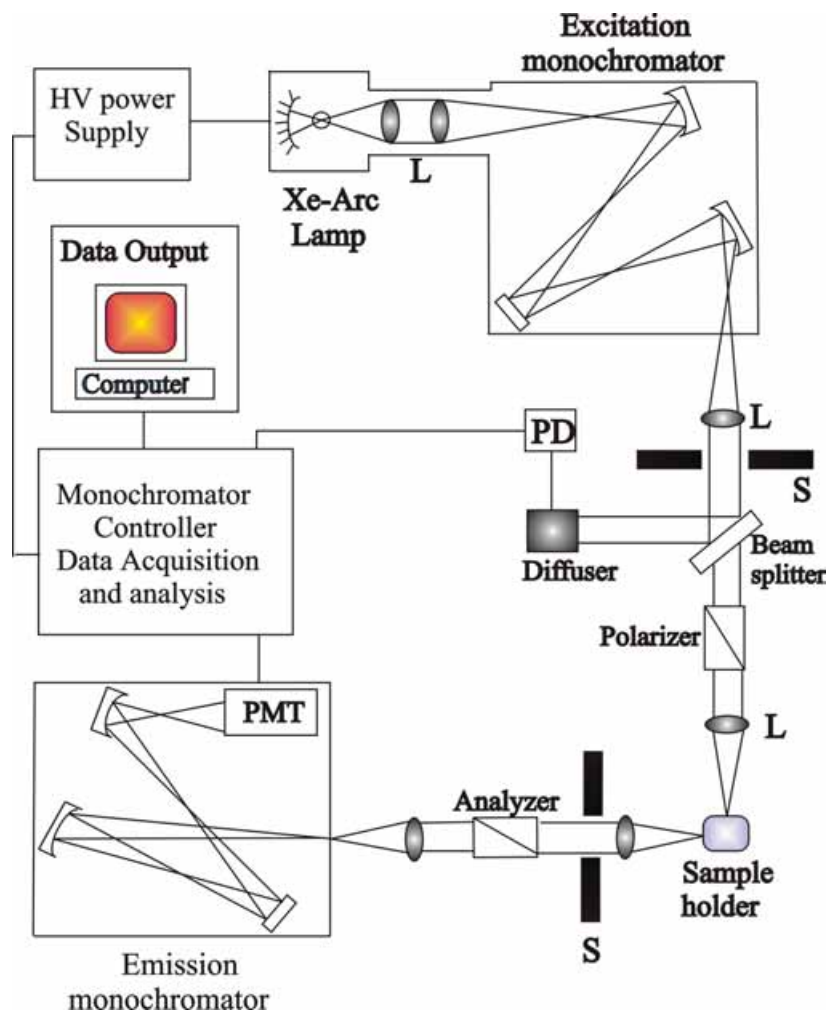
Figure 3.2. *Schematic ray diagram of an emission spectrofluorimeter. M, G, L, S, PMT and PD represent mirror, grating, lens, shutter, photomultiplier tube and reference photodiode, respectively.*

UV-2600 spectrophotometer and Jobin Yvon Fluorolog-3 fluorimeter, respectively. Schematic ray diagrams of these two instruments are shown in Figures 3.1 and 3.2.

3.1.2. Time-Correlated Single Photon Counting (TCSPC) Technique: All the picosecond-resolved fluorescence transients were recorded using TCSPC technique. The schematic block diagram of a TCSPC system is shown in Figure 3.3. TCSPC setup from Edinburgh instruments, U.K., was used during fluorescence decay acquisitions. The instrument response functions (IRFs) of the laser sources at different excitation wavelengths varied between 60 ps to 100 ps. The fluorescence from the sample was detected by a photomultiplier after dispersion through a

grating monochromator [1]. For all transients, the polarizer in the emission side was adjusted to be at 54.7° (magic angle) with respect to the polarization axis of excitation beam.
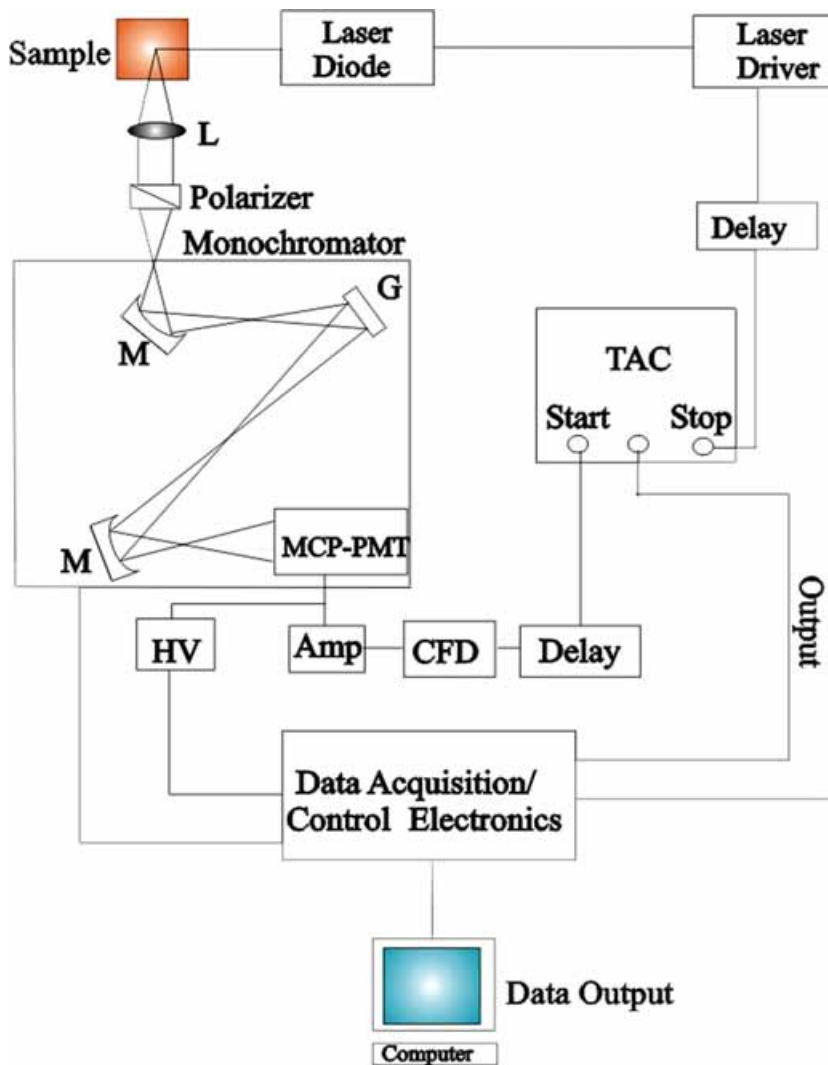
Figure 3.3. Schematic ray diagram of a time correlated single photon counting (TCSPC) spectrophotometer. A signal from microchannel plate photomultiplier tube (MCP-PMT) is amplified (Amp) and connected to start channel of time to amplitude converter (TAC) via constant fraction discriminator (CFD) and delay. The stop channel of the TAC is connected to the laser driver via a delay line. L, M, G and HV represent lens, mirror, grating and high voltage source, respectively.

3.1.3. Femtosecond-Resolved Transient Absorption Technique: In this study, a Helios UV-NIR femtosecond transient absorption spectroscopy system (Figure 3.4) was employed to measure transients of the samples. Helios is equipped with CMOS VIS and InGaAs NIR spectrometers covering the range of 350-800 nm with 1.5 nm resolution at 9500 spectra/s and

range of 800-1600 nm with 3.5 nm resolution at 7900 spectra/s, respectively. The probe beam is provided by Spectra-Physics Spitfire Pro 35F-XP regenerative femtosecond amplifier, which produces 35fs pulses at 800 nm with 4 mJ of energy per pulse. A small portion ($\approx$ 60 µJ) of the Spitfire output is routed via a delay line, adjustable pinholes, focusing lens, and a variable
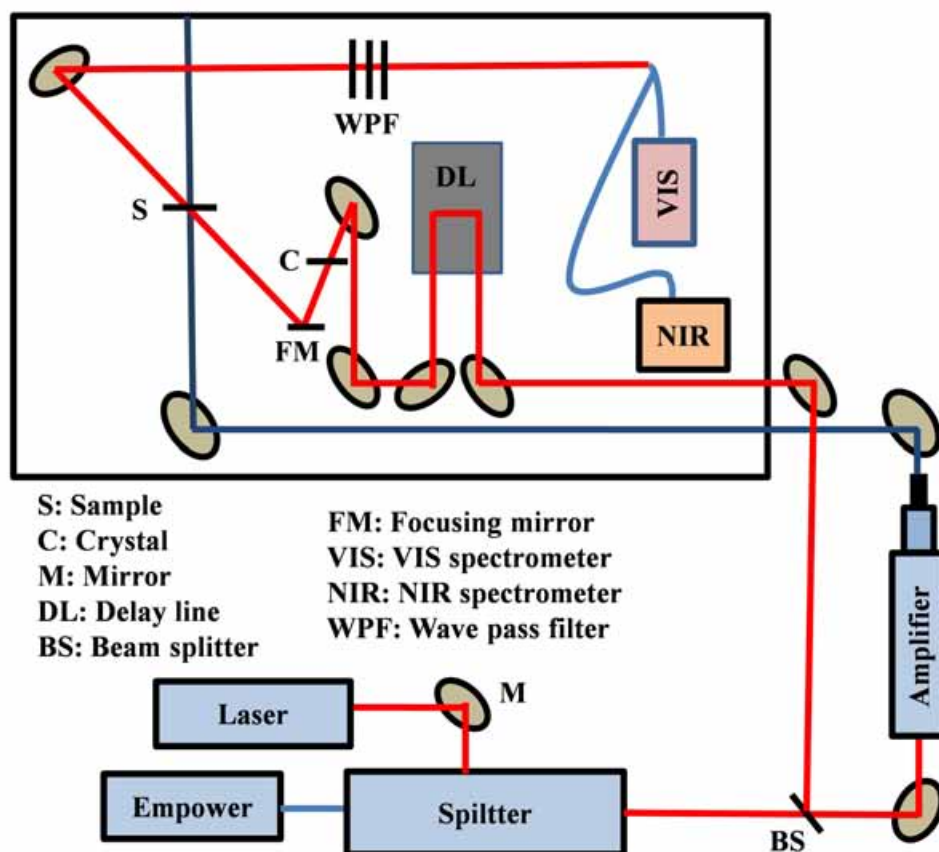
Figure 3.4. *Schematic ray diagram of femtosecond transient absorption spectrophotometer.*

neutral density filter to a crystal for white light continuum (WLC) generation; and further to the sample via a focusing mirror. Two crystals are available to cover Vis and NIR ranges. A computer-controlled delay line is used to vary the delay between the pump and probe pulses that allow transient absorption measurements within a 3.3 ns time window. One mJ of the Spitfire output is used to pump the TOPAS-C two-stage parametric amplifier equipped with frequency mixing stages and a non-collinear difference frequency generator that allows tuning from 240 to 2600 nm. The TOPAS-C output beam is routed via adjustable pinholes, a variable neutral density

filter, a depolarizer, a chopper wheel and a focusing lens to excite the sample. Pump and probe beams overlap spatially and temporally in the sample. The probe beam is collected by the spectrometer via collimating and focusing lenses and wave pass filters to attenuate the white light around the Spitfire fundamental at 800 nm. All transient absorption experiments were conducted at room temperature. The observed transients were fitted using a nonlinear least-squares fitting procedure (software SCIENTIST) to a function composed of the convolution of the instrument response function with a sum of exponentials. The purpose of this fitting is to obtain the decays in an analytic form suitable for further data analysis.

3.1.4. Transmission Electron Microscopy (TEM): A FEI Tecnai S-Twin high-resolution TEM (HRTEM) (Figure 3.5) equipped with an energy dispersive X-ray (EDAX) spectrometer was used to characterize the microscopic structures of samples and to analyze their elemental
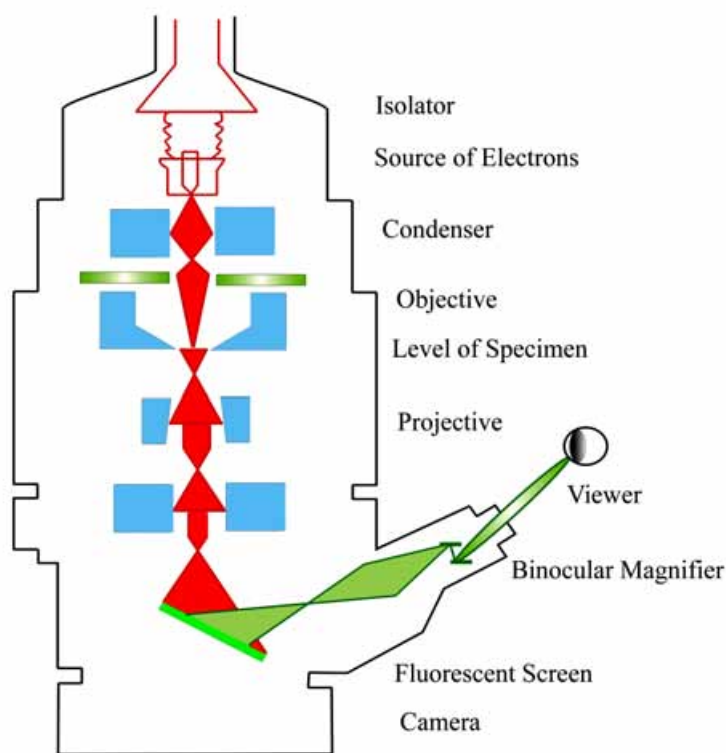
Figure 3.5. *Schematic diagram of a typical transmission electron microscope (TEM). After the transmission of electron beam through a specimen, the magnified image is formed either in the fluorescent screen or can be detected by a CCD camera.*

composition. The sizes of the nanoparticles were determined from the TEM images obtained at 200 kV. Samples for TEM were prepared by placing a drop of the colloidal solution on a carbon-coated copper grid and allowing the film to evaporate overnight at room-temperature.

3.1.5. Scanning Electron Microscopy (SEM): Surface characteristics of samples were done by scanning electron microscope FE (field emission)-SEM; QUANTA FEG 250. A Electron-gun is attached to SEM and the electrons from filament triggered by 0 KV to 30 KV voltages. These electrons go first through a condenser lens and then through an objective lens, then through an aperture and finally reach to the specimen. The high energy electrons go a bit in the sample and back again give secondary electrons. The signal from secondary electrons are detected by detector and amplified. The ray diagram of the SEM setup is shown in Figure 3.6.
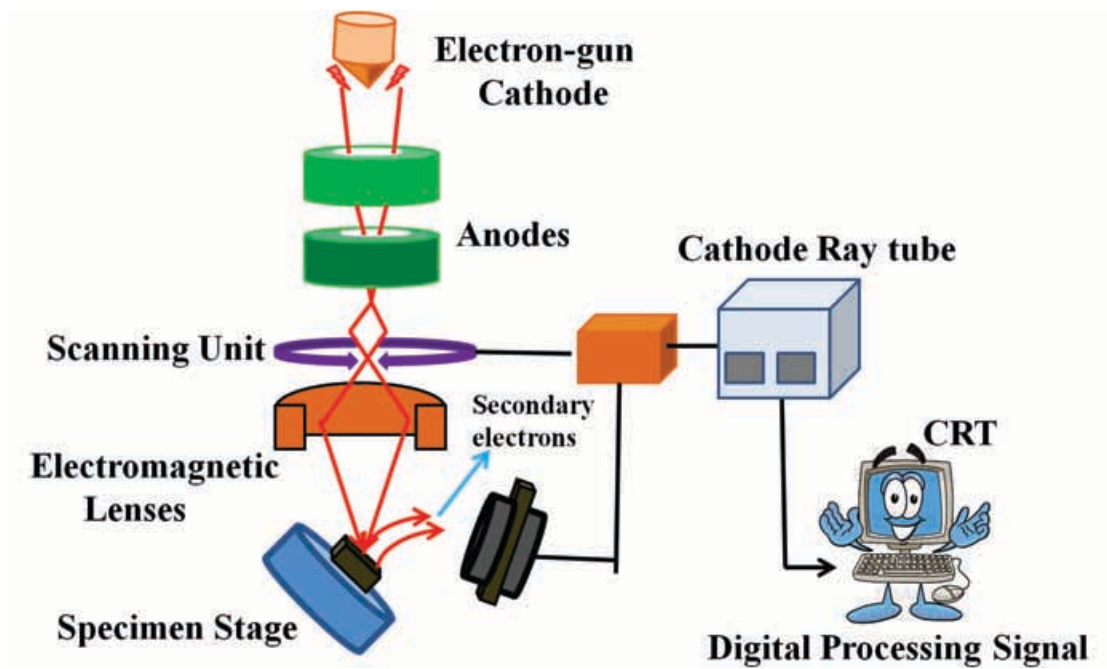
Figure 3.6. *Schematic diagram of typical scanning electron microscope (SEM).*

3.1.6. Thermogravimetric-Differential Thermal Analyzer (TG-DTA) Setup: The thermogravimetric (TG) analysis was carried out using Diamond thermogravimetric (TG)-differential thermal analyzer (DTA) from Perkin Elmer. The TG determines the weight change of a sample whereas the DTA measures the change in temperature between a sample and the reference as a function of temperature and/or time. The schematic of the TG-DTA setup is shown

in Figure 3.7. When a weight change occurs on the sample side, the beam holding the platinum pans is displaced. This movement is detected optically and the driving coil current is changed to return the displacement to zero. The detected driving coil current change is proportional to the sample weight change and the output is the TG signal. The DTA detects the temperature difference between the sample holder and the reference holder using the electromotive force of thermocouples, which are attached to the holders. This difference is measured as the DTA signal.
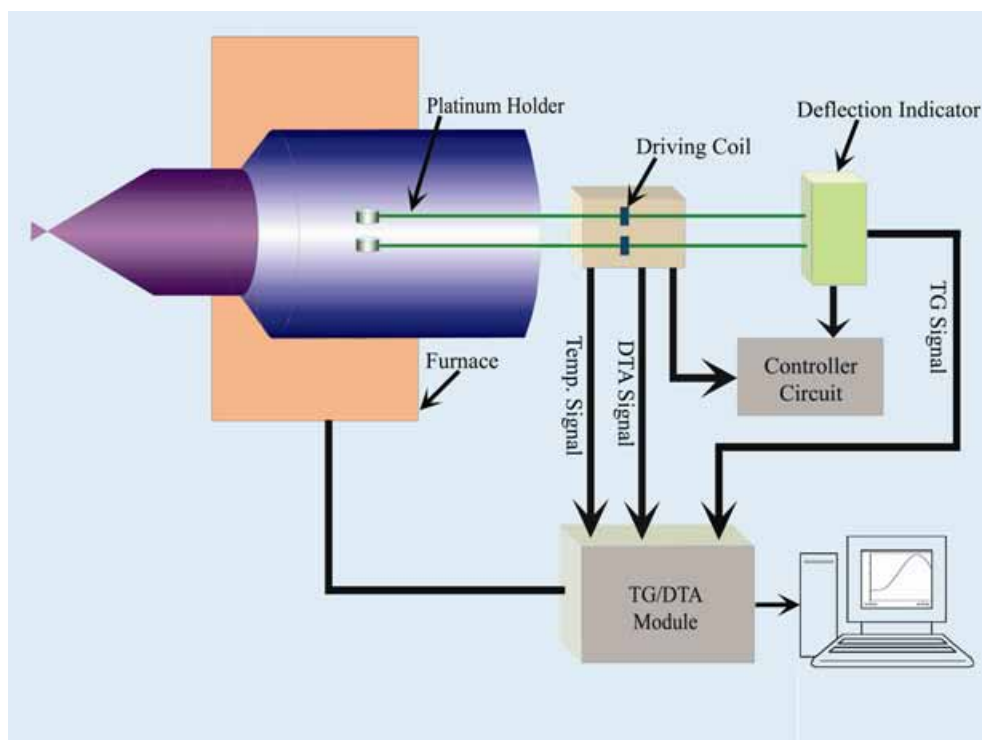
Figure 3.7. *The schematic representation of thermogravimetric-differential thermal analyzer (TG-DTA) setup.*

3.1.7. X-ray Diffraction (XRD) Measurement: XRD is a popular and powerful technique for determining crystal structure of crystalline materials. By examining the diffraction pattern, one can identify the crystalline phase of the material. Small angle scattering is useful for evaluating the average interparticle distance while wide-angle diffraction is useful for refining the atomic structure of nanoclusters. The widths of the diffraction lines are closely related to strain and defect size and distribution in nanocrystals. As the size of the nanocrystals decreases, the line

width is broadened due to loss of long-range order relative to the bulk. This XRD line width can be used to estimate the size of the particle by using the Debye-Scherrer formula,

$$D = \frac{0.9\lambda}{\beta \cos \theta} \qquad (3.1)$$

where, D is the nanocrystal diameter, λ is the wavelength of light, β is the full-width half-maximum (fwhm) of the peak in radians, and θ is the Bragg angle. XRD measurements were performed on a PANalytical XPERT-PRO diffractometer (Figure 3.8) equipped with CuKα radiation ($\lambda = 1.5418$ Å at 40 mA, 40 kV). XRD patterns were obtained by employing a scanning rate of $0.02°$ s^{-1} in the 2θ range from $15°$ to $90°$.
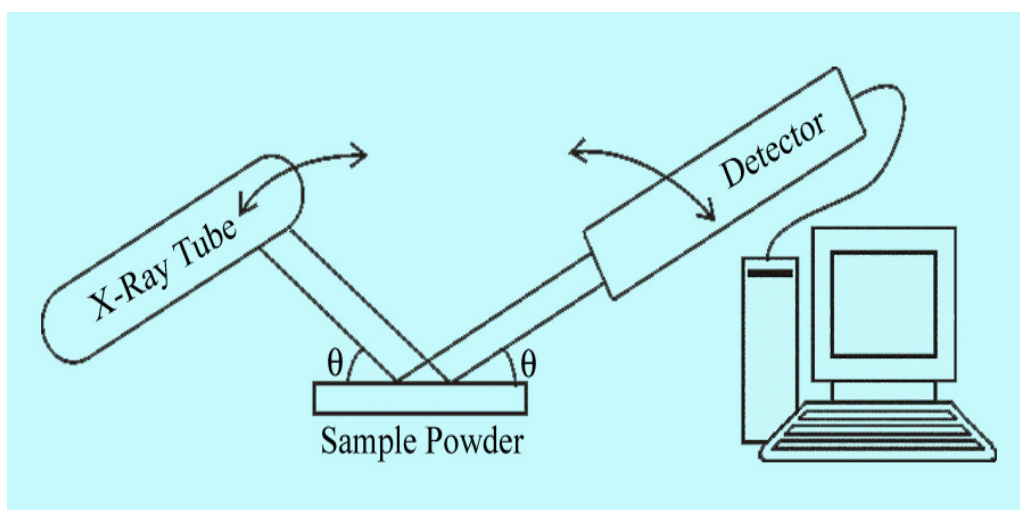
Figure 3.8. *Schematic diagram of X-ray diffraction (XRD) instrument. By varying the angle θ, the Bragg's Law conditions, $n\lambda=2d\sin\theta$ are satisfied by different d-spacings in polycrystalline materials. Plotting the angular positions and intensities of the resultant diffracted peaks of radiation produces a pattern, which is characteristic of the sample.*

3.1.8. Fourier Transform Infrared (FTIR) Measurement: FTIR spectroscopy is a technique that can provide very useful information about functional groups in a sample. An infrared spectrum represents the fingerprint of a sample with absorption peaks which correspond to the frequencies of vibrations between the bonds of the atoms making up the material. Because each different material is a unique combination of atoms, no two compounds produce the exact same infrared spectrum. Therefore, infrared spectroscopy can result in a positive identification (qualitative analysis) of every different kind of material. In addition, the size of the peaks in the spectrum is a direct indication of the amount of material present. The two-beam Michelson

interferometer is the heart of FTIR spectrometer. It consists of a fixed mirror (M4), a moving mirror (M5) and a beam-splitter (BS1), as illustrated in Figure 3.9. The beam-splitter is a laminate material that reflects and transmits light equally. The collimated IR beam from the source is partially transmitted to the moving mirror and partially reflected to the fixed mirror by the beam-splitter. The two IR beams are then reflected back to the beam-splitter by the mirrors. The detector then sees the transmitted beam from the fixed mirror and reflected beam from the moving mirror, simultaneously. The two combined beams interfere constructively or destructively depending on the wavelength of the light (or frequency in wavenumbers) and the optical path difference introduced by the moving mirror. The resulting signal is called an interferogram which has the unique property that every data point (a function of the moving mirror position) which makes up the signal has information about every infrared frequency which comes from the source. Because the analyst requires a frequency spectrum (a plot of the intensity at each individual frequency) in order to make identification, the measured interferogram signal cannot be interpreted directly. A means of "decoding" the individual frequencies is required. This can be accomplished *via* a well-known mathematical technique called the Fourier transformation. This transformation is performed by the computer which then
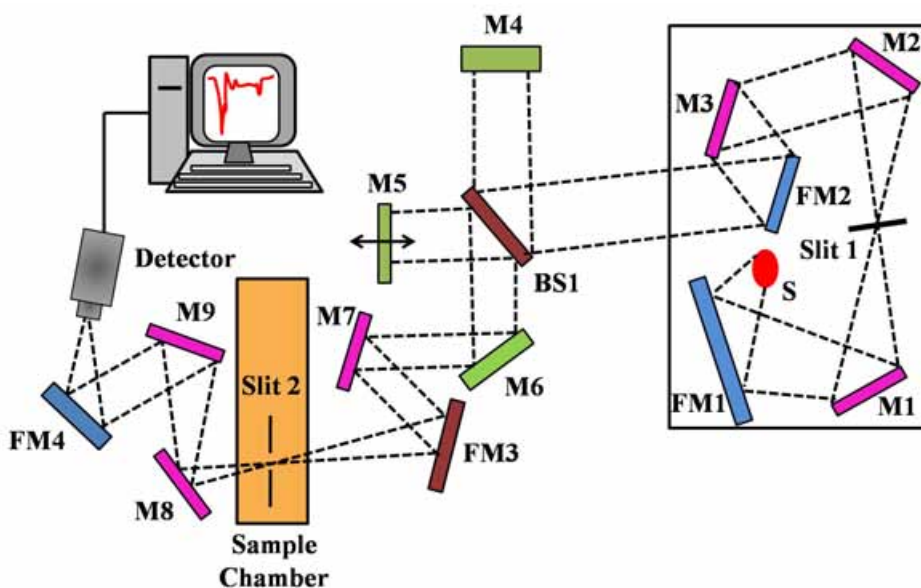
Figure 3.9. *Schematic of Fourier transform infrared (FTIR) spectrometer. It is basically a Michelson interferometer in which one of the two fully-reflecting mirrors is movable, allowing a variable delay (in the travel-time of the light) to be included in one of the beams. M, FM and BS1 represent the mirror, focussing mirror and beam splitter, respectively. M5 is a moving mirror.*

presents the user with the desired spectral information for analysis. FTIR measurements were performed on a JASCO FTIR-6300 spectrometer (transmission mode). For the FTIR measurements, samples were mixed with KBr powder and pelletized. The background correction was made using a reference blank of KBr pellet. In situ-FTIR study was carried out using a FTIR spectrometer (Bruker Vertex 70v) which is connected to a potentiostatgalvanostat (PGSTAT30, AUTOLAB).

3.1.9. Laser Raman Spectroscopy: Raman spectroscopy is a useful technique for the identification of a wide range of substances− solids, liquids, and gases. It is a straightforward, non-destructive technique requiring no sample preparation. Raman spectroscopy involves illuminating a sample with monochromatic light and using a spectrometer to examine light scattered by the sample.

At the molecular level photons can interact with matter by absorption or scattering processes. Scattering may occur either elastically, or inelastically. The elastic process is termed Rayleigh scattering, while the inelastic process is termed Raman scattering. The electric field component of the scattering photon perturbs the electron cloud of the molecule and may be regarded as exciting the system to a 'virtual' state. Raman scattering occurs when the system exchanges energy with the photon, and the system subsequently decays to vibrational energy levels above or below that of the initial state. The frequency shift corresponding to the energy difference between the incident and scattered photon is termed the Raman shift. Depending on whether the system has lost or gained vibrational energy, the Raman shift occurs either as an up or down-shift of the scattered photon frequency relative to that of the incident photon. The down-shifted and up-shifted components are called, respectively, the Stokes and anti-Stokes lines. A plot of detected number of photons versus Raman shift from the incident laser energy gives a Raman spectrum. Different materials have different vibrational modes, and therefore characteristic Raman spectra. This makes Raman spectroscopy a useful technique for material identification. There is one important distinction to make between the Raman spectra of gases and liquids, and those taken from solids− in particular, crystals. For gases and liquids it is meaningful to speak of the vibrational energy levels of the individual molecules which make up the material. Crystals do not behave as if composed of molecules with specific vibrational energy

levels, instead the crystal lattice undergoes vibration. These macroscopic vibrational modes are called phonons.

In modern Raman spectrometers (LabRAM HR, Jobin Yvon), lasers are used as a photon source due to their highly monochromatic nature, and high beam fluxes (Figure 3.10). This is necessary as the Raman effect is weak, typically the Stokes lines are ~10^5 times weaker than the Rayleigh scattered component. In the visible spectral range, Raman spectrometers use notch filters to cut out the signal from a very narrow range centred on the frequency corresponding to the laser radiation. Most Raman spectrometers for material characterization use a microscope to
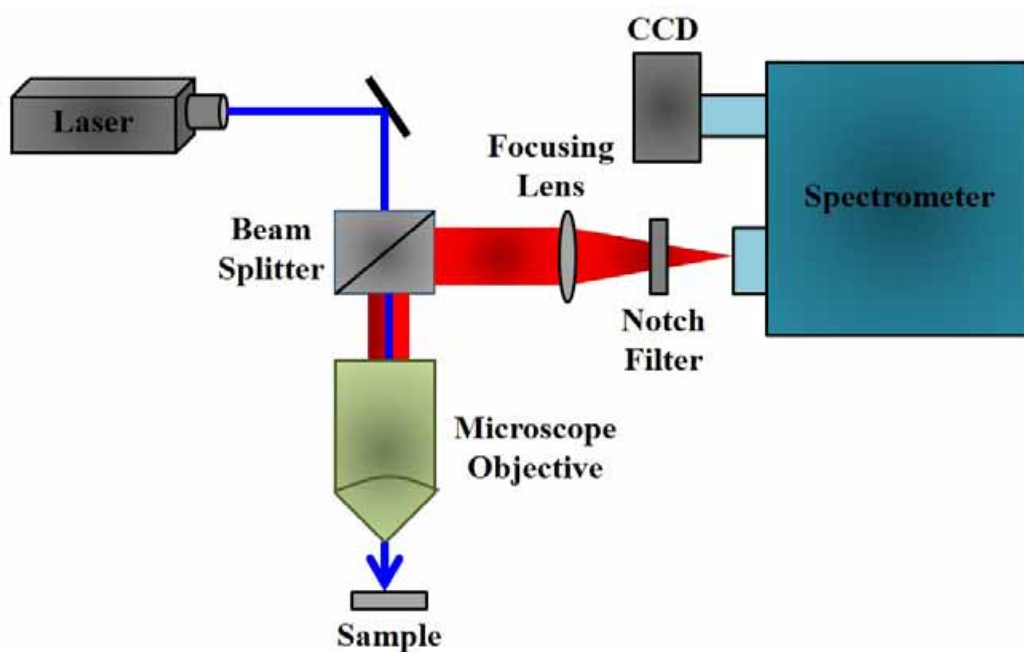
Figure 3.10. *Schematic diagram of a Raman spectrometer is shown.*

focus the laser beam to a small spot (<1−100 μm diameter). Light from the sample passes back through the microscope optics into the spectrometer. Raman shifted radiation is detected with a charge-coupled device (CCD) detector, and a computer is used for data acquisition and curve fitting. These factors have helped Raman spectroscopy to become a very sensitive and accurate technique.

3.1.10. X-Ray Photoelectron Spectroscopy (XPS): XPS works on the principle of photoelectric effect discovered by Heinrich Hertz in 1887. When radiation of appropriate energy incident,

electrons are emitted from the surface of the metal. The relation between the energy of the excitation radiation, work function of the metal and the maximum kinetic energy of the emitted electron as proposed by Einstein in 1905 is:

$$h\upsilon = \phi + KE_{max}$$ (3.2)

Φ is the work function of the metal, hυ is the energy of the radiation, KE_{max} is the maximum kinetic energy of the emitted electron. For analysing the core electronic structure (0 – 1300 eV) of elements, radiation of high energy were used like X-rays, hence the corresponding spectroscopy is termed X-ray Photoelectron Spectroscopy (XPS) (Figure 3.11).
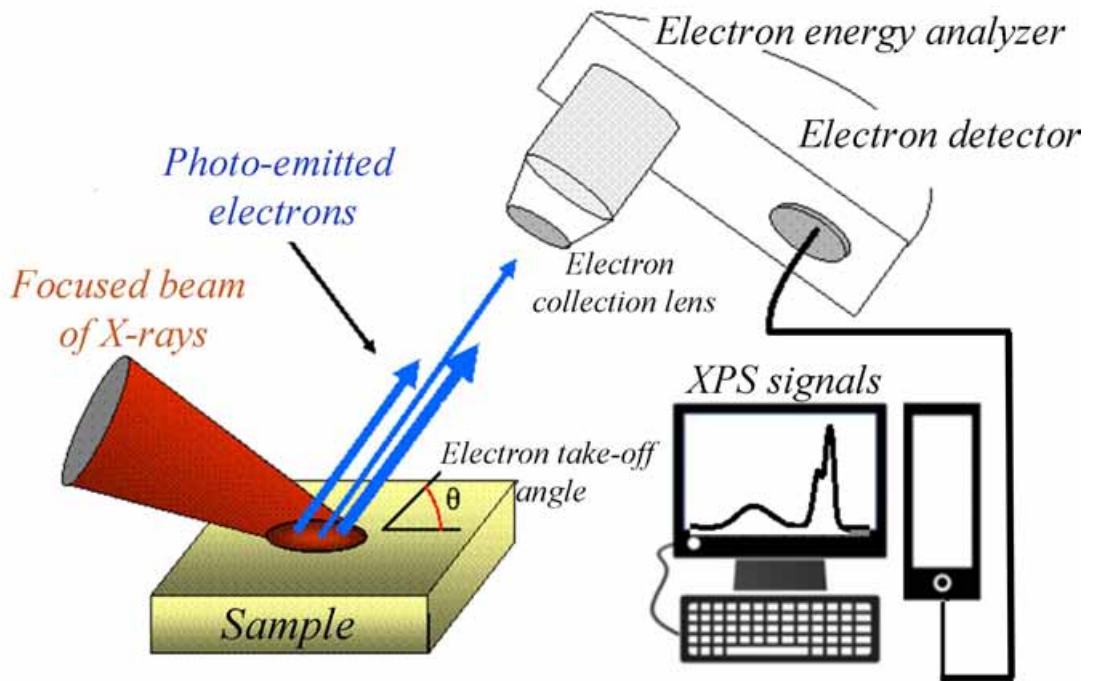
Figure 3.11. *Schematic diagram of a typical X-ray photoelectron spectroscopy (XPS).*

Surface analysis by XPS is accomplished by irradiating a sample with monoenergetic soft X-rays and analysing the energy of the detected electrons. Mg Kα (1253.6 eV), Al Kα (1486.6 eV), or monochromatic Al Kα (1486.7 eV) X-rays are usually used. These photons have limited penetrating power in a solid of the order of 1 – 10 μm. They interact with atoms in the surface

region, causing electrons to be emitted by the photoelectric effect. The emitted electrons have measured kinetic energies given by:

$$KE = h\upsilon - BE - \phi_S \qquad (3.3)$$

where hυ is the energy of the photon, BE is the binding energy of the atomic orbital from which electron originates, Φ_S is the work function of the spectrometer. The binding energy may be regarded as the energy difference between the initial and final states after the photoelectron has left the atom. Because there is a variety of a possible final state of the ions from each type of atom, there is a corresponding variety of kinetic energies of the emitted electrons. Moreover, there is a different probability or cross section for each final state. Because each element has a unique set of binding energies, XPS can be used to identify and determine the concentration of the elements in the surface. Variation in the elemental binding energies (the chemical shifts) arise from differences in the chemical potential and polarizability of compounds. These chemical shifts can be used to identify the chemical state of the material being analysed. In our studies, X-ray photoelectron spectroscopy (XPS) measurement were carried out using a Kratos Axis Ultra DLD spectrometer equipped with a monochromatic Al K_α X-ray source (hv = 1486.6 eV) operated at 150 W, a multichannel plate, and a delay line detector under a vacuum of 1.3×10^{-19} Torr.

3.1.11. Zeta Potential : The zeta potential of colloidal dispersions is routinely measured using the technique of micro-electrophoresis, where a voltage is applied across a pair of electrodes at either end of a cell containing the particle dispersion. Charged particles are attracted to the oppositely charged electrode and their velocity is measured and expressed in unit field strength as their electrophoretic mobility. Light scattering is one of the most commonly used techniques for determining the electrophoretic mobility of particles. Laser Doppler electrophoresis measures small frequency shifts in the scattered light that arise owing to the movement of particles in an applied electric field. The frequency shift Δf is equal to

$$\Delta f = \frac{2\gamma \sin\left(\dfrac{\theta}{2}\right)}{\lambda} \qquad (3.4)$$

where γ is the particle velocity, λ is the laser wavelength and θ is the scattering angle. The measured electrophoretic mobility (U_E) is converted into zeta potential (ζ) through Henry's equation,

$$U_E = \frac{2\varepsilon\zeta F(\kappa a)}{3\eta} \qquad (3.5)$$

where ε is the dielectric constant of the dispersant, $F(\kappa a)$ is the Henry function and η is the viscosity.

Zeta potential measurements were performed by DLS-nanoZS, Zeta sizer, Nanoseries, Malvern Instruments. A schematic ray diagram of this instrument is shown in Figures 3.12.
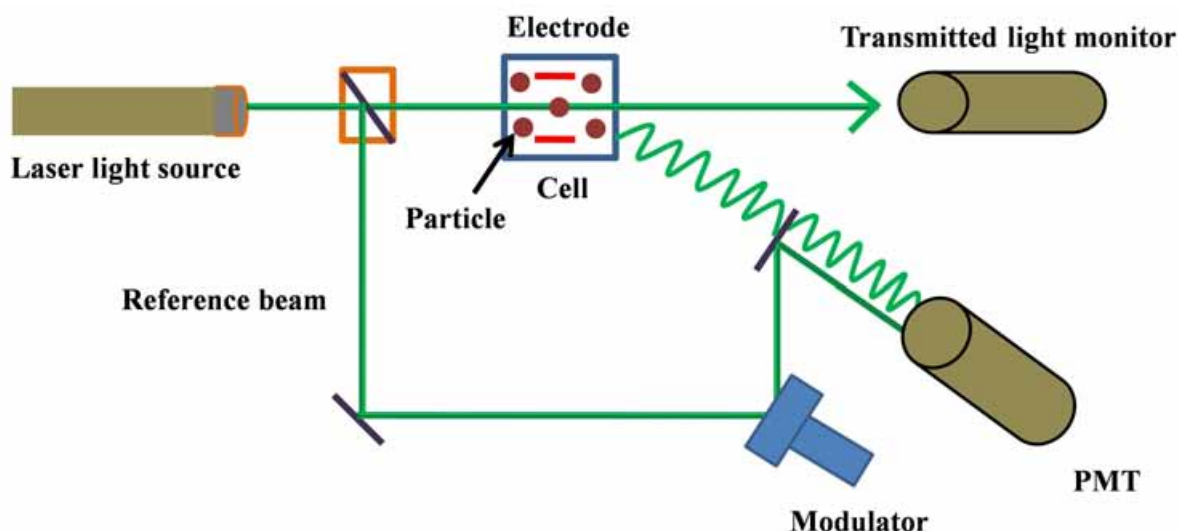
Figure 3.12. Schematic diagram for a zeta potential measurement in the DLS-nanoZS is shown.

3.1.12. Cyclic Voltammetry (CV): CV is a useful technique for studying electrochemical reactions. In case of CV, the voltage is swept between two potential values (V_1 and V_2) at a fixed rate, however now when the voltage reaches V_2 from V_1, the scan is reversed and the voltage is swept back to V_1. The current response is plotted as a function of the applied potential. Electrochemical experiments were performed using potentiostat/galvanostat system and CH analyser potentiostat. The schematic presentation of the CV set up is shown in Figure 3.13. A typical electrochemical measurement circuit made up of an electrochemical cell, an adjustable

voltage source (V_S), an ammeter (A_M) and a voltmeter (V_M). The three electrodes of the electrochemical cell are the working electrode (WE), reference electrode (RE) and the counter (or auxiliary) electrode (CE). The voltage source (V_S) for the potential scan is applied between the working electrode and the counter electrode. The potential (E) between the reference electrode and the working electrode is measured with the voltmeter and the overall voltage (Vs) is adjusted to maintain the desired potential at the working electrode with respect to the reference electrode. The resulting current (i) flowing to or from the working electrode is measured with the ammeter (A_M).
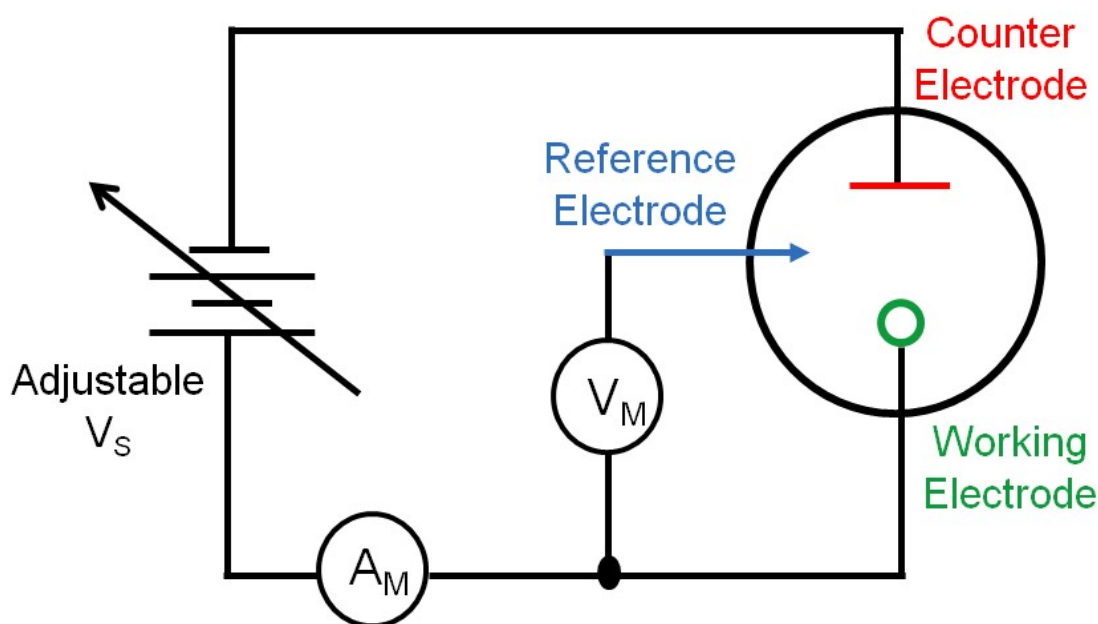
Figure 3.13. *Schematic diagram of a simplified measurement circuit for performing cyclic voltammetry (CV).*

3.1.13. Rotating Disk Electrode (RDE): The rotating-disc electrode is a type of electrode which comprises of a cylinder made of an insulating material encasing a disc made of a conductive material. The cylinder is usually made of PTFE or PEEK, whereas the disc, which is the electrode itself, is made of various conductive materials, such as platinum, gold, copper, glassy carbon etc. The whole cylinder is screwed onto a metal shaft, which is fastened inside a rotator. The rotator is a device which operates much like a common drill. But its rotation speed can be

precisely controlled by the operator. Rotating disk electrode (RDE) is one of the most frequently used techniques for ORR and OER catalysis studies. Rotating disk electrode voltammetric studies were carried out using RRDE-3A Rotating Ring Disk Electrode Apparatus (BioLogic Science Instruments, France) connected to DY2300 potentiostat (Digi-Ivy Inc., USA) The RDE system is a valuable experimental tool because it allows us to study the effects that convection (the transport of the reactants in the solution due to the solvent's flow) and diffusion (the transport of the reactants in the solution due to the non-uniform concentration of the reactants) have on chemical reactions. When the electrode is rotated, it pumps fresh solution from the core of the electrolyte onto the disc. Thickness of the diffusion layer can be changed by varying the rotation speed of the RDE. The schematic presentation of the RDE set up is shown in Figure 3.14.
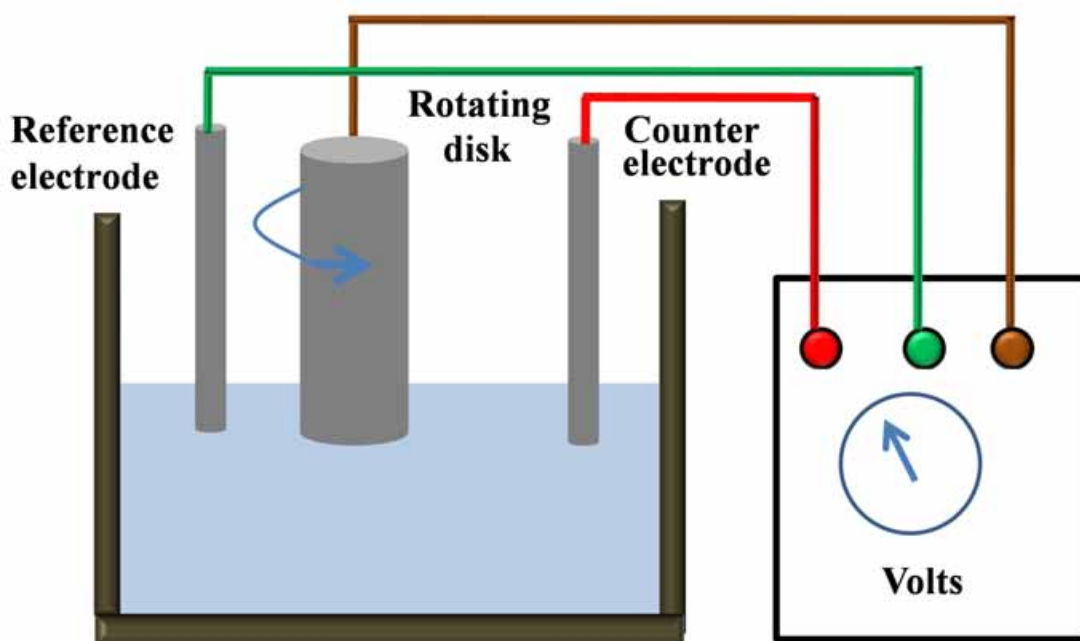
Figure 3.14. Schematic diagram of rotating disk electrode (RDE).

3.1.14. Inductively Coupled Plasma Mass Spectrometry (ICP-MS): An ICP-MS combines a high-temperature ICP (Inductively Coupled Plasma) source with a mass spectrometer (Figure 3.15). The ions formed in the plasma are extracted via a conical water cooled sampler into the first vacuum stage and then pass through the skimmer placed a few cm behind the sampler. Ion

lenses focus the ion beam in the high vacuum provided by a turbomolecular pump. The detector measures the ion intensities. A 7500 ce ICP-MS (Agilent) was used as elemental detector. Detection of Pd was performed by selecting an abundant isotope free of interferences, i.e., ^{105}Pd. The amount of palladium on the glassy carbon for nafion and RGO-nafion was found to be 4.9 µg and 2.48 µg respectively by ICP-MS.
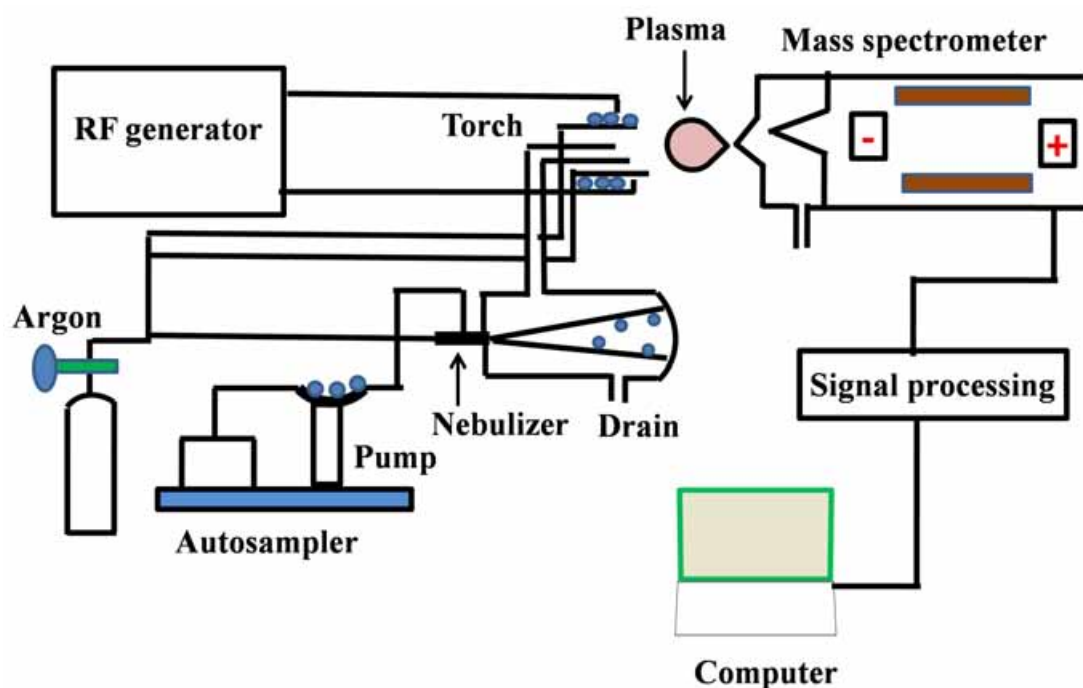
Figure 3.15. Schematic diagram of inductively coupled plasma mass spectrometry (ICP-MS) instrument.

3.1.15. Solar Cell Characterization: The characterization of DSSCs involves the electrical current−voltage (I−V) characteristics, and photovoltage decay measurements. The current density-voltage characteristics of the cells were recorded by a keithley multimeter under irradiance of 100 mW cm^{-2} (AM 1.5 simulated illuminations, Photo Emission Tech). The electrical circuit used to measure the I−V characteristics of the solar cells is shown in Figure 3.16. The short-circuit current (I_{SC}) and open-circuit voltage (V_{OC}) of the solar cells were determined from their respective I−V characteristic curves. The fill factor (FF) and efficiency (η) of the solar cells were calculated by using equations 2.69 and 2.70, respectively.
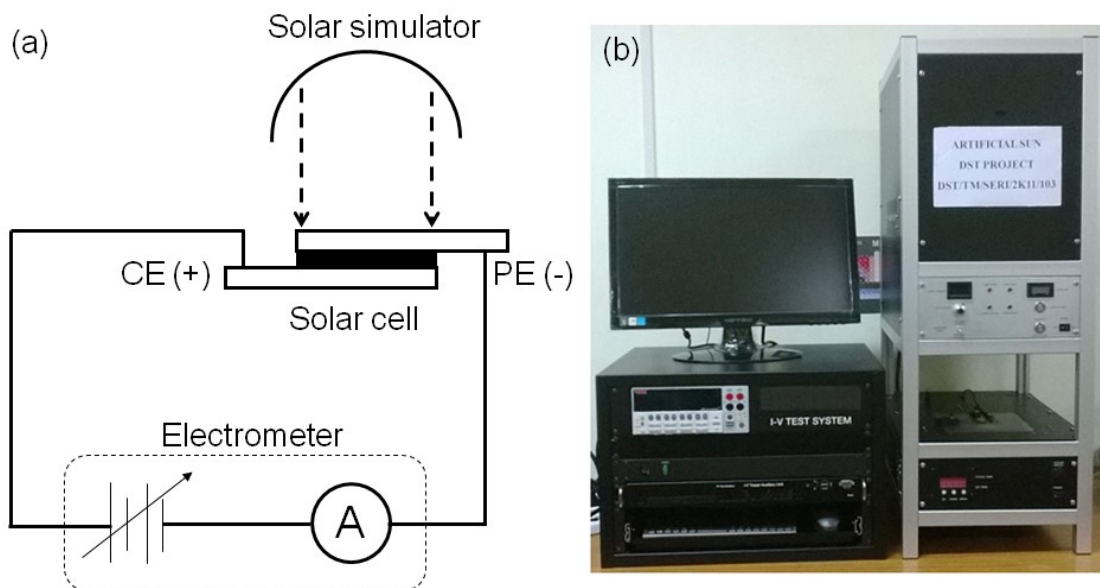
Figure 3.16. *(a) Electrical setup and (b) photograph of the solar simulator used for the solar cell characterization.*

Photovoltage decay measurements were carried out after illuminating the cells under 1 Sun condition. The photovoltage decays after switching off the irradiation were monitored by an oscilloscope (Owon) through computer interface as shown in Figure 3.17. The decays were fitted with exponential decay functions using Origin software.
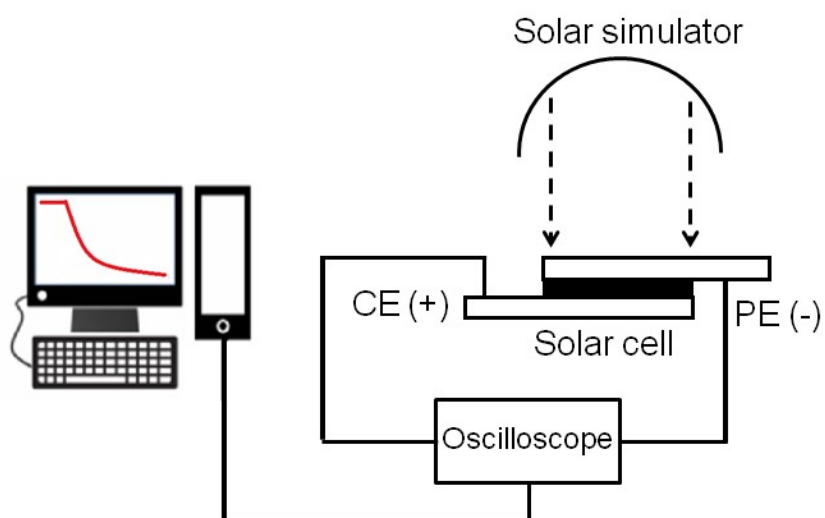
Figure 3.17. *Schematic diagram of the photovoltage decay measurement setup.*

3.1.16. Fiber-Optic Coupled System for Photocatalytic Measurements: Increased sensitivity in the signal detection in the presence of strong ambient light in our experimental setup lies on the confocal geometry of the excitation and detection sides [2]. As shown in the schematic ray-
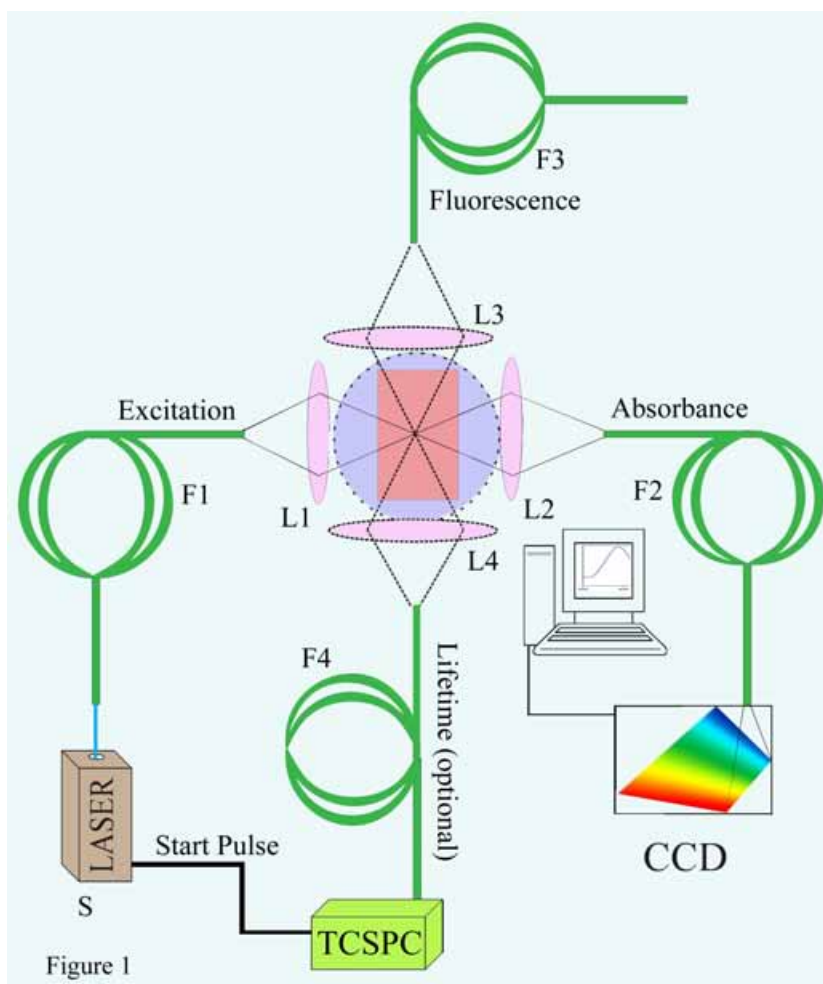
Figure 3.18. *Schematic diagram of the universal setup. S is the source, F1-F4 are the optical fibers, L1-L4 are the fiber coupler lenses, the violate circle represents the ambient light around the sample (reddish rectangle). CCD is the photo-signal detector, connected with computer.*

diagram of the experimental setup (Figure 3.18) the excitation fiber (400 μM core diameter) carrying laser light is connected to an optical coupler (Ocean Optics, USA, model: 74-UV) in order to focus excitation light at the middle of a sample holder, which is an all-side polished quartz-cuvette from Starna cells (U.S.A). The numerical aperture (NA) of the excitation fiber (NA=0.45) and focal length of the optical coupling lens (0.5 cm) systems are to achieve out-of-

70

focus rejection by two strategies: firstly by illuminating a single point of the specimen at any one time with a focused beam, so that illumination intensity drops off rapidly above and below the plane of focus and secondly by the use of optical fiber as a collecting unit with similar coupling lens so that light emitted away from the point in the specimen being illuminated is blocked from reaching the detector. The collection fiber is arranged in 'I' geometry and connected with the commercially available CCD based miniaturized spectrograph (Ocean Optics, USA, model: HR4000) in order to measure absorption of the sample of interest. More flexibility in the measurement can also be achieved by using Shimadzu spectrophotometer (UV-2600) or Jobin Yvon (Fluorolog-3) fluorimeter to measure absorption and photoluminescence, respectively. In order to establish the fact that the absorption of a sample can be measured in presence of strong ambient light effectively, we have placed the quartz cell containing test sample on a home-made UV bath (8W). We have used the same setup in order to investigate the photodegradation of methylene blue [3, 4]. The photodegradation reaction of MB (initial concentration $C_0 = 0.5 \times 10^{-5}$ M) was carried out in a 10 mm optical path quartz cell reactor containing 2 mL of a model MB solution with a concentration of 0.5 g L^{-1} of the photocatalyst in deionized water (DI). The percentage degradation (%DE) of MB was determined using:

$$\% \, DE = \frac{I_o - I}{I_o} \times 100 \qquad (3.6)$$

3.1.17. Surface Area Analysis: The Brunauer, Emmett and Teller (BET) technique is the most common method for determining the surface area of powders and porous materials (Figure 3.19). The BET theory applies to systems of multi layer adsorption, and usually utilizes probing gases that do not chemically react with material surfaces as adsorbates to quantify specific surface area. Nitrogen gas is generally employed as the probe molecule and is exposed to a solid under investigation at liquid nitrogen conditions (i.e. 77 K). Specific surface area is a scale-dependent property, with no single true value of specific surface area definable, and thus quantities of specific surface area determined through BET theory may depend on the adsorbate molecule utilized and its adsorption cross section. A Quantachrome Autosorb-1-C instrument was used for surface area measurement.
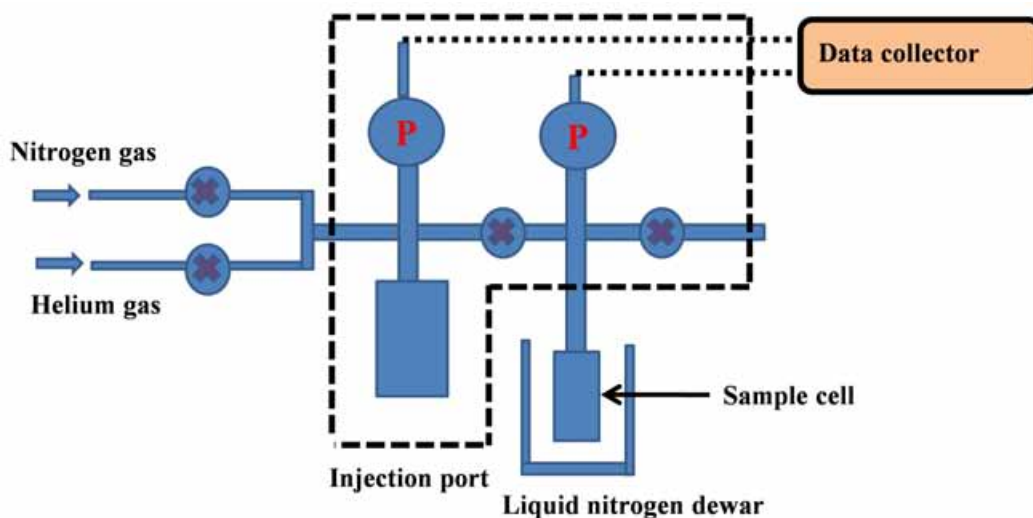
Figure 3.19. Schematic diagram of surface area analyzer setup.

3.1.18. Hydrothermal Technique: The hydrothermal technique has been the most popular one, gathering interest from scientists and technologists of different disciplines, for the synthesis of different nanomaterials. Hydrothermal reaction defined as any heterogenous chemical reaction in the presence of a solvent (whether aqueous or nonaqueous) above room temperature and at pressure greater than 1 atm in a closed system. Crystal growth under hydrothermal conditions requires a reaction vessel called an autoclave. The autoclave must be capable of sustaining highly corrosive salt, which are used to synthesis inorganic materials at high temperature and pressure for a longer duration of time. For selecting a suitable autoclave, the first and foremost parameter is the experimental temperature and pressure conditions and the corrosion resistance in that pressure-temperature range in a given solvent or hydrothermal fluid. To avoid corrosion of autoclave material it should coated with non reactive material called Teflon from inside. Due to the larger coefficient of thermal expansion of Teflon versus metal, the Teflon will expand and contract much more upon heating and cooling cycles than its enclosure material. For the synthesis of nanomaterials, we have used teflon-lined stainless steel autoclave of 30 mL capacity (Figure 3.20). The autoclave was rested at desired temperature under autogenous pressure for the desired period of time.
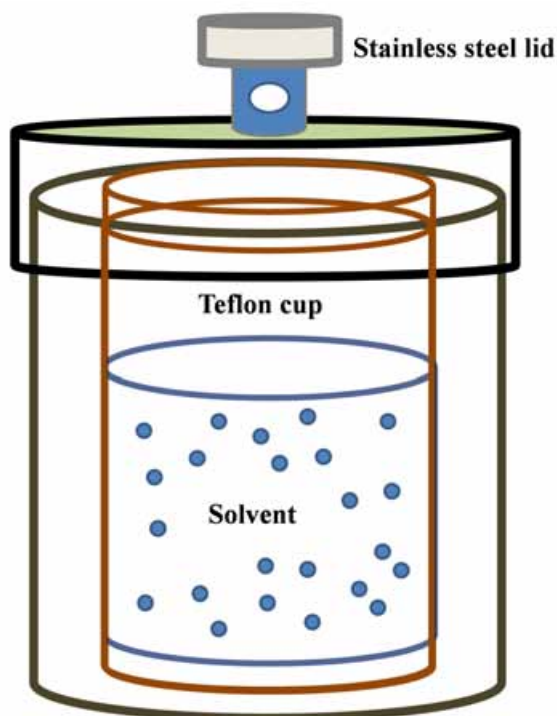
Figure 3.20. *Schematic representation of teflon-lined stainless steel autoclave.*

3.1.19. **Microwave-Assisted** **Hydrothermal** **(MAH)** **Method:** Microwave-assisted hydrothermal method is the processes for the synthesis of inorganic nanocrystals using aqueous or nonaqueous as solvent in a closed system at a certain temperature and pressure with help of microwave irradiation (Figure 3.21). During the process of microwave heating, the reaction depended on the interaction between microwave and materials. Under the electromagnetic field, the particles of materials can produce polarization such as electron polarization, atom polarization, orientation polarization, and space charge polarization. In comparison with traditional external heating methods, microwave heating is rapid volumetric heating without the heat conduction process, which can achieve uniform heating in a short period of time. For the synthesis of nanomaterials by MAH, we have used teflon-lined stainless steel autoclave of 150 mL capacity. The autoclave was microwave heated under autogenous pressure for the desired period of time.
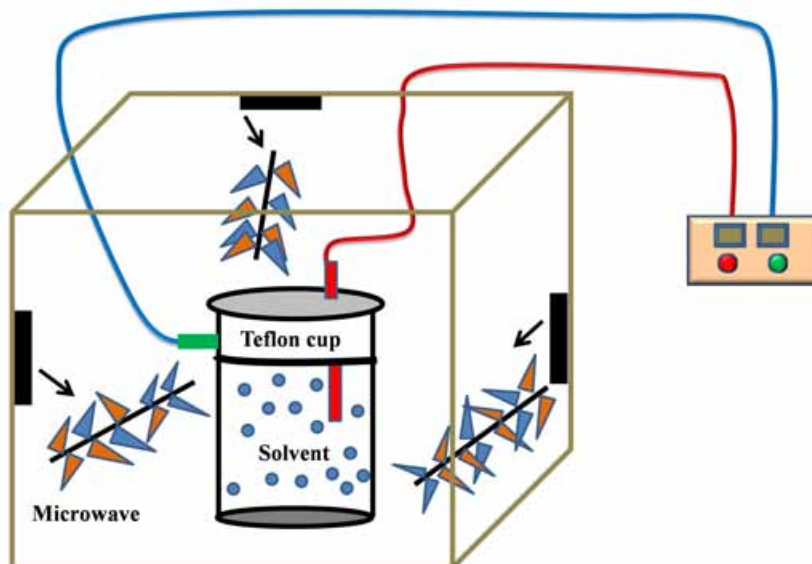
Figure 3.21. *Schematic representation of microwave-assisted hydrothermal technique.*

3.2. Sample Preparation:

In this section the different sample preparation methods have been discussed.

3.2.1. Chemicals Used: The chemicals, spectroscopic probes, and dyes were procured from the following sources. Deionized (DI) water, obtained from Millipore, was used to prepare all aqueous solutions. Tetraammine palladium(II) chloride ($Pd(NH_3)_4Cl_2$, (99% purity), cetylpyridinium chloride (CPCl, 98% purity), sodium chloride, cyclohexane (>99%), pentanol (≥99%), graphite powder, 2-propanol, ethanol, ferric chloride, sodium citrate, sodium hydroxide, manganese acetate dihydrate, copper chloride dihydrate, n-Trioctylphosphine oxide (TOPO, 99%), nafion, polyvinyl alcohol, gold acetate, copper sulphate pentahydrate, zinc oxide nanoparticles (50 nm average size, ZnO NPs), TiO_2, platinum chloride (H_2PtCl_6), lithium iodide (LiI), iodine (I_2), 4-tert-butylpyridine (TBP), bismuth nitrate pentahydrate [$Bi(NO_3)_3.5H_2O$], cityl trimethyl ammonium bromide (CTAB), sodium carbonate (Na_2CO_3) were purchased from Sigma Aldrich. Potassium bromide, ethylene glycols (EG), sodium sulfate and absolute alcohol were obtained from Merck. Stainless steel mesh was purchased from Shangyu metal mesh company, China. The probes 4-(dicyanomethylene)-2-methyl-6-(p-dimethylamino-styryl) 4H-pyran (DCM)

(Sigma Aldrich), coumarin (C500) (Sigma Aldrich), methylene blue (Carlo Erba), Crystal violet (Sigma Aldrich), Eosin (Sigma Aldrich), Rhodamine 123 (Sigma Aldrich), and the solar cell dyes N719 (Solaronix, Switzerland), protoporphyrin (Sigma Aldrich) were used without any further purification. All other chemicals used in this study were of analytical grade.

3.2.2. Preparation of Pd Nanoparticle: The swollen hexagonal mesophases with CPCl as surfactant were prepared following the previously published method with some modifications [5, 6]. Typically, 1 g of the surfactant (CPCl) was dissolved in 2 mL of brine (an aqueous solution containing 0.1 mol.L^{-1} NaCl or 0.1 mol.L^{-1} Pd(NH$_3$)$_4$Cl$_2$ in pyrex glass tubes. After a vigorous agitation at 30°C, the surfactant had completely dissolved to give a transparent and viscous micellar solution. The subsequent addition of cyclohexane in the micellar solution under stirring leads to a white unstable emulsion. A cosurfactant, pentanol-1 was added to the mixture, which was then strongly vortexed for a few minutes. This led to a perfectly colorless, translucent, birefringent and stable gel: a hexagonal mesophase. All experiments were performed at room temperature. The doped mesophases with the Pd salt were used as soft templates to synthesize palladium nanostructures induced by irradiation by UV light. For in-situ photoreduction, the doped mesophases were transferred in quartz cells and irradiated with an Oriel 300 W Xenon UV-visible lamp at a distance of 5 cm for 12 hours. After reaction, the metal NPs were easily extracted from the mesophases by a simple washing process with 2-propanol, centrifuged, and washed several times to remove the surfactant, the cosurfactant and the salt. For solvation dynamics study, we doped hexagonal mesophases with two common solvation probes such as coumarin (C500) and 4-(dicyanomethylene)-2-methyl-6-(p-dimethylamino-styryl) 4H-pyran (DCM).

3.2.3. Preparation of RGO: The graphene used here was prepared with the modified Hummer method [7, 8]. Firstly, 1 g of graphite, 0.5 g of NaNO$_3$ and 30 mL of H$_2$SO$_4$ (98 wt%) were added into a flask with stirring in an ice bath. Then 3.0 g of KMnO$_4$ was added gradually in one hour. After cooling, the mixture was continually stirred at room temperature for 3 days. The mixture was then slowly added into 100 mL of 5 wt% H$_2$SO$_4$ in one hour under stirring. After another two hours of stirring, 2.7 mL of 30 wt% H$_2$O$_2$ was added into the mixture and stirred again for two more hours. The mixture was then filtered and washed with a solution of 0.5 wt% H$_2$O$_2$ and 3 wt% H$_2$SO$_4$ for several times. Finally, the mixture was washed with distilled water to remove residual metal ions and acid. The product graphene oxide (GO) was dried in air. The GO

(mg/mL) was then dispersed in 2-propanol and exfoliated in an ultrasonic bath followed by deoxygenated under a N_2 flow. The GO sample was then exposed to γ-irradiation at room temperature for 10 h (irradiation dose of 6.4 kGy) under N_2 atmosphere. The γ-irradiation source, located at Orsay, was a panoramic ^{60}Co gamma-facility of 7000 Curies with a maximum dose rate of 6400 Gy. h^{-1}. After reaction, the reduced GO was centrifuged, and washed several times with ethanol.

3.2.4. Synthesis of Mn$_2$O$_3$ Nanoballs: In a typical synthesis of Mn_2O_3, 0.03 mol of manganese acetate dihydrate, and 0.12 mol of n-trioctylphosphine oxide were dissolved in 30 ml ethylene glycol. The resultant mixture was continuously stirred for 2 hours and then transferred into a 30 mL Teflon-lined stainless-steel autoclave. EG has been a selected as polar and high microwave absorbing solvent. The Teflon-lined autoclave was microwave-heated to 120^0C and maintained at this temperature for 5 hours. The final product was collected and washed with distilled water and absolute alcohol at least three times. Then as-prepared samples were further annealed at 450°C for 6 hours in air. The effect of TOPO concentration on the formation of Mn_2O_3 was studied by preparing precursor with different molar ratio of Mn^{2+}: TOPO using 1:1, 1:2 and 1: 4. The synthesis of copper ion doped manganese oxides nanoballs (designated as Cu-Mn$_2$O$_3$ NBs) were made by addition of 0.003 M copper chloride dihydrate under similar reaction conditions. In an another set, 0.03 mol of manganese acetate dihydrate and 1.2 mol of urea were added into 30 ml ethylene glycol to prepare Mn_2O_3 without using TOPO.

3.2.5. Synthesis of Mn$_2$O$_3$ Hierarchical: In a typical procedure, 0.03 mol of manganese acetate dihydrate, and 0.05mol of polyvinyl alcohol or 0.12 mol of n-trioctylphosphine oxide were dissolved 30 ml ethylene glycol. The resultant mixture was continuously stirred for 2 hours to form a homogeneous solution and then transferred into a 30 mL Teflon-lined stainless-steel autoclave. The autoclave was sealed and maintained at 180^0C for 6 h for both polyvinyl alcohol and n-trioctylphosphine oxide. Then it was naturally cooled to ambient temperature. The final products were collected and washed with absolute alcohol three times. Then as-prepared samples were further annealed at 450°C for 6 hours under air atmosphere and black products were obtained.

3.2.6. Synthesis of Mn$_2$O$_3$ Supported on Reduced Graphene Oxide: The graphene oxide (GO) was synthesized from graphite powder by the modified Hummers method as reported in our previous publication [7, 9]. The GO (0.5 mg mL^{-1}) was then dispersed in EG and exfoliated

in an ultrasonic bath for 30 min. Then 0.03 mol of manganese acetate dihydrate, and 0.05 mol of polyvinyl alcohol or 0.12 mol of n-trioctylphosphine oxide was added to the GO dispersion. Then the mixture was loaded into a 30 mL Teflon-lined stainless-steel autoclave and heated at elevated temperature for several hours (at 180^0C for 6 h). Then as-prepared samples were further annealed at 450°C for 6 hours under air atmosphere and the samples were then washed with water and ethanol, and dried. The reduced GO was synthesized following the same procedure without adding the manganese salt. In an another set, 0.03 mol of manganese acetate dehydrate and GO were added into 30 ml ethylene glycol to prepare Mn_2O_3 without using PVA or TOPO. To investigate the morphology effect of the as-prepared Mn_2O_3 on the ORR performance, PVA, and TOPO have been used to control the Mn_2O_3 structure in presence and absence of graphene support by keeping other conditions the same and these samples are denoted as Mn_2O_3/PVA, Mn_2O_3/TOPO, Mn_2O_3/PVA/rGO and Mn_2O_3/TOPO/rGO.

3.2.7. Sensitization of PP, Fe(III)PP and Cu(II)PP on ZnO NPs Surface: A 0.5 mM PP, $C_{34}H_{36}N_4O_5$, solution was prepared in a mixture of dimethyl sulfoxide (DMSO) and deionized (DI) water (V/V) under constant stirring for 1 h. The sensitization of ZnO NPs with PP dye was carried out at room temperature in the dark by adding ZnO NPs into a 0.5 mM PP solution with continuous stirring for 12 h. After the sensitization process, the solution was centrifuged for a few minutes and the clear supernatant solution of unattached dyes was removed. Then the sensitized material was washed with DMSO-water mixture several times to remove any unattached dye. The nanohybrid was then dried in a water bath and stored in the dark until further use. For the synthesis of Fe(III)PP or Cu(II)PP, we used 1:1 PP (0.5 mM) and metal ions (ferric chloride and copper sulphate pentahydrate) in a 1:1 water-DMSO mixture and stirred for 12 hours. After the metallation, the ZnO NPs were added to the Fe(III)PP and Cu(II)PP solution and then again stirred for 12 hours. The prepared nanohybrids were washed several times with the DMSO-water mixture to remove the unattached dyes. The nanohybrids were dried in a water bath and stored in the dark.We have verified the dye loading by synthesizing the hybrids in a slightly different way. In that case, first we synthesized the PP-ZnO nanohybrids as described in the experimental section and then we added 1:1 metal ions and PP-ZnO in 1:1 DMSO-water mixture and stirred for 12 hours. Here, the porphyrin loading was found to be same. After washing, the nanohybrids were dried in a water bath.

3.2.8. Sensitization of PP and Cu(II)PP on TiO$_2$ NPs Surface: A 0.5 mM PP (C$_{34}$H$_{36}$N$_4$O$_5$) solution was prepared in dimethyl sulfoxide (DMSO) under constant stirring for 1 h. Sensitization of PP with TiO$_2$ nanoparticles was done by addition of TiO$_2$ nanoparticles into PP followed by overnight stirring. Next, the nanohybrid was filtered out and washed several times with DMSO in order to remove unbound PP. Finally, as synthesized nanohybrid was dried in an oven and put in dark until further use. The synthesis of Cu(II)PP was carried by addition of 1:1 PP (0.5 mM) and copper sulphate pentahydrate (CuSO$_4$.5H$_2$O) followed by overnight stirring. Next sensitization with TiO$_2$ nanoparticles was performed in the similar method as described above.

3.2.9. Synthesis of Au-reduced Graphene Oxide Nanohybrid: At first GO was synthesized from graphite powder according to our previously published work [9]. The GO (1 mg mL^{-1}) was then dispersed in 2-propanol and exfoliation takes place in an ultrasonic bath for 20 min. Then 3 mM of gold (III) acetate was dissolved in GO solution followed by deoxygenation under a N$_2$ flow. The GO sample was then exposed to UV-irradiation at room temperature for 5 h. Then as synthesized Au-reduced graphene oxide nanohybrid was dried in oven. Reduced graphene oxide was obtained using similar procedure without using metal salts.

3.2.10. Synthesis of Bi-Bi$_2$O$_2$CO$_3$ Heterojunction: In a typical synthesis of Bi-Bi$_2$O$_2$CO$_3$, 0.2 millimol of Bi(NO$_3$)$_3$.5H$_2$O was first dissolved in 20 ml of 1M HNO$_3$ (denoted as solution A). Meanwhile, 1.6 millimol of Na$_2$CO$_3$ and 50 mg of CTAB were dissolved in 20 ml of ethanol-water mixture (denoted as solution B). Then, solution B was added into solution A under stirring for 30 min at 30°C. In the following, the resulting mixture was then transferred into a 20 mL Teflon-lined stainless-steel autoclave. The Teflon-lined autoclave has been placed into an oven at 180°C for 6 hours. The system was then cooled to ambient temperature naturally. The final product was collected and washed with distilled water and absolute alcohol at least five times. Then as-prepared samples were dried at 60°C for 6 hours. The reductive nature of EtOH and CTAB allowed an in-situ formation of Bi nanoparticles on the Bi$_2$O$_2$CO$_3$ nanosheet. As a result, a heterojunction structure consisting of Bi$_2$O$_2$CO$_3$ sheets and metallic Bi nanoparticles has been produced. For the synthesis of Bi$_2$O$_2$CO$_3$ nanosheets we follow a preparation as reported by Zhou et al. [10].

3.2.11. Synthesis of Mn$_2$O$_3$ Microspheres: In a typical synthesis of Mn$_2$O$_3$ microsphere, 0.03 mol of manganese acetate dihydrate, 0.27 mol of urea were added into 30 ml ethylene glycol to

form the solution [11]. The resultant mixture was continuously stirred for 2 hours and then transferred into a 30 mL Teflon-lined stainless-steel autoclave. The Teflon-lined autoclave was put into an oven at 180°C for 24 hours. The system was then cooled down to ambient temperature naturally. The final product was collected and washed with distilled water and absolute alcohol at least five times. Then as-prepared samples were further annealed at 500°C for 10 hours in air [12]. The synthesis of metal ion doped manganese oxides microspheres designated as Cu-Mn_2O_3 and Fe-Mn_2O_3 were made by addition of 0.003 M copper chloride dihydrate and 0.003 M ferric chloride respectively, under similar reaction conditions.

In order to prepare microsphere on stainless steel mesh, initially the mesh was cleaned through bath sonication in acetone for 30 min and dried on a hot-plate at 60°C. Then deposition of C-Mn_2O_3 on mesh was done by a nebulizer followed by an annealing at 400°C for 10 hours which has been used as a seeding layer for the synthesis of Mn_2O_3 microspheres. After, 0.03 mol of manganese acetate dihydrate, 0.27 mol of urea were dissolved into 30 ml ethylene glycol. The resultant mixture was continuously stirred for 2 h and then transferred into a 30 mL Teflon-lined stainless-steel autoclave containing the mesh. The Teflon-lined autoclave was put into an oven at 180°C for 24 h. The system was then cooled down to ambient temperature. Then the mesh was washed thoroughly by water to remove excess unreacted reagents. The as-synthesized Mn_2O_3 microspheres on the mesh were further annealed at 500°C for 10 h in air. The Cu-Mn_2O_3 and Fe-Mn_2O_3 microspheres on the mesh were synthesized by following the above mentioned conditions with the addition of 0.003 M copper chloride dihydrate and ferric chloride, respectively.

3.2.12. Synthesis of Citrate Functionalized Mn_2O_3: For the citrate functionalization of the Mn_2O_3 microspheres (C-Mn_2O_3 NPs), 0.5 M sodium citrate was prepared in Milli-Q water. Then 10 mg of Mn_2O_3 microspheres were added, followed by extensive mixing for 16 hours in a cyclo mixer. Finally, the non-functionalized bigger particles were filtered out and the resulting filtrate solution was used. In the same way, citrate functionalized doped Mn_2O_3 NPs (C-Fe-Mn_2O_3 and C-Cu-Mn_2O_3) were synthesized. For the surface modification of the citrate functionalized NPs, pH of the solution was adjusted to 12 by addition of 1 M sodium hydroxide. The resulting solution was then finally heated at 60°C for 12 hours. Finally, the solution becomes highly photoluminescent and the color of the solution turned into yellowish-brown. Generally, Mn^{3+} in acid/neutral solution is unstable and has a tendency to disproportionate into Mn^{2+} and Mn^{4+}, whereas in alkali medium it is stabilized by comproportionation of Mn^{4+} and Mn^{2+} [13]. The C-

Fe-Mn$_2$O$_3$ and C-Cu-Mn$_2$O$_3$ samples also become highly luminescent by above described treatment. Then the functionalization of the microspheres on stainless steel mesh by citrate was performed accordingly.

3.2.13. Synthesis of Gold and Aluminum Modified TiO$_2$: The Au-TiO$_2$ nanohybrid was obtained by chemical reduction of Au (III) in the TiO$_2$ suspension following simple one-step chemical reduction method [14, 15]. An aqueous solution of TiO$_2$ suspension is sonicated for 20 min, then 5 μL of 100 mM HAuCl$_4$ added under continuous starring for 5 min. After that 200 μL of 10 mM NaBH$_4$ was added, the reaction was allowed to continue for another 30 min. The Au-TiO$_2$ nanohybrid were centrifuged and dried at 80°C.

The aluminum nanoparticles were synthesized following the previous report with some modification [16]. At first 0.01 mmole of aluminum acetylacetonate [Al(acac)$_3$] along with TiO$_2$ were added to the toluene which was already placed in a two neck round-bottom flask (RBF) equipped with a magnetic stirring bar. Then, 0.03 mmole of lithium aluminum hydride (LiAlH$_4$) was added into the reaction flask. The reaction mixture was then refluxed continuously with stirring approximately for 72 h under nitrogen atmosphere. After completion, the reaction mixture was cooled down to room temperature and a gray-colored precipitate was settled down. The crude product obtained was washed with ice cold methanol for several times in order to wash out organic part and the unreacted starting materials. Finally the product was dried at low pressure under a nitrogen sink. In order to synthesize the nanoparticles (Au/Al) without TiO$_2$ matrix, we have followed above procedures excluding the addition of TiO$_2$ nanoparticles in the procedures. We have conjugated PP with the synthesized nanoparticles by overnight stirring and repeated washing using dimethyl sulfoxide.

3.2.14. Photocurrent Measurements: Photocurrent measurements were done in a dye-sensitized solar cell (DSSC) setup [17]. To prepare the working and counter electrodes for the photocurrent responses, FTO glasses were ultrasonically cleaned in soap-suds, deionized water and acetone, respectively. For preparation of the counter electrode, platinum (Pt) was deposited on the FTO substrates by thermal decomposition of 10 mM platinum chloride (in isopropanol) at 385 °C for 30 min. Bi$_2$O$_2$CO$_3$ and Bi-Bi$_2$O$_2$CO$_3$ were used as the photoelectrode. The two electrodes were placed on top of each other with a single layer of 60 μm thick Surlyn (Solaronix) as a spacer between the two electrodes. A liquid electrolyte composed of 0.5 M lithium iodide (LiI), 0.05 M iodine (I$_2$) and 0.5 M 4-tert-butylpyridine (TBP) in acetonitrile was used as the

hole conductor and filled in the inter electrode space using capillary force, through two small holes (diameter = 1 mm) predrilled on the counter electrode. Finally, the two holes were sealed by using another piece of Surlyn to prevent a leakage of the electrolyte from the cell. In all our experiments, the active area of the DSSCs was fixed to 1 cm^2.

3.2.15. Adsorption Experiments: Methylene blue, Eosin, Rhodamine 123, Coumarin and Crystal violet stock solutions were prepared by dissolving in water (1mg mL^{-1}). The desired dye concentration used in this study was 10 μM, obtained by diluting the stock solution in accurate proportions. The pH of the solution was maintained by using 0.01 N HCl and NaOH solution. The detailed adsorption kinetics of Rh123 on the Au-RGO nanohybrid was monitored based on absorption spectroscopy. To probe adsorption behavior, different concentrations of Rh123 solution (total volume 2 mL) were prepared from stock solution with proper dilution using deionized water (DI). In each case the equal amount of adsorbent (0.5 mg/mL) were added. Therefore, the adsorption capacity, q_e (μmol g^{-1}) can be calculated by using the following equation:

$$q_e = \frac{V}{m}(C_0 - C_t) \qquad\qquad (3.7)$$

where, C_0 is the initial concentration of dye (μM), C_t is the concentration at time t (μM), V is the volume of the suspension (L) and m is the mass of the adsorbent (g). pH dependency studies were performed at different pH (2, 4, 6, 8 and 10) by adjusting with 1 N NaOH or HCl solution. In order to find out the influence of temperature on adsorption kinetics of Rh123 on Au-RGO nanohybrid was carried out at five different temperatures (20, 30, 40, 50 and 60 °C) at pH 6.

3.2.16. Fabrication of DSSCs: For the fabrication of DSSCs, at first TiO$_2$ was pasted on a FTO glass substrate. The ratio of the metal nanoparticles (Au and Al) to TiO$_2$ could be readily adjusted by changing the concentration of the nanoparticles. These photoanode were annealed at 450°C for 1 h. After that photoanode were immersed in a 0.5 mM PP, 0.5 mM (Cu)PP and N719 solutions for 24 h at room temperature. For preparation of counter electrode, the platinum (Pt) was deposited on the FTO substrates by thermal decomposition of 10 mM platinum chloride (in isopropanol) at 385 °C for 30 min. The two electrodes were placed on top of each other with a single layer of 60 μm thick Surlyn (Solaronix) as a spacer between the two electrodes. A liquid electrolyte composed of 0.5 M lithium iodide (LiI), 0.05 M iodine (I$_2$) and 0.5 M 4-tert-butylpyridine (TBP) in acetonitrile was used as the hole conductor and filled in the inter

electrode space by using capillary force, through two small holes (diameter = 1 mm) predrilled on the counter electrode. Finally, the two holes were sealed by using another piece of Surlyn to prevent the leakage of electrolyte from the cell. In all our experiments, the active area of the DSSCs was fixed at 0.64 cm^2.

3.2.17. Electrochemical Measurements: The electrochemical measurements were conducted at 30°C in a two compartment glass-cell fitted with a conventional three electrode assembly. In all electrochemical measurements, a glassy carbon rod used as working electrode and Hg/HgO/OH (1 M) (designated as MMO) having an equilibrium electrode potential of ~ 0.1 V with respect to the standard hydrogen electrode (SHE). A large Pt-foil (1 cm ×1 cm) was used as counter electrode and potential data were recorded with respect to MMO. Cyclic voltammetric study was performed using a computer aided Potentiostat/Galvanostat (AEW-2, Munistst, Sycopel Scientific Ltd., UK). Cyclic voltammogram (CV) of each electrode was recorded at the scan rate 50 mVs^{-1} for several consecutive cycles until a steady profile was obtained. Chronopotentiometry was also performed by applying a current density of 5 mA cm^{-2} with the help of a constant current charger (DB-300, DB Electronics) and the potential was recorded with an EC digital multimeter (DM 610 4B) as described before [18]. The glassy carbon electrode was pretreated using the following process. First, the surface of a glassy carbon electrode was polished with 1.0, 0.3 and 0.05 μm α-alumina powders in sequence, rinsed thoroughly with twice distilled water and placed in a water-filled ultrasonic bath over a 2 min period. After dried in air, Pd NPs were deposited for further use.

Pd nanostructure suspension consisting of 0.5 mg of Pd NPs in 500 μL of 0.5 % wt nafion (as Pd/Nafion) and another suspension consisting of 0.25 mg of Pd NPs with 0.25 mg reduced GO nanosheets (RGO) in 500 μL of 0.5 % wt nafion (Pd/RGO-Nafion) in ethanol solution were used for the electrochemical characterization. A layer was prepared by deposing 10 μL of the homogeneous solution of Pd NPs suspensions on a polished glassy carbon electrode surface.

For another voltammetry measurements, a three-electrode cell was used with Ag/AgCl as a reference electrode and a Pt wire as the counter electrode. The electrolyte comprised of a 0.5 M aqueous Na$_2$SO$_4$ solution. The working electrode was fabricated by coating catalysts on a glassy carbon substrate. For electrode preparation, 2 mg of Mn$_2$O$_3$ and Cu-Mn$_2$O$_3$ were dissolved in 20 μl of ethanol containing 5 wt% nafion as a binder. Then 10 μl of sample solution were deposited

on glassy carbon (working electrode). The multichannel potentiostat–galvanostat system (AutoLab 302N) was used to study the cyclic voltammetry (CV) and charge–discharge cycling studies in the potential window of −0.2 to 0.8 and at different scan rate of 5-50 mVs^{-1}.

Cyclic voltammetry (CV) and Chronoamperometry (CA) were performed for ORR and OER using a potentiostat galvanostat (SP150, BioLogic Science Instruments, France). A Pt wire and an Ag/AgCl/KCl (Sat. KCl) were used as counter and reference electrodes, respectively and 0.1 M KOH was used as an electrolyte. To evaluate the electrochemical activity for the oxygen evolution reaction (OER) of the Mn_2O_3, CV were performed under saturated N_2 solution. Pt wire and Ag/AgCl (Saturated KCl) were used as counter and reference electrodes, respectively and 0.1 M KOH was used as an electrolyte [19]. Catalyst ink was prepared by ultrasonically mixing 6.0 mg of catalyst sample with 3 mL of pure deionized water and 10 µL of 5 wt% nafion solution for 1 h in order to make a homogeneous suspension. Then, 5 µL of prepared catalytic ink was transferred to the surface of a glassy carbon electrode of 3 mm diameter using a micropipette. Finally, the ink was allowed to dry for 10 min at room temperature to form a thin catalyst film on a glassy carbon electrode as a working electrode.

For another electrochemical measurements cyclic voltametry (CV) were carried out in an electrochemical cell using 0.01 M KCl electrolyte. 2 mg of Mn_2O_3 sphere and 6 mg of C-Mn_2O_3 were dissolved in 50 µl of ethanol containing 5 wt% Nafion as a binder. Then 10 µl of sample solution were deposited on glassy carbon (working electrode). CV was carried out using CH Instruments and swept at 50 mVs^{-1} between 0 to 3 V applied versus an Ag/AgCl reference electrode.

3.2.18. Oxygen Reduction Reaction (ORR) and Oxygen Evolution Reaction (OER) Measurements: To evaluate the electrochemical activity for ORR and OER rotating disk electrode (RDE) experiments were performed. Pt wire and Ag/AgCl (Sat. KCl) were used as counter and reference electrodes, respectively and 0.1 M KOH was used as an electrolyte. High-purity O_2 gas was purged for 30 mins before each RDE experiment to make the electrolyte saturated with O_2. Rotating disk electrode voltammetric study was carried out with a scan rate of 10 mV/s and potential range from 0 to −0.6 V under ambient conditions. Another, rotating disk electrode voltammetric study was carried out with a scan rate of 10 mV/s and potential range from 0 to −1 V under ambient conditions. Catalyst ink was prepared by ultrasonically mixing 6.0

mg of catalyst sample with 3 mL of pure deionized water and 10 µL of 5 wt% Nafion solution for 1 h in order to make a homogeneous suspension. Then, 5 µL of prepared catalytic ink was transferred to the surface of a glassy carbon electrode of 3 mm diameter using a micropipette. Finally, the ink was allowed to dry for 10 min at room temperature to form a thin catalyst film on a glassy carbon electrode as a working electrode.

To evaluate the electrochemical activity for the oxygen evolution reaction (OER) rotating disk electrode (RDE) experiments were performed under saturated N_2. Pt wire and Ag/AgCl (Sat. KCl) were used as counter and reference electrodes, respectively and 0.1 M KOH was used as an electrolyte [20]. Electrochemical characterization was conducted using a single potentiostat with a scan rate of 10 mV/s and potential range from 0 to 1 V. Ink was prepared according to the method described above for ORR.

References

[1]   D. V. O'Conner, D. Philips, *Time-Correlated Single Photon Counting*, Academic Press, London, 1984.

[2]   S. S. Sinha, P. K. Verma, A. Makhal, S. K. Pal, A Versatile Fiber-Optic Coupled System for Sensitive Optical Spectroscopy in Strong Ambient Light, *Rev. Sci. Instrum.* 80 (2009) 053109.

[3]   S. Sarkar, A. Makhal, T. Bora, S. Baruah, J. Dutta, S. K. Pal, Photoselective Excited State Dynamics in ZnO-Au Nanocomposites and their Implications in Photocatalysis and Dye-Sensitized Solar Cells, *Phys. Chem. Chem. Phys.* 13 (2011) 12488-12496.

[4]   A. Makhal, S. Sarkar, S. K. Pal, Protein-Mediated Synthesis of Nanosized Mn-Doped ZnS: A Multifunctional, UV-Durable Bio-Nanocomposite, *Inorg. Chem.* 51 (2012) 10203-10210.

[5]   E. Pena dos Santos, M. S. Tokumoto, G. Surendran, H. Remita, C. Bourgaux, P. Dieudonné, E. Prouzet, L. Ramos, Existence and Stability of New Nanoreactors: Highly Swollen Hexagonal Liquid Crystals, *Langmuir* 21 (2005) 4362-4369.

[6]   S. Ghosh, N. A. Kouamé, L. Ramos, S. Remita, A. Dazzi, A. Deniset-Besseau, P. Beaunier, F. Goubard, P.-H. Aubert, H. Remita, Conducting Polymer Nanostructures as Promising Photocatalysts under VisibleLight, *Nat Mater* 14 (2015) 505-511.

[7]   W. S. Hummers, R. E. Offeman, Preparation of Graphitic Oxide, *J. Am. Chem. Soc.* 80 (1958) 1339-1339.

[8]   D. Li, M. B. Muller, S. Gilje, R. B. Kaner, G. G. Wallace, Processable Aqueous Dispersions of Graphene Nanosheets, *Nat. Nanotechnol.* 3 (2008) 101-105.

[9]   S. Ghosh, H. Remita, P. Kar, S. Choudhury, S. Sardar, P. Beaunier, P. S. Roy, S. K. Bhattacharya, S. K. Pal, Facile Synthesis of Pd Nanostructures in Hexagonal Mesophases As a Promising Electrocatalyst for Ethanol Oxidation, *J. Mater. Chem. A* 3 (2015) 9517-9527.

[10]   Z. Zhao, Y. Zhou, F. Wang, K. Zhang, S. Yu, K. Cao, Polyaniline-Decorated {001} Facets of $Bi_2O_2CO_3$ Nanosheets: In Situ Oxygen Vacancy Formation and Enhanced Visible Light Photocatalytic Activity, *ACS Appl. Mater. Interfaces* 7 (2015) 730-737.

[11] Q. Li, L. Yin, Z. Li, X. Wang, Y. Qi, J. Ma, Copper Doped Hollow Structured Manganese Oxide Mesocrystals with Controlled Phase Structure and Morphology as Anode Materials for Lithium Ion Battery with Improved Electrochemical Performance, *ACS Appl. Mater. Interfaces* 5 (2013) 10975-10984.

[12] J. Li, S. Xiong, X. Li, Y. Qian, Spinel $Mn_{1.5}Co_{1.5}O_4$ Core-Shell Microspheres as Li-Ion Battery Anode Materials with a Long Cycle Life and High Capacity, *J. Mater. Chem.* 22 (2012) 23254-23259.

[13] T. Takashima, K. Hashimoto, R. Nakamura, Mechanisms of pH-Dependent Activity for Water Oxidation to Molecular Oxygen by MnO_2 Electrocatalysts, *J. Am. Chem. Soc.* 134 (2012) 1519-1527.

[14] N. Zhou, J. Wang, T. Chen, Z. Yu, G. Li, Enlargement of Gold Nanoparticles on the Surface of a Self-Assembled Monolayer Modified Electrode: A Mode in Biosensor Design, *Anal. Chem.* 78 (2006) 5227-5230.

[15] Y. Liu, R. Guo, The interaction Between Casein Micelles and Gold Nanoparticles, *J. Colloid Interface Sci.* 332 (2009) 265-269.

[16] S. R. Ghanta, K. Muralidharan, Chemical Synthesis of Aluminum Nanoparticles, *J. Nanopart. Res.* 15 (2013) 1715.

[17] S. Sardar, P. Kar, H. Remita, B. Liu, P. Lemmens, S. Kumar Pal, S. Ghosh, Enhanced Charge Separation and FRET at Heterojunctions between Semiconductor Nanoparticles and Conducting Polymer Nanofibers for Efficient Solar Light Harvesting, *Sci. Rep.* 5 (2015) 17313.

[18] J. Bagchi, S. K. Bhattacharya, The Effect of Composition of Ni-Supported Pt-Ru Binary Anode Catalysts on Ethanol Oxidation for Fuel Cells, *J. Power Sources* 163 (2007) 661-670.

[19] S. Ghosh, P. Kar, N. Bhandary, S. Basu, S. Sardar, T. Maiyalagan, D. Majumdar, S. K. Bhattacharya, A. Bhaumik, P. Lemmens, S. K. Pal, Microwave-Assisted Synthesis of Porous Mn_2O_3 Nanoballs as Bifunctional Electrocatalyst for Oxygen Reduction and Evolution Reaction, *Catal. Sci. Technol.* 6 (2016) 1417-1429.

[20] M. R. V. Lanza, R. Bertazzoli, Selection of a Commercial Anode Oxide Coating for Electro-Oxidation of Cyanide, *J. Braz. Chem. Soc.* 13 (2002) 345-351.

Chapter 4

Synthesis and Characterization of Various Applied Nanomaterials

4.1. Introduction:

The development of advanced materials and processes is a central issue which contributes to the ultimate goal of accelerating the implementation of novel nanomaterials-based technology providing clean and affordable energy [1-3]. Platinum is the superlative electrocatalyst for most of the relevant reactions involved in fuel cells which constitute promising future power sources. However, several critical issues such as the migration, aggregation and dissolution in harsh electrochemical environments as well as the weak tolerance to CO poisoning and the high cost must be resolved before Pt-based electrocatalysts can be commercialized [4, 5]. Alternatively, Pd based nanostructured materials play a crucial role in the catalysis of various relevant reactions in fuel cells, resulting in enhanced intrinsic electroactivity with high energy conversion efficiency, which is suitable for direct ethanol fuel cells (DEFCs) [6-8]. Therefore, many recent efforts have been devoted to control the morphology and composition of Pd-based catalysts that can offer a great opportunity to achieve enhanced catalytic performance and higher utilization of Pd [9-14]. In our earlier reports, Pd nanowires, and porous Pd nanoballs connected with three-dimensional Pd nanowires demonstrated superior electro-catalytic activity for the ethanol oxidation and appear as promising candidates for fuel cell applications [15, 16]. In spite of these successful demonstrations, it is important to note that their mass activity (in terms of Pd) for the ethanol electrooxidation is still not satisfactory [17-19]. Hence, it is highly desirable to develop a simple method for the synthesis of novel Pd nanoparticles (NPs) based electrocatalysts with high activity and durability for fuel cell applications. Moreover, various shape-controlled Pd nanostructures have been extensively explored for electrocatalysis. Nevertheless, the reports regarding self-assembled Pd nanostructures are scarce. Herein, we demonstrate a very simple and efficient route to synthesize Pd nanostructures in liquid crystals by photoreduction.

A liquid crystal (LC) appears as a perfect candidates for the matrix-guided synthesis and self-assembly of nanoscale materials as it combines order and mobility at the molecular (nanoscale) level [20-23]. Few examples have been reported for the preparation of

nanostructures in nematic LC as structure-directing templates [22, 24]. One of the significant problems associated with templating of nematic domains is that nanoparticles are expelled to domain boundaries which leads to the formation of particulate networks and consequently, free-standing porous materials can not achieved using this route [25-27]. Attard et al. successfully demonstrated that direct hexagonal LCs made by a ternary mixture (nonionic surfactant, metal salts, and water) can be used as template for the synthesis of bulk porous materials and porous metal films by electro-deposition [28, 29]. Recently, we reported a systematic study of the effect of templating approach allowing the synthesis of bimetallic nanoballs of tunable porosity and composition in a swollen hexagonal mesophase (SLC) [30]. The swollen mesophases consist of surfactant-stabilized oil-swollen tubes that are arranged on a triangular lattice in an aqueous medium [31, 32]. In the past years, we employed doped SLC with various compounds and used as nanoreactors to synthesize diverse nanostructured materials (such as metal, polymer or oxides) both in the aqueous and in the oil phases [33-36]. Here, the photoreduction of the palladium salt is induced by UV light irradiation within the aqueous phase of hexagonal mesophases. By virtue of employing Pd as an active electrocatalyst, we studied the ethanol oxidation reaction (EOR) using as prepared Pd nanostructures as the anode material. Additionally, in order to enhance the dispersion and accessibility of catalyst reduced graphene oxide nanosheets (RGO) modified Pd nanostructure has been used in combination with a Nafion support during electrooxidation.

Despite the immense advances in unsupported nanostructured noble metals as electrocatalysts, the relatively low efficiency and high usage of noble metals in such unsupported metal catalysts still limit their practical applications. Hence, the design and fabrication of more active electrocatalysts with excellent performance, durability and low cost are of great importance. To improve the electrochemical performance of these catalysts, carbon based conductive substrates such as carbon nanotubes (CNT), carbon fibers and Vulcan XC-72 (VXC) etc are widely used as supports to disperse the metal NPs [37-40]. Supported metal NPs play a pivotal role as catalysts for energy storage/conversion, however, the aggregation tendency of NPs is an impediment for stable performance and loss of active surface area is a major cause of deactivation for supported catalysts [41, 42]. Recently, we demonstrated that the utilization of conducting polymer nanostuctures improve the electrocatalytic activity and durability of Pd catalysts [43]. A good catalyst support should possess good conductivity and mechanical strength and long term stability with high surface area [44, 45]. In this respect, graphene oxides

possess high surface area, low cost and enhanced conductivity, and they have been chosen as excellent carbon supports for catalysts to achieve enhanced electrochemical performance for fuel oxidation, oxygen reduction and water splitting reactions [46-49]. The ease of processibility and functionalization make graphene-based functional materials ideal candidates for a variety of energy applications [50, 51]. Hence, reduced RGO nanosheets in combination with nafion can be used as an efficient support for metal NPs which would exhibit fascinating catalytic properties. We report the synthesis and characterization of assembled palladium nanostructures in hexagonal mesophases. We demonstrate that the Pd nanostructures synthesized in soft templates are promising electrocatalysts having superior activity and stability for EOR. Moreover, the introduction of RGO nanosheets along with nafion into the electrode containing the Pd nanostructures leads to high electrocatalytic activity and durability for EOR.

In recent years, significant efforts have been devoted to the fabrication of metal oxides having large surface area, superior thermal stability and possible utilization in fundamental research as well as technological applications [52-55]. Among the transition metal oxides, manganese oxides nanostructures are attractive due to their involvement in active redox reactions which are consequently beneficial for a broad range of electrochemical applications from energy storage in lithium ion batteries and fuel cells to water splitting and chemical sensing [56-62]. A prerequisite for such applications of oxides nanostructures is novel synthetic routes leading to low cost and large-scale production of materials at the nano-scale with well-defined morphologies. Up to now, various methodologies have been employed to synthesize manganese oxide, however, most of these complicated synthetic procedures are associated with high temperature synthesis, low-yield and they are time-consuming [62-64].

The development of sustainable synthetic processes using alternate energy inputs and greener reaction media has been recognized as an alternative approach for large-scale production of functional materials [35, 43, 65]. In this regard, the microwave-assisted hydrothermal (MAH) method offers a rapid and highly reproducible technique for the preparation of metal oxide nanomaterials with several advantages such as reduced energy consumption, shorter reaction time and higher product yield [66-68]. The microwave-assisted synthesis of metal oxides nanostructures with various morphologies such as Co_3O_4, MnO_2 and TiO_2, etc., has been well documented in the literature [66, 69]. Rapid synthesis of ZnO nanostructures using a microwave-assisted approach to accelerate nucleation and growth has been previously reported by our group

[70]. Although microwave-assisted growth has been in vogue for preparation of various metal oxides nanostructures for the past decade, the reports regarding manganese oxides are scarce [68, 71, 72]. Here, we have reported the synthesis of porous Mn_2O_3 nanoballs (NBs) through microwave-assisted route which are of useful for electrocatalytic applications.

The implementation of environment-friendly clean energy technologies is a vital issue and an alternative to traditional fossil-fuel, as fuel cells devices endows efficient clean energy production and conversion [73, 74]. A considerable number of nanomaterials with superior electrocatalytic activity are emerging as a new class of electrode materials to fulfill the increasing demands for high power conversion and durability [65, 75, 76]. Recently, there has been immense interest in the design and development of highly efficient oxygen reduction reaction (ORR) and oxygen evolution reaction (OER) catalysts which can resolve the crucial issues related to fuel cells and rechargeable metal-air batteries [77]. Pt-based metals or alloys are regarded as robust and efficient catalysts for oxidation reaction but their high cost and limited abundance necessitate the exploitation of new nonprecious metal catalysts [78]. On the other hand, precious metal oxide nanomaterials such as iridium dioxide (IrO_2) and ruthenium dioxide (RuO_2) have demonstrated the best overall performance for catalyzing ORR and OER [79, 80]. Despite this activity, the development of active material *via* a naturally abundant and economically viable method has remained an unresolved issue in energy conversion applications. In fact, the oxygen reduction reaction is a challenging reaction due to slower ORR kinetics and the stability of cathode catalyst material under cycling in acidic or alkaline condition during operation. However, one critical issue to be addressed is the lack of effective electrocatalysts for the four electron ($4e^-$) reduction of O_2 (ORR) at relatively low overpotential [81]. Accordingly, non-precious transition metal oxides and in particular, manganese oxides (MnO_x) have been regarded as alternative ORR catalysts with reasonable catalytic activity, low cost, and structural stability for primary alkaline based fuel cells [82-86]. In contrast to other manganese oxides (Mn_3O_4 or MnO_2), little attention has been paid to exploring the potential of the catalytic activity of Mn_2O_3 nanostructured materials [83-85]. Suib et al. reported a manganese oxide (MnO_2) catalyst having a dual nature (OER and ORR catalysis), a potential alternative for the high cost Pt and its alloys, iridium, and ruthenium oxide catalysts [86]. Recently, mixed metal oxides display excellent catalytic activities have been investigated as one of the most promising candidates for ORR in an alkaline medium [87, 88]. Muhler et al. described the excellent

electrocatalytic activities of cobalt–manganese-based spinels as synergistic bifunctional catalysts for OER and ORR [89].

In another study, we developed a simple and convenient microwave assisted approach for the controlled synthesis of pure and metal doped Mn_2O_3 balls at the nano-scale. The structure and chemical composition have been studied along with the growth process and the merits of the MAH method using trioctylphosphine oxide (TOPO) as a chelating agent for the formation of Mn_2O_3 nanoballs are highlighted. To the best of our knowledge, this is the first report on the synthesis of porous Mn_2O_3 nanostructures with controlled shape and composition by the MAH method. A systematic investigation has been conducted in order to control average size of the Mn_2O_3 nanostructures by optimizing the concentration of the chelating agent (TOPO) and moreover, a mechanism of the formation of nanoballs has also been proposed. The cyclic voltammetry measurements have been employed to investigate the electrocatalytic activity of these Mn_2O_3 nanostructures for both oxygen reduction and evolution reaction.

The superior efficiency of fuel-cell to converts chemical energy directly into electrical energy with low emission of pollutants makes a potentially viable option as an alternative future power source [90]. However, technological hurdles that still prevent the commercialization of fuel cell technologies require designing of low-cost, durable and nonprecious metal catalysts as alternatives to the bench marked Pt-based materials [91, 92]. Recently, the excellent structural versatility of manganese oxides, which include MnO, MnO_2, Mn_2O_3, and Mn_3O_4, have received considerable interest for wide range applications in catalysis, energy storage in lithium ion batteries and fuel cells [93-95]. In this regards, the possibility of improving electrochemical properties by tailoring morphologies and surface structures, enormous effort is therefore devoted to developing morphology-controllable synthesis, however, suffer from the requirements of high temperature and tedious process [63, 64, 96, 97]. Emerging research trends focus on hydrothermal synthesis as a rapid and facile route for metal oxide catalysts, however, only a few Mn_2O_3 porous structures having enhanced electrochemical performances, including high capacity, good cycling stability, and rate capability, as cathode materials reported till date [98, 99]. Very recently, rapid synthesis of Mn_2O_3 microspheres using a hydrothermal approach has been reported by our group [55]. However, the role of structure controlling agent during hydrothermal synthesis in order to tune morphology of metal oxides structures is not addressed. Recently, the assembly of metal oxide molecules into three-dimensional (3D) hierarchical

microstructured materials have attracted considerable interest because of multiphase heterogeneous interfaces, controllable physical and chemical microenvironment, high surface area, optimized pore size distribution and abundance of inner voids provides improved performance towards their potential application such as catalysts, super capacitors and solar cells etc [100-102]. Hence, it is crucial to develop facile routes for controlled formation of 3D hierarchical structures and assembly of complex nanostructures at low cost which still remains a challenge. One feasible approach is the synthesis of oxides materials using porous matrix as conductive support or template such as carbon nanotubes, metal–organic frameworks (MOFs) etc via a simple calcinations with controlled composition and microstructure on the nanoscale [103-105]. In particular, hierarchical structures, which are assembled by oxides materials and combined with electronically conductive agents, for example, carbon nanofibers, carbon nanotubes, conducting polymers, graphene, reduced graphene oxide (rGO) sheets have attracted a considerable attention [43, 106-109]. In comparison to other supports, graphene sheets have been aroused great promise because of its excellent electrical conductivity, high surface area (calculated value = 2630 m^2g^{-1}), as well as chemical stability [65, 110]. Hence, graphene functionalized metal oxides as electrode materials have many advantages such as high surface area, preventing the aggregation of catalysts, possess good electrical conductivity to facilitate electronic transfer, offering easy access of the electrolyte to the electrode surface, allowing increased utilization of active material and enhanced stability [111]. Moreover, doped graphene oxides can be also used as efficient electrocatalysts having large number active sites generated from doping [112]. Here, we have designed a series of hierarchical transition metal oxides based microstructure supported on graphene nanosheets via one pot hydrothermal route for the elctrooxidation of water.

Bifunctional catalysis is a novel concept in modern energy technologies, where the catalyst can be used for water splitting with oxygen evolution reactions (OER) as well as oxygen reduction reactions (ORR) during energy conversion between fuel and electricity [85, 113]. The various electrochemical devices, fuel cells and metal–air batteries, direct solar or electricity-driven water splitting operates via electrochemical reactions involving oxygen supplied from the ambient air on the cathode, i.e., the oxygen reduction reaction during discharge and the oxygen evolution reaction during charge [114, 115]. There has been extensive research on electro-catalytic materials that are capable of promoting both the ORR and the OER, however, transition

metal oxides has been extensively used as alternative low cost, excellent electrocatalytic activity and high stability [48, 87, 116-119]. Dai and coworkers deposited Co_3O_4 nanoparticles on a graphene support and investigated their electrocatalytic activity [48]. Lee et al. developed a multistep process for the synthesis of highly efficient oxygen reduction electrocatalyst based on nitrogen-doped (N-doping) graphene nanosheets (NG) using mussel-inspired dopamine as a nitrogen source [116]. It has been proposed that N-doping may leads to improve catalytic activity as well as provides anchoring sites for the growth of manganese oxide nanowires on the graphene nanosheets (NG/MnOx). However, there is a contradiction about the role of doping in graphene nanosheets which may causes structural destabilization and make them prone to oxidation. Kokoh et al. also reported low oxide mass loading (ca. 30 wt %) Co_3O_4/nitrogen doped graphene-based composites as efficient electrocatalysts for ORR and OER [117]. In order to improve the electrochemical performance of metal oxides, further a series of mixed metal oxides have also been coupled with reduced graphene oxide as a highly active and stable bifunctional electrocatalyst [118-122]. Recently, Xu and co-workers development a high performance $Au/NiCo_2O_4$ based OER catalysts supported on the three-dimensional hierarchical porous graphene-like (3D HPG) material by ion-exchange/activation combination method using a metal ion exchanged resin as carbon precursor [123]. Very recently, Kannan et al. employed 3D graphene-mixed metal oxide-supported carbon palladium quantum dot nanoarchitectures as a bifunctional electrocatalyst for direct ethylene glycol fuel cells and oxygen evolution reactions [124]. However, the high cost and limited availability of Pt, Pd and Au metals are key barriers to the development of large scale oxygen catalysts using Pt-based, Pd-based and Au-based catalysts. Alternatively, Wen et al. reported reduced graphene oxide supported chromium oxide hybrid as a promising low cost and highly efficient catalyst for ORR by the pyrolysis of chromium-urea coordination compound [125]. Manganese oxides supported on graphene have also been employed as active, stable and low-cost electrocatalysts for fuel cells and Li–air batteries [126]. Kim and coworkers reported ionic liquid mediated Mn_3O_4 supported on graphene sheets as efficient ORR electrocatalysts with tunable oxygen reduction pathway [127]. Qiao et al. also developed a mesoporous Mn_3O_4/graphene hybrid material which illustrates stable and high ORR catalytic activity [128]. In spite of huge attempt have been made to developed transition metal oxides based hybrid catalysts, reports regarding hirarchical Mn_2O_3/graphene hybrid materials using one pot synthesis is very limited. For the first time, we developed a facile and

effective, one pot hydrothermal-assisted route for the synthesis of hierarchical, porous and electrochemically active graphene supported manganese oxide hybrid materials. Consequently, this simple synthetic methodology is a viable approach in making manganese oxide nanostructure as a highly active catalyst which can be extended for other metal oxides for application in fuel cells. Here in another work, we report the controlled synthesis of pure and graphene supported Mn_2O_3 by a hydrothermal process exploring the role common chelating agents and their electrochemical behavior for ORR and OER in alkaline medium. These newly fabricated Mn_2O_3 microstructures were extensively characterized by using a wide range of methods including transmission electron microscopy, scanning electron microscopy, X-ray diffraction and thermal analysis.

4.2. Results and Discussion:

4.2.1. Facile Synthesis of Pd Nanostructures in Hexagonal Mesophases as a Promising Electrocatalyst for Ethanol Oxidation [65]:

Swollen hexagonal mesophases, resulting from the surfactant mediated self-assembly in a quaternary system (water, surfactant, cosurfactant, and oil) serves as versatile templates for synthesizing various nanomaterials [31, 35]. For Pd nanostructure synthesis, we prepared mesophases doped with 0.1 M Pd complex with a volume ratio of oil over water (O/W) (v/v) fixed at 1.5 for the in-situ photo reduction. The Pd nanostructures synthesized in doped CPCl-based mesophases were extracted with 2-propanol. Figure 4.1 shows the UV-Vis spectra of Pd

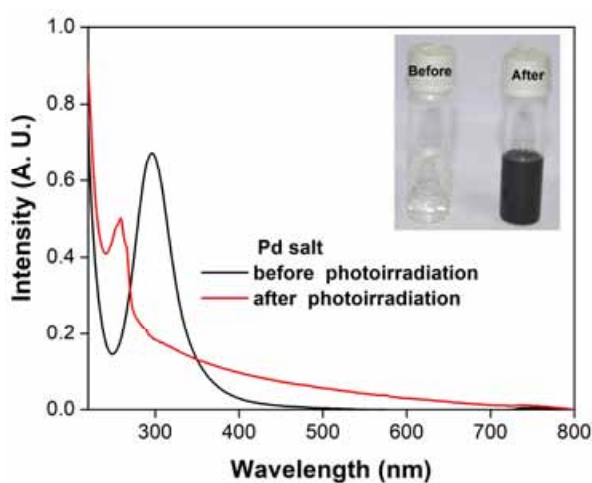**Figure 4.1.** *UV-visible spectra of Pd $(NH_3)_4Cl_2$ complex before and after photo irradiation. Inset: Photographs of hexagonal mesophases doped with 0.1 M Pd $(NH_3)_4Cl_2$ complex before and after UV irradiation exposure. The color change indicates the photo reduction of Pd complex by UV irradiation.*

$(NH_3)_4Cl_2$ complex (solid black line) and the suspensions of the Pd nanostructure (solid red line) extracted from mesophases after 12 hours of photoirradiation. The Pd complex shows a peak at 297 nm and after photoirradiation, the intensity of peak is decreases. After the reduction, a new band appears at 258 nm along with a featureless absorption profile in the range 300-500 nm which indicates the photo induced reduction of the Pd complex and formation of palladium nanoparticles (Figure 4.1) [33]. FTIR analysis was also carried out to investigate the chemical structure of the Pd complex before and after photoreduction followed by the Pd nanostructures formation. Figure 4.2 illustrates the FTIR spectra of pure surfactant, the Pd complex and Pd
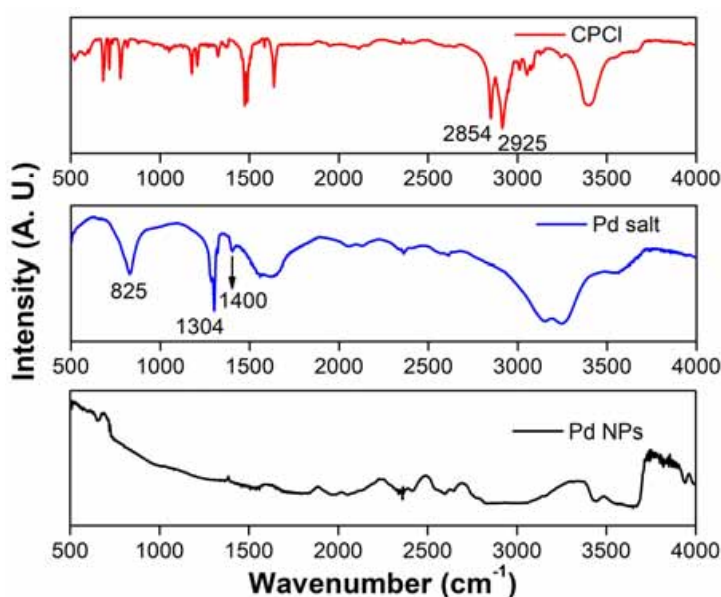
Figure 4.2. *FTIR spectra of surfactant, Pd complex and Pd nanoparticles synthesized in hexagonal mesophases.*

nanostructures after extraction from the mesophases. It appears that the band between 1300-1415 cm^{-1} (symmetric type) and 1553-1660 cm^{-1} (antisymmetric type) due to NH$_2$-deformation and 825 cm^{-1} ascribed to the rocking modes of NH$_3$ of the Pd complex which disappeared after photoirradiation also indicate photoreduction of Pd salt [129]. It is also observed that the bands at 2854 and 2925 cm^{-1} corresponding to the CH$_2$ stretching modes of surfactant are absent in the as prepared Pd nanostructures after mesophases template removal [130]. The Pd nanostructure exhibit a broad absorption which is consistent with other previously reported Pd based nanostructures [131, 132]. Typically, the formation of Pd nanoparticles via chemical or photochemical route is indicated by the emergence of black color. The Pd complex doped

mesophases remains colorless and upon photoirradiation, turns to a black color gel after 12 hours but remains translucent (Figure 4.1 inset). In fact, immediately after photo irradiation, the hexagonal mesophases turns into faint black gel but the darkness of the gel increases with the progress of reduction of Pd (II).

After photoreduction of the Pd complex within the hexagonal mesophases, it is important to ensure the stability of hexagonal mesophases in order to understand the effect of confinement. The hexagonal phases are birefringent and exhibit characteristic textures between crossed polarizing windows when the surfactant cylinders are parallel to the walls of the observation cell. The polarized optical microscopy image (Figure 4.3a-d) demonstrates that the presence of Pd complex (Figure 4.3b) and photo induced chemical transformation (Figure 4.3c-d) does not affect the birefringent nature of the gels or their texture. After photo reduction of the Pd
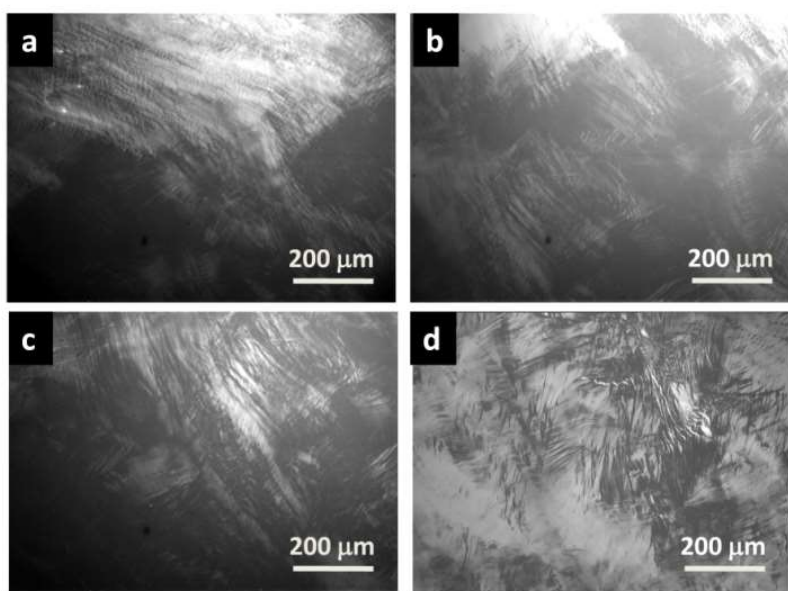
Figure 4.3. *(a) Polarized light micrograph of pure mesophases in the presence of 0.1 M NaCl,(b) Polarized light micrograph of doped mesophases with 0.1 M Pd complex, (c) and (d) Pd complex doped mesophases after 12 and 24 hours photo irradiation respectively. After photo reduction of Pd complex, Pd nanostructures shows a large degree of preservation of the birefringent pattern indicative of the stability of hexagonal LC phase.*

complex, the hexagonal LC phase shows a large degree of preservation of the birefringent pattern indicative of their stability. The photoreduction of the Pd complex in hexagonal mesophases leads to Pd nanostructures as shown in Figure 4.4. The as prepared Pd

Figure 4.4. *Transmission electron micrographs of (a-c) Pd nanostructures synthesized in hexagonal mesophases by 12 h UV-irradiation. The inset shows the corresponding indexed SAED pattern. (d) HRTEM high magnification image of palladium nanoparticles. (e) XRD patterns of palladium nanoparticles with JCPDS (05-0681) data. (f) Reduced graphene oxides nanosheets induced by gamma (γ)-irradiation (dose rate: 6.4 kGy h^{-1}, at dose of 64 kGy) using a solution containing graphene oxides in 2-propanol under N$_2$ atmosphere. The inset: SAED pattern of graphene oxide nanosheets.*

nanostructures assembled together as prolate ellipsoids-like structures composed of self assembly of small Pd nanoparticles (NPs) of 3-4 nm in size (Figure 4.4a-c). A magnified image (Figure 4.4b-c) reveals that the nanoparticles have a narrow size distribution and are well dispersed. It can be clearly seen that the prolate ellipsoids-like nanostructures are formed by the agglomeration of smaller Pd nanoparticles. This can be assumed that after template removal, the nanoparticles are close to each other and their inter particle interaction may contribute to the assembled structure. The selected area electron diffraction (SAED) pattern recorded from one of the Pd nanostructures (Inset of Figure 4.4a) shows diffraction rings corresponding to various facets of the cubic (fcc) crystal structure of palladium. The HRTEM image (Figure 4.4d) further confirms that each nanostructure is composed of many single crystalline grains (see white dashed circles in Figure 4.4d with their crystallographic orientations). The inter-planar distance in the lattice fringes of one domain is measured to be 0.22 nm (inset), which corresponds to the (111) planes of metallic Pd. The XRD pattern of the typical product is presented in Figure 4.4e. The broad diffraction peaks are present at $2\theta = 40.6°$, $46.6°$, $68.4°$, $82°$ and $87°$ and can be indexed as the (111), (200), (220), (311) and (222) facets of face-centered cubic (fcc) Pd (JCPDS No 05-0681), respectively. This indicates that the Pd NPs have a high purity and crystallinity. Both the XRD and SAED patterns demonstrate that the Pd nanostructures are well crystallized. Time evolution of Pd nanostructures implied that small Pd particles were generated at the early stage of the reaction by fast reduction via the particle attachment growth mechanism (Figure 4.5). The
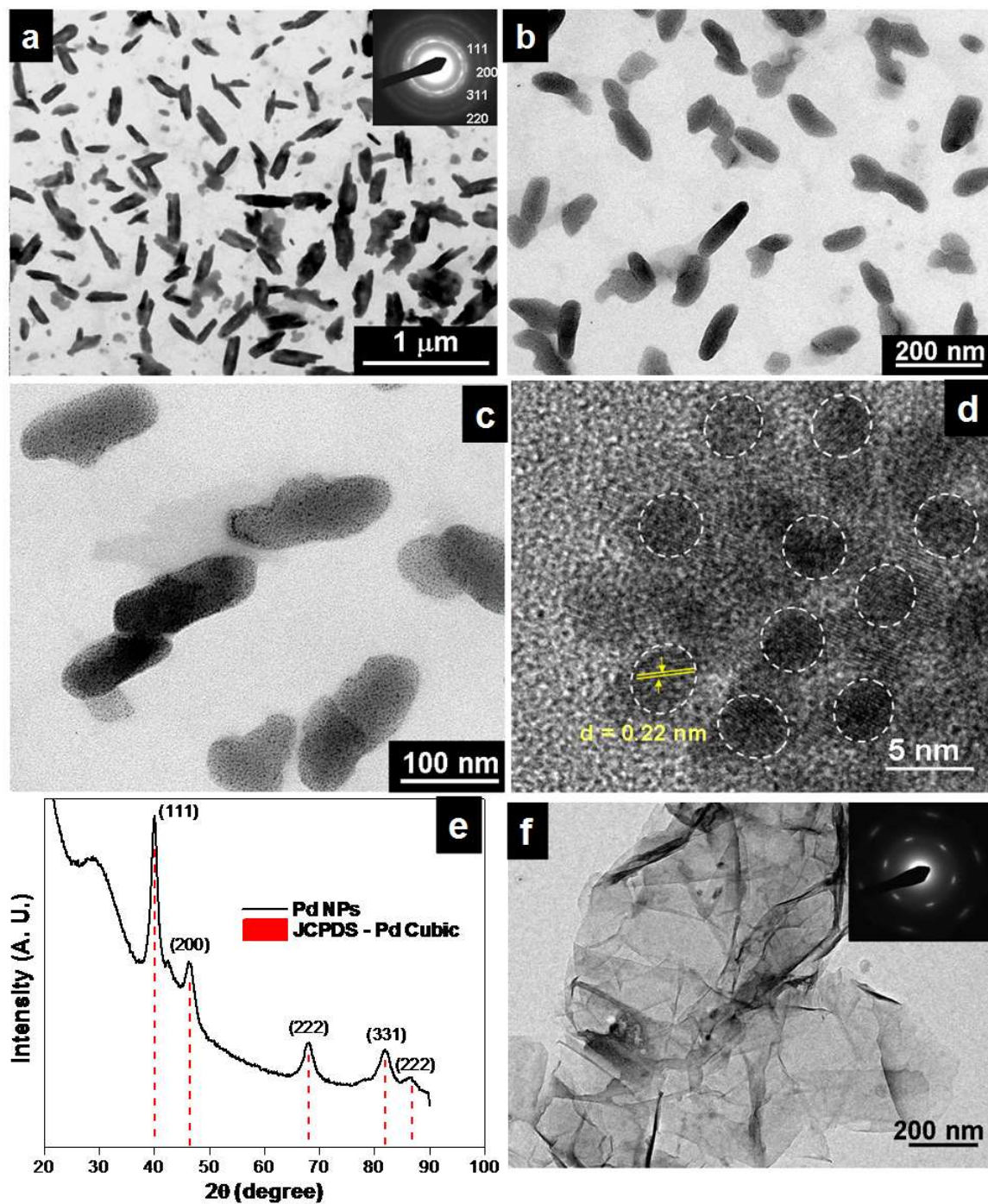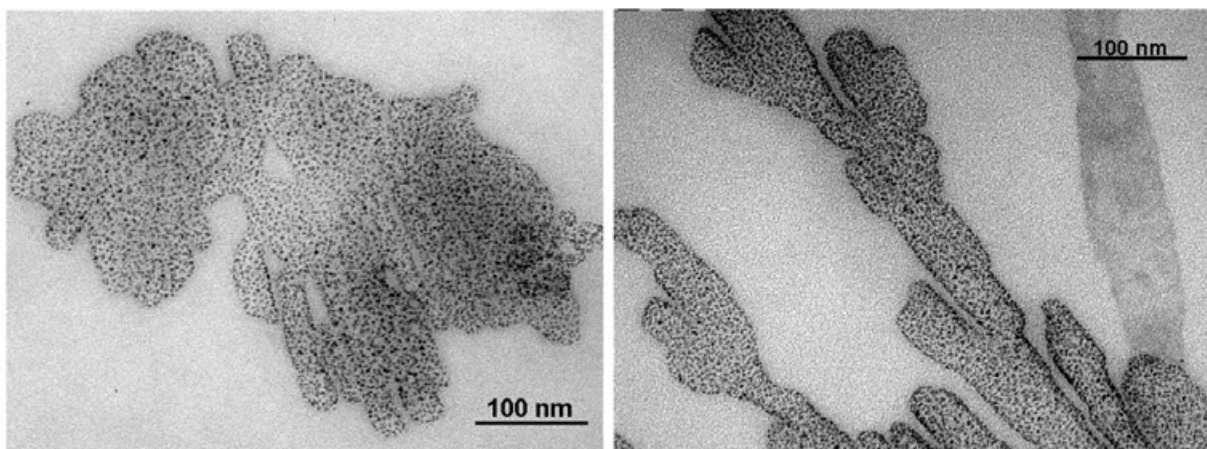

Figure 4.5. *Transmission electron micrographs of Pd nanostructures synthesized in hexagonal mesophases by 5 hrs UV-irradiation.*

98

dendritic Pd nanostructures seem to be assembled from many small Pd NPs in the range of 3-4 nm. Figure 4.4e shows the TEM image of reduced graphene oxides (RGO) which exhibit typical wrinkled and paper-like sheets morphologies with a mixture of single and few-layer graphene nanosheets. The observed corrugation and scrolling of sheets is nanosheets. The observed corrugation and scrolling of sheets is the intrinsic nature of graphene, which may originated from the thermodynamic stabilization of the 2D membrane structures via bending. Figure 4.4e inset depicts the SAED pattern of RGO, which clearly demonstrates a highly crystalline structure. The six membered inner rings originate from the [100] plane, while the six brilliant points relate to the [110] diffractions, clearly confirming that the resulting RGO has been restored into the hexagonal graphene framework (Images at higher resolutions and layered morphologies are shown in the Figure 4.6) [133]. The ability to produce graphene nanosheets with a scalable, clean without using any chemical reducing agent and low-cost approach should take us a step closer to real-world applications of graphene. The control experiment carried out in micellar solutions formed by CPCl containing $Pd(NH_3)_4Cl_2$ (with the same ratio [CPCl]/[Pd] = 14). The photoreduction of Pd complex leads in this case to the formation of small and spherical dispersed nanoparticles of 3–5 nm (Figure 4.7).
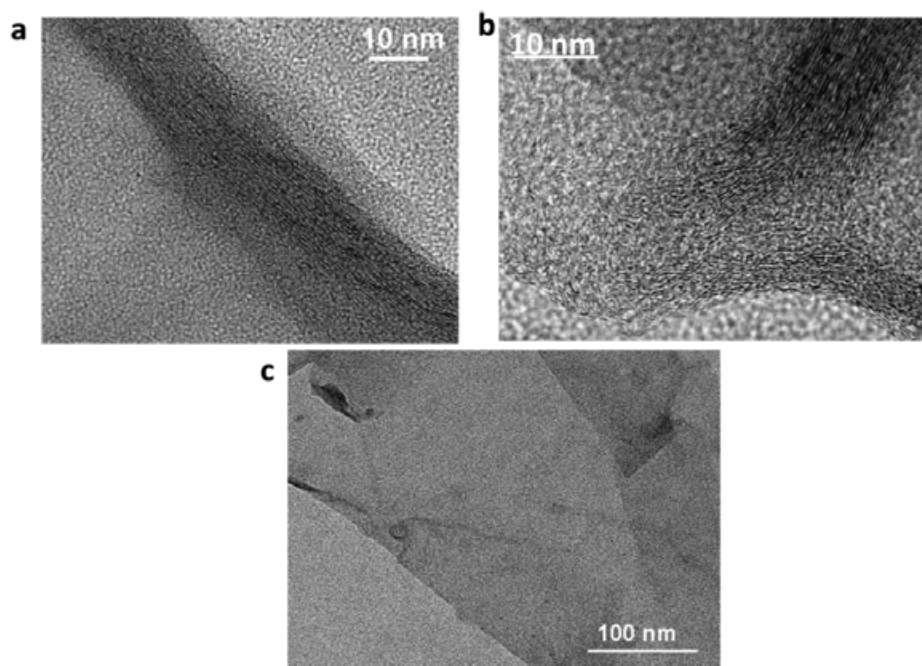
Figure 4.6. (a-b) Higher resolution transmission electron micrographs and (c) Layered morphologies RGO nanosheets synthesized by gamma-irradiation.
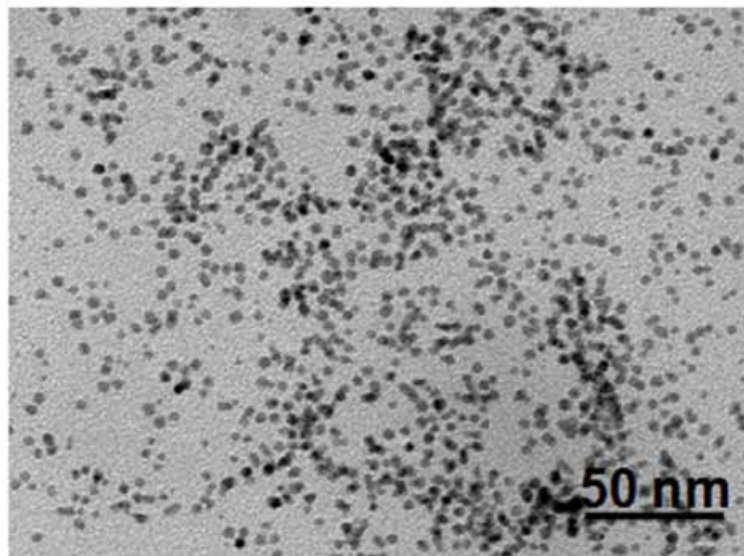
Figure 4.7. *TEM micrographs of Pd nanoparticles obtained from the micellar solution of CPCl containing Pd(NH$_3$)$_4$Cl$_2$ ([CPCl]/[Pd] = 14) at 12 hours photo-irradiation.*

Additionally, Pd complex doped hexagonal mesophases kept in the dark for several days but there was no sign of evolution of Pd (0). Under UV irradiation, Pd(II) is reduced at the oil-water interface [33, 134]. Initially, nuclei are formed and then they tend to aggregate to form bigger particles or successive reduction of Pd (II) may results in its adsorption on the surface of preformed particles. In this regard, surfactant molecules protect the metal clusters and control the aggregation via hydrophobic chain mediated electrostatic repulsion and steric hindrance. However, it is intricate to convey the exact mechanism of formation of prolate ellipsoids-like structures within the hexagonal mesophases. The confined geometry of mesophases is certainly involved directing the nanoparticle growth leading to these assembled Pd nanostructures. The hexagonal mesophases consist of infinite nonpolar tubes organized on a hexagonal lattice with surfactants at the interface of the tubes in a continuous aqueous salt solution. It has been demonstrated that the suitable correct adjustment between cyclohexane and the ionic force of the aqueous solution by addition of a salt allowed the diameter of the nonpolar cylinders to be tuned over 1 order of magnitude (from 3 to 30 nm), while the distance between adjacent cylinders is kept small and nearly constant (about 3 nm) [21, 32]. Here, we demonstrate that the confined aqueous phase can be used as nanoreactors for the preparation of Pd nanostructures as shown in Scheme 4.1.
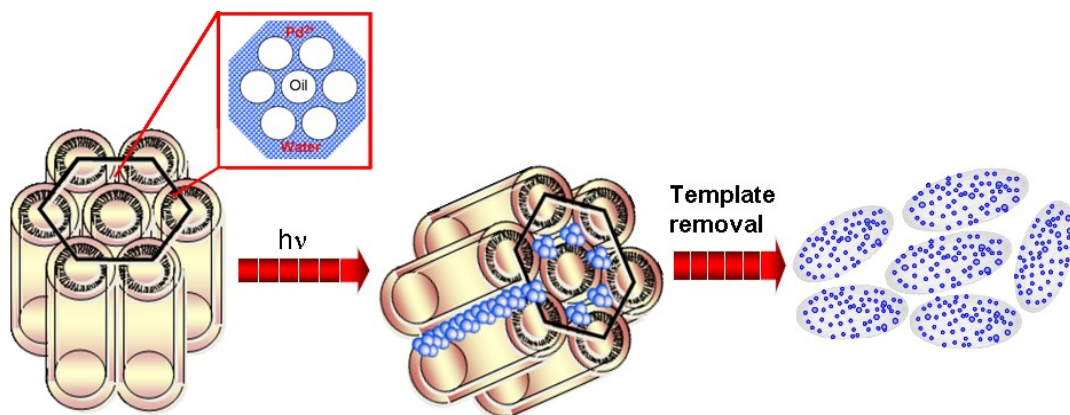
Scheme 4.1. *Schematic representation of light induced synthesis of Pd nanostructures in hexagonal mesophases.*

In order to shed light on the mechanism of formation of Pd nanostructures within the confined geometry of hexagonal mesophases, we studied the solvation dynamics in the water surface and hydrophobic region of the oil tube of the LC followed by doping with solvation probe such as coumarin 500 (C500) and 4-(dicyanomethylene)-2-methyl-6-(p-dimethylamino-styryl) 4H-pyran (DCM) respectively. The picosecond resolved fluorescence transients of C500 and DCM in mesophases across the emission wavelengths are shown in Figure 4.8a and 4.8b respectively. An ultrafast decay component in the blue end is eventually converted into a rise component of similar time constant in both the cases. The observation is consistent with the solvation probe C500 and DCM in the corresponding medium [135, 136]. Figure 4.8c and 4.8d show the constructed time-resolved emission spectra (TRES) of C500 and DCM with a spectral shift of 1790 and 2268 cm^{-1} respectively, in a 1.4 ns time window, which indicate that both probes are stabilized by the corresponding immediate solvent molecules in the excited state. To determine the water relaxation dynamics within the hexagonal mesophases, we composed solvation correlation functions [C(t)] for both probe C500 and DCM and fitted with bi-exponential decay function as shown in Figure 4.8e and 4.8f. For C500, the decays time constants are 20 ps (92%) and 319 ps (8%) and for DCM, the obtained time constants are 170 ps (96%) and 1.49 ns (4%). The slower water dynamics for the hydrophobic DCM molecule is associated with the confinement of DCM in the hydrophobic region (oil tube) of the hexagonal mesophases in comparison to less hydrophobic C500 in the oil-water interface. Hence, more water can access the C500 probe in the excited state compared to DCM. In order to investigate the location and physical movement of C500 and DCM molecules within the LC during the

course of the solvent relaxation, we have measured the fluorescence anisotropy of the probe molecules as shown in the insets of Figure 4.8e-f. The fluorescence anisotropy decays depict rotational relaxation time constants of C500 and DCM in the liquid crystal are 653 ps and 325 ps respectively. The observed faster rotational time constants in case of DCM is consisting with the

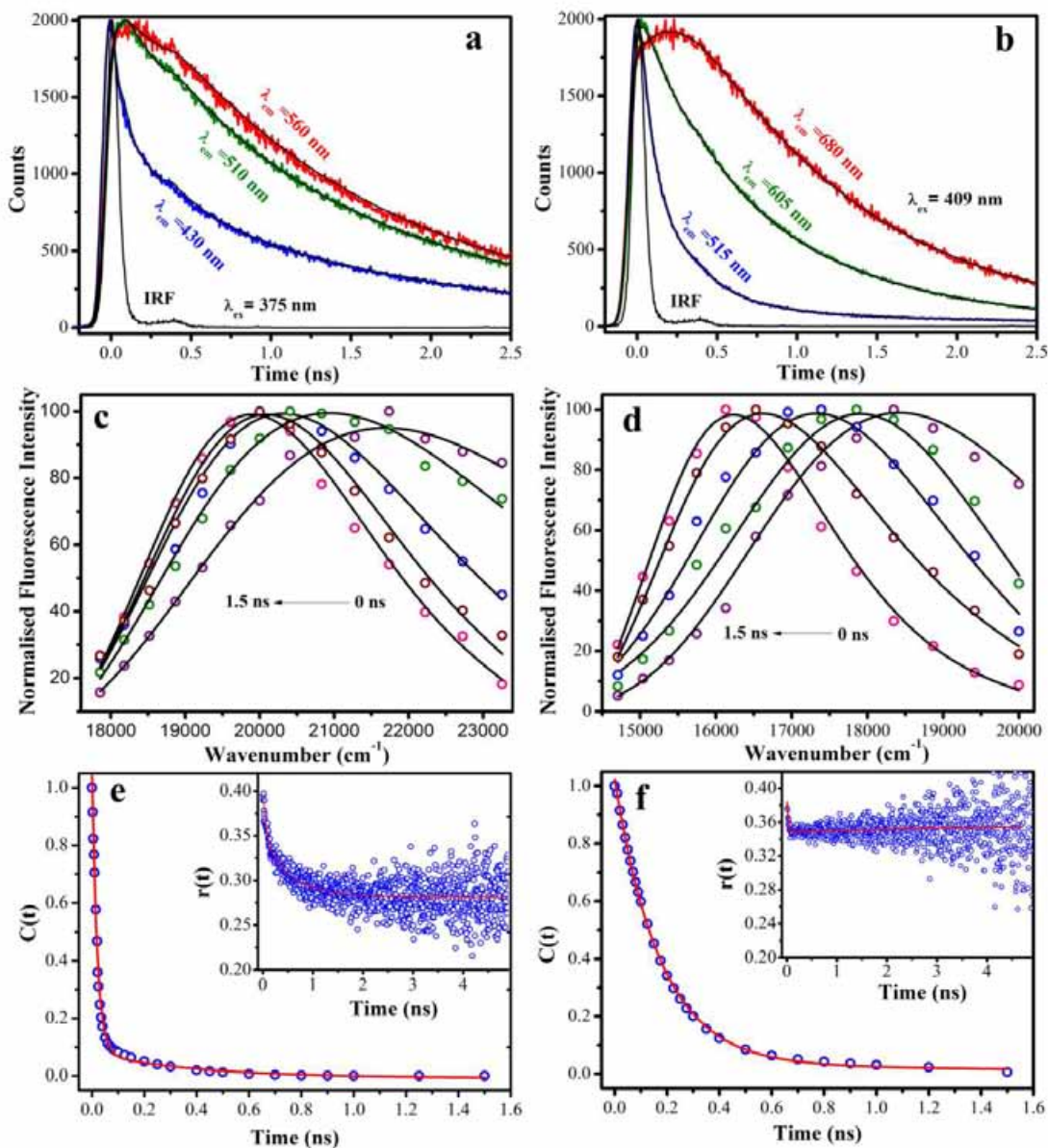**Figure 4.8.** *Picosecond resolved fluorescence transients of (a) C500 and (b) DCM in three representative detection wavelengths across the emission spectrum in hexagonal metaphases. Time dependent emission spectra of (c) C500 and (d) DCM in the liquid crystal are shown. Plot of solvation correlation functions against time for (e) C500 and (f) DCM are shown. Insets depict the picosecond fluorescence anisotropy decays of C500 and DCM.*

fact that DCM resides on the more compact oil phase while on the other hand C500 is more flexible on the oil-water interface. Hence, we can conclude that due to the hydrophobicity as well as the compact nature of the oil phase, the reduction of Pd complex takes place in the aqueous phase consequently, the nanoparticles formed in the oil-water interface within the mesophases as proposed in the Scheme 4.1.

4.2.1.1. Electrochemical behavior: As Pd-modified electrodes were demonstrated to be very active for ethanol electrooxidation in the alkaline medium, EOR was selected for electrocatalytic studies [10, 15, 16, 137, 138]. Figure 4.9a and 4.9b depict the cyclic voltammogram (CV) of Pd-Nafion (the green solid line) and Pd/RGO-Nafion (the blue solid line) in pure 1 M NaOH and voltammetric pattern associated with a characteristic feature of Pd electrodes which is consistent with earlier reports [15, 16, 43]. The Pd nanostructures embedded in a proton conducting phase, Nafion and RGO-Nafion matrix were used as the catalyst for the electrocatalytic oxidation of ethanol in an alkaline medium. Figure 4.9a and 4.9b, shows superposition of the first cyclic voltammogram (black solid line curve) and the 100 cycle (red solid line curve) of Pd/Nafion and Pd/RGO-Nafion run in 1M NaOH containing 1M EtOH at a scan rate of 50 mVs^{-1}. The voltammetric pattern is represented by two well-defined current peaks, one on the forward and the other on the reverse potential scans. The peak in the positive-going sweep corresponds to the ethanol oxidation activity, while the peak in the reverse sweep arises due to oxidation of both freshly adsorbed ethanol and adsorbed carbonaceous species formed before Pd-O blocking [139]. The forward scan peak current is related to the oxidation of freshly chemisorbed species generated from alcohol adsorption. The initial increment of current with number of triangular potential sweep may be attributed to the generation of Pd-OH on the surface after each scan and development of channels of electron collection by rearrangement of the materials at the surface [42]. The oxygen desorption method is applicable to evaluate the electrochemically active surface area (ECSA) of Pd, the mass normalized ESCA was calculated for the two electrodes by computing the area under the cathodic peaks corresponding to the reaction of the Pd oxide monolayers. The data presented (within the parenthesis) reveal that ECSA of Pd/RGO-Nafion (192 m^{2}g^{-1}) is about 4.6 times greater than that of Pd/Nafion (40 m^{2}g^{-1}) electrode. This signifies that the former electrode is more exposed and available in the solvent environment for undergoing the reactions and hence shows increased surface area induced catalytic effect. The
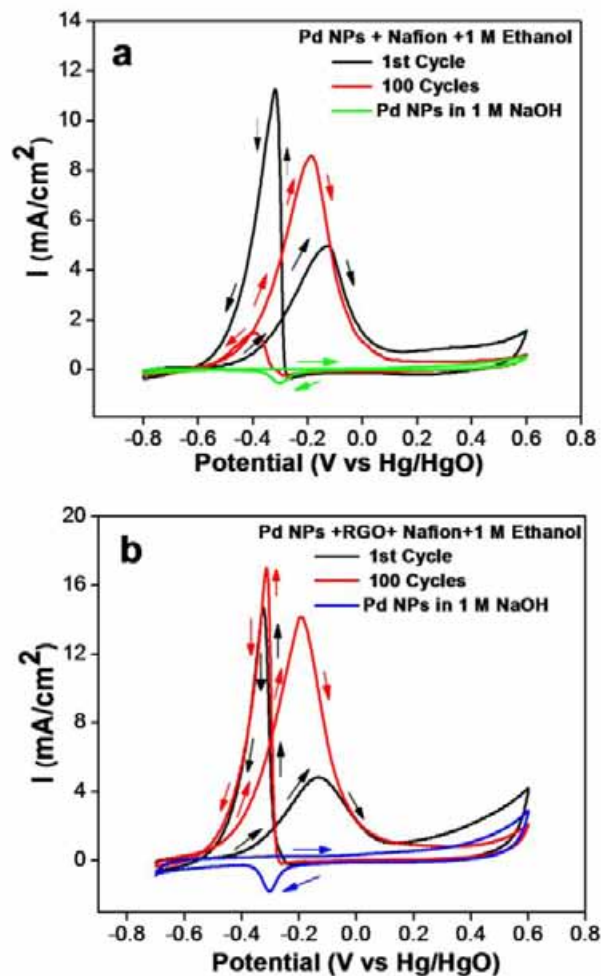
Figure 4.9. *(a) Cyclic voltammograms of Pd NPs/Nafion in 1M NaOH (green solid line), superposition of the first (black solid line curve) and the 100th (red solid line curve) cyclic voltammetric runs associated with the electrocatalytic oxidation of 1 M EtOH in 1 M NaOH. (b) Cyclic voltammograms of Pd NPs/ RGO-Nafion in 1M NaOH (blue solid line), superposition of the first (black solid line curve) and the 100th (red solid line curve) cyclic voltammetric runs associated with the electrocatalytic oxidation of 1 M EtOH in 1 M NaOH. The working electrode was a glassy carbon disk modified with the Pd nanostructures. The reference electrode was an Hg/HgO (1 M KOH) electrode. The scan rate was 50 mVs⁻¹.*

peak current and the onset potential of the faradaic current (E_{onset}) on the forward scan indicate the electrocatalytic activity of the catalyst for EOR. The main quantitative parameters measured from these two voltammograms have been tabulated (Table 4.1). It can be clearly seen from Table 4.1, the electroactivity (considering current per cm^{-2} of real area) of Pd/Nafion-RGO is higher than that of Pd/Nafion electrode. During the potential cycles, the E_{onset} shifts to a more negative potential (from -534 mV at the 1st cycle to -590 mV after 100 cycles, Table 4.1).

Table 4.1. Comparison of the electrochemical performance of Pd nanoparticle catalysts with nafion and reduced graphene oxides nanosheets modified nafion as supports for the oxidation of ethanol. The main characteristics measured from cyclic voltammograms associated with the electrocatalytic oxidation of 1 M EtOH in 1 M NaOH. The working electrode was a glassy carbon disc modified with the Pd nanostructures. The reference electrode was an Hg/HgO (1 M NaOH) electrode. The scan rate was 50 mV s^{-1}. The current density is referred to the geometric area of the glassy carbon support.

Electrodes (after 100 cycles)	I_f (mA. cm^{-2})	I_b (mA. cm^{-2})	I_f/I_b	E_{onset} (mV)	I_f (mA. cm^{-2}). mg^{-1}	I_b (mA. cm^{-2}). mg^{-1}
Pd/Nafion	8.55	1.43	5.98	-590	1745	292
Pd/RGO-Nafion	14.22	17.08	0.83	-622	5925	7166

It has to be noted that the stable cycle and 100 cycles are similar and used for further calculation of electrochemical parameters. A negative shift of E_{onset} underscores the enhancement in the kinetics of ethanol oxidation. Upon cycling, the peak current density is also modified: the forward anodic peak current density (I_f) increased from 4.93 mA/cm² to 8.55 mA/cm² whereas the backward anodic peak current density (I_b) decreased from 11.20 mA/cm² to 1.43 mA/cm², leading to an increase of the ratio I_f/I_b from 0.44 to 5.98. This observation indicates that the catalyst is not lost during the reaction and also shows a relatively significant increase of electro-catalytic activity of the electrode material toward EOR during cycling. Indeed, a high I_f/I_b ratio indicates efficient oxidation of alcohol during the forward anodic scan, with little accumulation of carbonaceous residues. Thus it measures the tolerance power towards carbonaceous poisons and represents the capability of an electrode to remove the poisons either by possible chemical or electrochemical reactions occurring in the system.

Here the ratio of Pd/RGO-Nafion (0.83) is much smaller than that for Pd/Nafion (5.98). This plausibly fact that the spectroscopically determined intermediates like Pd-CH$_3$, PdCH$_3$CO, Pd-H etc are eliminated from the surface both by chemical and electrochemical reactions leading to the opening of fresh metal surface. Since the rate of formation of these intermediates is greater for the electrode for which peak current density is larger, the rate of elimination of these intermediate from the surface is also greater [44, 140]. If Pd-CH$_3$ or Pd-H is removed by electrochemical oxidation reaction the following reactions would take place:

$$Pd\text{-}CH_3 + 9OH^- = Pd + CO_3^{2-} + 6H_2O + 7e^- \qquad (4.1)$$

$$Pd\text{-}H + OH^- = Pd + H_2O + e^- \qquad (4.2)$$
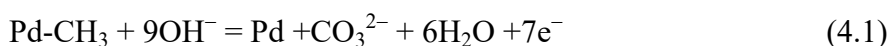
In contrast, if they are removed chemically, the following reaction would occur:

$$Pd-CH_3 + Pd-CH_3 = 2Pd + C_2H_6 \qquad (4.3)$$

$$Pd-CH_3 + Pd-H = 2Pd + CH_4 \qquad (4.4)$$
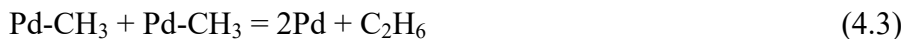
The loss in I_f which corresponds to both faster dehydrogenation and slower decarbonaceous oxidation, is more than I_b which mainly occurs due to surface-adsorbed carbonaceous oxidation. Thus the ratio, I_f/I_b is much smaller for Pd/RGO-Nafion than Pd/Nafion. This type of increased I_f/I_b ratio for performance is a general phenomenon as observed in our previous study [44]. However, the increment in the forward anodic peak current density with respect to the backward anodic peak current density was evaluated from potentiostatic experiments to identify the catalyst tolerance to carbonaceous species accumulation [15]. Similar results have been also obtained for the Pd-nanowires and palladium/gold nanostructures and such improvement in modified electrode characteristics might be attributed to some reorganization of the surface film [10, 43] or to a gradual cleaning of the surfactant that remains after the synthesis [15]. The similar electrochemical behavior upon cycling was observed with Pd NPs supported by RGO-Nafion (Pd/RGO-Nafion), assuming that the particular behavior is inherent to the metallic NPs. We verified the contribution of control RGO nanosheets during EOR. Figure 4.10 shows the
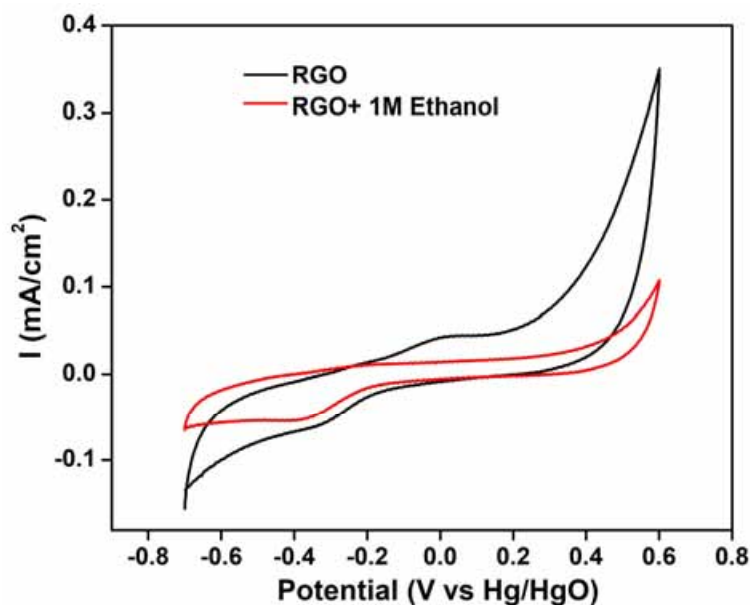

Figure 4.10. *Cyclic voltammograms of reduced RGO nanosheets in 1M NaOH (black solid line curve) and with the electrocatalytic oxidation of 1 M EtOH in 1 M NaOH (red solid line). The working electrode was a glassy carbon disk modified with the RGO nanosheets. The reference electrode was an Hg/HgO (1 M NaOH) electrode. The scan rate was 50 mVs^{-1}.*

Table 4.2. Comparison of the electrochemical performance of Pd electrocatalysts for the ethanol oxidation.

Electrode	E_{onset}, mV/SCE	E_f, mV/SCE	E_b, mV/SCE	I_f, mA.cm^{-2}	I_f, mA.cm^{-2}.mg^{-1} of Pd	Reference
Pd/Nafion	-590	-185	-382	8.55	1745	This work
Pd/RGO-Nafion	-622	-186	-312	14.22	5925	This work
Commercial Pd black catalyst	-550	~-200	~-301	0.65		8
Tetrahedral Pd nanocrystal	-590	-219	~-305	3.83		8
Pd/Nf-graphene	-600		-	0.56		2
C-Pd Nanoballs/ Nafion	-550	-151	-296			16
Pd nanowires /Nafion	-664	-166	-278		1327	15
CNT-Pd/Nafion	-564	-242	-451		364	37
CNT-Pd/Nafion	-670	-245	-332		3540	37
C-Pd	-680	-209	~-310		63	63
C-Pd	-579	-219	~-360		42	64
C-Pd	-619	-203	~-330		85	64

cyclic voltammograms for RGO nanosheets before and after addition of EtOH. However, the presence of RGO in combination with nafion as a support for Pd NPs influenced the values of the E_{onset}, the measured current density and the I_f/I_b ratio (Table 4.2). The onset of ethanol oxidation occurs at −0.590 V for Pd/Nafion whereas it is −0.622 V for Pd/RGO-Nafion suggesting that the electrocatalytic activity towards ethanol oxidation occurs more favorably in Pd/RGO-Nafion than in Pd/Nafion. It has been observed that in the first cycle, the peak current densities increased for both the forward and the backward scans and in contrast to Pd/Nafion, strikingly, backward current density increases after 100 cycles (Figure 4.9b). According to the values extracted from the voltammograms, Pd NPs in nafion were the less active system compared to those in the RGO-Nafion support, but they exhibited the best I_f/I_b ratio. An explanation for the high I_f/I_b ratio of Pd/Nafion could be that the nature of support RGO influences the adsorbed organic functions at the surface of the Pd NPs. The forward peak current density of Pd/Nafion and Pd/RGO-Nafion was 8.55 and 14.22 mA cm^{-2}, respectively. The forward peak current of Pd/RGO-Nafion catalyst is 1.66 times that of the Pd/Nafion catalysts. Since, loading of the catalyst is different for the electrode, peak current densities of the CVs were

expressed also by dividing current densities (mA cm^{-2}) by the mass of Pd adsorbed per unit area of the surface (mg^{-1} of catalyst) as shown in Table 4.1. The influence of high surface area of RGO as support (Table 4.1) clearly highlight that RGO-Nafion support exhibited higher current density [141]. The comparison of the electrochemical performance of the present Pd nanostructure with other Pd based nanostructures under the comparable reaction conditions are listed in Table 4.2. Interestingly, the superiority of Pd/RGO-Nafion in terms of current density (7166 mA cm^{-2} mg^{-1}) is obvious, being nearly 4.4 times higher than that of previously reported Pd nanowires (1327 mA cm^{-2} mg^{-1}) synthesized in hexagonal mesophases as shown in Table 4.2) [15]. In fact, the Pd/RGO-Nafion catalyst has superior catalytic activity with high energy density among these Pd catalysts. This may be due to synergistic effect assembled Pd nanoparticles and reduced graphene oxides nanosheets that can efficiently promote the breaking of C-C bond of ethanol and enhance its oxidation. In contrast to Pd assembly, the Pd NPs synthesized within micelles are not active due to presence of surfactant molecules which limit the accessibility of Pd electrocatalyst on the electrode.

The catalyst stability as a function of time is also important for its practical application in direct ethanol fuel cells. The stability of the catalytic performance was then investigated by chronoamperometric (CA) measurements where the current density-time (I vs t) curves at constant potentials were recorded as shown in Figure 4.11. The CA experiments were carried out in 1M NaOH with 1 M ethanol solution under a constant potential of 0.3 V for 1600 s. In the first several minutes, both catalysts exhibited a pronounced current decay, which could be caused by the accumulation of poisonous intermediates [142]. The current density decayed in the first 500 s and attained a steady state thereafter, indicating that these Pd NPs form very stable film on glassy carbon electrode surface and also exhibit stable electrocatalytic performance towards EOR. After 500 s, the order of activity in the CA tests was similar with the activity order in the CV measurements: Pd/RGO-Nafion catalyst exhibited the highest limiting as well as the initial current, showing the highest activity than the Pd/ Nafion catalysts. Moreover, Pd/RGO-Nafion exhibits a lower degradation rate during the progress of the reaction, which demonstrates its improved stability for ethanol electro-oxidation. The enhanced EOR activity and stability for the Pd/RGO-Nafion electrocatalyst compared to Pd/Nafion are probably related to the surface structure and properties of the reduced graphene oxide nanosheets. The chronoamperometric response confirms that the RGO nanosheets help in the effective dispersion of the Pd NPs,

facilitating an easier access of ethanol molecules to the catalytic sites. Additionally, the RGO nanosheets containing the holes, oxygen, carbon vacancies and defects which are generated as
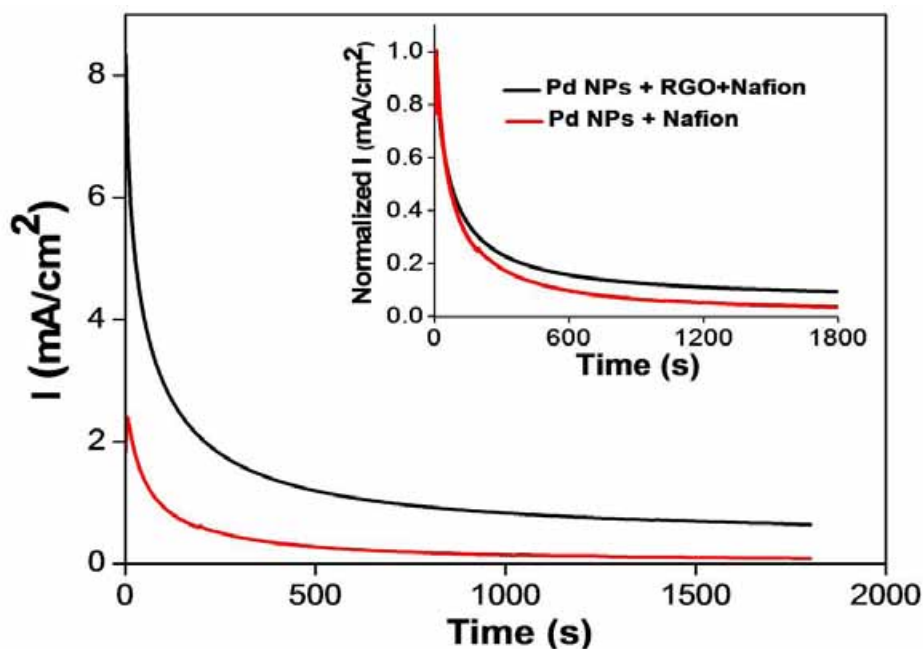
Figure 4.11. *Chronoamperometric curves for the ethanol electrooxidation at -0.30 V vs Hg/HgO on a glassy carbon electrode modified with Pd/Nafion (black curve) and Pd/RGO-Nafion (red curve). The solution was 1 M NaOH + 1 M EtOH. Inset: the comparison of chronoamperometric response of Pd/Nafion and Pd/RGO-Nafion at normalized current (I).*

partial oxidation produces sheets with graphitic domains. This may efficiently introduce chemically active sites for use in catalytic reactions and also act as anchoring sites for deposition of metal NPs [49, 143]. Furthermore, it is also beneficial to prevent the metal nanoclusters from coalescence because of homogeneous dispersion of the Pd NPs on the support and consequently the accessibility of metal catalyst during electro catalytic reaction increases [144]. Hence, the addition of reduced GO nanosheets as a support could remarkably improve the stability of Pd nanostructure for EOR, which is crucial for a practical catalyst.

4.2.2. Microwave-Assisted Synthesis of Porous Mn_2O_3 Nanoballs as Bifunctional Electrocatalyst for Oxygen Reduction and Evolution Reaction [113]:

4.2.2.1. Synthesis and characterization of Mn_2O_3 nanostructure: The Mn_2O_3 and Cu doped Mn_2O_3 were synthesized by microwave assisted hydrothermal method and the structural as well as the electrochemical properties of the as prepared oxides samples were examined by common

techniques as discussed below. The sizes and morphologies of the Mn_2O_3 samples were characterized by Transmission electron microscopy (TEM) (Figure 4.12). Figure 4.12a illustrated the formation of well-ordered spherical type Mn_2O_3 nanoballs (NBs) with a mean diameter of 550–620 nm. As evident from Figure 4.12b, the NBs were fabricated by the aggregation of small particles, which presumably led to a rough surface. In addition, the intrinsic crystal structure of the as-prepared NBs was further characterized by high resolution transmission electron microscopy (HRTEM). As shown in Figure 4.12c, the inter-planar distance between the fringes is found to be about 0.27 nm consistent with (222) planes of Mn_2O_3 [64]. The similar structure of
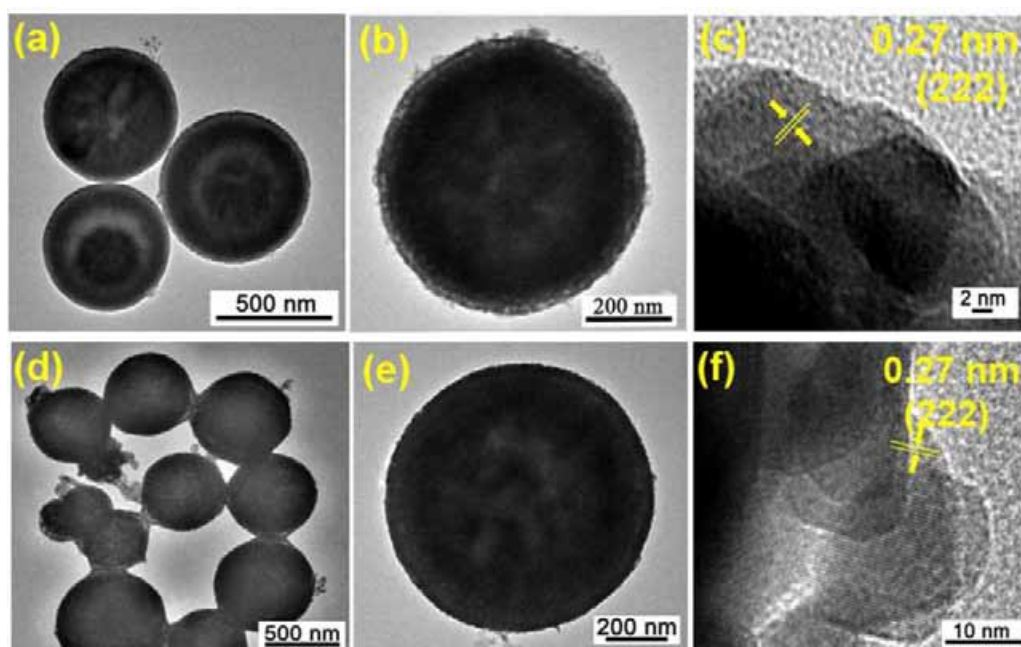
Figure 4.12. *Transmission electron microscopy (TEM) images of Mn_2O_3 and Cu doped Mn_2O_3 nanoballs. (a), (b) TEM images at different magnification and (c) HRTEM image of Mn_2O_3 NBs. (d), (e) TEM images at different magnification and (f) HRTEM image of Cu-Mn_2O_3 NBs.*

Mn_2O_3 after Cu doping as revealed by the representative TEM images (Figure 4.12d-e) suggests that doping might not influenced the growth of the NBs. The Cu-Mn_2O_3 NBs exhibited a slightly higher size ranging from 550–650 nm. The HRTEM image also demonstrated the highly crystalline nature of Cu-Mn_2O_3 NBs with cubic phase (Figure 4.12f). The shape of NBs was found to be small grains of 5-10 nm diameter. Hence, highly crystalline and pure cubic phase Mn_2O_3 could be obtained under a mild temperature through the MAH synthesis.
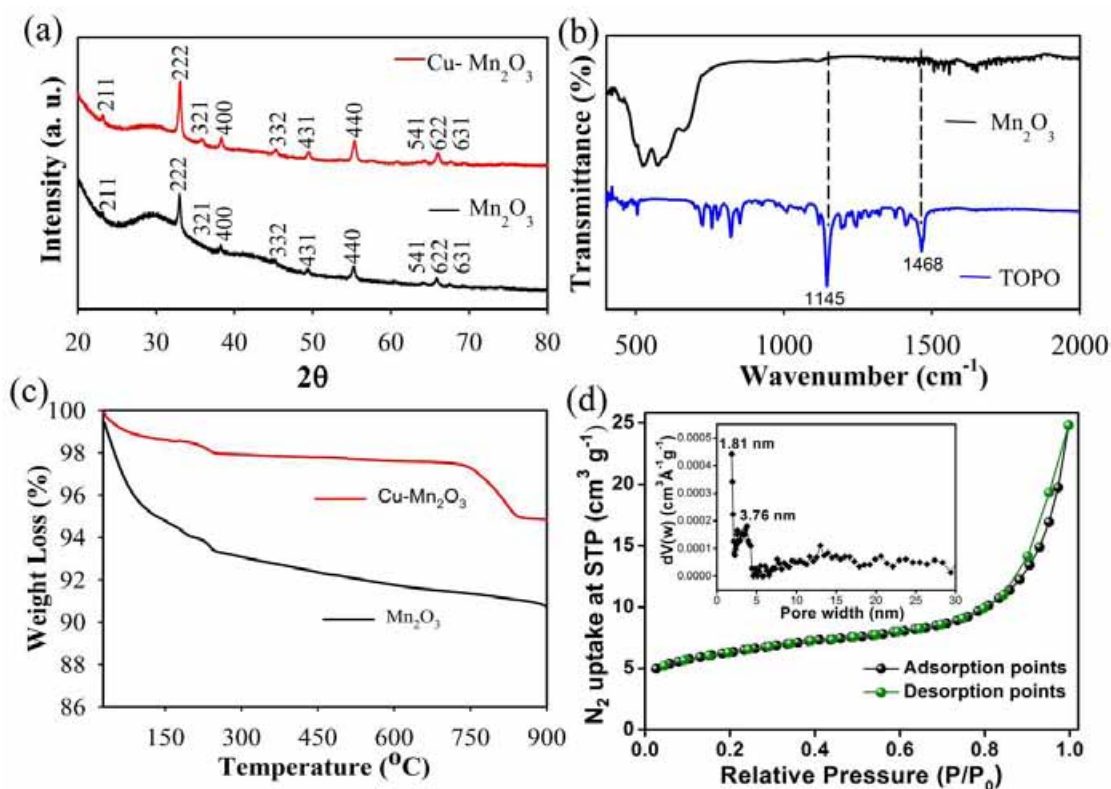
Figure 4.13. *Structural characterization of Mn_2O_3 and Cu doped Mn_2O_3 nanoballs. (a) XRD patterns of Mn_2O_3 and Cu doped Mn_2O_3 NBs. (b) FTIR spectra of Trioctylphosphine oxide (TOPO) and Mn_2O_3 NBs. (c) Thermogravimetric analysis (TGA) profile of Mn_2O_3 and $Cu-Mn_2O_3$ NBs. (d) N_2 adsorption and desorption isotherms of porous Mn_2O_3 NBs. Adsorption and desorption points are marked by black and red symbols, respectively. Inset: The pore size distribution pattern employing the nonlocal density functional theory (NLDFT).*

The X-ray diffraction (XRD) patterns were recorded to confirm the lattice facets of Mn_2O_3 and $Cu-Mn_2O_3$. Figure 4.13a shows the XRD patterns of pure and doped Mn_2O_3 and the diffraction peak position could be readily indexed as a cubic phase Mn_2O_3 crystal (JCPDS No. 41-1442). It is evident from the differences between the breadths of the XRD reflections that the doping increases the crystallinity of the Mn_2O_3 structures. No other impurity peaks have been detected in both cases, indicating that the highly crystalline pure and metal doped manganese oxides have been successfully synthesized using the microwave irradiation process. Moreover, FTIR analysis was carried out to investigate the chemical structure of trioctylphosphine oxide (TOPO) after microwave irradiation followed by the Mn_2O_3 NBs formation. Figure 4.13b illustrates the FTIR spectra of pure TOPO and annealed Mn_2O_3 NBs. It appears that the band at 1145 cm^{-1} (P=O symmetric type) and 1468 cm^{-1} (CH$_3$ bending) of TOPO disappeared after microwave irradiation and followed by hydrothermal treatment, suggests the surface of NBs free

from organic ligands which can be ideal for catalytic application [145]. Thermogravimetric analysis of Mn_2O_3 powder showed a weight loss ~8% up to 580 °C which should be attributed to the removal of surface-adsorbed water which is consistent with previous reports [146]. Moreover, the weight remains nearly unchanged suggests high thermal stability of the as prepared Mn_2O_3 NBs (Figure 4.13c). Similarly, Cu doped Mn_2O_3 demonstrated a high thermal stability with ~5% weight loss up to 800 °C. Further, the N_2 adsorption-desorption measurement was performed to determine the surface area analyses of Mn_2O_3 NBs. As shown in Figure 4.13d, a type IV isotherm with an H3 hysteresis loop can be observed which confirms the mesoporosity of Mn_2O_3 NBs. Pore size distributions (PSD) of Mn_2O_3 NBs have been estimated by employing the nonlocal density functional theory (NLDFT) as shown in the inset of Figure 4.13d, which suggest mesopore diameter centered at 1.8 nm and 3.7 nm. The Brunauer-Emmett-Teller (BET) surface area and pore volume are 22 m^2 g^{-1} and 0.038 cm^3 g^{-1}, respectively, which is comparable from manganese oxides nanostructures synthesized by other common methods [99, 147].
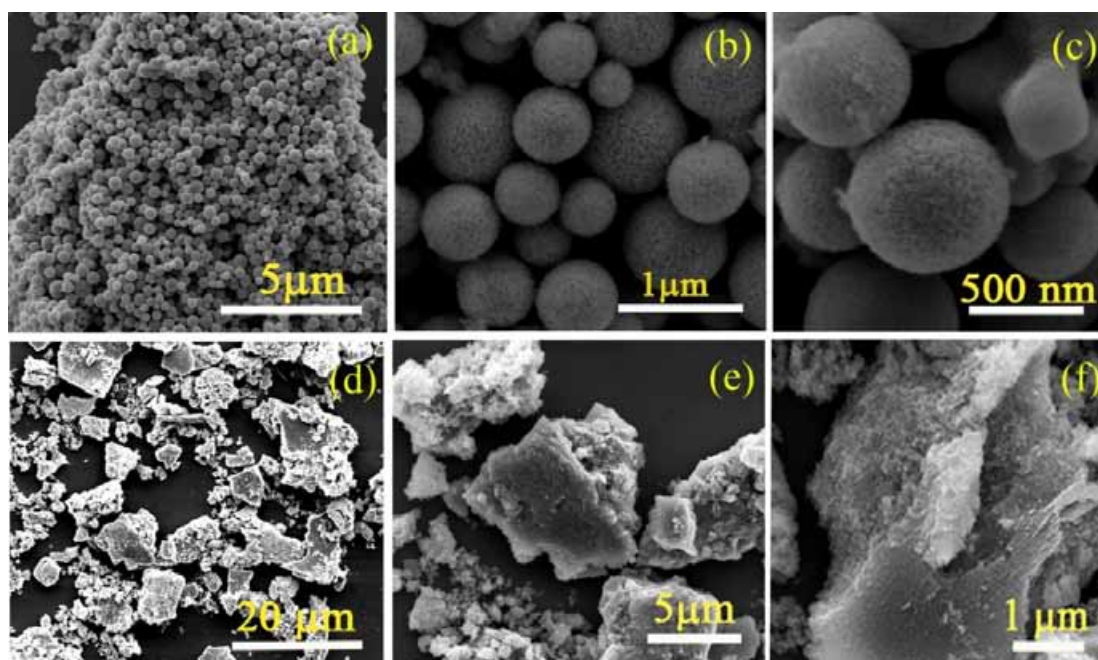

Figure 4.14. *Scanning electron microscopy (SEM) images of Mn_2O_3 nanoballs with different magnification using TOPO and urea as structure controlling agent. (a-c) SEM images of Mn_2O_3 NBs prepared using TOPO as capping ligand (Mn^{2+}: TOPO, 1:4). (d-e) SEM images of Mn_2O_3 prepared using urea as capping ligand (Mn^{2+}: urea, 1:4).*

The FESEM images revealed that the Mn_2O_3 consist of spherical morphology with a mean diameter of 600–860 nm (Figure 4.14a). Moreover, at higher magnification (Figure 4.14b and c), it has been found that these solid NBs were formed by the self-assembly of very small nanoparticles as evident from the SEM image (Figure 4.14b and 4.14c). Mn_2O_3 demonstrated homogeneous size-distribution and the average diameter of the NBs prepared from 4 equivalent of TOPO (Mn^{2+}: TOPO, 1:4) was estimated to be ~600 nm. The control over the morphology of Mn_2O_3 NBs using TOPO as a chelating agent which can plays dual role of controlling the chemical reaction from both the thermodynamic and kinetic aspects, has been confirmed further using urea as the structure controlling agent (Figure 4.14d-f). In control experiment, the microwave-assisted hydrothermal decomposition of manganese salt without using TOPO did not produce any visible precipitate of manganese oxides. On the other hand, an equivalent amount of a very common capping as well as reducing agent, urea has been used but micrometric aggregates were obtained with an average size of ~2 to 10 μm under similar reaction condition [99]. At a higher magnification, porous-cracked flake structures have been observed as shown in (Figure 4.14f). This suggests that the formation and morphology of as prepared Mn_2O_3 NBs strongly depended on the presence of TOPO. It has to be noted that the chemical structure of TOPO has a tetrahedral structure with three long carbon chains, which is differs significantly from the linear chain of the urea ligand [148]. The major chemical binding interaction of TOPO with the metal oxide surface is through the oxygen. Due to unique structural feature of the TOPO molecule and lower intermolecular interaction, the density of TOPO molecules at Mn_2O_3 NBs surfaces is expected to be lower. Consequently, the particle growth in presence of TOPO is well controlled via lower intermolecular interaction [149]. It has been further supported with density functional theory (DFT) calculation that due to the strong chemical interaction between O of TOPO and the metal site stabilized the formation of metal oxide clusters [150]. On the other hand, weaker N-M chemical bond primarily provides the main contribution toward the intermolecular interaction with the metal oxides surface along with the formation of N-H…O hydrogen bond in the case of urea. Hence, due to strong chemical interaction between TOPO and metal precursors, morphology controlled Mn_2O_3 nanostructures have been achieve in the present case.

For a better understanding of the formation of these porous NBs, the concentration of TOPO, (Metal: TOPO concentration ratio of 1.5 to 4) and the reaction time were varied during

the synthesis. The average sizes of these Mn_2O_3 NBs can be tuned by controlling the concentration of TOPO. As discussed above, when the reaction was carried out at a ratio of 1: 4, porous NBs were obtained (Figure 4.15). The average diameter of Mn_2O_3 NBs produced was strongly dependent on the TOPO concentration and no dependency has been observed in reaction time (data not shown). At a lower precursor concentration (1:1.5), micron size solid balls were obtained with 1.2 μm in average diameter, as shown in Figure 4.15a-c. Further increasing the
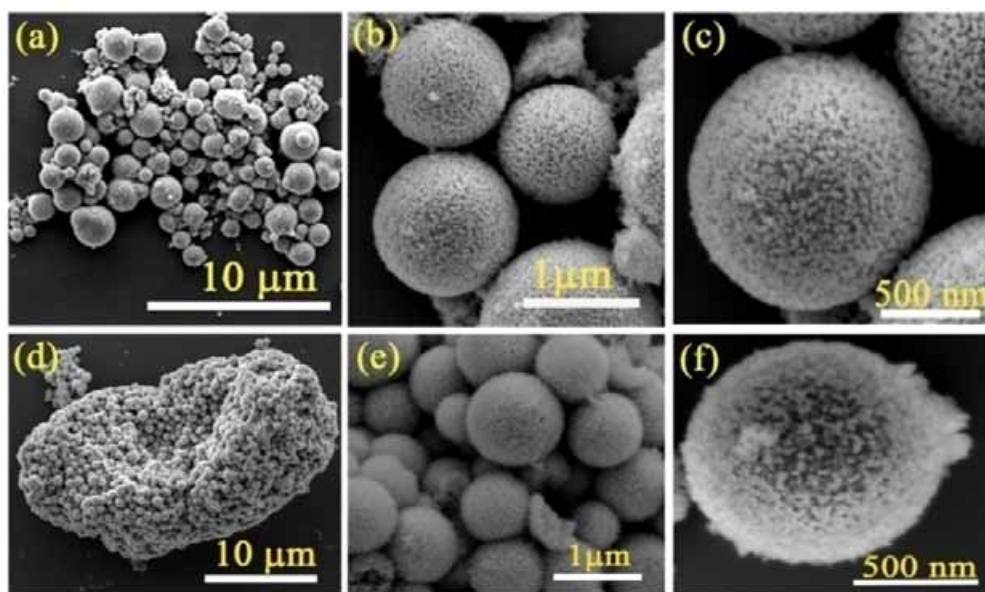
Figure 4.15. *Scanning electron microscopy (SEM) images of Mn_2O_3 nanoballs with different magnification at varied concentration of TOPO. (a-c) SEM images of Mn_2O_3 NBs prepared using Mn^{2+}: TOPO, (1:2) and (d-f) SEM images of Mn_2O_3 NBs prepared using Mn^{2+}: TOPO, (1:1).*

precursor concentration to 1:2, NBs typically ranging from 750 nm to 830 nm in diameter were obtained with aggregated structure (Figure 4.15d-f at different magnification). The driving force by TOPO as a chelating agent dominates the Mn_2O_3 NBs formation and at a higher ratio, uniform nucleation and controlled growth facilitates the formation of uniform NBs. Hence, a higher concentration of TOPO might be preferable for the formation of uniform NBs, whereas relatively lower reactant concentrations could result in micron-size slightly irregular balls in the MAH synthesis procedure.
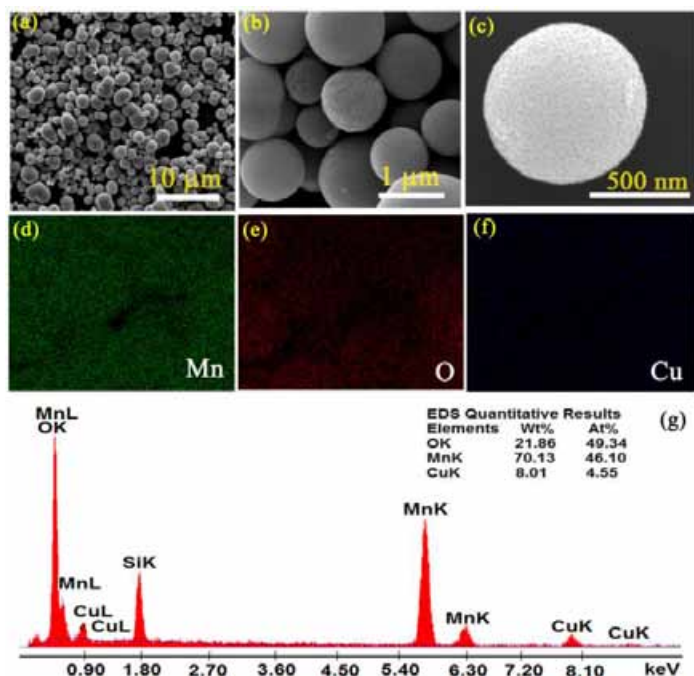
Figure 4.16. *SEM images and elemental mappling of Cu doped Mn_2O_3 nanoballs. (a-c) SEM images with different magnification, (d) Mn, (e) O, (f) Cu elemental mapping and (g) EDS spectrum of Cu doped Mn_2O_3 NBs (using Mn^{2+}: TOPO, 1:4).*

Figure 4.16a-c illustrated the morphology of the as-synthesized Cu^{+2} doped Mn_2O_3 NBs as evident from FESEM. The average diameter of the Cu-Mn_2O_3 NBs was found to be 800 nm higher in comparison with pure Mn_2O_3 NBs which is consistent with the TEM image. The elemental distribution of the material was further characterized by energy dispersive spectroscopic (EDS) mapping. The EDS elemental mapping clearly confirmed the presence and distribution of Mn, O, and Cu elements in the Cu-Mn_2O_3 NBs as shown in Figure 4.16c-f. The EDS spectrum indicates that 8 wt % of Cu has been doped into Mn_2O_3 crystal lattice (Figure 4.16g).

On the basis of the experimental results, a possible formation mechanism of Mn_2O_3 NBs was proposed. Initially, Mn_2O_3 nuclei can form through the reaction between Mn^{2+} cations and O^- anions in the microwave-solvothermal process and further Mn_2O_3 nuclei grow to nanocrystals, which are unstable under the solvothermal conditions. Consequently, they self-assemble into solid NBs and spontaneously adjust themselves to share the common crystallographic orientation driven by the minimization of the surface energy of the nanocrystals. This leads to the assembly of these nanocrystals which is well documented in the literature [151]. Due to the high viscosity of ethylene glycol, the energy of the Brownian motion of the Mn_2O_3

nanocrystallites is not large enough to fully counterbalance the van der Waals interaction between the nanoparticles, forming spherical agglomerates of Mn_2O_3 [152].

4.2.2.2. Electrochemical properties of Mn_2O_3 nanostructures: Before electrocatalytic investigation, it is crucial to measure the electrochemically active surface areas, an important factor associated with electrode reaction rates and double layer parameters [153]. The electrochemical active surface area (EASA) of the Mn_2O_3 and $Cu-Mn_2O_3$ electrodes have been estimated by considering the ratio of the electrochemical double-layer capacitance of the catalytic surface (C_{dl}) and the double layer capacitance of an atomically smooth planar surface of the material per unit area (Cs, specific capacitance) under same electrolyte conditions [154]. Further, C_{dl} can be determined by measuring the non-Faradaic capacitive current related with double-layer charging from the scan rate dependence of the cyclic voltammograms (CVs). A typical CV of Mn_2O_3 and $Cu-Mn_2O_3$ NBs has been shown at scan rate of 50 mV/s between -0.2 and 0.8 V (vs. Ag/AgCl) (Figure 4.17a). The double layer charging current (i_c) is equal to the product of scan rate (v) and double layer capacitance (C_{dl}) as given by following eqn.

$$i_c = v C_{dl} \qquad (4.5)$$

Hence, a plot of i_c *versus* v follows a straight line with a slope equal to the C_{dl} as shown in Figure 4.17b. The current vs. scan rate in Figure 4.17b does not passing through origin, shows an intercept on the current axis at zero scan rate which is not clear at this level. The estimated C_{dl} values of Mn_2O_3 and $Cu-Mn_2O_3$ were 0.018 mF and 0.097 mF. Specific capacitances values for carbon electrode materials have been reported in the range between Cs = 0.005–0.055 mF cm^{-2} in an alkaline medium [155]. We used a specific capacitance of Cs = 0.020 mF cm^{-2} for both Mn_2O_3 and $Cu-Mn_2O_3$ as representative reported values. The estimated EASA values of Mn_2O_3 and $Cu-Mn_2O_3$ are 3.7 cm^2 and 19.46 cm^2. The EASA value of $Cu-Mn_2O_3$ is 15 times higher than that of Mn_2O_3. Galvanostatic discharge/charge measurements were performed in a potential range of -0.2 and 0.7 V (vs. Ag/AgCl). Upon galvanostatic charging/discharging, a slow discharge process was observed for Mn_2O_3 after 10 cycles as evidenced by a voltage drop (IR drop) and a bent discharge curve indicating that the stored energy could not be delivered in a fast manner (Figure 4.17c-d). In contrast, the $Cu-Mn_2O_3$ can be charged/discharged rapidly even after 100 cycles showing a well-defined discharge straight line. The high EASA value and the nearly triangular charge/discharge curves indicate that a nearly ideal electrical-double-layer capacitive behavior of the $Cu-Mn_2O_3$ can open up exciting opportunities for energy storage application.

116
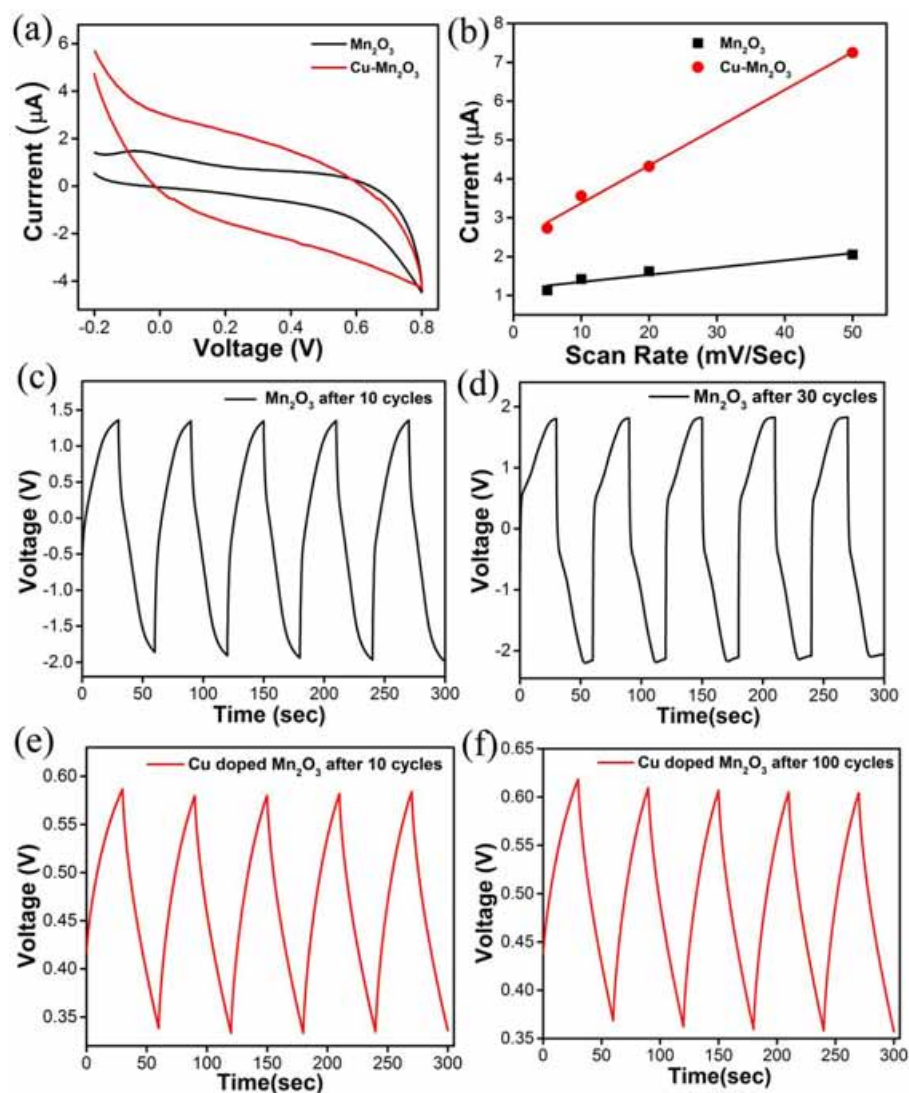
Figure 4.17. *Electrochemical properties of Mn_2O_3 and Cu doped Mn_2O_3 nanoballs. (a) Representative cyclic voltammograms of Mn_2O_3 (black line) and Cu doped Mn_2O_3 (red line) NBs in the potential range of −0.2 V to +0.8 V versus Ag/AgCl reference electrode (non-Faradaic region) at scan rates of 50 mV s^{-1} in a N_2 saturated 0.5 M Na_2SO_4 solution.(b) The cathodic charging current measured as a function of scan rate (5 mV s^{-1}, 10mV s^{-1}, 20 mV s^{-1}, and 50 mV s^{-1}) for Mn_2O_3 NBs and Cu-Mn_2O_3 NBs. (c) and (d) Galvanostatic charge-discharge curves of Mn_2O_3 NBs after 5 and 30 cycles. (e) and (f) Galvanostatic charge-discharge curves of Cu-Mn_2O_3 NBs after 5 and 100 cycles.*

4.2.2.3. Electrocatalytic activity of Mn_2O_3 nanostructures: Manganese oxides are well known as efficient catalysts and the controlled synthesis of Mn_2O_3 nanomaterials promotes us to evaluate the catalytic properties.[156, 157] The electrocatalytic performance of Mn_2O_3 and Cu-Mn_2O_3 NBs for oxygen reduction reaction (ORR) was characterized by CV in 0.1 M KOH on glassy carbon electrodes (with equal mass loading). The CV curves of the catalysts are shown at a scan rate of 50 mV s^{-1} in O_2-saturated and N_2-saturated 0.1 M KOH solutions (Figure 4.18a-b).

117

Compared with the nearly featureless reduction current in N_2-saturated electrolyte, the detected current under O_2 atmosphere was attributed to the catalytic oxygen reduction. RDE measurements were further carried out to reveal the ORR kinetics of the as prepared catalysts.
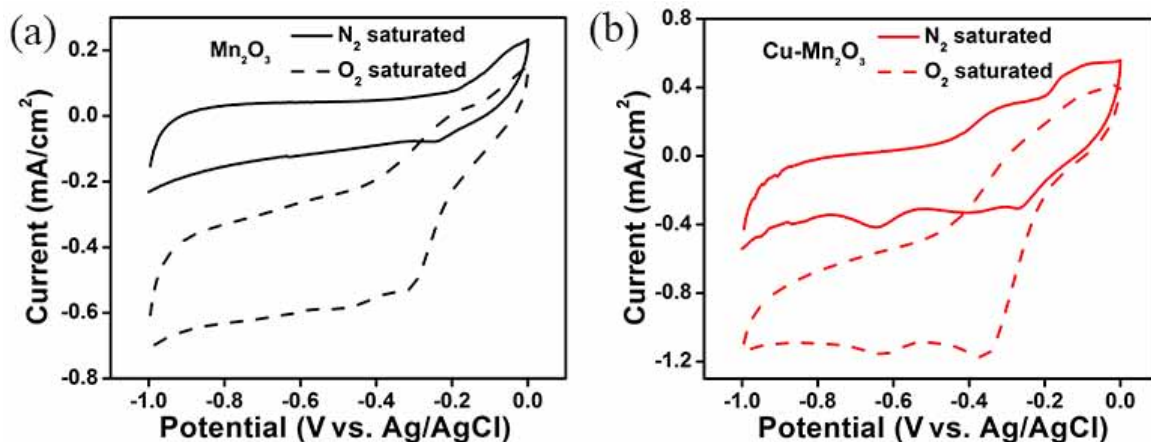
Figure 4.18. _Electrochemical properties of Mn_2O_3 and Cu doped Mn_2O_3 nanoballs. Cyclic Voltammetry curves for (a) Mn_2O_3 NBs and (b) Cu-Mn_2O_3 NBs on glassy carbon electrodes in O_2-saturated and N_2-saturated 0.1 M KOH solutions at a scan rate of 50 mV s^{-1}._

As shown in Figure 4.19a, the ORR onset potential of the Mn_2O_3 electrode commenced at around − 0.36 V. A clear reduction pre-wave was observed at low over potential which suggests efficient electrocatalytic active sites of Mn_2O_3 NBs for oxygen reduction. The RDE polarization curves at different rotation rates are used to study the kinetics of the Mn_2O_3 NBs. With the increase in rotation rate, mass transport at the electrode surface improves, leading to the enhancement of current density (0.9 mAcm^{-2}) (Figure 4.19b). From the analysis of the Koutecky-Levich plot, the value of n was found to be in the range in the range of 3.16-3.8, which is close to the theoretical value for 4e$^-$ reduction of O_2 as shown in Figure 4.19c. Oxygen can be directly reduced to water with the concomitant consumption of four electrons per O_2 molecule (equation 4.5). Alternatively, oxygen can be reduced indirectly, forming H_2O_2 as an intermediate and only two electrons per O_2 molecule are consumed (equation 4.6):

$$_2 + 2 \ _2 \ + 4e^- \rightarrow \ _2 \ + 4 \qquad ^- \qquad (4.6)$$

$$_2 + 2 \ _2 \ + 2e^- \rightarrow \ _2 \ _2 + 2 \qquad ^- \qquad (4.7)$$
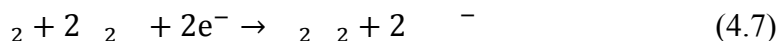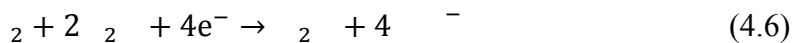
This indicates that the Mn_2O_3 NBs possesses a good electrocatalytic activity toward the 4e$^-$ reduction of O_2 through a redox-mediation mechanism and sequential disproportionations of the reduction intermediates of O_2 reduction (i.e., superoxide and peroxide ion in alkaline media).

Figure 4.19. *Catalytic activity of Mn_2O_3 nanoballs for oxygen reduction reaction (ORR) (a-c) and Oxygen evolution reaction (OER) (d). (a) Rotating disk voltammograms in O_2 saturated 0.1 M KOH at different rotation rates for the oxygen reduction on the Mn_2O_3 NBs electrodes. (b) The corresponding Koutecky–Levich plots (J^{-1} vs. $\omega^{-0.5}$) at different potentials of Mn_2O_3 NBs. (c) The electron transfer number (n) profiles obtained from Koutecky–Levich plots. (d) Rotating disk voltammograms in N_2 saturated 0.1 M KOH at different rotation rates for the oxygen evolution on the Mn_2O_3 NBs electrodes.*

To evaluate the OER activity, CV of the thin films of Mn_2O_3 NBs on glassy carbon electrodes was performed in N_2-saturated 0.1 M KOH solution. A set of polarization curves (Figure 4.19d) were recorded on RDE at different rotating speeds to quantitatively verify the apparent 4 electron reaction on Mn_2O_3 NBs. The anodic current started at 0.6 V (vs. the reversible hydrogen electrode, RHE) with a maximum current density of 1 mAcm^{-2} at 1 V for Mn_2O_3 NBs. Similarly, the Cu-doped Mn_2O_3 NBs exhibited a bifunctional catalytic activity for both OER and ORR (Figure 4.20a-c). The ORR polarization curves of Cu-Mn_2O_3 NBs with the increase of rotation rate, leading to the enhancement of current density ~5.8 mAcm^{-2} as shown in
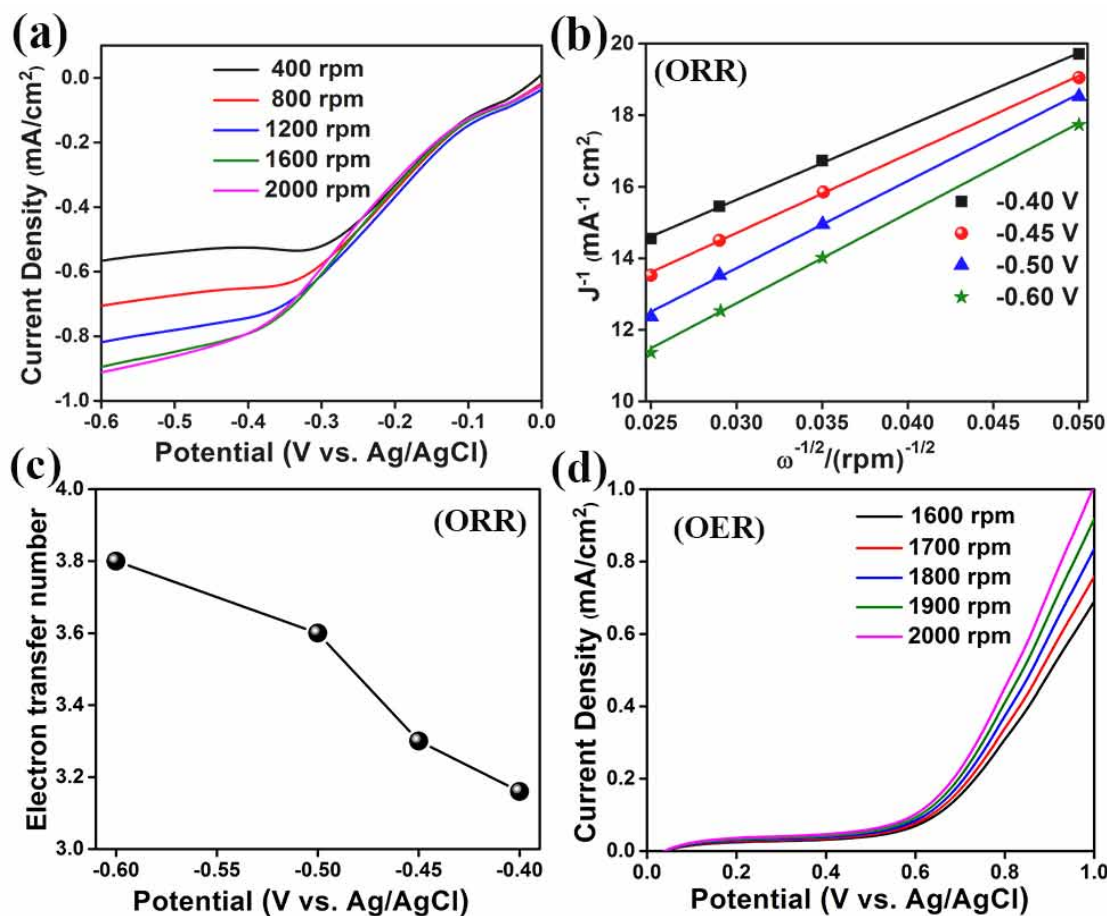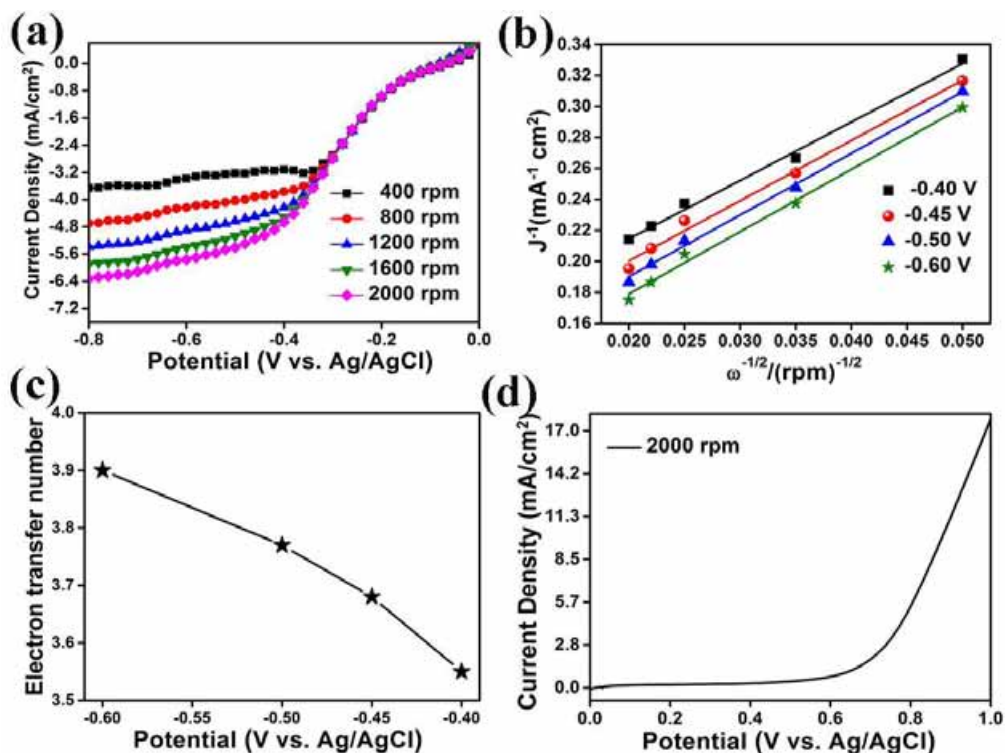
Figure 4.20. *Catalytic activity of copper doped Mn_2O_3 nanoballs for oxygen reduction reaction (ORR) and Oxygen evolution reaction (OER). (a) Rotating disk voltammograms of $Cu-Mn_2O_3$ in O_2 saturated 0.1 M KOH at different rotation rates for the oxygen reduction. (b) The corresponding Koutecky–Levich plots (J^{-1} vs. $\omega^{-0.5}$) at different potentials of $Cu-Mn_2O_3$ NBs. (c) The electron transfer number (n) profiles obtained from Koutecky–Levich plots. (d) Representative rotating disk voltammogram in N_2 saturated 0.1 M KOH at 2000 rpm rotation rates for the oxygen evolution on the $Cu-Mn_2O_3$ NBs electrodes.*

Figure 4.20b. The Koutecky-Levich plot follows parallel straight lines for different potentials in mixed kinetic-diffusion controlled region, indicating the number of electrons transferred per O_2 molecule and the active surface area for the reaction do not change significantly within the potential range studied (Figure 4.20b). From the analysis of the Koutecky-Levich plot, the value of n was found to be in the range of 3.4-3.9 (Figure 4.20c). For OER, the anodic current with a maximum current density of 17 mAcm^{-2} at 1 V for $Cu-Mn_2O_3$ NBs has been achieved, which is much higher than Mn_2O_3 NBs as shown in Figure 4.20d. This increase in the current density might be due to the fact that the catalysts stimulate not only the oxygen evolution reaction but also the redox couple due to presence of Cu in the Mn_2O_3 crystals as well as increasing the effective surface area ultimately improving the catalytic efficiency which is consistent with earlier report [158, 159]. We further compared the catalytic activity of pure and Cu-doped Mn_2O_3 NBs catalyst with other catalysts (Table 4.3). Although the Pt/C, a state-of-the-art Pt

catalyst showed higher activity, non-precious transition metal based catalysts have shown excellent ORR activity in an alkaline medium.

Table 4.3. Comparative values of Kinetic parameters for the ORR. Considering potentials at current on-set, current densities (j) corresponding mass activities (MA).

Electrode	Onset potential V/Ag/AgCl	No. e− from KL plot	Half-wave potential ($E_{1/2}$) (V)	J/mA cm^{-2} geom.	MA (mA/mg)	Reference
Mn_2O_3	-0.15	3.8	-0.29	0.536	6.1	*This work*
Cu-Mn_2O_3	-0.12	3.9	-0.25	5.36	18.9	*This work*
Mn_2O_3/C	-	3.9	-	1.66	26.6	*ACS Appl. Mater. Interfaces 2009, 1, 460.*
Mn_3O_4/N-rGO	-0.075	3.7	-	1.99	-	*ACS Appl. Mater. Interfaces 2014, 6, 2692*
MnO_x/C	0.1	2.8	-	-	60	*J. Phys. Chem. C 2012, 116, 11032.*
α MnO_2	0.1	3.6	-	3.3	-	*Chem. Mater. 2010, 22, 898.*
β MnO_2	-0.45	3.7	-	3.87	-	*Chem. Mater. 2010, 22, 898.*
γ MnO_2	-0.45	3.7	-	4.0	-	*Chem. Mater. 2010, 22, 898.*
Cu-α MnO_2	-0.1	3.2	-0.292	-	-	*J. Phys. Chem. C 2014, 118, 17342.*
Ag/C	0.023	3.5	-	-	7.6	*J. Phys. Chem. C 2012, 116, 11032.*
Pt/C	0.13	4	-	-	136	*J. Phys. Chem. C 2012,116, 11032.*

The stability of the as synthesized catalysts were investigated by chronoamperometric (CA) measurements where the current density-time (I vs t) curves at constant potentials were recorded as shown in Figure 4.21. Both Mn_2O_3 NBs and Cu-Mn_2O_3 NBs exhibited distinct long term choronoamperometic stabity which is one of the key chalenges for alkaline fuel cells. The ORR current values obtained for both Mn_2O_3 and Cu-Mn_2O_3 NBs were highly stable over 10000 s of continuos operation at a constant potential of -0.4 V as shown in Figure 4.21a. During chronoamperometric measurement for OER, initially, both catalysts exhibited a pronounced current decay, which could be caused by the accumulation of gas bubbles which may partially block the active sites of the electrode. The current density attained a steady state in the first ~700

s thereafter, indicating that these both Mn_2O_3 NBs catalyst form a very stable film on glassy carbon electrode surface and also exhibit stable electrocatalytic performance towards OER. The excellent durability of the as-synthesized catalysts for both ORR and OER has been associated with the unique structural and chemical stability of the transition metal oxides in an alkaline medium.
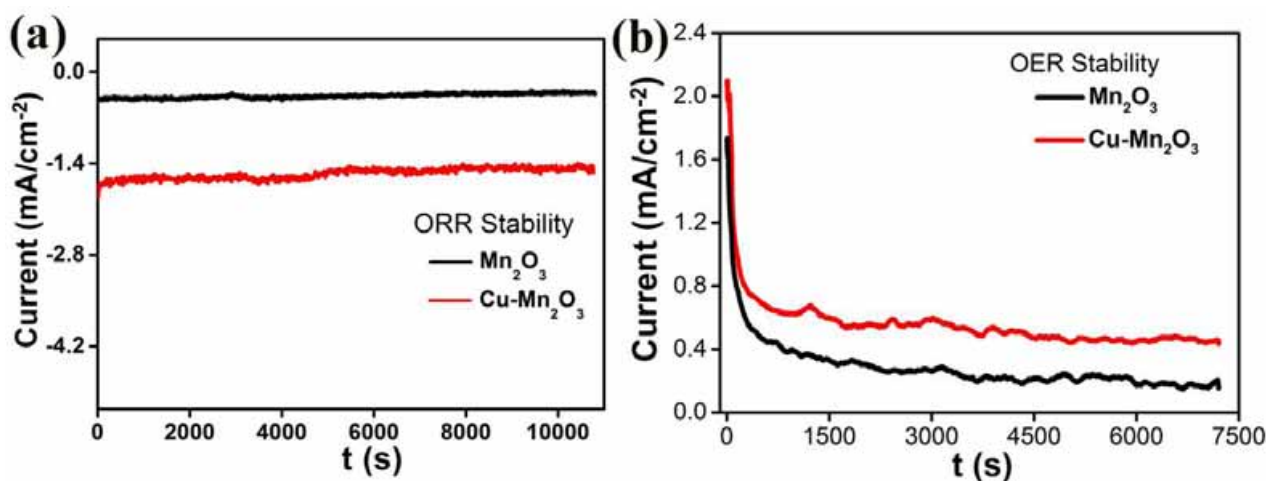
Figure 4.21. *Stability of pure and copper doped Mn_2O_3 nanoballs for oxygen reduction reaction (ORR) and Oxygen evolution reaction (OER). Chronoamperometric curves for the (a) ORR and (b) OER of pure Mn_2O_3 NBs (black curve) and copper doped Mn_2O_3 (red curve) NBs.*

4.2.3. Reduced Graphene Oxide Supported Hierarchical Flower like Manganese Oxide as Efficient Electrocatalysts toward Reduction and Evolution of Oxygen [160]:

4.2.3.1. Characterization of Mn_2O_3: A facile and mild hydrothermal route has been used to synthesize Mn_2O_3 without the use of any template. The crystal structures and formation of the manganese oxides and graphene supported hybrid composites have been verified by powder X-ray diffraction. Typical XRD patterns of the as-prepared Mn_2O_3/PVA, Mn_2O_3/TOPO, Mn_2O_3/PVA/rGO and Mn_2O_3/TOPO/rGO are shown in Figure 4.22. The peaks in the XRD patterns of the as–prepared manganese oxides can be well indexed to the (211), (222), (321), (311), (332), (400), (431), (440), (521), (541), (611), (622), (631) and (721) planes of the cubic phase Mn_2O_3 crystal (JCPDS No. 41-1442) indicating that they are all well-crystallized. These results are in consistent with our previous reports. For the hybrid sample, in addition to the peaks from Mn_2O_3 phase, there is additional diffraction peaks located at $2\theta = 26.0°$ which can be
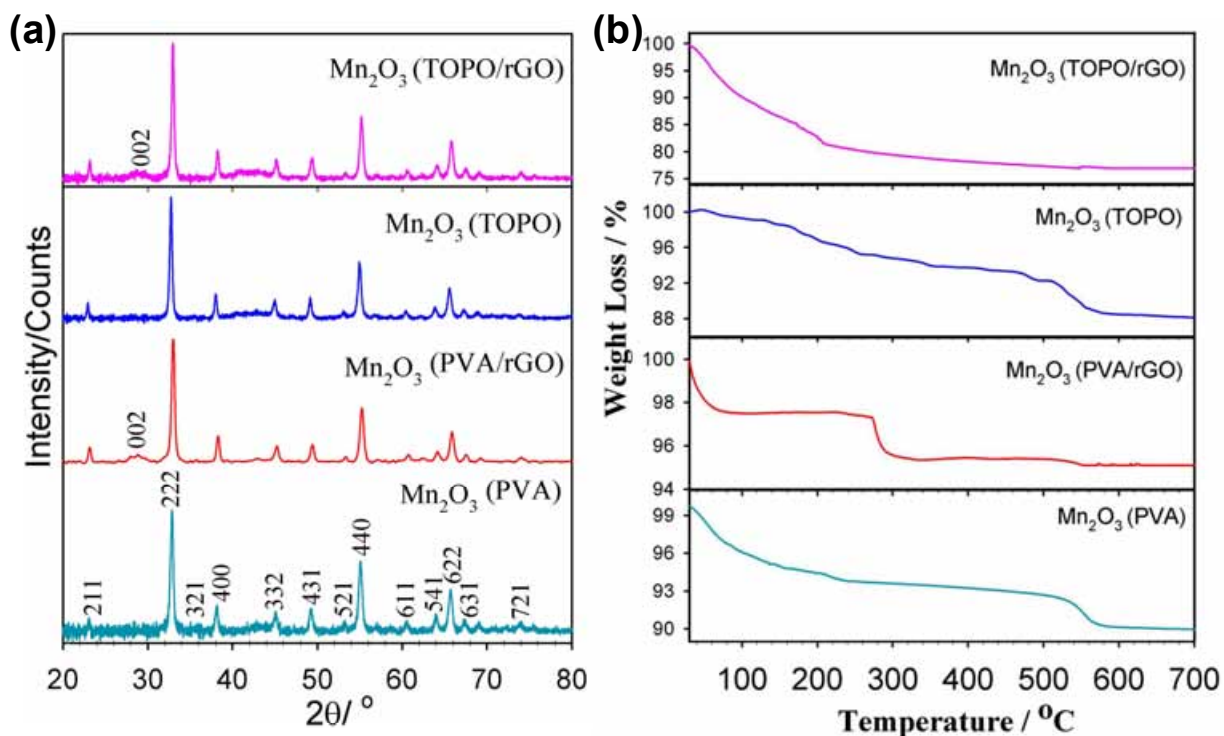
Figure 4.22. *Structural characterization of Mn_2O_3 and graphene supported hierarchical Mn_2O_3. (a) XRD patterns of Mn_2O_3/PVA, Mn_2O_3/TOPO, Mn_2O_3/PVA/rGO and Mn_2O_3/TOPO/rGO. (b) Thermogravimetric analysis (TGA) profiles of Mn_2O_3/PVA, Mn_2O_3/TOPO, Mn_2O_3/PVA/rGO and Mn_2O_3/TOPO/rGO.*

attributed to the (002) reflection of reduced GO sheets (JCPDS No. 75-1621). In the Mn_2O_3/PVA/rGO and Mn_2O_3/TOPO/rGO, the diffraction peaks can be indexed as the planes of cubic phase Mn_2O_3 crystal and the broad diffraction peak at 26.0° corresponds to the (002) plane of the graphitic carbon, and indicates the presence of reduced graphene. Thus, XRD patterns indicate that Mn_2O_3 successfully incorporated on rGO layers. No other impurity peaks have been detected in both cases and the results confirm the successful formation of highly crystalline pure Mn_2O_3 over the rGO nanosheets by the present hydrothermal process. The thermogravimetric (TG) data for the thermal decomposition of the Mn_2O_3 samples are shown in Figure 4.22b. TG analysis of Mn_2O_3 powder showed a weight loss ~8% at 580°C should be attributed to the removal of surface-adsorbed water which is consistent with previous reports [55, 161, 162]. Further, the weight remains nearly unchanged suggests high thermal stability of the as prepared Mn_2O_3 (Figure 4.22b). Similarly, graphene supported Mn_2O_3/PVA/rGO demonstrated high thermal stability with ~5% weight loss up to 800°C. For, Mn_2O_3/TOPO/rGO, the weight loss of ~20-30% occurs between 200 to 280ºC may be associated with the decrease of labile oxygen-

123

containing functional groups of rGO yielding CO, CO_2 and steam [163]. A residual mass of about 80–95% indicating loading of Mn_2O_3 oxides in the nanocomposites.
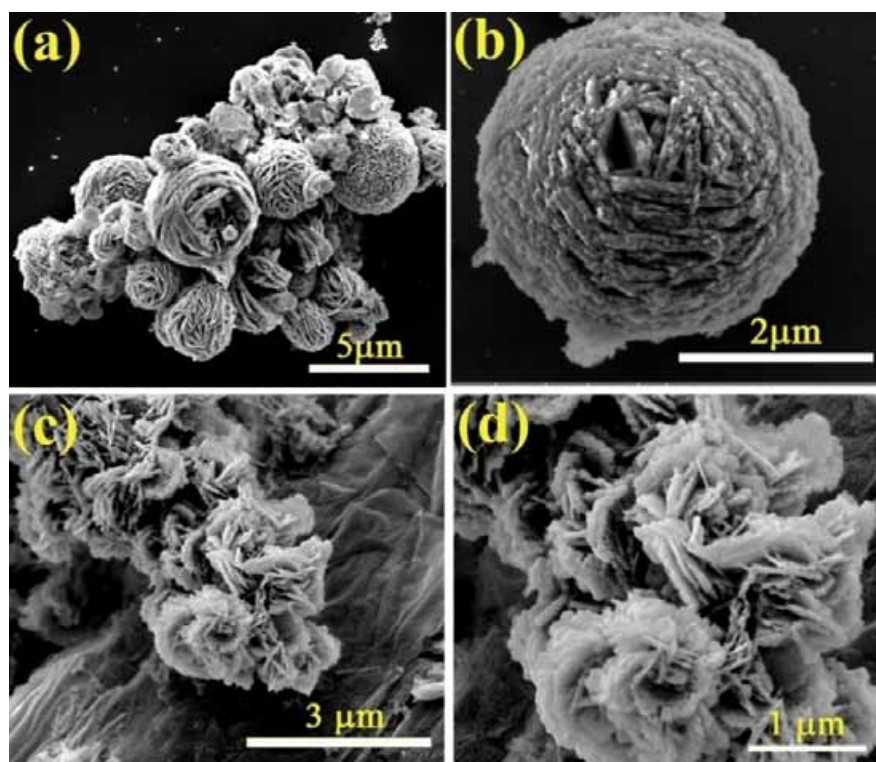
Figure 4.23. *Scanning electron microscopy (SEM) images of Mn_2O_3 using PVA as structure controlling agent and graphene supported hierarchical Mn_2O_3 using PVA as structure controlling agent at different magnification. (a, b) Mn_2O_3/PVA, (c, d) Mn_2O_3/PVA/rGO.*

The structure and morphology of the as prepared Mn_2O_3 and Mn_2O_3/rGO composites were investigated by field-emission scanning electron microscopy (FESEM) and transmission electron microscopy (TEM). Figure 4.23a and 4.23b illustrate the formation of hierarchical Mn_2O_3 microstructure in the range of 2.5-4 μm using PVA as a structure controlling agent without any support. The morphologies of the Mn_2O_3/PVA/rGO composites using PVA as controlling agent in presence of graphene oxides as support are shown in Figure 4.23c and 4.23d. The flower-like Mn_2O_3 micro-spheres with size ~2 μm are anchored on graphene sheets are noticeably observed in Figure 4.23c. Additionally, the Mn_2O_3 micro-spheres supported on graphene sheets exhibit partially overlapped and crumpled at many regions as shown in Figure 4.23c. The low magnification SEM image (Figure 4.23d) displays that the flower-like

microspheres are constructed from numerous 2D nanoflakes with several tens of nanometers in
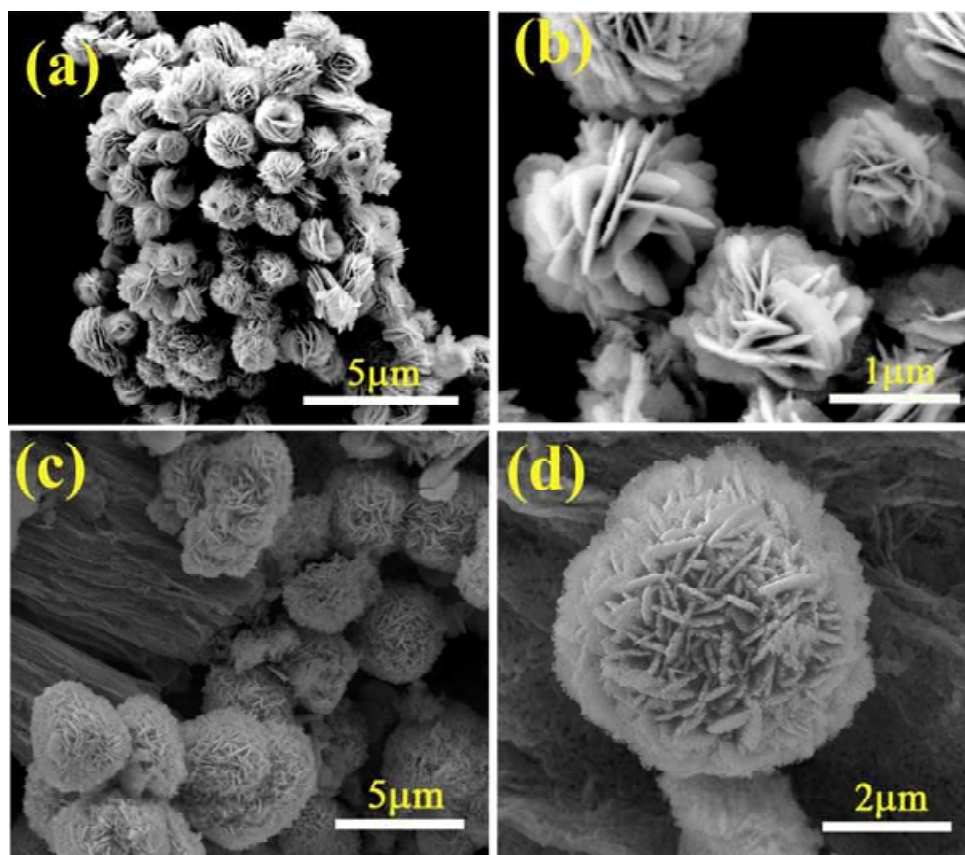
Figure 4.24. *Scanning electron microscopy (SEM) images of Mn$_2$O$_3$ TOPO as structure controlling agent and graphene supported hierarchical Mn$_2$O$_3$ using TOPO as structure controlling agent at different magnification. (a, b) Mn$_2$O$_3$/TOPO and (c, d) Mn$_2$O$_3$/TOPO/rGO.*

thickness. For Mn$_2$O$_3$ using TOPO as chelating ligand, SEM image (Figure 4.24a and 4.24b) reveals rose-like characteristic which are assembled with ultrathin Mn$_2$O$_3$with diameters in the range of 1.5 μm. When GO was predispersed in the reaction solution, the as prepared composites display a 3D architecture consisting of rGO nanosheets and Mn$_2$O$_3$ microstructure (Figure 4.24c and 4.24d) with diameter of ~3.5 μm, also possess petal-like morphology composed of ultrathin Mn$_2$O$_3$ nanosheets as nanobuilding blocks. From the high magnification SEM image (Figure 4.24d) it can be clearly seen that Mn$_2$O$_3$ with hierarchical flower structures formed with the rGO nanosheets. Such hierarchical flower-like micro-spheres appear to be suitable for catalytic applications. Energy Dispersive Spectrometer (EDS) pattern for Mn$_2$O$_3$/TOPO shows the peaks
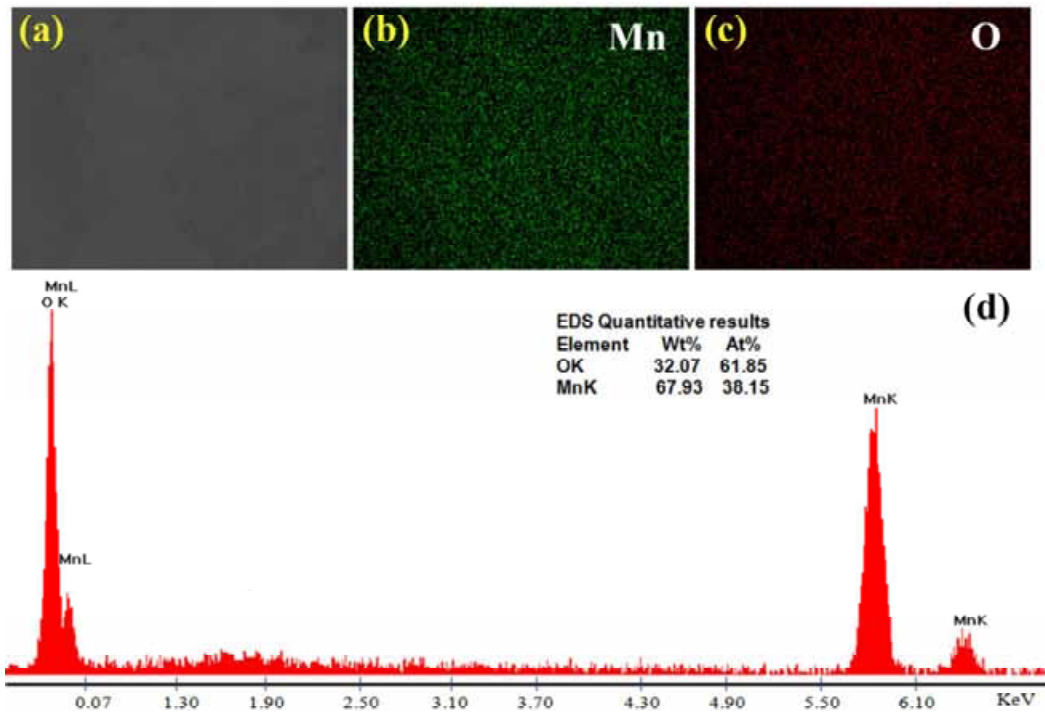
Figure 4.25. *SEM images and elemental mappling of Mn₂O₃/TOPO. (a) SEM image (b) Mn, (c) O elemental mapping and (d) EDS spectrum of Mn₂O₃/TOPO.*

of Mn and O further confirming the formation of Mn_2O_3 (Figure 4.25). Further, the EDS elemental mapping clearly confirmed the presence and distribution of Mn, O, and C elements in the Mn_2O_3/TOPO/rGO as shown in Figure 4.26. Quantitative EDS analysis confirms the formation of Mn_2O_3 in the composites as well as presence of graphene.
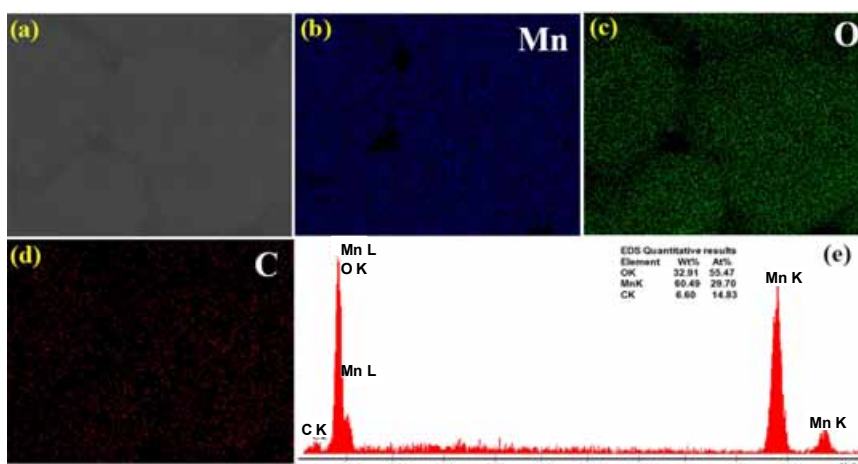
Figure 4.26. *SEM images and elemental mappling of Mn₂O₃/TOPO/rGO. (a) SEM image (b) Mn, (c) O, (d) C elemental mapping and (e) EDS spectrum of Mn₂O₃/TOPO/rGO.*

To reveal detailed microstructures and morphology of Mn_2O_3 and Mn_2O_3/rGO composites, transmission electron microscopy (TEM) and High Resolution TEM (HRTEM) was also employed (Figure 4.27 and 4.28). Figure 4.27a showed the formation of spherical type
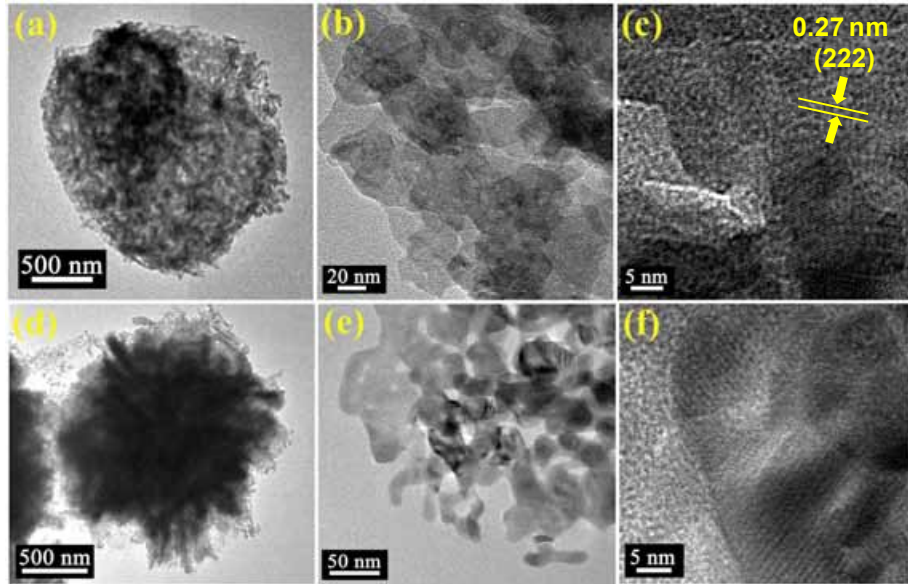
Figure 4.27. *Transmission electron microscopy (TEM) images of Mn_2O_3/PVA and $Mn_2O_3/PVA/rGO$. (a), (b) TEM images at different magnification and (c) HRTEM image of Mn_2O_3/PVA. (d), (e) TEM images at different magnification and (f) HRTEM image of $Mn_2O_3/PVA/rGO$.*

Mn_2O_3 with a mean diameter of 2.1 µm for Mn_2O_3/PVA. A low magnification TEM image of Mn_2O_3/PVA shows that large scale microspheres which assembled by small particles are obtained (Figure 4.27b), which is in agreement with the FESEM observations. As shown in Figure 4.27c, the inter-planar distance between the fringes is found to be about 0.27 nm consistent with (222) planes of Mn_2O_3. Figure 4.27d–f illustrates the TEM and HRTEM results for $Mn_2O_3/PVA/rGO$ composites, from which the Mn_2O_3 formed a 3D architecture of petal-like morphology with an average diameter of about 1.8 µm which is well consistent with those observed by SEM. The HRTEM image also demonstrated highly crystalline nature of $Mn_2O_3/PVA/rGO$ with cubic phase (Figure 4.27f). As shown in Figure 4.28a–c and d–f, the TEM images of $Mn_2O_3/TOPO$ and $Mn_2O_3/TOPO/rGO$ formed revealed flower-like morphology comprise a large number of thin nanosheets with an average diameter of 1.6 µm and aggregated microspheres with an average diameter of about 3 µm, respectively, which is well consistent

with those observed by SEM. The HRTEM images of the individual flower (Figure 4.28b-c) and
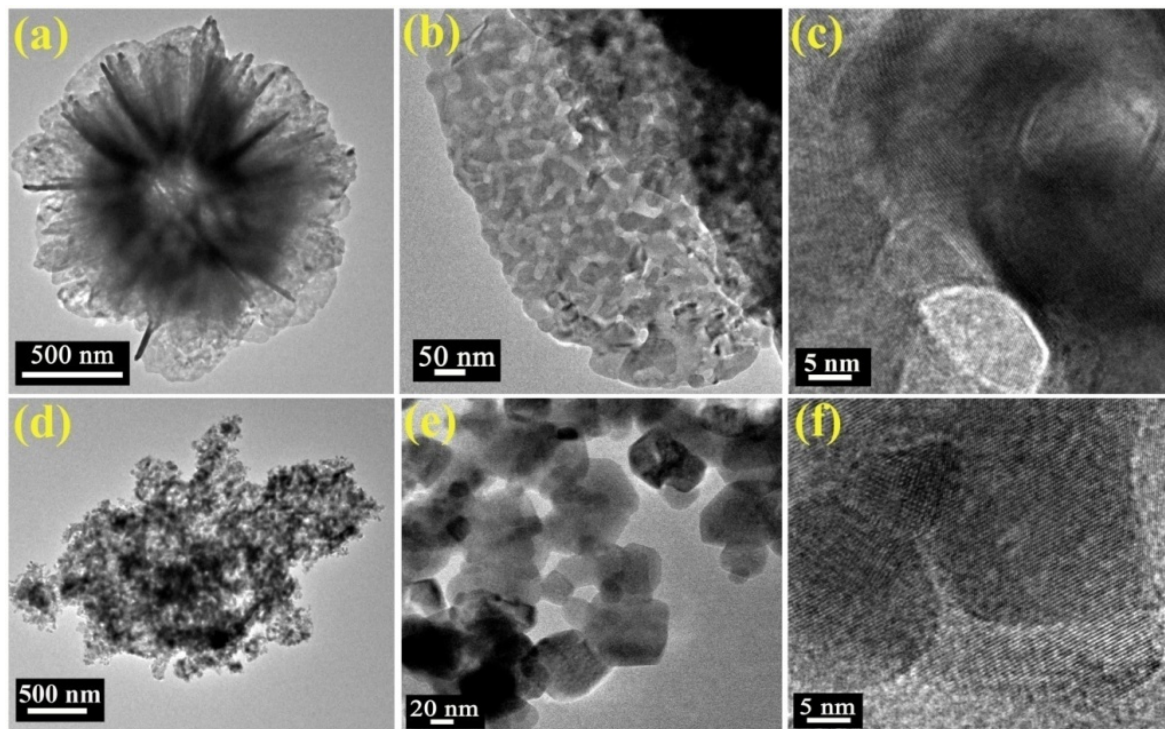
Figure 4.28. *Transmission electron microscopy (TEM) images of Mn_2O_3/TOPO and Mn_2O_3/TOPO/rGO. (a), (b) TEM images at different magnification and (c) HRTEM image of Mn_2O_3/TOPO. (d), (e) TEM images at different magnification and (f) HRTEM image of Mn_2O_3/TOPO/rGO.*

sphere (Figure 4.28e-f) displayed well-resolved lattice planes with an inter-planar distance of 0.27 nm consistent with (222) planes of Mn_2O_3 which correspond to the cubic structure. However, it is difficult to observed graphene nanosheets in presence of assembled Mn_2O_3 structures in TEM images. This result obviously suggests that the preferential assembly of Mn_2O_3 in crystalline phase. To investigate the effect of PVA and TOPO on the morphology of Mn_2O_3, the control experiments were operated without using TOPO and PVA while the other experimental parameters were maintained the same as aforementioned samples but produce irregular shape of manganese oxides (data not shown). On the other hand, irregular particle aggregates obtained in presence of graphene oxides without using capping agent under similar reaction condition also suggests significant role of PVA and TOPO as shown in Figure 4.29. This suggests that the formation and morphology of the as prepared Mn_2O_3 strongly depended on the presence of TOPO, PVA and graphene oxides. PVA, a kind of nonionic surfactant, can
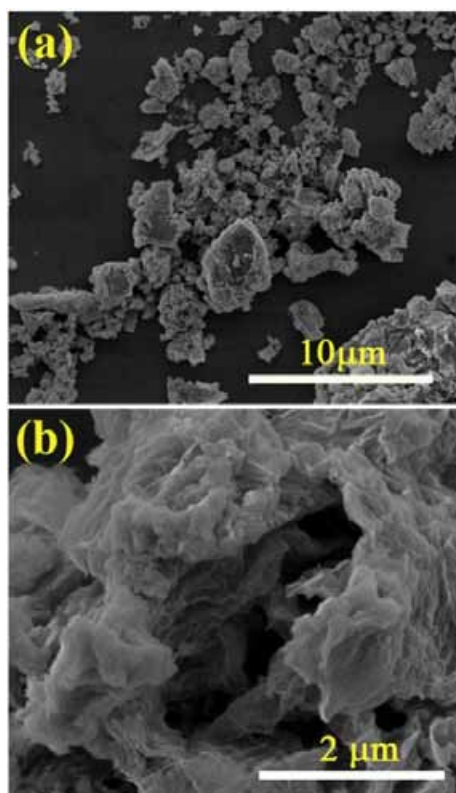
***Figure 4.29.** (a, b) SEM images of Mn_2O_3 synthesized by hydrothermal process in presence of graphene oxides without using structure controlling agent.*

physically absorb on the surface of manganese oxides subunits to control the grain growth and link the subunits to form a more stable morphology during the reaction process [94, 164]. The particle growth in presence of TOPO is well controlled via lower intermolecular interaction which is differs significantly from the linear chain PVA ligand [148, 165]. Generally, the growth process of crystals consists of two steps, an initial nucleating stage and a subsequent crystal growth process. At the nucleating stage, the crystalline phase of the seeds is critical for directing the intrinsic shapes of the crystals and Mn_2O_3 nuclei can form through the reaction between Mn^{2+} cations and O^- anions in the thermal process. At the subsequent step, the crystal growth stage strongly governs the final architecture of the crystals through the self-assembly of nanocrystals driven by the minimization of the surface energy which is consistent with the literature [151]. Moreover, higher supersaturation due to formation of large concentration of Mn_2O_3 nuclei causes the three-dimensional growth of preformed nuclei which leads to the formation of hierarchical structures which is common in the synthesis of inorganic nanomaterials [166].

4.2.3.2. Catalytic Activity: Manganese oxides have been identified as one of excellent candidates as cathode material. In the present case, the electrochemical ORR and OER tests are performed using three-electrode system in the alkaline condition. The morphology controllable preparation of Mn_2O_3 allows a systematical investigation of their structure–performance relationship towards the oxygen reduction and evolution electrocatalysis. Cyclic voltammetry (CV) curves (Figure 4.30) were found to exhibit oxygen reduction peaks for all the Mn_2O_3 electrodes in O_2-saturated KOH solution, but not the N_2-saturated KOH solution. Figure 4.31a shows the ORR catalytic properties of nanocrystalline Mn_2O_3 supported on rotating ring disk electrodes (RRDE) and the polarization profiles display typical ORR current-potential response. The key performance parameters such as onset potential, half-wave potential, kinetic current density and transferred electron transfer number of Mn_2O_3 have been summarized in Table 4.4. To evaluate the OER activity, cyclic voltammetry of Mn_2O_3 on glassy carbon electrodes was performed in N_2-saturated 0.1 M KOH solution (Figure 4.32). The anodic current started at 0.6 V (vs. Ag/AgCl/sat.KCl) with a maximum current density in the range of 7-11 $mAcm^{-2}$ at 1 V. As
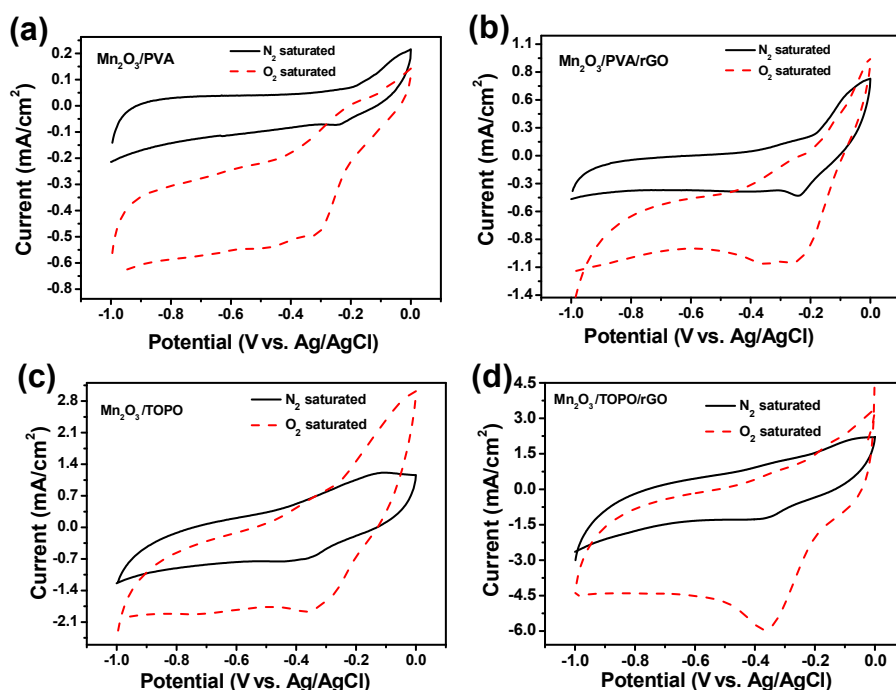
Figure 4.30. *Electrochemical properties of Mn_2O_3. Cyclic Voltammetry curves for (a) Mn_2O_3/PVA, (b) Mn_2O_3/PVA/rGO, (c) Mn_2O_3/TOPO and (d) Mn_2O_3/TOPO/rGO on glassy carbon electrodes in O_2-saturated and N_2-saturated 0.1 M KOH solutions at a scan rate of 50 mV s^{-1}.*

can be seen, the Mn_2O_3/TOPO/rGO has the highest electrocatalytic activity of all the aforementioned Mn_2O_3 catalysts in terms of both the onset potential and limiting current, highlighting the importance of the graphene support both for ORR and OER (Figure 4.31b). The current density of Mn_2O_3/PVA/rGO slightly lower than that of Mn_2O_3/PVA, however, a significant low onset potential for Mn_2O_3/PVA/rGO justify the superior catalytic activity. The catalytic activity for ORR follow an order, Mn_2O_3/TOPO/rGO>Mn_2O_3/PVA>Mn_2O_3/PVA/rGO> Mn_2O_3/TOPO based on current density. However, the reason behind lower ORR catalytic activity of Mn_2O_3/PVA/rGO is not clear. On the other hand, the catalytic activity for OER is as follows: Mn_2O_3/TOPO/rGO> Mn_2O_3/PVA/rGO >Mn_2O_3/TOPO> Mn_2O_3/PVA. For graphene
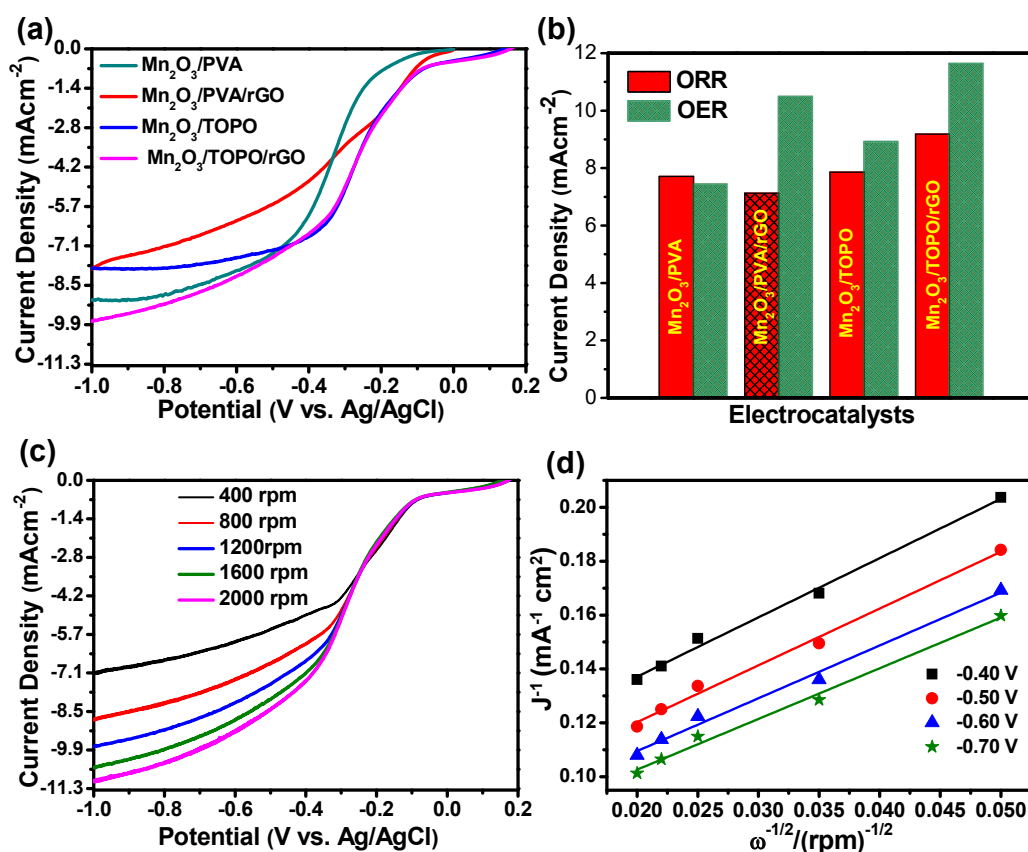
Figure 4.31. *Electrocatalytic activities for ORR and OER. (a) Linear scan voltammogram (LSV) curves for Mn_2O_3/PVA, Mn_2O_3/TOPO, Mn_2O_3/PVA/rGO and Mn_2O_3/TOPO/rGO at an RDE (1,200 rpm) in O_2-saturated 0.1M KOH solution. Scan rate, 5 mV s^{-1}. (b) Comparative kinetic current of various samples for both O_2 reduction at 0.8 V at the RRDE measurements (1,200 rpm) and evolution OER at 1.0 V, showing the electrocatalytic activities towards both ORR and OER. (c) LSV curves of Mn_2O_3/TOPO/rGO in oxygen-saturated 0.1M KOH at various rotating speeds. (d) K–L plots for Mn_2O_3/TOPO/rGO at various potentials.*

Table 4.4. Comparison of the electrochemical performance of Mn₂O₃ electrocatalysts for ORR.

Electrode	Onset potential V/Ag/AgCl	No. e− from KL plot	Half-wave potential ($E_{1/2}$) (V)	J/mA cm^{-2} (geom.) @1200 rpm and -0.8 V	MA (mA/mg) @ -0.8 V vs Ag/AgCl
Mn₂O₃/PVA	-0.15	3.91	-0.34	8.82	31.1
Mn₂O₃/PVA/rGO	-0.08	3.75	-0.26	7.11	25.1
Mn₂O₃/TOPO	-0.04	3.42	-0.22	7.86	27.7
Mn₂O₃/TOPO/rGO	-0.09	3.99	-0.24	9.18	32.4

supported Mn_2O_3 electrocatalysts, presence of graphene nanosheets allow the effective dispersion as well as act as anchoring sites for the Mn_2O_3 NPs. Moreover, graphene nanosheets having holes, carbon vacancies, oxygen, and defects due to partial oxidation may generates additional chemically active sites for catalytic reactions which cause enhanced OER activity. Further, with the increase of rotation rate, mass transport at the electrode surface improves,
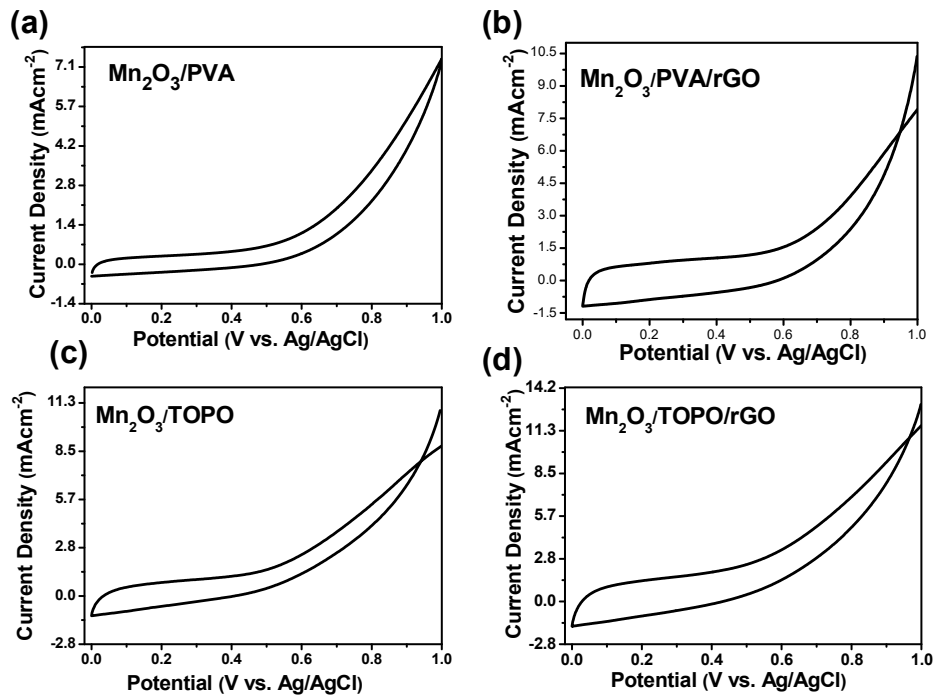
Figure 4.32. *Cyclic Voltammetry curves for (a) Mn₂O₃/PVA, (b) Mn₂O₃/PVA/rGO, (c) Mn₂O₃/TOPO, and (d) Mn₂O₃/TOPO/rGO on glassy carbon electrodes in N₂-saturated 0.1 M KOH solutions at a scan rate of 50 mV s⁻¹. Current densities are normalized against geometric area.*

leading to the enhancement of current density (from 9.18 to 11.2 mAcm^{-2}) for ORR (Figure 4.31c). The similar trend has been observed for all other Mn_2O_3 catalyts (Figure 4.33). A comparative study (Table 4.5) has been added in order to provide the comparison (e.g. in terms of catalytic activity) of the synthesized Mn_2O_3 to the similar work done in the same field. Moreover, evaluation of the ORR catalytic behaviors is studied by determining the transferred electron number (n). From the Koutecky-Levich plot analysis, the value of n was found to 3.99, which is close to the theoretical value for 4e$^-$ reduction of O_2 as shown in Figure 4.31d. The other Mn_2O_3 catalyst the value of n was found to be in the range of 3.4-3.9. During the ORR electrocatalysis on transition metal oxides under alkaline media, involve multistep steps of O_2 adsorption, formation of peroxide intermediate and further reduction or decomposition of peroxide to OH$^-$ ions [77]. These processes are mediated by electron transfer, redox reactions and the surface oxygen adsorption ability that can be tuned by electronic structure [167].
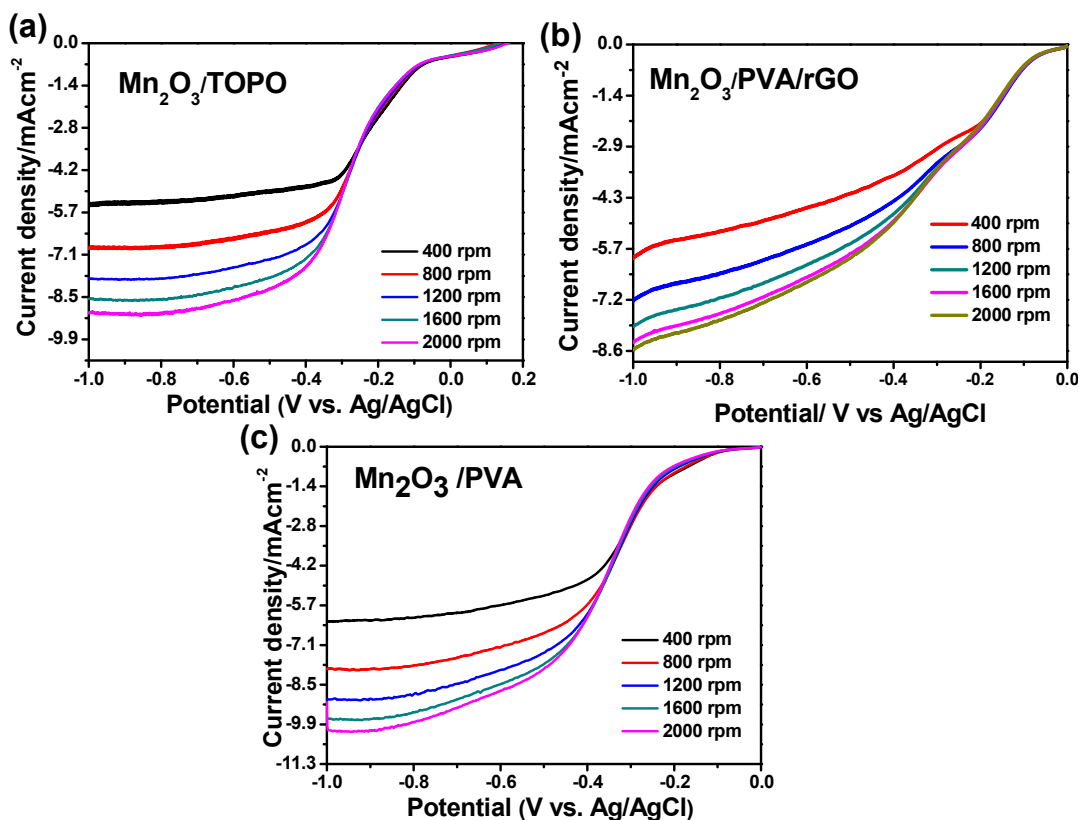
Figure 4.33. *LSV curves of (a) Mn_2O_3/TOPO, (b) Mn_2O_3/PVA/rGO, and (c), Mn_2O_3/PVA in oxygen-saturated 0.1M KOH at various rotating speeds. Current densities are normalized against geometric area.*

Table 4.5. Comparative values of kinetic parameters for the ORR. Considering potentials at current on-set, current densities (j) corresponding mass activities (MA).

Electrode	Onset potential V/Ag/Ag Cl	No. e− from KL plot	Half-wave potential ($E_{1/2}$) (V)	J /mA cm^{-2} geom.	MA (mA/mg)	Reference
Mn_2O_3/PVA	-0.15	3.91	-0.34	8.82	31.1	*This work*
Mn_2O_3/PVA/ rGO	-0.08	3.75	-0.26	7.11	25.1	*This work*
Mn_2O_3/TOPO	-0.04	3.42	-0.22	7.86	27.7	*This work*
Mn_2O_3/TOPO /rGO	-0.09	3.99	-0.24	9.18	32.4	*This work*
Mn_2O_3	-0.15	3.8	-0.29	0.536	6.1	*Catal. Sci. Tech. 2016, 6, 1417.*
$Cu-Mn_2O_3$	-0.12	3.9	-0.25	5.36	18.9	*Catal. Sci. Tech. 201, 6, 1417.*
Mn_2O_3/C	-	3.9	-	1.66	26.6	*ACS Appl. Mater. Interfaces 2009, 1, 460.*
Mn_3O_4/N-rGO	-0.075	3.7	-	1.99	-	*ACS Appl. Mater. Interfaces 2014, 6, 2692.*
MnO_x/C	0.1	2.8	-	-	60	*J. Phys. Chem. C 2012, 116, 11032.*
α MnO_2	0.1	3.6	-	3.3	-	*Chem. Mater. 2010, 22, 898.*
β MnO_2	−0.45	3.7	-	3.87	-	*Chem. Mater. 2010, 22, 898.*
γ MnO_2	−0.45	3.7	-	4.0	-	*Chem. Mater. 2010, 22, 898.*
$Cu-\alpha$ MnO_2	−0.10	3.20	−0.292	-	-	*J. Phys. Chem. C 2014, 118, 17342 .*
Ag/C	0.023	3.5	-	-	7.6	*J. Phys. Chem. C 2012, 116, 11032*
Pt/C	0.13	4	-	-	136	*J. Phys. Chem. C 2012, 116,11032.*

One of the practical issues concerning stability of electrocatalysts can be studied by chronoamperometric (CA) measurement, where the current at a constant applied voltage is recorded during an appropriate time period under working conditions. For ORR, Mn_2O_3/TOPO/rGO electrode shows excellent durability with no obvious activity decay
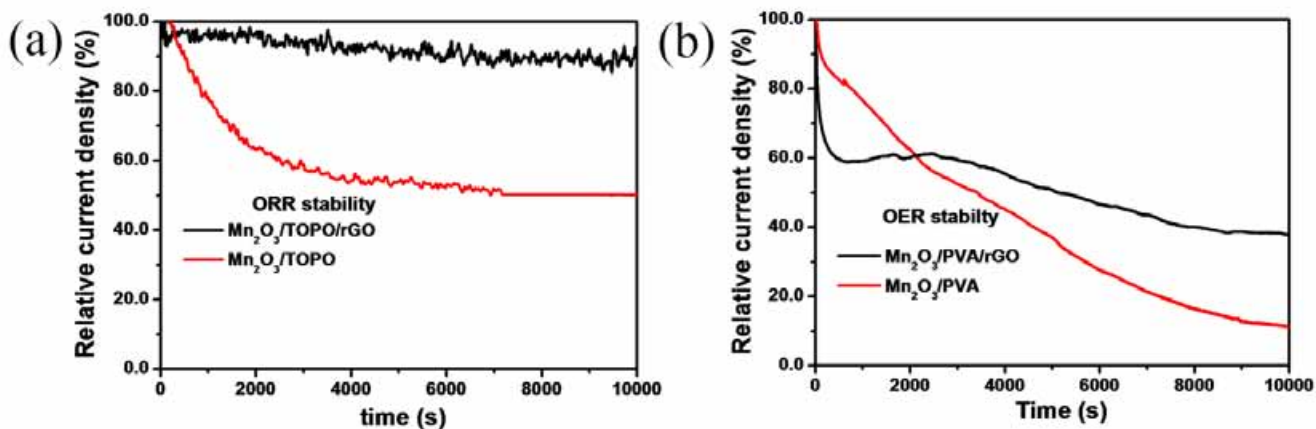
Figure 4.34. *Stability of Mn₂O₃ for oxygen reduction reaction (ORR) and Oxygen evolution reaction (OER). Chronoamperometric curves for the (a) ORR of Mn₂O₃/TOPO (red curve), and Mn₂O₃/TOPO/rGO (black curve) and (b) OER of Mn₂O₃/PVA (red curve), Mn₂O₃/PVA/rGO (black curve), under 0.1M KOH with scan rate 20mVs⁻¹.*

compared with the initial value over 10000 s of continuos operation at a constant potential of - 0.4 V as shown in Figure 4.34a. Similarly, Mn_2O_3/PVA/rGO also shows ~10% but more than ~70% decay observed for Mn_2O_3/PVA suggests rGO play a important role as a support (Figure 4.35a). For OER, Mn_2O_3/PVA/rGO catalysts, initially exhibited a current decay, which could be caused by partially block the active sites of the electrode due to accumulation of gas bubbles. The current density decayed in the first 80 s and attained a steady state thereafter, indicating that these Mn_2O_3 exhibit stable electrocatalytic performance towards OER (Figure 4.34b). In contrast, for Mn_2O_3/PVA, pronounced current decay observed with almost 90% current decay. Hence, graphene supported Mn_2O_3 catalyst exhibits good stability in the alkaline solutions, which is important factor for energy conversion systems. For OER, Mn_2O_3/TOPO/rGO is followed similar trend with slightly better stability that Mn_2O_3/TOPO (Figure 4.35).

Further, GCE was coated with the catalyst ink and in-situ study was performed with N_2 saturated as well as O_2 saturated electrolyte solution with varying applied potential from -200 mV to -800 mV , exactly the region where linear sweep voltammetry for ORR is recorded. It is evident from Figure 4.36a, there is no significant O-H stretching peak range from 3100-3350 cm⁻¹ in N_2 saturated solution. Whereas in O_2 saturated solution, a strong peak for O-H stretch is observed prominently (Figure 4.36b). This O-H stretching peak corresponds to water generated during oxygen reduction reaction on catalyst coated glassy carbon electrode surface [167]. In the
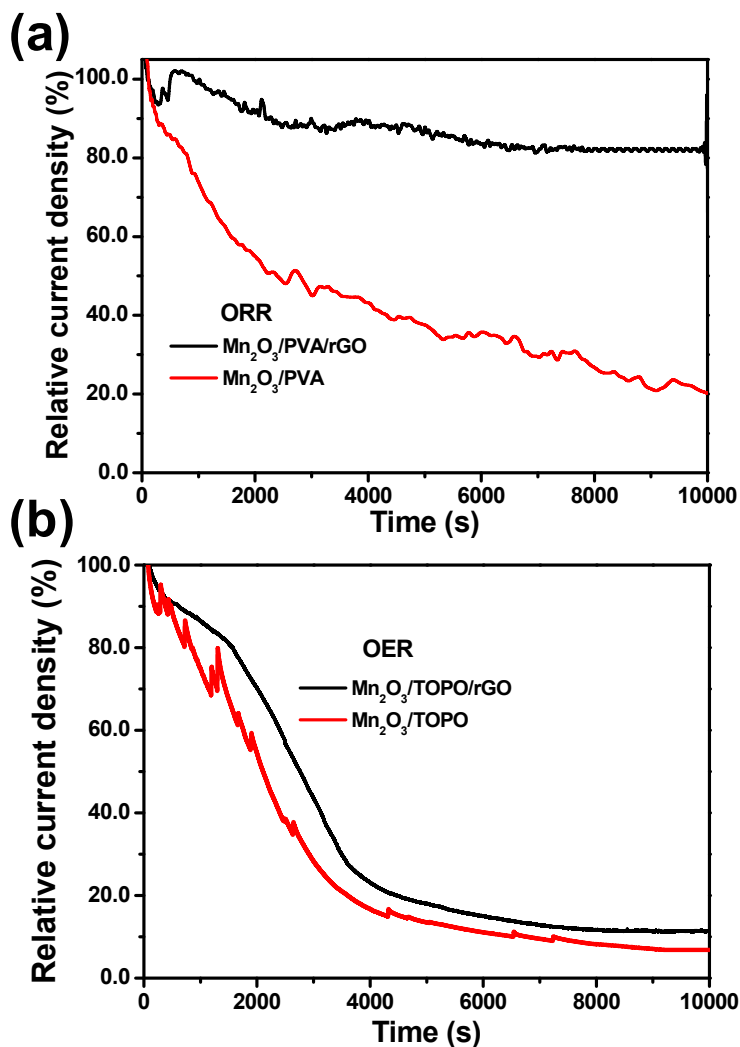
Figure 4.35. *Chronoamperometric curves for the (a) ORR of Mn₂O₃/PVA (red curve), Mn₂O₃/PVA/rGO (black curve), and (b) OER Mn₂O₃/TOPO (red curve), and Mn₂O₃/TOPO/rGO (black curve) under 0.1M KOH with scan rate 20mVs⁻¹.*

Figure 4.36c, a comparative plot is shown which clearly differentiate that there is ORR process occurring in O_2 saturated solution whereas there is no O-H peak in N_2 saturated solution. Furthermore, an enlarged portion of O-H stretching frequency in O_2 is shown in Figure 4.36d. From the Figure 4.36d, it is observed that with increasing negative potential from -200 mV to -800 mV, the O-H absorption peak is getting more intense. This can be explained as, with increasing potential higher amount of water is produced i.e. diffusion of oxygen is higher on electrode surface at -800 mV comparative O_2 diffusion is lower at -200 mV. Linear sweep

voltammetry supports this explanation as with increasing negative potential from -800 mV to -200 mV a higher current density is obtained i.e. diffusion of O_2 is higher.
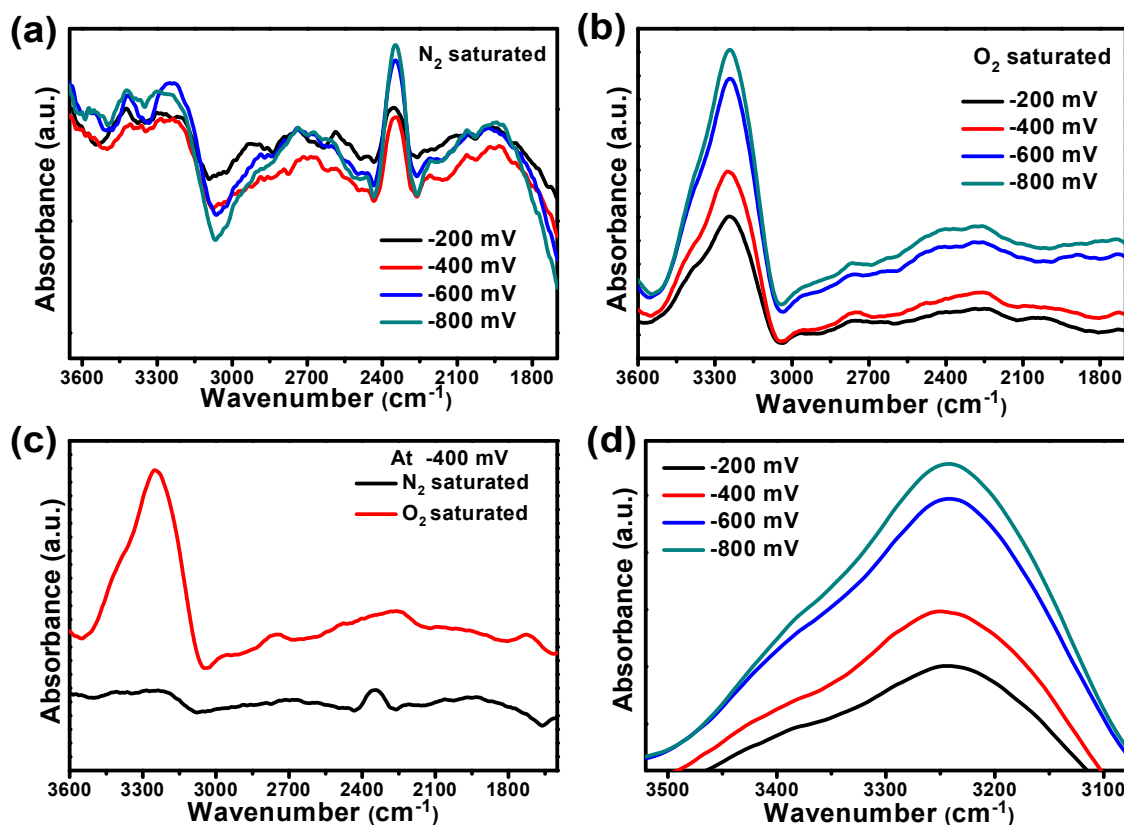
Figure 4.36. *In-situ FTIR spectra for oxygen reduction reaction (ORR) using Mn_2O_3/TOPO/rGO as catalyst (a) in N_2 saturated, (b) in O_2 saturated, (c) comparative study in N_2 and O_2 and (d) enlarged portion of ν_{O-H} stretching frequency.*

4.3. Conclusion:

In summary, we have successfully developed a facile and reproducible method for the high-yield synthesis of assembled Pd nanostructures in hexagonal mesophases by photoreduction. The as-prepared electrocatalysts supported with RGO nanosheets exhibit dramatically enhanced activity and stability for ethanol electrooxidation in alkaline conditions, demonstrating that they can be used as effective electrocatalysts for direct ethanol fuel cells. Hence, the RGO-Nafion support can eventually affect the overall quality of the electro-catalytic activity of the Pd nanostructure with high current density and more negative onset potentials of the faradaic current which is also supported with 4.6 times higher ECSA in comparison with Nafion alone. In light of the important role of nanostructures in catalysis and their facile synthetic process, the as-synthesized

catalysts may also find suitable applications in other fuel cells relevant reactions, such as formic acid oxidation, methanol oxidation and oxygen reduction reaction. The coupling of graphene oxide nanosheets with metal nanostructures leads to superior activity. The use of graphene nanosheets synthesized by a scalable, clean approach without using any chemical reducing agent via a low-cost approach may encourage real-world applications in the field of fuel cells. Moreover, the electrochemical performance of Pd based materials is strongly dependent on individual components and their interactions with each other. Hence, further studies are required to understand the underlying complex interactions between Pd catalyst and graphene based support. Finally, exploration of novel Pd assembled nanostructures supported with graphene oxide nanosheets and nafion can be extended to design other advanced materials for a promising anode catalyst in DEFCs.

Additionally, we have successfully developed a facile and large scale synthesis of thermally stable, crystalline, pure and copper doped Mn_2O_3 NBs by a microwave assisted hydrothermal method. More importantly, low cost of the synthetic method combined with their promising bifunctional catalytic activity makes Mn_2O_3 NBs as a new class of electrocatalysts for the next generation fuel cells. Doped Mn_2O_3 NBs showed a improvement in the charge discharging over the pure Mn_2O_3 NBs may be suitable for high-energy storage devices. The pure and doped Mn_2O_3 NBs can be effectively used as electrode materials with an electrocatalytic activity toward 4 electron oxygen reduction reaction. Copper doping in Mn_2O_3 NBs reveals the enormous impact on the electrocatalytic activity with a high current density both for ORR and OER, which is supported with 5.2 times higher electrochemically active surface area (EASA) in comparison to pure Mn_2O_3. The pure and doped Mn_2O_3 NBs also exhibited stability for both ORR and OER under alkaline condition, demonstrating that they can be used as effective electrocatalysts for alkaline fuel cells. Hence, the microwave assisted approach is suitable for the synthesis of electrochemically active Mn_2O_3 nanostructures that are highly desirable for energy conversion and storage and can also be extended to prepare other transition metal-doped metal oxide for fuel cell applications.

A facile one-pot thermal reduction strategy was employed to fabricate hierarchical flower like manganese oxide and graphene–manganese oxide nanocomposites using PVA, TOPO and graphene oxide as precursors. The manganese oxide and graphene–manganese oxide nanocomposites demonstrated superior and stable electrocatalytic activity with high current

density both for ORR and OER. It is suggested that the good electrochemical performance can be attributed to the 3D assembled hierarchical architecture and the presence of rGO network. In situ FTIR study can monitor the adsorbed reaction intermediate of hydroxyl bands as a function of potential under ORR conditions. This facile and efficient reduction approach via hydrothermal process, cheapness, and availability of raw materials, without the need of template further can be extended to other metal oxides preparation and suitable for industrial manufacturing in scaled-up process. Moreover, the compositions of catalysts can be widely adjusted, which opens up new avenues in the effective application of graphene nanosheet-supported metal oxides as promising electrode materials in near future.

References

[1] A. S. Arico, P. Bruce, B. Scrosati, J.-M. Tarascon, W. van Schalkwijk, Nanostructured Materials for Advanced Energy Conversion and Storage Devices, *Nat. Mater.* 4 (2005) 366-377.

[2] Q. Zhang, E. Uchaker, S. L. Candelaria, G. Cao, Nanomaterials for Energy Conversion and Storage, *Chem. Soc. Rev.* 42 (2013) 3127-3171.

[3] P. Kar, S. Sardar, E. Alarousu, J. Sun, Z. S. Seddigi, S. A. Ahmed, E. Y. Danish, O. F. Mohammed, S. K. Pal, Impact of Metal Ions in Porphyrin-Based Applied Materials for Visible-Light Photocatalysis: Key Information from Ultrafast Electronic Spectroscopy, *Chem. Eur. J.* 20 (2014) 10475-10483.

[4] X. Cheng, Z. Shi, N. Glass, L. Zhang, J. Zhang, D. Song, Z.-S. Liu, H. Wang, J. Shen, A Review of PEM Hydrogen Fuel Cell Contamination: Impacts, Mechanisms, and Mitigation, *J. Power Sources* 165 (2007) 739-756.

[5] E. Christoffersen, P. Liu, A. Ruban, H. L. Skriver, J. K. Nørskov, Anode Materials for Low-Temperature Fuel Cells: A Density Functional Theory Study, *J. Catal.* 199 (2001) 123-131.

[6] C. Bianchini, P. K. Shen, Palladium-Based Electrocatalysts for Alcohol Oxidation in Half Cells and in Direct Alcohol Fuel Cells, *Chem. Rev.* 109 (2009) 4183-4206.

[7] P. S. Roy, J. Bagchi, S. K. Bhattacharya, The Size-Dependent Anode-Catalytic Activity of Nickel-Supported Palladium Nanoparticles for Ethanol Alkaline Fuel Cells, *Catal. Sci. Technol.* 2 (2012) 2302-2310.

[8] N. Tian, Z.-Y. Zhou, N.-F. Yu, L.-Y. Wang, S.-G. Sun, Direct Electrodeposition of Tetrahexahedral Pd Nanocrystals with High-Index Facets and High Catalytic Activity for Ethanol Electrooxidation, *J. Am. Chem. Soc.* 132 (2010) 7580-7581.

[9] X. Huang, Y. Li, Y. Li, H. Zhou, X. Duan, Y. Huang, Synthesis of PtPd Bimetal Nanocrystals with Controllable Shape, Composition, and Their Tunable Catalytic Properties, *Nano Lett.* 12 (2012) 4265-4270.

[10] F. Ksar, L. Ramos, B. Keita, L. Nadjo, P. Beaunier, H. Remita, Bimetallic Palladium−Gold Nanostructures: Application in Ethanol Oxidation, *Chem. Mater.* 21 (2009) 3677-3683.

[11] C. Koenigsmann, A. C. Santulli, E. Sutter, S. S. Wong, Ambient Surfactantless Synthesis, Growth Mechanism, and Size-Dependent Electrocatalytic Behavior of High-Quality, Single Crystalline Palladium Nanowires, *ACS Nano* 5 (2011) 7471-7487.

[12] X. Huang, S. Tang, X. Mu, Y. Dai, G. Chen, Z. Zhou, F. Ruan, Z. Yang, N. Zheng, Freestanding Palladium Nanosheets with Plasmonic and Catalytic Properties, *Nat. Nanotechnol.* 6 (2011) 28-32.

[13] P. S. Roy, S. K. Bhattacharya, Size-Controlled Synthesis and Characterization of Polyvinyl Alcohol-Coated Platinum Nanoparticles: Role of Particle Size and Capping Polymer on the Electrocatalytic Activity, *Catal. Sci. Tech.* 3 (2013) 1314-1323.

[14] H. Zhang, M. Jin, Y. Xiong, B. Lim, Y. Xia, Shape-Controlled Synthesis of Pd Nanocrystals and Their Catalytic Applications, *Acc. Chem. Res.* 46 (2013) 1783-1794.

[15] F. Ksar, G. Surendran, L. Ramos, B. Keita, L. Nadjo, E. Prouzet, P. Beaunier, A. Hagège, F. Audonnet, H. Remita, Palladium Nanowires Synthesized in Hexagonal Mesophases: Application in Ethanol Electrooxidation, *Chem. Mater.* 21 (2009) 1612-1617.

[16] G. Surendran, F. Ksar, L. Ramos, B. Keita, L. Nadjo, E. Prouzet, P. Beaunier, P. Dieudonné, F. Audonnet, H. Remita, Palladium Nanoballs Synthesized in Hexagonal Mesophases, *J. Phys. Chem. C* 112 (2008) 10740-10744.

[17] L.-F. Zhang, S.-L. Zhong, A.-W. Xu, Highly Branched Concave Au/Pd Bimetallic Nanocrystals with Superior Electrocatalytic Activity and Highly Efficient SERS Enhancement, *Angew. Chem. Int. Ed.* 52 (2013) 645-649.

[18] S. Guo, S. Dong, E. Wang, Pt/Pd Bimetallic Nanotubes with Petal-Like Surfaces for Enhanced Catalytic Activity and Stability towards Ethanol Electrooxidation, *Energy Environ. Sci.* 3 (2010) 1307-1310.

[19] P. K. Shen, C. Xu, Alcohol Oxidation on Nanocrystalline Oxide Pd/C Promoted Electrocatalysts, *Electrochem. Commun.* 8 (2006) 184-188.

[20] T. Hegmann, H. Qi, V. M. Marx, Nanoparticles in Liquid Crystals: Synthesis, Self-Assembly, Defect Formation and Potential Applications, *J. Inorg. Organomet. Polym. Mater.* 17 (2007) 483-508.

[21] G. Surendran, G. Apostolescu, M. Tokumoto, E. Prouzet, L. Ramos, P. Beaunier, P. J. Kooyman, A. Etcheberry, H. Remita, From Self-Assembly of Platinum Nanoparticles to Nanostructured Materials, *Small* 1 (2005) 964-967.

[22] K. Kanie, T. Sugimoto, Organic−Inorganic Hybrid Liquid Crystals: Hybridization of Calamitic Liquid-Crystalline Amines with Monodispersed Anisotropic TiO$_2$ Nanoparticles, *J. Am. Chem. Soc.* 125 (2003) 10518-10519.

[23] S. Kubo, R. Taguchi, S. Hadano, M. Narita, O. Watanabe, T. Iyoda, M. Nakagawa, Surface-Assisted Unidirectional Orientation of ZnO Nanorods Hybridized with Nematic Liquid Crystals, *ACS Appl. Mater. Interfaces* 6 (2014) 811-818.

[24] J. Mirzaei, M. Urbanski, H.-S. Kitzerow, T. Hegmann, Synthesis of Liquid Crystal Silane-Functionalized Gold Nanoparticles and Their Effects on the Optical and Electro-Optic Properties of a Structurally Related Nematic Liquid Crystal, *ChemPhysChem* 15 (2014) 1381-1394.

[25] V. J. Anderson, E. M. Terentjev, S. P. Meeker, J. Crain, W. C. K. Poon, Cellular Solid Behaviour of Liquid Crystal Colloids 1. Phase Separation and Morphology, *Eur. Phys. J. E* 4 (2001) 11-20.

[26] P. G. Petrov, E. M. Terentjev, Formation of Cellular Solid in Liquid Crystal Colloids, *Langmuir* 17 (2001) 2942-2949.

[27] S. P. Meeker, W. C. K. Poon, J. Crain, E. M. Terentjev, Colloid–Liquid-Crystal Composites: An Unusual Soft Solid, *Phys. Rev. E* 61 (2000) R6083-R6086.

[28] G. S. Attard, P. N. Bartlett, N. R. B. Coleman, J. M. Elliott, J. R. Owen, J. H. Wang, Mesoporous Platinum Films from Lyotropic Liquid Crystalline Phases, *Science* 278 (1997) 838-840.

[29] G. S. Attard, J. M. Corker, C. G. Göltner, S. Henke, R. H. Templer, Liquid-Crystal Templates for Nanostructured Metals, *Angew. Chem. Int. Ed.* 36 (1997) 1315-1317.

[30] A. Lehoux, L. Ramos, P. Beaunier, D. B. Uribe, P. Dieudonné, F. Audonnet, A. Etcheberry, M. José-Yacaman, H. Remita, Tuning the Porosity of Bimetallic Nanostructures by a Soft Templating Approach, *Adv. Funct. Mater.* 22 (2012) 4900-4908.

[31] E. Pena dos Santos, M. S. Tokumoto, G. Surendran, H. Remita, C. Bourgaux, P. Dieudonné, E. Prouzet, L. Ramos, Existence and Stability of New Nanoreactors: Highly Swollen Hexagonal Liquid Crystals, *Langmuir* 21 (2005) 4362-4369.

[32] G. Surendran, M. S. Tokumoto, E. Pena dos Santos, H. Remita, L. Ramos, P. J. Kooyman, C. V. Santilli, C. Bourgaux, P. Dieudonné, E. Prouzet, Highly Swollen Liquid

Crystals as New Reactors for the Synthesis of Nanomaterials, *Chem. Mater.* 17 (2005) 1505-1514.

[33] T. Redjala, G. Apostolecu, P. Beaunier, M. Mostafavi, A. Etcheberry, D. Uzio, C. Thomazeau, H. Remita, Palladium Nanostructures Synthesized by Radiolysis or by Photoreduction, *New J. Chem.* 32 (2008) 1403-1408.

[34] P. F. Siril, L. Ramos, P. Beaunier, P. Archirel, A. Etcheberry, H. Remita, Synthesis of Ultrathin Hexagonal Palladium Nanosheets, *Chem. Mater.* 21 (2009) 5170-5175.

[35] S. Ghosh, N. A. Kouamé, L. Ramos, S. Remita, A. Dazzi, A. Deniset-Besseau, P. Beaunier, F. Goubard, P.-H. Aubert, H. Remita, Conducting Polymer Nanostructures for Photocatalysis under Visible Light, *Nat. Mater.* 14 (2015) 505-511.

[36] S. Ghosh, H. Remita, L. Ramos, A. Dazzi, A. Deniset-Besseau, P. Beaunier, F. Goubard, P.-H. Aubert, F. Brisset, S. Remita, PEDOT Nanostructures Synthesized in Hexagonal Mesophases, *New J. Chem.* 38 (2014) 1106-1115.

[37] N. Mackiewicz, G. Surendran, H. Remita, B. Keita, G. Zhang, L. Nadjo, A. Hagège, E. Doris, C. Mioskowski, Supramolecular Self-Assembly of Amphiphiles on Carbon Nanotubes: A Versatile Strategy for the Construction of CNT/Metal Nanohybrids, Application to Electrocatalysis, *J. Am. Chem. Soc.* 130 (2008) 8110-8111.

[38] R. Krishna, E. Titus, O. Okhay, J. C. Gil, J. Ventura, E. V. Ramana, J. J. Gracio, Rapid Electrochemical Synthesis of Hydrogenated Graphene Oxide using Ni Nanoparticles, *Int. J. Electrochem. Sci.* 9 (2014) 4054-4069.

[39] H. T. Zheng, Y. Li, S. Chen, P. K. Shen, Effect of Support on the Activity of Pd Electrocatalyst for Ethanol Oxidation, *J. Power Sources* 163 (2006) 371-375.

[40] P. Kanninen, M. Borghei, V. Ruiz, E. I. Kauppinen, T. Kallio, The Effect of Nafion Content in a Graphitized Carbon Nanofiber-Based Anode for the Direct Methanol Fuel Cell, *Int. J. Hydrogen Energy* 37 (2012) 19082-19091.

[41] M. A. Newton, C. Belver-Coldeira, A. Martinez-Arias, M. Fernandez-Garcia, Dynamic In Situ Observation of Rapid Size and Shape Change of Supported Pd Nanoparticles During CO/NO Cycling, *Nat. Mater.* 6 (2007) 528-532.

[42] H. L. Xin, J. A. Mundy, Z. Liu, R. Cabezas, R. Hovden, L. F. Kourkoutis, J. Zhang, N. P. Subramanian, R. Makharia, F. T. Wagner, D. A. Muller, Atomic-Resolution

Spectroscopic Imaging of Ensembles of Nanocatalyst Particles Across the Life of a Fuel Cell, *Nano Lett.* 12 (2012) 490-497.

[43] S. Ghosh, A.-L. Teillout, D. Floresyona, P. de Oliveira, A. Hagège, H. Remita, Conducting Polymer-Supported Palladium Nanoplates for Applications in Direct Alcohol Oxidation, *Int. J. Hydrogen Energy* 40 (2015) 4951-4959.

[44] P. Mukherjee, P. S. Roy, K. Mandal, D. Bhattacharjee, S. Dasgupta, S. K. Bhattacharya, Improved Catalysis of Room Temperature Synthesized Pd-Cu Alloy Nanoparticles for Anodic Oxidation of Ethanol in Alkaline Media, *Electrochim. Acta* 154 (2015) 447-455.

[45] Y. Zhao, L. Zhan, J. Tian, S. Nie, Z. Ning, Enhanced Electrocatalytic Oxidation of Methanol on Pd/Polypyrrole–Graphene in Alkaline Medium, *Electrochim. Acta* 56 (2011) 1967-1972.

[46] E. Antolini, Graphene as a New Carbon Support for Low-Temperature Fuel Cell Catalysts, *Appl. Catal. B* 123–124 (2012) 52-68.

[47] Y. Li, H. Wang, L. Xie, Y. Liang, G. Hong, H. Dai, MoS_2 Nanoparticles Grown on Graphene: An Advanced Catalyst for the Hydrogen Evolution Reaction, *J. Am. Chem. Soc.* 133 (2011) 7296-7299.

[48] Y. Liang, Y. Li, H. Wang, J. Zhou, J. Wang, T. Regier, H. Dai, Co_3O_4 Nanocrystals on Graphene as a Synergistic Catalyst for Oxygen Reduction Reaction, *Nat. Mater.* 10 (2011) 780-786.

[49] E. Yoo, T. Okata, T. Akita, M. Kohyama, J. Nakamura, I. Honma, Enhanced Electrocatalytic Activity of Pt Subnanoclusters on Graphene Nanosheet Surface, *Nano Lett.* 9 (2009) 2255-2259.

[50] C. Huang, C. Li, G. Shi, Graphene Based Catalysts, *Energy Environ. Sci.* 5 (2012) 8848-8868.

[51] S. Stankovich, D. A. Dikin, G. H. B. Dommett, K. M. Kohlhaas, E. J. Zimney, E. A. Stach, R. D. Piner, S. T. Nguyen, R. S. Ruoff, Graphene-Based Composite Materials, *Nature* 442 (2006) 282-286.

[52] F. Wang, Z. a. Tan, Y. Li, Solution-Processable Metal Oxides/Chelates as Electrode Buffer Layers for Efficient and Stable Polymer Solar Cells, *Energy Environ. Sci.* 8 (2015) 1059-1091.

[53] Z. Zhang, J. Liu, J. Gu, L. Su, L. Cheng, An Overview of Metal Oxide Materials as Electrocatalysts and Supports for Polymer Electrolyte Fuel Cells, *Energy Environ. Sci.* 7 (2014) 2535-2558.

[54] S. Sardar, P. Kar, S. Sarkar, P. Lemmens, S. K. Pal, Interfacial Carrier Dynamics in PbS-ZnO Light Harvesting Assemblies and their Potential Implication in Photovoltaic/Photocatalysis Application, *Sol. Energ. Mat. Sol. Cells* 134 (2015) 400-406.

[55] P. Kar, S. Sardar, S. Ghosh, M. R. Parida, B. Liu, O. F. Mohammed, P. Lemmens, S. K. Pal, Nano Surface Engineering of Mn_2O_3 for Potential Light-Harvesting Application, *J. Mater. Chem. C* 3 (2015) 8200-8211.

[56] T. T. Truong, Y. Liu, Y. Ren, L. Trahey, Y. Sun, Morphological and Crystalline Evolution of Nanostructured MnO_2 and Its Application in Lithium–Air Batteries, *ACS Nano* 6 (2012) 8067-8077.

[57] G. Shen, P.-C. Chen, K. Ryu, C. Zhou, Devices and Chemical Sensing Applications of Metal Oxide Nanowires, *J. Mater. Chem.* 19 (2009) 828-839.

[58] P. R. Solanki, A. Kaushik, V. V. Agrawal, B. D. Malhotra, Nanostructured Metal Oxide-Based Biosensors, *NPG Asia Mater.* 3 (2011) 17-24.

[59] P. Zhang, Y. Zhan, B. Cai, C. Hao, J. Wang, C. Liu, Z. Meng, Z. Yin, Q. Chen, Shape-Controlled Synthesis of Mn_3O_4 Nanocrystals and Their Catalysis of the Degradation of Methylene Blue, *Nano Res.* 3 (2010) 235-243.

[60] A. Giri, N. Goswami, M. Pal, M. T. Zar Myint, S. Al-Harthi, A. Singha, B. Ghosh, J. Dutta, S. K. Pal, Rational Surface Modification of Mn_3O_4 Nanoparticles to Induce Multiple Photoluminescence and Room Temperature Ferromagnetism, *J. Mater. Chem. C* 1 (2013) 1885-1895.

[61] A. Giri, A. Makhal, B. Ghosh, A. K. Raychaudhuri, S. K. Pal, Functionalization of Manganite Nanoparticles and Their Interaction with Biologically Relevant Small Ligands: Picosecond Time-Resolved FRET Studies, *Nanoscale* 2 (2010) 2704-2709.

[62] P. Li, C. Nan, Z. Wei, J. Lu, Q. Peng, Y. Li, Mn_3O_4 Nanocrystals: Facile Synthesis, Controlled Assembly, and Application, *Chem. Mater.* 22 (2010) 4232-4236.

[63] G. Salazar-Alvarez, J. Sort, S. Suriñach, M. D. Baró, J. Nogués, Synthesis and Size-Dependent Exchange Bias in Inverted Core−Shell $MnO|Mn_3O_4$ Nanoparticles, *J. Am. Chem. Soc.* 129 (2007) 9102-9108.

[64] G. Yang, W. Yan, J. Wang, H. Yang, Fabrication and Formation Mechanism of Mn_2O_3 Hollow Nanofibers by Single-Spinneret Electrospinning, *CrystEngComm* 16 (2014) 6907-6913.

[65] S. Ghosh, H. Remita, P. Kar, S. Choudhury, S. Sardar, P. Beaunier, P. S. Roy, S. K. Bhattacharya, S. K. Pal, Facile Synthesis of Pd Nanostructures in Hexagonal Mesophases as a Promising Electrocatalyst for Ethanol Oxidation, *J. Mater. Chem. A* 3 (2015) 9517-9527.

[66] Y.-J. Zhu, F. Chen, Microwave-Assisted Preparation of Inorganic Nanostructures in Liquid Phase, *Chem. Rev.* 114 (2014) 6462-6555.

[67] M. B. Gawande, S. N. Shelke, R. Zboril, R. S. Varma, Microwave-Assisted Chemistry: Synthetic Applications for Rapid Assembly of Nanomaterials and Organics, *Acc. Chem. Res.* 47 (2014) 1338-1348.

[68] H. Huang, S. Sithambaram, C.-H. Chen, C. King'ondu Kithongo, L. Xu, A. Iyer, H. F. Garces, S. L. Suib, Microwave-Assisted Hydrothermal Synthesis of Cryptomelane-Type Octahedral Molecular Sieves (OMS-2) and Their Catalytic Studies, *Chem. Mater.* 22 (2010) 3664-3669.

[69] K. Manseki, Y. Kondo, T. Ban, T. Sugiura, T. Yoshida, Size-Controlled Synthesis of Anisotropic TiO_2 Single Nanocrystals using Microwave Irradiation and their Application for Dye-Sensitized Solar Cells, *Dalton Trans.* 42 (2013) 3295-3299.

[70] S. Sardar, P. Kar, S. K. Pal, The Impact of Central Metal Ions in Porphyrin Functionalized ZnO/TiO_2 for Enhanced Solar Energy Conversion, *J. Mat. NanoSci.* 1 (2014) 19.

[71] Y. Li, J. Wang, Y. Zhang, M. N. Banis, J. Liu, D. Geng, R. Li, X. Sun, Facile Controlled Synthesis and Growth Mechanisms of Flower-Like and Tubular MnO_2 Nanostructures by Microwave-Assisted Hydrothermal Method, *J. Colloid Interface Sci.* 369 (2012) 123-128.

[72] B. Ming, J. Li, F. Kang, G. Pang, Y. Zhang, L. Chen, J. Xu, X. Wang, Microwave–Hydrothermal Synthesis of Birnessite-type MnO_2 Nanospheres as Supercapacitor Electrode Materials, *J. Power Sources* 198 (2012) 428-431.

[73] S. Chu, A. Majumdar, Opportunities and Challenges for a Sustainable Energy Future, *Nature* 488 (2012) 294-303.

[74] H. A. Gasteiger, N. M. Markovic, Just a Dream-or Future Reality?, *Science* 324 (2009) 48-49.

[75] Y. Jiao, Y. Zheng, M. Jaroniec, S. Z. Qiao, Design of Electrocatalysts for Oxygen- and Hydrogen-Involving Energy Conversion Reactions, *Chem. Soc. Rev.* 44 (2015) 2060-2086.

[76] S. Ghosh, A.-L. Teillout, D. Floresyona, P. de Oliveira, A. Hagège, H. Remita, Conducting polymer-supported palladium nanoplates for applications in direct alcohol oxidation, *Int. J. Hydrogen Energy* 40 (2015) 4951-4959.

[77] J. Zhang, Z. Zhao, Z. Xia, L. Dai, A Metal-Free Bifunctional Electrocatalyst for Oxygen Reduction and Oxygen Evolution Reactions, *Nat. Nanotechnol.* 10 (2015) 444-452.

[78] N. Jung, D. Y. Chung, J. Ryu, S. J. Yoo, Y.-E. Sung, Pt-Based Nanoarchitecture and Catalyst Design for Fuel Cell Applications, *Nano Today* 9 (2014) 433-456.

[79] K. A. Stoerzinger, L. Qiao, M. D. Biegalski, Y. Shao-Horn, Orientation-Dependent Oxygen Evolution Activities of Rutile IrO_2 and RuO_2, *J. Phys. Chem. Lett.* 5 (2014) 1636-1641.

[80] E. A. Paoli, F. Masini, R. Frydendal, D. Deiana, C. Schlaup, M. Malizia, T. W. Hansen, S. Horch, I. E. L. Stephens, I. Chorkendorff, Oxygen Evolution on Well-Characterized Mass-Selected Ru and RuO_2 Nanoparticles, *Chem. Sci.* 6 (2015) 190-196.

[81] Y. Li, W. Zhou, H. Wang, L. Xie, Y. Liang, F. Wei, J.-C. Idrobo, S. J. Pennycook, H. Dai, An Oxygen Reduction Electrocatalyst Based on Carbon Nanotube-Graphene Complexes, *Nat. Nanotechnol.* 7 (2012) 394-400.

[82] X. Deng, H. Tüysüz, Cobalt-Oxide-Based Materials as Water Oxidation Catalyst: Recent Progress and Challenges, *ACS Catal.* 4 (2014) 3701-3714.

[83] E. M. Benbow, S. P. Kelly, L. Zhao, J. W. Reutenauer, S. L. Suib, Oxygen Reduction Properties of Bifunctional α-Manganese Oxide Electrocatalysts in Aqueous and Organic Electrolytes, *J. Phys. Chem. C* 115 (2011) 22009-22017.

[84] Y. Gorlin, T. F. Jaramillo, A Bifunctional Nonprecious Metal Catalyst for Oxygen Reduction and Water Oxidation, *J. Am. Chem. Soc.* 132 (2010) 13612-13614.

[85] Y. Gorlin, B. Lassalle-Kaiser, J. D. Benck, S. Gul, S. M. Webb, V. K. Yachandra, J. Yano, T. F. Jaramillo, In Situ X-ray Absorption Spectroscopy Investigation of a

Bifunctional Manganese Oxide Catalyst with High Activity for Electrochemical Water Oxidation and Oxygen Reduction, *J. Am. Chem. Soc.* 135 (2013) 8525-8534.

[86] Y. Meng, W. Song, H. Huang, Z. Ren, S.-Y. Chen, S. L. Suib, Structure–Property Relationship of Bifunctional MnO_2 Nanostructures: Highly Efficient, Ultra-Stable Electrochemical Water Oxidation and Oxygen Reduction Reaction Catalysts Identified in Alkaline Media, *J. Am. Chem. Soc.* 136 (2014) 11452-11464.

[87] T. Maiyalagan, K. A. Jarvis, S. Therese, P. J. Ferreira, A. Manthiram, Spinel-Type Lithium Cobalt Oxide as a Bifunctional Electrocatalyst for the Oxygen Evolution and Oxygen Reduction Reactions, *Nat. Commun.* 5 (2014) 3949.

[88] P. W. Menezes, A. Indra, N. R. Sahraie, A. Bergmann, P. Strasser, M. Driess, Cobalt–Manganese-Based Spinels as Multifunctional Materials that Unify Catalytic Water Oxidation and Oxygen Reduction Reactions, *ChemSusChem* 8 (2015) 164-171.

[89] A. Zhao, J. Masa, W. Xia, A. Maljusch, M.-G. Willinger, G. Clavel, K. Xie, R. Schlögl, W. Schuhmann, M. Muhler, Spinel Mn–Co Oxide in N-Doped Carbon Nanotubes as a Bifunctional Electrocatalyst Synthesized by Oxidative Cutting, *J. Am. Chem. Soc.* 136 (2014) 7551-7554.

[90] M. Z. Jacobson, W. G. Colella, D. M. Golden, Cleaning the Air and Improving Health with Hydrogen Fuel-Cell Vehicles, *Science* 308 (2005) 1901-1905.

[91] B. C. H. Steele, A. Heinzel, Materials for Fuel-Cell Technologies, *Nature* 414 (2001) 345-352.

[92] M. K. Debe, Electrocatalyst Approaches and Challenges for Automotive Fuel Cells, *Nature* 486 (2012) 43-51.

[93] K. Zhang, X. Han, Z. Hu, X. Zhang, Z. Tao, J. Chen, Nanostructured Mn-Based Oxides for Electrochemical Energy Storage and Conversion, *Chem. Soc. Rev.* 44 (2015) 699-728.

[94] A. Verma, A. K. Jha, S. Basu, Manganese Dioxide as a Cathode Catalyst for a Direct Alcohol or Sodium Borohydride Fuel Cell with a Flowing Alkaline Electrolyte, *J. Power Sources* 141 (2005) 30-34.

[95] Z. Cai, L. Xu, M. Yan, C. Han, L. He, K. M. Hercule, C. Niu, Z. Yuan, W. Xu, L. Qu, K. Zhao, L. Mai, Manganese Oxide/Carbon Yolk–Shell Nanorod Anodes for High Capacity Lithium Batteries, *Nano Lett.* 15 (2015) 738-744.

[96] J. Cao, Y. Zhu, K. Bao, L. Shi, S. Liu, Y. Qian, Microscale Mn_2O_3 Hollow Structures: Sphere, Cube, Ellipsoid, Dumbbell, and Their Phenol Adsorption Properties, *J. Phys. Chem. C* 113 (2009) 17755-17760.

[97] H. Rahaman, R. M. Laha, D. K. Maiti, S. K. Ghosh, Fabrication of Mn_2O_3 Nanorods: An Efficient Catalyst for Selective Transformation of Alcohols to Aldehydes, *RSC Adv.* 5 (2015) 33923-33929.

[98] Y. Zhang, Y. Yan, X. Wang, G. Li, D. Deng, L. Jiang, C. Shu, C. Wang, Facile Synthesis of Porous Mn_2O_3 Nanoplates and Their Electrochemical Behavior as Anode Materials for Lithium Ion Batteries, *Chem. Eur. J.* 20 (2014) 6126-6130.

[99] Q. Li, L. Yin, Z. Li, X. Wang, Y. Qi, J. Ma, Copper Doped Hollow Structured Manganese Oxide Mesocrystals with Controlled Phase Structure and Morphology as Anode Materials for Lithium Ion Battery with Improved Electrochemical Performance, *ACS Appl. Mater. Interfaces* 5 (2013) 10975-10984.

[100] A. S. Poyraz, C.-H. Kuo, S. Biswas, C. K. King'ondu, S. L. Suib, A General Approach to Crystalline and Monomodal Pore Size Mesoporous Materials, *Nat. Commun.* 4 (2013) 2952.

[101] J. Cheng, R. Che, C. Liang, J. Liu, M. Wang, J. Xu, Hierarchical Hollow $Li_4Ti_5O_{12}$ Urchin-Like Microspheres with Ultra-High Specific Surface Area for High Rate Lithium Ion Batteries, *Nano Res.* 7 (2014) 1043-1053.

[102] J. Kao, K. Thorkelsson, P. Bai, B. J. Rancatore, T. Xu, Toward Functional Nanocomposites: Taking the Best of Nanoparticles, Polymers, and Small Molecules, *Chem. Soc. Rev.* 42 (2013) 2654-2678.

[103] L. Zhang, H. B. Wu, S. Madhavi, H. H. Hng, X. W. Lou, Formation of Fe_2O_3 Microboxes with Hierarchical Shell Structures from Metal–Organic Frameworks and Their Lithium Storage Properties, *J. Am. Chem. Soc.* 134 (2012) 17388-17391.

[104] J. Duan, S. Chen, S. Dai, S. Z. Qiao, Shape Control of Mn_3O_4 Nanoparticles on Nitrogen-Doped Graphene for Enhanced Oxygen Reduction Activity, *Adv. Funct. Mater.* 24 (2014) 2072-2078.

[105] Y. Cheng, Y. Fan, Y. Pei, M. Qiao, Graphene-Supported Metal/Metal Oxide Nanohybrids: Synthesis and Applications in Heterogeneous Catalysis, *Catal. Sci. Technol.* 5 (2015) 3903-3916.

[106] K. Mette, A. Bergmann, J.-P. Tessonnier, M. Hävecker, L. Yao, T. Ressler, R. Schlögl, P. Strasser, M. Behrens, Nanostructured Manganese Oxide Supported on Carbon Nanotubes for Electrocatalytic Water Splitting, *ChemCatChem* 4 (2012) 851-862.

[107] A. L. M. Reddy, M. M. Shaijumon, S. R. Gowda, P. M. Ajayan, Coaxial MnO_2/Carbon Nanotube Array Electrodes for High-Performance Lithium Batteries, *Nano Lett.* 9 (2009) 1002-1006.

[108] O. S. Kwon, T. Kim, J. S. Lee, S. J. Park, H.-W. Park, M. Kang, J. E. Lee, J. Jang, H. Yoon, Fabrication of Graphene Sheets Intercalated with Manganese Oxide/Carbon Nanofibers: Toward High-Capacity Energy Storage, *Small* 9 (2013) 248-254.

[109] D. Yu, K. Goh, H. Wang, L. Wei, W. Jiang, Q. Zhang, L. Dai, Y. Chen, Scalable Synthesis of Hierarchically Structured Carbon Nanotube-Graphene Fibres for Capacitive Energy Storage, *Nat. Nanotechnol.* 9 (2014) 555-562.

[110] M. F. El-Kady, V. Strong, S. Dubin, R. B. Kaner, Laser Scribing of High-Performance and Flexible Graphene-Based Electrochemical Capacitors, *Science* 335 (2012) 1326-1330.

[111] B. Xia, Y. Yan, X. Wang, X. W. Lou, Recent Progress on Graphene-Based Hybrid Electrocatalysts, *Mater. Horiz.* 1 (2014) 379-399.

[112] L. Wang, F. Yin, C. Yao, N-Doped Graphene as a Bifunctional Electrocatalyst for Oxygen Reduction and Oxygen Evolution Reactions in an Alkaline Electrolyte, *Int. J. Hydrogen Energy* 39 (2014) 15913-15919.

[113] S. Ghosh, P. Kar, N. Bhandary, S. Basu, S. Sardar, T. Maiyalagan, D. Majumdar, S. K. Bhattacharya, A. Bhaumik, P. Lemmens, S. K. Pal, Microwave-Assisted Synthesis of Porous Mn_2O_3 Nanoballs as Bifunctional Electrocatalyst for Oxygen Reduction and Evolution Reaction, *Catal. Sci. Technol.* 6 (2016) 1417-1429.

[114] M. Prabu, P. Ramakrishnan, P. Ganesan, A. Manthiram, S. Shanmugam, $LaTi_{0.65}Fe_{0.35}O_3-\delta$ Nanoparticle-Decorated Nitrogen-Doped Carbon Nanorods as an Advanced Hierarchical Air Electrode for Rechargeable Metal-Air Batteries, *Nano Energy* 15 (2015) 92-103.

[115] P. Ganesan, M. Prabu, J. Sanetuntikul, S. Shanmugam, Cobalt Sulfide Nanoparticles Grown on Nitrogen and Sulfur Codoped Graphene Oxide: An Efficient Electrocatalyst for Oxygen Reduction and Evolution Reactions, *ACS Catal.* 5 (2015) 3625-3637.

[116] T. Lee, E. K. Jeon, B.-S. Kim, Mussel-Inspired Nitrogen-Doped Graphene Nanosheet Supported Manganese Oxide Nanowires as Highly Efficient Electrocatalysts for Oxygen Reduction Reaction, *J. Mater. Chem. A* 2 (2014) 6167-6173.

[117] K. Kumar, C. Canaff, J. Rousseau, S. Arrii-Clacens, T. W. Napporn, A. Habrioux, K. B. Kokoh, Effect of the Oxide–Carbon Heterointerface on the Activity of Co_3O_4/NRGO Nanocomposites toward ORR and OER, *J. Phys. Chem. C* 120 (2016) 7949-7958.

[118] M. Prabu, P. Ramakrishnan, S. Shanmugam, $CoMn_2O_4$ Nanoparticles Anchored on Nitrogen-Doped Graphene Nanosheets as Bifunctional Electrocatalyst for Rechargeable Zinc–Air Battery, *Electrochem. Commun.* 41 (2014) 59-63.

[119] W. Bian, Z. Yang, P. Strasser, R. Yang, A $CoFe_2O_4$/Graphene Nanohybrid as an Efficient Bi-Functional Electrocatalyst for Oxygen Reduction and Oxygen Evolution, *J. Power Sources* 250 (2014) 196-203.

[120] Y. Liu, J. Li, W. Li, Y. Li, Q. Chen, Y. Liu, Spinel $LiMn_2O_4$ Nanoparticles Dispersed on Nitrogen-Doped Reduced Graphene Oxide Nanosheets as an Efficient Electrocatalyst for Aluminium-Air Battery, *Int. J. Hydrogen Energy* 40 (2015) 9225-9234.

[121] M. Zhao, X. Li, L. Song, D. He, Z. Zhang, Substrate-Assisted Deposition of Metal Oxides on Three-Dimensional Porous Reduced Graphene Oxide Networks as Bifunctional Hybrid Electrocatalysts for the Oxygen Evolution and Oxygen Reduction Reactions, *ChemCatChem* 8 (2016) 2808-2816.

[122] H. Lu, J. Yan, Y. Zhang, Y. Huang, W. Gao, W. Fan, T. Liu, In Situ Growth of Co_3O_4 Nanoparticles on Interconnected Nitrogen-Doped Graphene Nanoribbons as Efficient Oxygen Reduction Reaction Catalyst, *ChemNanoMat* 2 (2016) 972-979.

[123] W.-Y. Xia, N. Li, Q.-Y. Li, K.-H. Ye, C.-W. Xu, Au-$NiCo_2O_4$ Supported on Three-Dimensional Hierarchical Porous Graphene-like Material for Highly Effective Oxygen Evolution Reaction, *Sci. Rep.* 6 (2016) 23398.

[124] R. Kannan, A. R. Kim, J. S. Kim, D. J. Yoo, 3D Graphene-Mixed Metal Oxide-Supported Carbonpalladium Quantum Dot Nanoarchitectures – A Facile Bifunctional Electrocatalyst for Direct Ethylene Glycol Fuel Cells and Oxygen Evolution Reactions, *Int. J. Hydrogen Energy* 41 (2016) 18033-18043.

[125] C. Wen, X. Gao, T. Huang, X. Wu, L. Xu, J. Yu, H. Zhang, Z. Zhang, J. Han, H. Ren, Reduced Graphene Oxide Supported Chromium Oxide Hybrid as High Efficient Catalyst for Oxygen Reduction Reaction, *Int. J. Hydrogen Energy* 41 (2016) 11099-11107.

[126] W. T. Hong, M. Risch, K. A. Stoerzinger, A. Grimaud, J. Suntivich, Y. Shao-Horn, Toward the Rational Design of Non-Precious Transition Metal Oxides for Oxygen Electrocatalysis, *Energy Environ. Sci.* 8 (2015) 1404-1427.

[127] J.-S. Lee, T. Lee, H.-K. Song, J. Cho, B.-S. Kim, Ionic Liquid Modified Graphene Nanosheets Anchoring Manganese Oxide Nanoparticles as Efficient Electrocatalysts for Zn-Air Batteries, *Energy Environ. Sci.* 4 (2011) 4148-4154.

[128] J. Duan, Y. Zheng, S. Chen, Y. Tang, M. Jaroniec, S. Qiao, Mesoporous Hybrid Material Composed of Mn_3O_4 Nanoparticles on Nitrogen-Doped Graphene for Highly Efficient Oxygen Reduction Reaction, *Chem. Commun.* 49 (2013) 7705-7707.

[129] M. Manfait, A. J. P. Alix, C. Kappenstein, Raman and Infrared Studies of the Square Planar Tetraammine Gold(III) Nitrate and its Deuterate, *Inorg. Chim. Acta* 50 (1981) 147-152.

[130] K. H. S. Kung, K. F. Hayes, Fourier Transform Infrared Spectroscopic Study of the Adsorption of Cetyltrimethylammonium Bromide and Cetylpyridinium Chloride on Silica, *Langmuir* 9 (1993) 263-267.

[131] K. R. Gopidas, J. K. Whitesell, M. A. Fox, Synthesis, Characterization, and Catalytic Applications of a Palladium-Nanoparticle-Cored Dendrimer, *Nano Lett.* 3 (2003) 1757-1760.

[132] M. N. Nadagouda, R. S. Varma, Green Synthesis of Silver and Palladium Nanoparticles at Room Temperature using Coffee and Tea Extract, *Green Chem.* 10 (2008) 859-862.

[133] G. Wang, J. Yang, J. Park, X. Gou, B. Wang, H. Liu, J. Yao, Facile Synthesis and Characterization of Graphene Nanosheets, *J. Phys. Chem. C* 112 (2008) 8192-8195.

[134] F. Dehouche, P. Archirel, H. Remita, N. Brodie-Linder, A. Traverse, Alcohol to Water Catalyzed by Pt Nanoparticles: An Experimental and Computational Approach, *RSC Adv.* 2 (2012) 6686-6694.

[135] S. Choudhury, S. Batabyal, T. Mondol, D. Sao, P. Lemmens, S. K. Pal, Ultrafast Dynamics of Solvation and Charge Transfer in a DNA-Based Biomaterial, *Chem. Asian J.* 9 (2014) 1395-1402.

[136] R. Sarkar, A. K. Shaw, M. Ghosh, S. K. Pal, Ultrafast Photoinduced Deligation and Ligation Dynamics: DCM in Micelle and Micelle-Enzyme Complex, *J. Photochem. Photobiol. B* 83 (2006) 213-222.

[137] C. Xu, P. k. Shen, Y. Liu, Ethanol Electrooxidation on Pt/C and Pd/C Catalysts Promoted with Oxide, *J. Power Sources* 164 (2007) 527-531.

[138] M. Grdeń, M. Łukaszewski, G. Jerkiewicz, A. Czerwiński, Electrochemical Behaviour of Palladium Electrode: Oxidation, Electrodissolution and Ionic Adsorption, *Electrochim. Acta* 53 (2008) 7583-7598.

[139] R. Mancharan, J. B. Goodenough, Methanol Oxidation in Acid on Ordered NiTi, *J. Mater. Chem.* 2 (1992) 875-887.

[140] K. Mandal, D. Bhattacharjee, P. S. Roy, S. K. Bhattacharya, S. Dasgupta, Room Temperature Synthesis of Pd–Cu Nanoalloy Catalyst with Enhanced Electrocatalytic Activity for the Methanol Oxidation Reaction, *Appl. Catal., A* 492 (2015) 100-106.

[141] X. Yang, Q. Yang, J. Xu, C.-S. Lee, Bimetallic PtPd Nanoparticles on Nafion-Graphene Film as Catalyst for Ethanol Electro-Oxidation, *J. Mater. Chem.* 22 (2012) 8057-8062.

[142] A. Kabbabi, R. Faure, R. Durand, B. Beden, F. Hahn, J. M. Leger, C. Lamy, In Situ FTIRS Study of the Electrocatalytic Oxidation of Carbon Monoxide and Methanol at Platinum–Ruthenium Bulk Alloy Electrodes, *J. Electroanal. Chem.* 444 (1998) 41-53.

[143] K. Erickson, R. Erni, Z. Lee, N. Alem, W. Gannett, A. Zettl, Determination of the Local Chemical Structure of Graphene Oxide and Reduced Graphene Oxide, *Adv. Mater.* 22 (2010) 4467-4472.

[144] G. Prieto, J. Zečević, H. Friedrich, K. P. de Jong, P. E. de Jongh, Towards Stable Catalysts by Controlling Collective Properties of Supported Metal Nanoparticles, *Nat. Mater.* 12 (2013) 34-39.

[145] M. Green, N. Allsop, G. Wakefield, P. J. Dobson, J. L. Hutchison, Trialkylphosphine Oxide/Amine Stabilised Silver Nanocrystals-the Importance of Steric Factors and Lewis Basicity in Capping Agents, *J. Mater. Chem.* 12 (2002) 2671-2674.

[146] G. D. Mukherjee, S. N. Vaidya, C. Karunakaran, High Pressure and High Temperature Studies on Manganese Oxides, *Phase Transitions* 75 (2002) 557-566.

[147] Z. Cai, L. Xu, M. Yan, C. Han, L. He, K. M. Hercule, C. Niu, Z. Yuan, W. Xu, L. Qu, K. Zhao, L. Mai, Manganese Oxide/Carbon Yolk–Shell Nanorod Anodes for High Capacity Lithium Batteries, *Nano Lett.* 15 (2015) 738-744.

[148] V. V. T. Doan-Nguyen, P. J. Carroll, C. B. Murray, Structure Determination and Modeling of Monoclinic Trioctylphosphine Oxide, *Acta Cryst. C* 71 (2015) 239-241.

[149] P. W. Sadik, S. J. Pearton, D. P. Norton, E. Lambers, F. Ren, Functionalizing Zn- and O-terminated ZnO with thiols, *J. Appl. Phys.* 101 (2007) 104514-104518.

[150] J. Chang, E. R. Waclawik, Experimental and Theoretical Investigation of Ligand Effects on the Synthesis of ZnO Nanoparticles, *J. Nanopart. Res.* 14 (2012) 1012.

[151] K.-S. Cho, D. V. Talapin, W. Gaschler, C. B. Murray, Designing PbSe Nanowires and Nanorings through Oriented Attachment of Nanoparticles, *J. Am. Chem. Soc.* 127 (2005) 7140-7147.

[152] C. Tian, W. Li, Q. Zhang, K. Pan, H. Fu, Controllable Fabrication of Various ZnO Micro/Nanostructures from a Wire-Like Zn–EG–AC Precursor via a Facile Solution-Based Route, *Mater. Res. Bull.* 46 (2011) 1283-1289.

[153] S. Trasatti, O. Petrii, Real Surface Area Measurements in Electrochemistry, *Pure Appl. chem.* 63 (1991) 711-734.

[154] C. C. L. McCrory, S. Jung, J. C. Peters, T. F. Jaramillo, Benchmarking Heterogeneous Electrocatalysts for the Oxygen Evolution Reaction, *J. Am. Chem. Soc.* 135 (2013) 16977-16987.

[155] S. K. Bikkarolla, P. Cumpson, P. Joseph, P. Papakonstantinou, Oxygen Reduction Reaction by Electrochemically Reduced Graphene Oxide, *Farad. Discuss.* 173 (2014) 415-428.

[156] A. Yamaguchi, R. Inuzuka, T. Takashima, T. Hayashi, K. Hashimoto, R. Nakamura, Regulating Proton-Coupled Electron Transfer for Efficient Water Splitting by Manganese Oxides at Neutral pH, *Nat. Commun.* 5 (2014) 4256.

[157] F. Cheng, J. Shen, B. Peng, Y. Pan, Z. Tao, J. Chen, Rapid Room-Temperature Synthesis of Nanocrystalline Spinels as Oxygen Reduction and Evolution Electrocatalysts, *Nat. Chem.* 3 (2011) 79-84.

[158] D. Strmcnik, D. F. van der Vliet, K. C. Chang, V. Komanicky, K. Kodama, H. You, V. R. Stamenkovic, N. M. Marković, Effects of Li^+, K^+, and Ba^{2+} Cations on the ORR at Model

and High Surface Area Pt and Au Surfaces in Alkaline Solutions, *J. Phys. Chem. Lett.* 2 (2011) 2733-2736.

[159] C. H. Choi, H.-K. Lim, M. W. Chung, J. C. Park, H. Shin, H. Kim, S. I. Woo, Long-Range Electron Transfer over Graphene-Based Catalyst for High-Performing Oxygen Reduction Reactions: Importance of Size, N-doping, and Metallic Impurities, *J. Am. Chem. Soc.* 136 (2014) 9070-9077.

[160] S. Ghosh, P. Kar, N. Bhandary, S. Basu, T. Maiyalagan, S. Sardar, S. K. Pal, Reduced Graphene Oxide Supported Hierarchical Flower Like Manganese Oxide as Efficient Electrocatalysts Toward Reduction and Evolution of Oxygen, *Int. J. Hydrogen Energy*, 42 (2017) 4111-4122.

[161] A. V. Fraioli, Investigation of Manganese Dioxide as an Improved Solid Desiccant, Proc. Electrochem. Soc., 1985.

[162] G. Qiu, H. Huang, S. Dharmarathna, E. Benbow, L. Stafford, S. L. Suib, Hydrothermal Synthesis of Manganese Oxide Nanomaterials and Their Catalytic and Electrochemical Properties, *Chem. Mater.* 23 (2011) 3892-3901.

[163] S. Stankovich, D. A. Dikin, R. D. Piner, K. A. Kohlhaas, A. Kleinhammes, Y. Jia, Y. Wu, S. T. Nguyen, R. S. Ruoff, Synthesis of Graphene-Based Nanosheets via Chemical Reduction of Exfoliated Graphite Oxide, *Carbon* 45 (2007) 1558-1565.

[164] J. P. Borah, J. Barman, K. Sarma, Structural and Optical Properties of ZnS Nanoparticles, *Chalcogenide Lett.* 5 (2008) 201-208.

[165] P. W. Sadik, S. J. Pearton, D. P. Norton, E. Lambers, F. Ren, Functionalizing Zn- and O-Terminated ZnO with Thiols, *J. Appl. Phys.* 101 (2007) 104514.

[166] L. Xi, Y. M. Lam, Controlling Growth of CdSe Nanowires through Ligand Optimization, *Chem. Mater.* 21 (2009) 3710-3718.

[167] K. Kunimatsu, T. Yoda, D. A. Tryk, H. Uchida, M. Watanabe, In Situ ATR-FTIR Study of Oxygen Reduction at the Pt/Nafion Interface, *Phys. Chem. Chem. Phys.* 12 (2010) 621-629.

Chapter 5

Electronic Spectroscopic Studies on Light Harvesting Nanomaterials

5.1. Introduction:

Sensitization of wide-band-gap semiconductors by organic dyes for all kind of solar devices is an essential requirement [1, 2]. The design of low-cost and environmentally friendly 'green' dye-sensitized nanoparticle-based solar-light-harvesting devices relies on the nature of the organic dyes used as light-absorbing materials. A considerable research effort in this direction stems from the desire to tackle a number of problems, including cost and environmental compatibility [3, 4]. The synthesis and purification of the best-performing ruthenium-based dyes for solar-light-harvesting devices is expensive. For example, terpyridine black dye sells for around $3500 per gram [5]. The second problem is the photo-toxicity of ruthenium-based dyes, raising potential environmental hazards [6, 7]. A detailed study of the mechanism of photo-toxicity of the $Ru(phen)_3^{2+}$ dyes has shown that upon illumination, extracellular and membrane-bound Ru(II) complex generates singlet oxygen molecules. A high local concentration of singlet oxygen molecules causes a sequence of undesirable events that eventually leads to plasma membrane damage, which is manifested in a loss of membrane integrity and entry of the dye into living cells [8]. In optimizing the balance between cost and biocompatibility, porphyrin-based solar devices are attracting interest in the contemporary literature [9-13]. Recently, Chen et al. [14] demonstrated a significant enhancement in visible light photocatalysis upon attachment of porphyrin (meso-tetra(*p*-hydroxyphenyl)porphyrin,*p*-THPP) nanoparticles (NPs) into macroscopic graphene (reduced graphene oxide, rGO) films. The use of porphyrin from natural sources (hematoporphyrin, protoporphyrin) in solar devices has been reported to meet the requirements relating to cost and toxicity [15-17]. Our previous studies on hematoporphyrin-sensitized ZnO nanorods indicated dual applications in efficient visible-light photocatalysis (VLP) and dye-sensitized solar cells (DSSC) [18]. ZnO nanoparticles are considered to be nontoxic and biocompatible, and have been used in many applications in our daily lives, including as drug carriers and cosmetics [19]. The role of metal ions in the central cavity of the porphyrin in the proximity of the host semiconductor for efficient decontamination of drinking

water has been a subject of several recent reports [20-22]. Tuning the photo response [23], the efficiency of photo-injected electrons, [24] and the stability of dyes upon metalation [25] have been addressed in a series of reports [26]. In our recent studies, we explored the critical role of the central metal ions (Fe^{3+}/Fe^{2+}) incorporated into hematoporphyrin-TiO_2 nanohybrids and their implications in photocatalysis [27].

From the practical application point of view, the use of porphyrin-based photocatalytic devices for water decontamination is very important, given the fact that water from natural resources contains metal ions (especially Fe^{3+} and Cu^{2+}). In the present study, we have synthesized and characterized a PP-ZnO nanohybrid for a flow-type photocatalytic solar device for a prototype water decontamination plant using visible light. We explored the role of metal ions, specifically, iron (III) and copper (II), in the test water, and have deployed a model contaminant, methylene blue (MB), a hazardous waste product from the textile industry, [28] in the photocatalytic device under visible light. Femtosecond time-resolved transient absorption studies have clearly unravel the key time component associated with ground-state recovery of the sensitized PP upon metalation for the change in overall photocatalytic efficiency. In addition, picoseconds-resolved fluorescence studies of the nanohybrids in the absence and presence of metal ions have clearly shown that excited-state electron-transfer dynamics is responsible for the photocatalytic action. Moreover, the role of UV light excitation of the nanohybrid, in which the host semiconductor is expected to be excited, is also been discussed. Our studies are expected to be of relevance to the large-scale use of the porphyrin-based nanomaterials for the decontamination of drinking water by solar light catalysis.

Recently, use of solar harvesting nanomaterials is found to be important to improve photocatalysis and dye sensitized solar cells efficiencies taking full advantage of the main part of the solar spectrum [29-36]. However, practical applications of the nanomaterials have been limited because of a serious drawback due to several interfacial dynamical processes at the interface of the sensitizer and host semiconductor [37-40]. It is well-known that the electron transfer on the interface between the sensitizer and the semiconductor is of great significance to the photocatalytic and photovoltaic efficiencies [27, 41-43]. Thus, efficient electron transfer at the interface due to coupling between the sensitizer and semiconductor cause a rapid photoinduced charge separation and a relatively slow charge recombination, and hence an improved efficiency of solar energy harvesting can be achieved [44, 45]. Therefore, study of

interfacial carrier dynamics of light harvesting nanohybrid is very much important in order to understand the alteration of photocatalysis and photovoltaic efficiencies. Yang et al. developed an organic-inorganic hybrid material where interfacial charge separation between TiO_2 and conjugated structure facilitates to improve the photocatalytic efficiency [46]. In this direction, extensive efforts have been devoted like metal-ion doping, non-metal doping, noble metal deposition, narrow bandgap semiconductor coupling, conducting polymer sensitization, and dye sensitization to modify the semiconductor in order to get better light harvesting ability [47-52]. In one of our recent studies, we have developed an efficient light harvesting heterostructure based on poly(diphenylbutadiyne) (PDPB) nanofibers and ZnO nanoparticles which is helpful in photocatalysis [53]. Previously, we sensitized ZnO nanorods with hematoporphyrin which exhibit twin applications in efficient visible light photocatalysis and dye sensitized solar cell [18]. We have also demonstrated how presence of naturally abundant iron(III) and copper(II) ions significantly alter visible light photocatalytic activity of PP-ZnO nanohybrid [50]. Recently, we have shown dipolar coupling between porphyrin and plasmonic nanoparticles facilitates enhanced solar energy conversation when they are embedded on a host semiconductor matrix [54]. Towards this direction, nanohybrid systems seem to be ideal to achieve enhanced light-harvesting and charge-transfer which is which is usually helpful to get better solar energy conversion.

Porphyrin, a well known photosensitizer has been extensively used as a light harvesting material upon sensitization with semiconductor due to low cost, low toxicity and environmental compatibility compared to ruthenium-based inorganic dyes [55-58]. Thus porphyrin based light harvesting nanomaterials have a wide application in photocatalysis, dye sensitized solar cell, photodynamic therapy [54, 59-61]. In our previous study, we observed that attachment of Protoporphyrin with ZnO nanoparticles has a potential application in drug delivery vehicle of cancer drugs [59]. Nolan et al. showed that tetra(4-carboxyphenyl)porphyrin (TCPP)-TiO_2 composite is very much efficient in the photo-degradation of the pharmaceuticals [62]. However, to the best of our knowledge, effect of interfacial carrier dynamics in dual application of photovoltaic and photocatalysis using same porphyrin based light harvesting nanohybrid are sparse in the existing literature and one of our motives in this present work.

In the present study, we have synthesized Protoporphyrin IX-Titanium dioxide (PP-TiO_2) nanohybrid as a model light harvesting nanohybrid for potential applications in photovoltaics and

photocatalytic devices. We observed that the presence of Cu (II) ion within the porphyrin moiety of the nanohybrid can alter overall photocatalytic and photovoltaic activity. Picosecond-resolved fluorescence studies of the nanohybrids in the absence and presence of metal ions have been employed to investigate the ultrafast interfacial charge transfer dynamics upon photoexcitation. We have further investigated that presence of copper within porphyrin moiety shows excellent photocatalytic activity for the degradation of Methylene Blue (MB) used as a model organic pollutant. We have fabricated DSSCs with the nanohybrid which exhibit much lower power conversation efficiencies compared to their counterparts.

Detoxification of waste water from dyes and pigments is a matter of great concern since every year 10-15% dyes are wasted during fabrication processes and directly discharged to water causing a pollution of the environment by potential carcinogens [63]. In this regards, efficient adsorption has been considered as the most preferred way for the easy and efficient removal of toxic dyes from waste water [64-67]. However, most of the common adsorbents including activated carbon, rice husk, zeolites and mesoporous silica suffer from low adsorption capacities, poor selectivity and an unsatisfactory recyclability [68-70]. Moreover, a number of advanced adsorbents have been reported using low-cost carbon and inorganic origin such as, carbon nanotubes, graphite, fullerene, nanostructured metal oxides and porous boron nitride nanosheets to circumvent this emerging problem [70-72]. However, the engineered carbon materials have a limited adsorption capacity and often are toxic to the environment [73]. Therefore, a versatile adsorbent with enhanced efficiency would be highly desirable for economical water purification. Recently, graphene consisting of single layer of carbon atoms with a honeycomb two-dimensional (2D) lattice crystal structure, has been recognized as a promising material in various fields, such as solar energy harvesting, drug delivery, nanoelectronics, sensor, H_2 production and water purification [74-76]. Li et al. have synthesized stable aqueous dispersions of graphene sheets by photophysical reduction of graphene oxide (GO) without using any chemical additives [77]. Recent activities focused on graphene or GO as an attractive adsorbent material due to its high surface area, negative surface charge and highly mobile π electrons. Its electronic configuration can easily undergo electrostatic and π-π interactions with dyes containing a π-electron rich structure. Nonetheless, the van der Waals and π-π interactions between individual graphene layers significantly decrease their hydrophilic character and consequently lead to their irreversible agglomeration [78].

Nanohybrids have attracted tremendous attention due to their potential functionality for tailored applications [79-83]. Graphene based composites are novel hybrid materials where inorganic particles are synthesized on graphene sheets which act as two dimensional substrate to prevent nanoparticles (NPs) aggregation [84, 85]. The nanohybrid displays fascinating physicochemical properties as a consequence of the intimate dispersion or mixing of the both components which are useful in catalysis, energy storage, water purification and drug delivery [76, 86, 87]. Furthermore, presence of metal NPs act as a spacer within the graphene sheet, preventing agglomeration and restacking of graphene layer during the reduction process this is used for adsorption and other catalytic application. Liu et al. showed that attachment of carbon coated Fe_3O_4 NPs on GO could be used as a promising applied material for toxic dye removal and could be recycled [88]. The synthesis of Au-RGO nanohybrid by using hydrothermal, chemical reduction, physical vapor deposition and electrostatic interaction is reported in the literature [89-92]. However, such techniques require multi-step fabricating processes, involved toxic chemicals and thereby reduce the efficiency of the Au-reduced graphene oxide (Au-RGO) hybrid. Therefore, it is essential to develop a facile approach for synthesis of Au-RGO nanohybrids with improved adsorption efficiency. One-pot reductant-free nanohybrid synthesis by photo-reduction is one of the aims of our present work. Up to now only very few reports on the synthesis of Au-RGO nanohybrid by photochemical reduction exist. Wang et al. synthesized Au-RGO nanohybrids by using UV illumination and N-hexadecyltrimethylammonium chloride (CTAC) used as a surfactant to protect NPs from agglomeration [93]. Uses of surfactants are not compatible with graphene and sometimes interfere between graphene and metal NPs interface. Moreover, details adsorption studies by Au-RGO nanohybrid and their correlation with the ultrafast electron transfer dynamics by spectroscopy is very sparse in the existing literature and also one of the motives of our present work.

Herein, we have developed a facile approach for the synthesis of Au-RGO nanohybrid *via* photochemical reduction technique. Adsorption capacity of the synthesized nanohybrid has been studied for a wide range of dyes. We further studied the effect of pH and temperature for the adsorption process. Details of adsorption kinetics and thermodynamic parameters are also investigated using Rhodamine 123 (Rh123) as a model dye. Picosecond resolved fluorescence technique has been employed to investigate the proximity of the dye after adsorption on an Au-RGO surface. Nanometal surface energy transfer is found be effective between Rh123 and Au

NPs after adsorption of Rh123 on Au-RGO nanohybrid. For potential application, we have developed a prototype device by loading Au-RGO nanohybrid in a syringe filter mesh (pore size 0.220 μm) and studied adsorption efficiency and recyclability of the device using Rh123 and crystal violet as model dyes.

5.2. Results and Discussion:

5.2.1. Impact of Metal Ions in Porphyrin-Based Applied Materials for Visible Light Photocatalysis: Key Information From Ultrafast Electronic Spectroscopy [50]:

5.2.1.1. Structural characterization of nanohybrids: A typical high-resolution transmission electron microscopic (HRTEM) image of ZnO NPs is shown in Figure 5.1a. From the TEM study, an average size of the ZnO NPs of 25 nm was estimated. TEM study on a single NP revealed crystal fringes with an inter-planar distance of 0.26 nm (inset in Figure 5.1a) corresponding to the spacing between two (002) planes of ZnO [94]. XRD study (Figure 5.1b) on the bare ZnO NPs (2θ range from $20^{°}$ to $70^{°}$) and upon sensitization with PP in the absence and
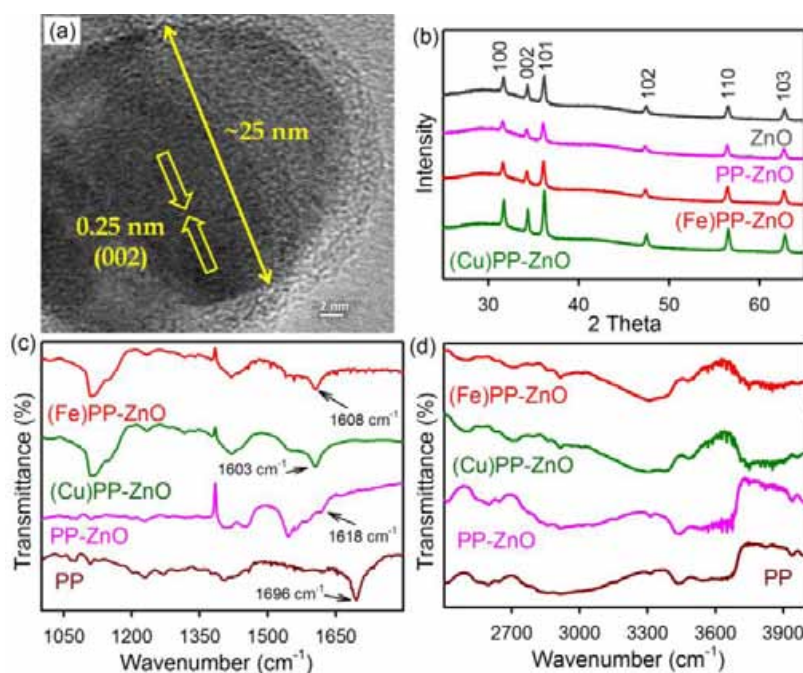

Figure 5.1. *(a) HRTEM images of ZnO NPs. (b) X-Ray diffraction pattern of ZnO, PP-ZnO, (Fe)PP-ZnO), (Cu)PP-ZnO. (c) FTIR spectra of PP, PP-ZnO, (Cu)PP-ZnO, (Fe)PP-ZnO. The spectra of PP-ZnO, (Fe)PP-ZnO and (Cu)PP-ZnO are taken on a ZnO background. (d) FTIR spectra of PP, PP-ZnO, (Cu)PP-ZnO and (Fe)PP-ZnO.*

presence of the metal ions (Fe^{III}, Cu^{II}) showed the characteristic planes of ZnO (100), (002), (101), (102), (110) and (103). Intactness of the crystal planes of ZnO upon sensitization of the PP dye and metal ions was also clear from the study. Wurtzite ZnO exhibits well-defined crystallographic faces, i.e., polar (002) and nonpolar (100), (101) surfaces. Mclaren et al. [95] showed the terminal polar faces to be more active surfaces for photocatalysis than the nonpolar surfaces perpendicular to them.

5.2.1.2. FTIR study: Fourier transform infrared (FTIR) spectroscopy was used to confirm the binding mode of PP on the ZnO surface. For free PP, stretching frequencies of the carboxylic group are located at 1696 cm^{-1} and 1402 cm^{-1} for the antisymmetric and symmetric stretching vibrations, respectively, as shown in Figure 5.1c. In PP-ZnO, the stretching frequencies of the carboxylic groups are located at 1618 cm^{-1} and 1405 cm^{-1} for the antisymmetric and symmetric stretching vibrations, respectively, providing clear evidence of the deprotonation of the carboxylic group upon addition of ZnO NPs. The difference between the carboxylate stretching frequencies, $\Delta = \nu_{as} - \nu_{sym}$, is useful in identifying the binding mode of the carboxylate ligand [96]. The observed Δ value for the PP-ZnO nanohybrid was 213 cm^{-1}, smaller than that of free PP (294 cm^{-1}). This suggests that the binding mode of PP on ZnO is predominantly bidentate. However, nanohybrids incorporating Fe^{III} and Cu^{II} also show bidentate covalent binding of PP to ZnO NPs through the carboxylic groups. The N-H stretching frequency has been used to investigate the attachment of the metal ions to the PP associated with the ZnO host. In free PP, the N-H stretching frequency is at 3441 cm^{-1} (Figure 5.1d). In the case of the PP-ZnO nanohybrid, the N-H stretching frequency of the PP cavity remains unperturbed as PP anchors onto the ZnO surface through its carboxylic group. In the presence of iron or copper, the N-H bond is perturbed, indicating that iron (III) and copper (II) bind to the PP through the pyrrole nitrogen atoms of the porphyrin [27]. The binding between PP and ZnO was also confirmed from raman spectroscopy. Raman spectra were collected from PP, ZnO NPs and PP−ZnO nanohybrids in the wavenumber region of 300−600 cm^{-1}. PP molecules do not show an obvious peak in the experimental range. However, four vibration peaks at 328, 378, 438, and 577 cm^{-1} are observed in the Raman spectrum of ZnO NPs, indicating the presence of a wurtzite structure. The strong peak at 438 cm^{-1} can be assigned to the nonpolar optical phonon, E$_2$, mode of the ZnO NPs at high frequency, which is associated with oxygen deficiency [97, 98]. Noticeably, the characteristic band of E$_2$

mode's of ZnO shifts toward lower wavenumber and its linewidth is larger upon its attachment to PP. This indicates the passivation of the ZnO surface states upon PP assembly.

5.2.1.3. Steady-state optical study of the nanohybrid: With extensively delocalized π electrons, the PP exhibits a soret band ($S_0 \rightarrow S_2$) and Q bands ($S_0 \rightarrow S_1$) due to the π-π^* electronic transition. UV-Vis absorption spectra of PP in DMSO-water clearly indicate the formation of H-type and J-
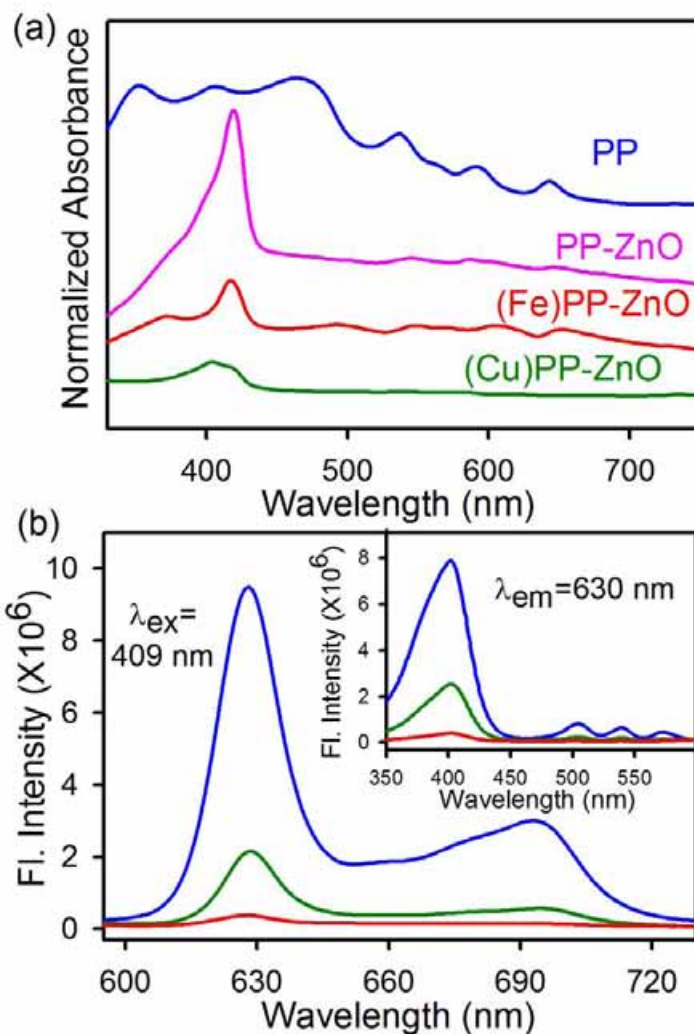
Figure 5.2. *(a) UV-Vis absorption spectra of PP, PP-ZnO, (Fe)PP-ZnO, (Cu)PP-ZnO in DMSO-water (V/V). (b) Room temperature PL spectra of PP, PP-Cu, PP-Fe in DMSO-water mixture(V/V). The inset shows excitation spectra monitored at 630 nm.*

type aggregates due to the presence of peaks at 352 nm and 465 nm, respectively (Figure 5.2a) [99, 100]. The soret band peak of PP appears at 405 nm, where as the Q-band peaks are observed in the range between 500 nm and 650 nm. The disappearance of the aggregate peak at 463 nm

and the red-shift in the soret band (405 to 421 nm, in Figure 5.2a) are indicative of direct interaction of PP with ZnO nanoparticles [17, 101]. As shown in Figure 5.2b, PP in DMSO-water exhibits strong emission at 630 nm and 700 nm upon excitation at the soret band by a laser source at 409 nm. However, after metalation with Fe (III) and Cu (II), steady-state emission of PP is significantly decreased, indicating non-radiative processes that can be attributed to fast intersystem crossing to the excitedtriplet state [102]. In addition, charge-transfer processes have also demonstrated to be responsible for the quenching [103].

5.2.1.4. Visible light photocatalysis by the nanohybrid and the effect of dissolved metal ions: Figure 5.3a shows a prototype photo-device for investigation of the photocatalytic efficiency of the nanohybrid under visible-light irradiation. Full details of the device may be found in our earlier publication [104]. The test water under investigation contains methylene blue (MB), a model water contaminant, in the absence and presence of iron and copper cations (44.5 mg/L copper and 39.2 mg/L iron). From the data shown in Figure 5.3b, the presence of iron in the water significantly decreased the photocatalytic efficiency, whereas copper enhances the degradation of MB within our experimental time window of two hours. Our observationa are consistent with previous literature reports [25, 27]. Oliveros et al. [17] investigated the photodegradation of atrazine in an aqueous solution under visible-light irradiation in the presence of tetra(4-carboxyphenyl)porphyrin (TcPP) in the absence/presence of different central metal ions (Fe(III), Cu(II), Zn(II)) adsorbed on a TiO_2 surface, and the maximum photocatalytic activity was obtained using Cu(II) porphyrin as the photosensitizer after the addition of hydrogen peroxide. The concentration of metal ions we used here (44.5 mg/L copper and 39.2 mg/L iron) are of the order of those recommended by the World HealthOrganization (WHO) in drinking water (30 mg/L copper and 10 mg/L iron) available from natural resources. In the photocatalytic reaction, MB reacts with the conduction-band electron of ZnO to form a well-known colourless product, leuco methylene blue (LMB) [105, 106] as shown in equation 5.1:

$$2MB + 2e^- + H^+ = MB + LMB. \qquad (5.1)$$

The energy-dispersive X-ray analysis (EDAX) spectra of PP-ZnO before and after two hours of photocatalysis in the presence of copper and iron ions are shown in Figure 5.3c-e. These spectra clearly indicate the presence of metal ions on the catalyst surface after the photocatalysis. The

complexation rate of copper with PP is higher than that of iron, which leads to the presence of
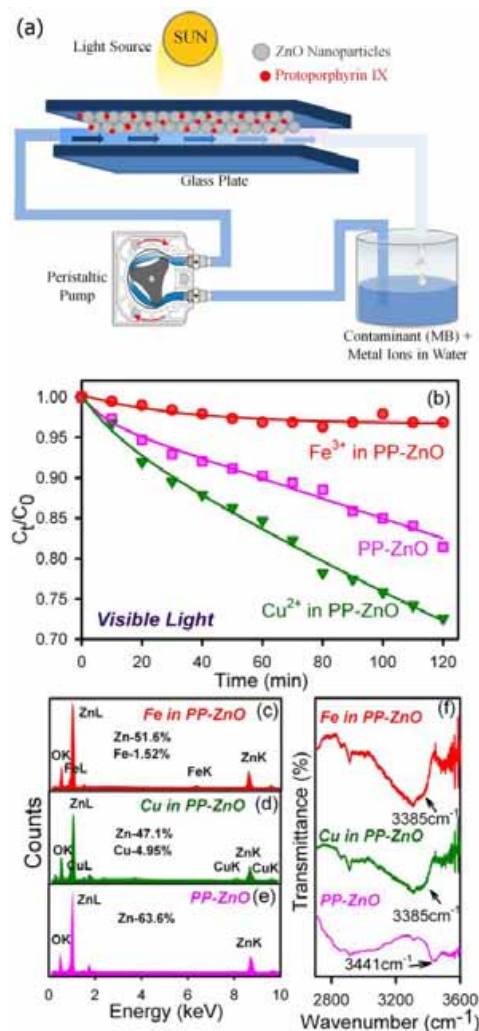
Figure 5.3. (a) Schematic representation of the flow device developed for photocatalysis. (b) Photocatalytic degradation of MB in the flow device using PP-ZnO as the photocatalyst in the presence of Cu^{2+} (dark green), Fe^{3+} (red) as contaminants in MB solution and without any metal ions (pink). EDAX spectra of PP-ZnO (pink, e) in the presence of Cu^{2+} (dark green, d) and Fe^{3+} (red, c). (f) FTIR spectra of PP-ZnO (pink) before photocatalysis and after photocatalysis in the presence of Cu^{2+} (dark green) and Fe^{3+} (red).

more copper (4.95%) on PP-ZnO than iron (1.52%) [107]. To confirm the complex formation, FTIR studies were conducted as shown in Figure 5.3f. For PP-ZnO, the N-H stretching frequency is at 3441 cm^{-1}. In the presence of iron and copper, the N-H bond is broadened and shifted to 3385 cm^{-1}, suggesting that iron (III) and copper (II) bind to the PP through pyrrole nitrogen atoms of the porphyrin. Thus, the metal ions present in the contaminant solution are

complex with PP. After two hours of photocatalysis, ~5-10% PP has leached out from the ZnO surface. To best of our knowledge, such study revealing the role of metal ions in test water in the photocatalytic activity of porphyrin-based nanohybrids and a detailed understanding of the molecular mechanism of photocatalysis have been rare in the literature. Hence, we identified a need of exploration of ultrafast dynamic studies on the nanohybrid.

5.2.1.5. Femtosecond Broadband Transient Absorption Study: The femtosecond-resolved transient absorption spectra (excitation wavelength = 350 nm) of the PP-ZnO nanohybrid in the presence and absence of iron and copper ions in the wavelength range of 360-440 nm are shown

Figure 5.4. *Transient absorption spectra of (a) PP-ZnO (b) (Cu)PP-ZnO and (c) (Fe)PP-ZnO at different time delays after excitation at 350 nm. (d) Time-resolved absorption changes of PP-ZnO (pink), (Cu)PP-ZnO (blue), (Fe)PP-ZnO (red) at a probe wavelength of 370 nm. All spectra are studied in a DMSO-water mixture (V/V).*

in Figure 5.4a-c. It should be noted that the peaks at 370 nm and ~415 nm correspond to the band gap of the ZnO (3.37 eV) and the soret band of PP guest, respectively. The decay profiles at a detection wavelength of 370 nm, revealing ground-state recovery of the excited ZnO in the nanohybrid in the presence and absence of the metal ions, are shown in Figure 5.4d. The

possiblity of interference by the absorption of PP at the detection wavelength (370 nm) was ruled out through a set of control experiments with pure PP, which revealed different time scales (~ns)

Table 5.1. Fits of the transient absorption data at different probe wavelengths.

Sample	Monitored Wavelength (nm)	τ_1 (ps)	τ_2 (ps)	τ_3 (ns)
PP-ZnO	370	16.91 (48.63%)	88.64 (34.14%)	7.44 (17.27%)
	415	6.00 (24.44%)	45.81 (26.54%)	1.60 (49.02%)
	543	3.73 (40.05%)	60.00 (29.92%)	1.60 (30.03%)
	590	5.84 (31.68%)	60.00 (26.11%)	1.60 (42.21%)
(Cu)PP-ZnO	370	16.20 (51.10%)	90.00 (30.98%)	7.85 (17.92%)
	415	5.69 (27.87%)	61.45 (33.27%)	1.60 (38.86%)
	543	3.59 (23.68%)	27.52 (49.70%)	1.60 (26.62%)
	586	5.10 (31.20%)	40.93 (33.64%)	1.60 (35.16%)
(Fe)PP-ZnO	370	25.00 (58.29%)	204.23 (22.99%)	11.01 (18.72%)
	415	15.00 (34.16%)	201.73 (17.90%)	1.60 (47.94%)
	550	13.41 (41.38%)	200.00 (7.56%)	1.60 (51.06%)
	590	13.06 (34.31%)	220.00 (11.82%)	1.60 (53.87%)

for ground-state bleach recovery. Numerical fitting of the transient absorption data of PP-ZnO gave decay time constants of 16.91 ps (48.63%), 88.64 ps (34.14%) and 7.44 ns (17.27%) for the ground-state recovery of the host ZnO in the nanohybrid. The nanohybrid in the presence of copper ions showed similar recovery time constants (16.20 ps (51.10%), 90.00 ps (30.98%) and 7.85 ns (17.92%)), but a significant retardation was observed in the presence of iron ions (25.00 ps (58.29%), 204.23 ps (22.99%) and 11.01 ns (18.72%)). The time constants imply that iron
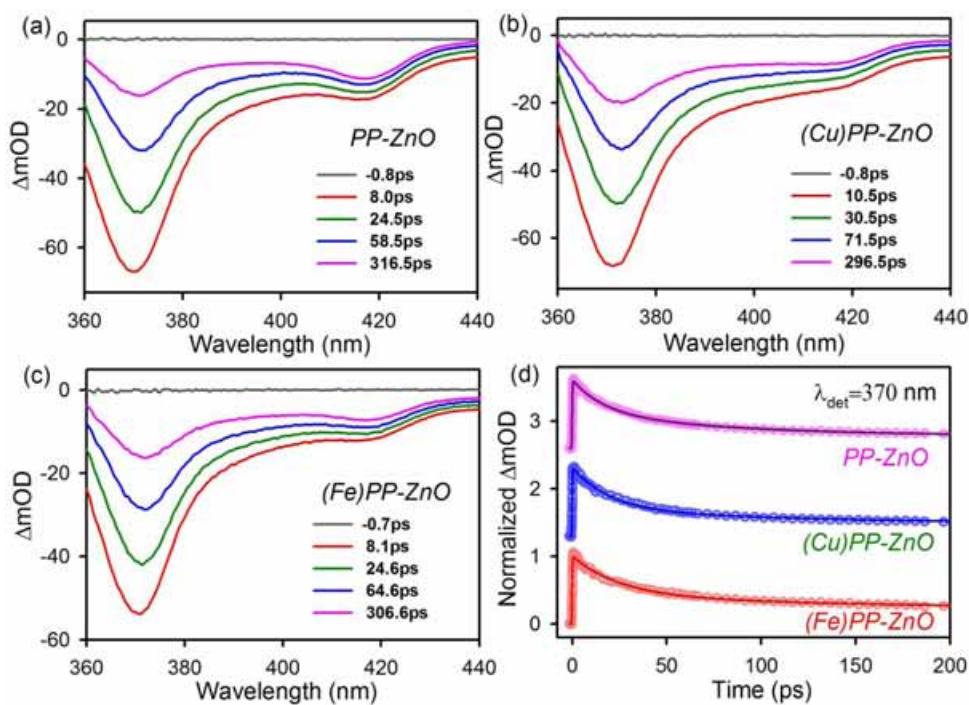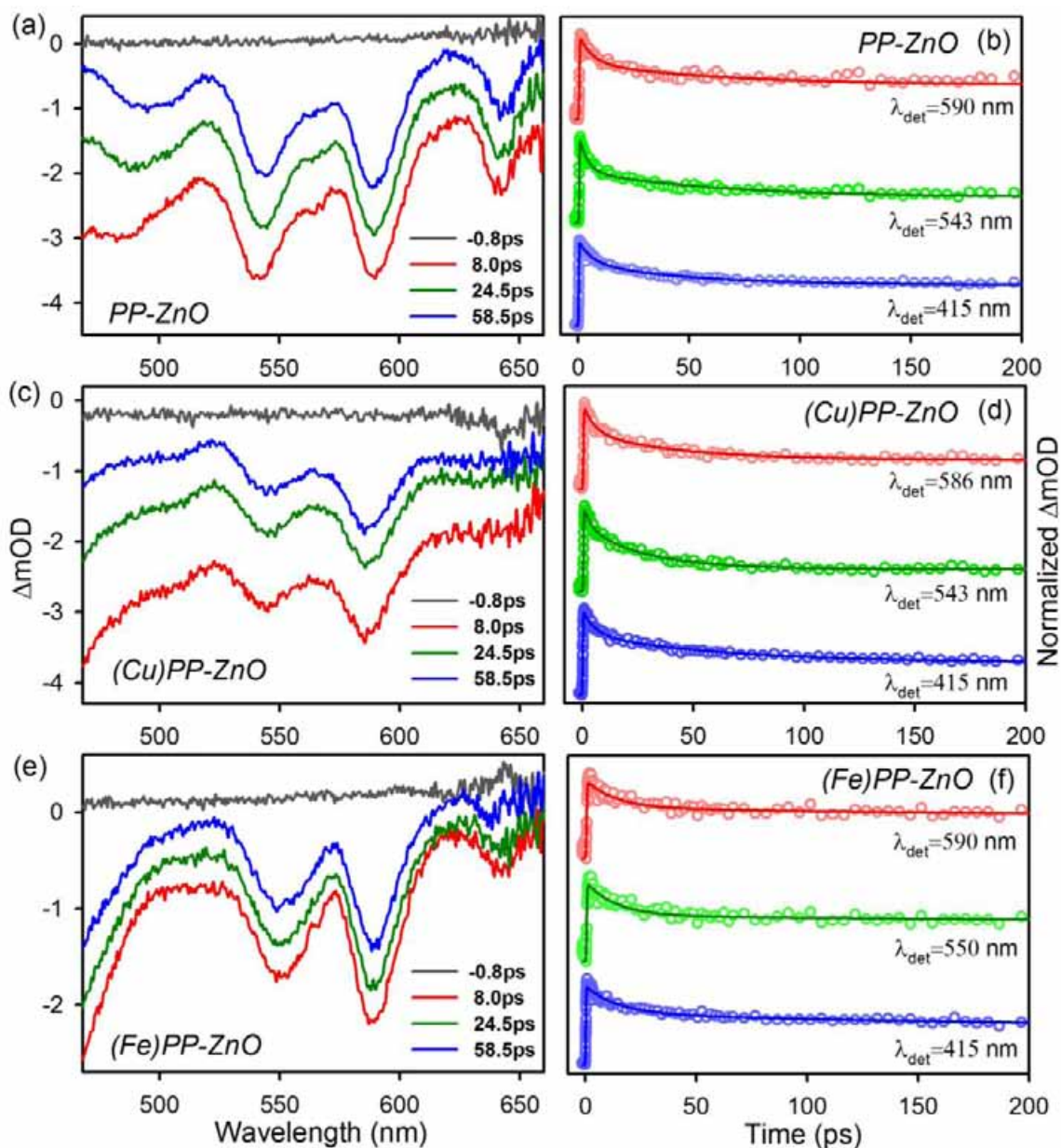
Figure 5.5. *Transient absorption spectra of (a) PP-ZnO, (c) (Cu)PP-ZnO and (e) (Fe)PP-ZnO at different time delays after excitation at 350 nm. Time-resolved absorption changes of (b) PP-ZnO (d) (Cu)PP-ZnO and (f) (Fe)PP-ZnO at different probe wavelengths. All the spectra are recorded in DMSO-water mixture (V/V).*

ions can efficiently separate the electron-hole pairs of the excited ZnO NPs, leading to slow recovery of the ground state of the ZnO NPs in the nanohybrid. Transient absorption spectra of the Q bands of PP in the nanohybrids in the wavelength range of 465 to 660 nm are shown in Figure 5.5a, c, and e. From this spectra, it is evident that the four Q bands seem for the free base PP essentially merged into two in the presence of the iron(III) and copper(II) ions due to the

higher molecular symmetry (D_{4h}) [108]. The decay profiles in the soret and Q bands revealing the ground state recovery of the excited PP in the nanohybrid in the presence and absence of metal ions are shown in the Figure 5.5b, d, f. The decay time constants are presented in Table 5.1. Table 5.1 and Figure 5.5 clearly indicate that the presence of iron (III) ions delays the recovery of the excited PP, whereas the presence of copper (II) ions does not significantly affect the time constants of PP compare to those in the nanohybrid. From the above observation on the ground-state recovery dynamics, upon UV excitation of ZnO in the nanohybrid in the presence of iron ions, the charge transfer is expected to be facilitated (longer exciton lifetime), leading to improved photocatalysis [109].

5.2.1.6. Picosecond-Resolved Fluorescence Studies: The fluorescence decays of PP and the PP-ZnO nanohybrid, monitored at 630 nm following excitation at 409 nm, in the absence and presence of iron (III) and copper (II) ions are shown in Figure 5.6a and 5.6b (shorter time window). The fluorescence transients of PP and (Cu)PP could be fitted with single exponential

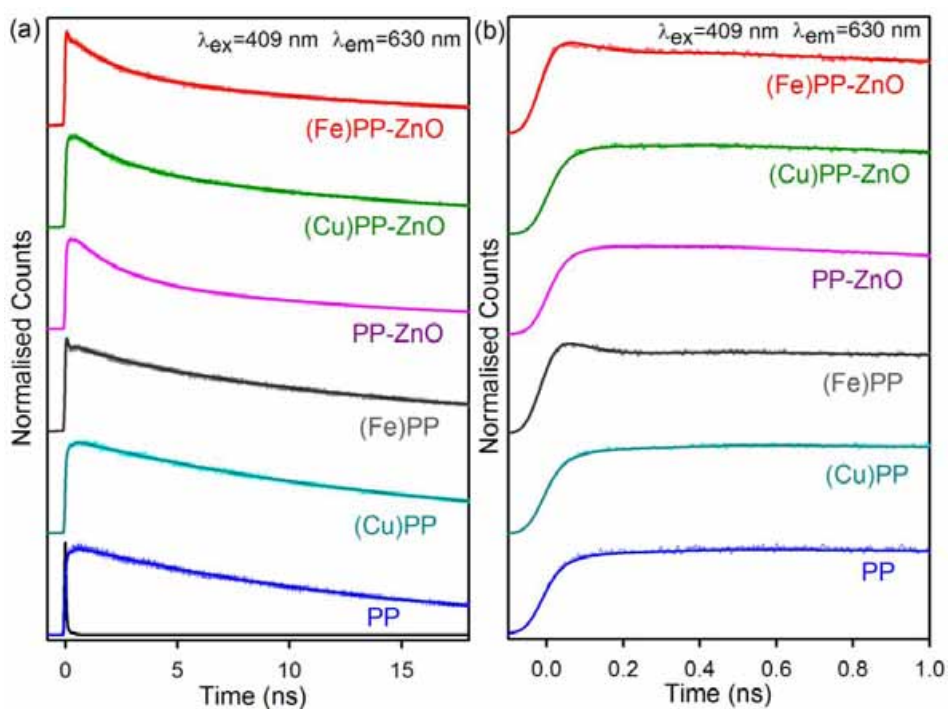***Figure 5.6.*** *Fluorescence decay profiles of PP, (Cu)PP, (Fe)PP, PP-ZnO, (Cu)PP-ZnO, (Fe)PP-ZnO with (a) a longer time window and (b) a shorter time window. All the spectra were recorded in DMSO-water mixture (V/V).*

decays with a lifetime of 16.03 ns and 17.29 ns, respectively (Table 5.2). The increase in the excited state lifetime of PP in the presence of copper ions may be indicative of the stability of the PP molecule as reported previously [25]. The time-resolved data for (Cu)PP exclude the

Table 5.2. Picosecond-resolved fluorescence transients of PP, (Fe)PP, (Cu)PP, PP-ZnO, (Fe)PP-ZnO and(Cu)PP-ZnO composites.[a]

Sample	τ_1 (ps)	τ_2 (ps)	τ_3 (ns)	τ_{avg}(ns)	$k_{nr} \times 10^7 (S^{-1})$
PP	16.03 ±0.01 (100%)			16.03 ±0.01	
(Fe)PP	16.61 ±0.05 (44.05%)	2.34 ±0.10 (5.95%)	0.048 ±0.001 (50%)	7.487 ±0.03	7.12±0.05
(Cu)PP	17.29 ±0.01 (100%)			17.29 ±0.01	
PP-ZnO	16.77 ±0.06 (43.75%)	2.06 ±0.01 (56.25%)		8.505 ±0.03	5.52±0.04
(Fe)PP-ZnO	16.64 ±0.06 (19.04%)	2.02 ±0.01 (26.67%)	0.024 ±0.002 (54.29%)	3.7220 ±0.01	20.63±0.13
(Cu)PP-ZnO	16.98 ±0.05 (63.04%)	2.06 ±0.01 (36.96%)		11.472 ±0.04	2.48±0.03

[a]**The emission (monitored at 630 nm) was detected with 409 nm laser excitation. Numbers in the parentheses indicate relative contribution.**

possibility of charge transfer transitions from PP to Cu (II) ions, and thus the steady-state quenching of the PP emission in the presence of Cu (II) can be attributed to the fast intersystem crossing, which is outside of our experimental time window [102]. However, the fluorescence decay profile of PP in the presence of iron (III) shows shorter time constants of 0.048 ns (50%) and 2.34 ns (5.95%) along with 16.61 ns (44.05%) with an average excited state lifetime of 7.48 ns. The shorter excited state lifetime of the PP in the presence of iron ion could be correlated to the electron transfer process from the former to the latter [27]. The apparent nonradiative rate constant (k_{nr}) [110] was determined by comparing the lifetimes of PP in the absence (τ_0) and in the presence (τ) of an acceptor, by using the following equation:

$$k_{nr} = 1/\langle \tau \rangle - 1/\langle \tau_0 \rangle .$$

(5.2)

As shown in Figure 5.6, in PP-ZnO nanohybrid, the fluorescence decay profile is composed of a faster component of 2.06 ns (56.25 %) and a slower component of 16.77 ns (43.75 %), indicating an electron transfer process from PP molecules to the ZnO NPs. Although the slower component is consistent with the excited state lifetime of PP without ZnO, the faster one may be rationalized as the electron migration time from PP to the ZnO host [111]. In the presence of copper (II) ions, the excited state dynamics of the nanohybrid essentially remains unaltered. However, in the presence of iron (III), the decay profile of PP-ZnO shows an additional time component of 0.024 ns (54.29 %), which is not seen for either PP-ZnO or PP-ZnO in the presence of copper ions and can be rationalized as an electron migration pathway from PP to centrally located Fe(III).

5.2.1.7. Photocatalytic Degradation of Methylene Blue: To understand the modulation of the photocatalysis of PP-ZnO in the presence of dissolved metal ions under visible light irradiation with our photo-device, as depicted in Figure 5.3, we have performed *in vitro* photocatalysis measurements on a sample of the nanohybrid with pre-included metal ions (12 hours incubation time) in a quartz cuvette under visible light. The results are presented in Figure 5.7a. The inclusion of iron ions in the PP-ZnO nanohybrid significantly reduced the photocatalytic efficiency for the degradation of MB under visible light irradiation compared to that in the case of the nanohybrid without metal ions or in the presence of copper ions. The relatively efficient photocatalysis by the nanohybrid containing copper ions may be correlated with the additional structural stability of the PP in this system [25]. Upon excitation with visible light, the sensitizer (PP) injects electrons into the conduction band (CB) of ZnO and the subsequent degradation of MB is initiated by CB electrons being transferred to it through reactive oxygen species (ROS). This sort of remote bleaching has been well characterized in the literature. For example Li et al. used porphyrin-sensitized TiO_2 photocatalysts to degrade acid chrome blue K, and the degradation mechanism was shown to follow an ROS pathway [112]. After one hour of visible light irradiation, 55% of MB was degraded in the presence of PP-ZnO. However, the presence of copper (II) ions enhances the photocatalytic activity and 80% MB degradation was observed. The copper (II) ions impart stability to the PP moiety attached to the ZnO NPs, which leads to the enhancement in the photocatalytic activity. The photocatalytic activity of the PP-ZnO nanohybrid was significantly suppressed in the presence of iron (III) ions and only 17% MB
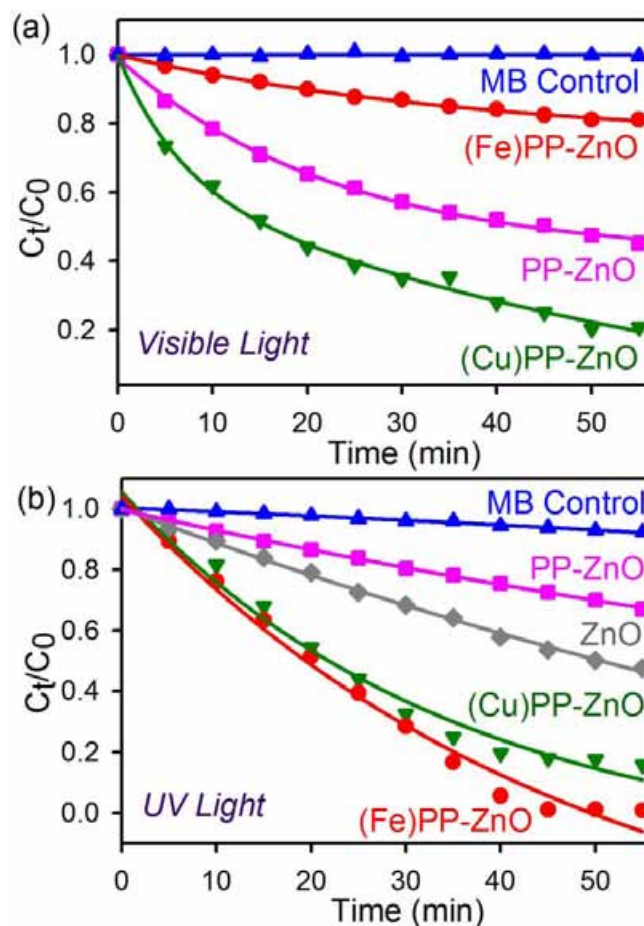
Figure 5.7. *Photocatalytic degradation of MB in the presence of ZnO, PP-ZnO, (Fe)PP-ZnO, (Cu)PP-ZnO and only MB nanohybrids under the (a) visible light and (b) UV light irradiation.*

degradation was observed. In this case, the photoexcited electrons of PP were preferentially trapped in the Fe(III) ions rather than ZnO, which was evident from the transient absorption (Figure 5.5) and TCSPC studies (Figure 5.6). The observation is consistent with the results obtained using the prototype flow device, as shown in Figure 5.3. Our transient absorption studies of the nanohybrid at 350 nm excitation reveal longer excitonic lifetimes in the presence of iron (III) ions compared to those obtained either without metal or in the presence of copper ions. As mentioned earlier, incorporation of iron in the central cavity of the porphyrin under UV light irradiation is expected to offer better photocatalysis that of the case under visible light irradiation. Another important factor is that any solar device should be exposed to the amount of UV radiation present in solar light (4-5%). Thus, in order to investigate the role of UV excitation, we have studiedthe photocatalytic activity of the nanohybrid in the presence and absence of metal ions under UV irradiation, as shown in Figure 5.7b. Under UV irradiation, 55% MB

degradation was observed in the presence of ZnO NPs, whereas, only 25% MB degradation was observed in the presence of the PP-ZnO nanohybrid. Under UV irradiation, the ZnO valence band (VB) electrons are excited to the conduction band (CB) and can then reduce dioxygen to superoxide, eventually leading to the production of hydroxyl radicals ($OH^{\bullet}$). The hole in the valence band accepts electrons from water to generate hydroxyl radicals ($OH^{\bullet}$), which can also participate in the degradation process [113]. Thus, the efficiency of the nanohybrid essentially depends on the number of photo-generated carriers (electrons and holes) and their exciton lifetimes. In the case of (Fe)PP-ZnO, the photo-generated electron has been shown to be trapped in the centrally located iron moiety of the nanohybrid, and ROS generation is essentially governed by the hole in the valence band and the enhanced exciton lifetime (as evidenced from transient absorption, discussed above). On the other hand, for (Cu)PP-ZnO, ROS generation is
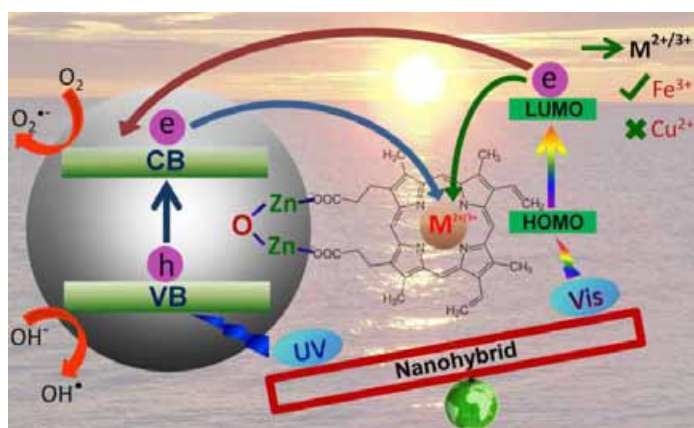
Scheme 5.1. *Schematic representation of ultrafast dynamical processes in a protoporphyrin-zinc oxide nanohybrid in the presence of different central metal ions under UV and visible light excitation.*

expected to be governed by the photo-generated carriers (both electrons and holes), although it may not acquire extra-advantage from the exciton lifetime (as evidenced from transient absorption), revealing comparable photocatalysis to that in the (Fe)PP-ZnO nanohybrid. The significant retardation of photocatalysis in the case of PP-ZnO without metalation may be rationalized in terms of photo-reduction of the attached PP by the photo-excited electron from ZnO. We have observed significant photo-bleaching of PP in PP-ZnO nanohybrids in the absence of metal ions under UV irradiation. The overall mechanistic pathway of the photo-catalysis of the nanohybrid upon visible and UV irradiation is shown in Scheme 5.1.

5.2.2. Can a Light Harvesting Material be Always Common in Photocatalytic and Photovoltaic Applications? [114]:

Figure 5.8a shows the HRTEM image of the TiO_2 nanoparticles. The average size of TiO_2 nanoparticle was found to be 25 nm. The HRTEM image of TiO_2 nanoparticles shows the high crystallinity of the nanoparticles. The inter-planar distance between the fringes is found to be about 0.327 nm which is consistent with (110) planes of bulk TiO_2 [115]. The X-ray diffraction patterns (As shown in Figure 5.8b) indicate that there is no significant change in the 2θ angle of
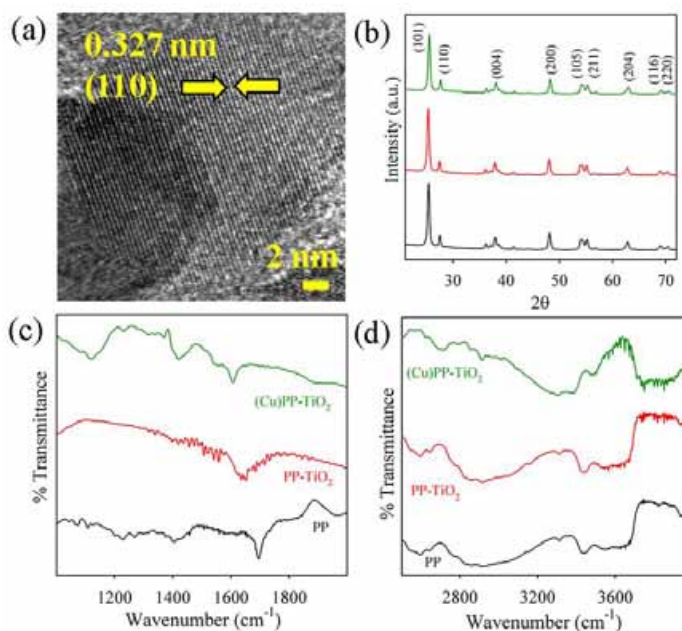
Figure 5.8. *(a) HRTEM images of TiO_2 NPs. (b) X-ray diffraction patterns of TiO_2, PP-TiO_2 and (Cu)PP-TiO_2. (c) FTIR spectra of PP, PP-TiO_2 and (Cu)PP-TiO_2. (d) FTIR spectra of PP, PP-TiO_2, and (Cu)PP-TiO_2.*

the signals for the sensitized TiO_2 nanohybrids compared to the unmodified TiO_2. Intactness of the crystal planes of TiO_2 upon sensitization with PP and Cu(II)PP also evident from this study. Fourier-transform infrared (FTIR) spectroscopy was used to confirm the binding mode of PP on the TiO_2 surface. For free PP, stretching frequencies of the carboxylic group are located at 1696 and 1402 cm^{-1} for the antisymmetric and symmetric stretching vibrations, respectively, as shown in Figure 5.8c. In PP-TiO_2, the perturbation of stretching frequencies of the carboxylic groups providing clear evidence for binding of the carboxylic groups with TiO_2 NPs. The difference in stretching frequencies, $\Delta = \gamma_{as} - \gamma_{sym}$ is a useful parameter in identifying the binding mode of the

carboxylate ligand [96]. For PP-TiO$_2$ nanohybrid the observed Δ value (198 cm^{-1}) is found to be smaller compared to free PP (294 cm^{-1}) which indicates that the binding mode of PP on TiO$_2$ is bidentate in nature. Similar bidentate covalent binding of (Cu)PP with TiO$_2$ is also observed from FTIR study. The perturbation of N-H stretching frequency confirms the successful metalation within the porphyrin moiety. In the presence of Cu (II) metal ion, the stretching frequency of N-H bond is perturbed (as shown in Figure 5.8d), which indicates the binding of Cu (II) metal ion with the pyrrole nitrogen atoms of the PP [50].
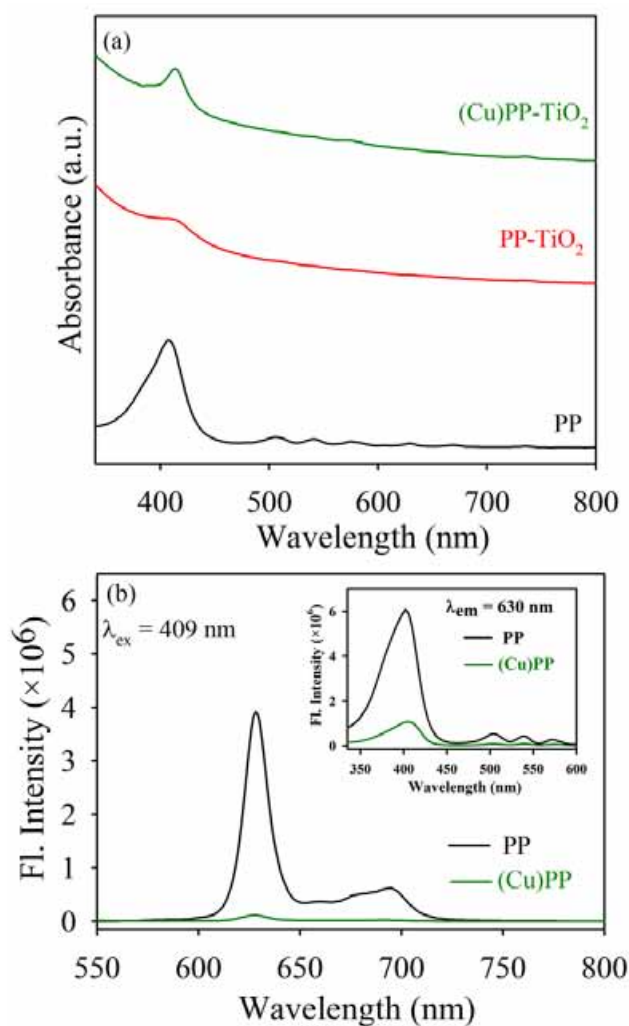
Figure 5.9. (a) UV-Vis absorption spectra of PP, PP-TiO$_2$ and (Cu)PP-TiO$_2$. (b) Room temperature fluorescence spectra of PP and (Cu)PP. The inset shows excitation spectra monitored at 630 nm.

The structure of PP has extensive delocalized π electrons which exhibits a Soret band (405 nm) and Q bands (500-700 nm) due to its π–π* electronic transitions [116, 117]. The PP–

TiO$_2$ nanohybrid exhibits a 5 nm bathochromic shift of the Soret band compare to the absorption of PP as shown in Figure 5.9a. Such bathochromic shift signifies different changes within the porphyrin molecules upon attachment with a solid surface. Kar et al. have proposed a 16 nm red shift in the absorption of PP molecule upon attachment with ZnO nanoparticles [50]. Sarkar et al. demonstrated that attachment of Hematoporphyrin molecule with TiO$_2$ nanoparticles exhibits a 3 nm bathochromic shift [18]. However, after metalation with copper (II) metal ion, steady-state emission of PP is significantly decreased (as shown in Figure 5.9b), indicating non-radiative processes that can be attributed to fast intersystem crossing to the excited triplet state. Kim et al. also reported a several charge transfer transitions which are responsible for the quenching of the emission of PP [103].

Picosecond resolved emission transients have been used in order to investigate the excited state electron transfer dynamics of the nanohybrids [44, 60]. The fluorescence decay of PP, (Cu)PP, PP-TiO$_2$ and (Cu)PP-TiO$_2$ are shown in Figure 5.10 and associated time constant

Figure 5.10. *Fluorescence decay profiles of PP, (Cu)PP, PP-TiO$_2$, and (Cu)PP- TiO$_2$ measured at 630 nm wavelength upon excitation at a wavelength of 409 nm.*

value are tabulated in Table 5.3. The average life time of both PP and (Cu)PP have comparable timescale. Thus excited state electron transfer from PP to Cu (II) metal is ruled out from our TCSPC results. However, decrease in average life time was observed for PP-Ti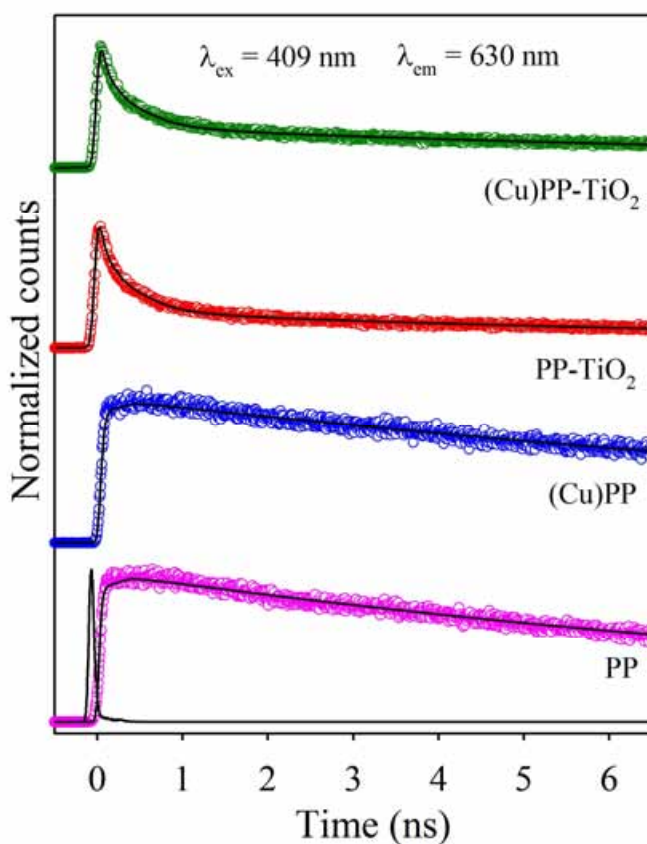O$_2$ in compare to PP and (Cu)PP. This is due to a significant faster component (200 ps) in case of PP-TiO$_2$ compare to PP showing excited state electron transfer from PP to TiO$_2$. Presence of Cu (II) metal ion within porphyrin moiety the fluorescence decay of (Cu)PP-TiO$_2$ remain essentially unaltered.

Table 5.3. Lifetimes of picosecond time-resolved PL transients of PP, PP-TiO$_2$ and (Cu)PP-TiO$_2$ detected at 630 nm PL maxima uopn excitation at 409 nm wavelength. The values in parentheses represent the relative weight percentages of the time components.

System	τ_1 (ps)	τ_2 (ps)	τ_{avg} (ns)
PP	11300 (100%)		11.3
(Cu)PP	11400 (100%)		11.4
PP-TiO$_2$	300 (59%)	9800 (41%)	4.2
(Cu)PP-TiO$_2$	300 (57%)	9712 (43%)	4.3

The photocatalytic activities of the nanohybrids were evaluated by photodegradation of the model organic contaminant MB under visible light irradiation. During the photocatalytic reaction, MB forms a well-known colorless product leucomethylene blue (LMB) as shown in equation (5.3) [105, 118].

$$2MB + 2e^- + H^+ = MB + LMB \qquad (5.3)$$

Figure 5.11a shows the time dependent UV-Vis spectra of MB in presence of the (Cu)PP-TiO$_2$ nanocomposite in a neutral aqueous solution under visible-light irradiation. Figure 5.11b shows changes in MB concentration as a function of time in presence and absence of photocatalysts under visible light irradiation. MB does not undergo decomposition reaction prior to illumination. The direct visible-light illumination without any catalyst is leading to insignificant decomposition of MB molecules within our experimental time window. The pure TiO$_2$ nanoparticles exhibit < 5% degradation of MB under the same conditions. In contrast, PP-TiO$_2$ shows an enhanced photocatalytic activity: 60% of MB degraded after 60 min illumination. (Cu)PP-TiO$_2$ nanohybrid showed almost complete degradation of MB (99%) within the same

experimental time window. Thus results demonstrate that presence of Cu (II) metal ions within porphyrin moiety further enhanced photocatalytic activity. The photocatalytic degradation efficiency of the light harvesting nanohybrid i.e. $(Cu)PP-TiO_2$ is reasonably good compared to the earlier reported literatures [25, 119-121]. Figure 5.11c shows photocatalysis of methylene blue (MB) at different wavelengths by $(Cu)PP-TiO_2$. Insignificant photocatalysis at 650 nm (MB absorbance maxima 660 nm) indicates that MB is unable to photosensitize $(Cu)PP-TiO_2$. Thus photocatalysis predominately takes place via sensitization of $(Cu)PP-TiO_2$. To explain reasons
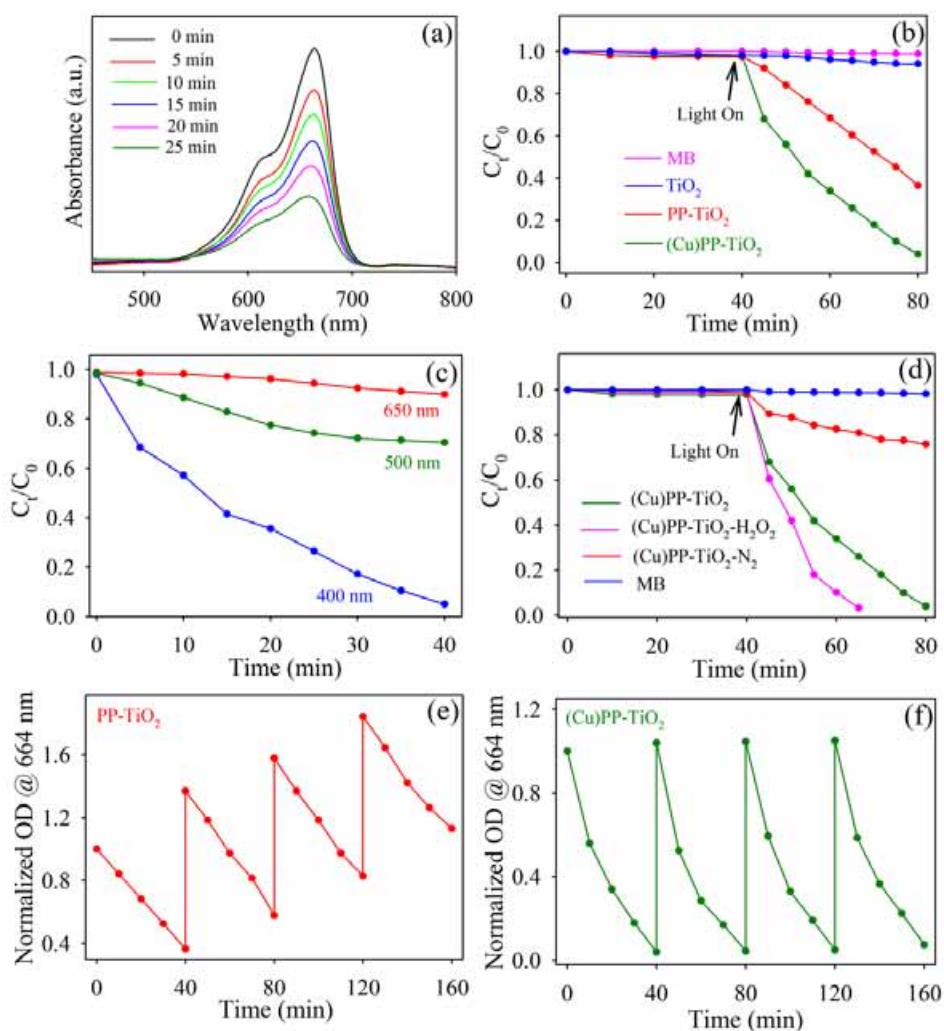
Figure 5.11. *(a) UV-Vis spectra for degradation of MB under visible light illumination by $(Cu)PP-TiO_2$.*
(b) Photocatalytic degradation of MB in presence of TiO_2, $PP-TiO_2$ and $(Cu)PP-TiO_2$ and only MB under visible light illumination. (c) Photocatalytic degradation of MB by $(Cu)PP-TiO_2$ at different wavelength.
(d) Photodegradation of MB by $(Cu)PP-TiO_2$ under conventional condition, presence of H_2O_2 and N_2 into the solution. A recyclability studies of (e) $PP-TiO_2$ and (f) $(Cu)PP-TiO_2$ under visible light illumination are also shown.

178

behind the enhanced photocatalytic behavior of the catalyst and underlying degradation mechanism, we further studied the photocatalytic activity of (Cu)PP-TiO$_2$ in the presence of a radical initiator (H$_2$O$_2$) and radical quencher (N$_2$ bubbling) separately (Figure 5.11d). Radical initiator and radical scavenger experiments were carried out to confirm the dominance of active species involved in the degradation process [122]. In fact, in the presence of H$_2$O$_2$, increases generation of OH$\cdot$ under solar light illumination which eventually increases the photocatalytic activity of (Cu)PP-TiO$_2$ for degradation of MB. The observation demonstrates the role of reactive oxygen species (ROS) in the degradation of MB. We further observed that the photodegradation efficiency of (Cu)PP-TiO$_2$ decreases with N$_2$ bubbling in the solution. The result implies that O$_2$ primarily acts as an efficient electron trap, leading to the generation of O$_2^{\cdot-}$ radicals during photocatalytic reaction [123]. Under visible light irradiation, the sensitizer (PP) injects electrons into the conduction band (CB) of TiO$_2$ and the subsequent degradation of MB takes place is initiated by CB electrons being transferred to it through reactive oxygen species (ROS). From the application point of view, photochemical stability and photocorrosion of the photocatalysts are also important parameters for evaluating their performance as it could reduces the cost of the process appreciably during photocatalytic reaction [124-126]. In order to further study photocatalytic performance of the as prepared nanohybrids, recycling experiment was carried out under repeated irradiation. Figure 5.11e-f show the repeated photocatalytic activity of different nanohybrids. The results indicate that there is insignificant decrease about the photodegradation efficiency for the CuPP-TiO$_2$ rate, which remains similar after four consecutive cycles, implying highest stability of the catalyst during the photodegration of MB. On the other hand, after four cycles, photocatalytic activity reduced to 30% (PP-TiO$_2$). The relatively efficient photocatalysis by the (Cu)PP-TiO$_2$ nanohybrid may be correlated with the additional structural stability due to presence of copper ion within the PP moiety [25, 127, 128]. The results also demonstrate that CuPP-TiO$_2$ is highly stable photocatalyst for practical application.

The light-harvesting ability of a sensitizer is a key parameter that determines the ability of solar energy capture and thus affects the photocurrent generated by the solar cell [129, 130]. The photocurrent measurements on the fabricated PP-TiO$_2$ and (Cu)PP-TiO$_2$ DSSC are shown in Figure 5.12a. The photocurrent spectra are found to be closely resembled with the absorption
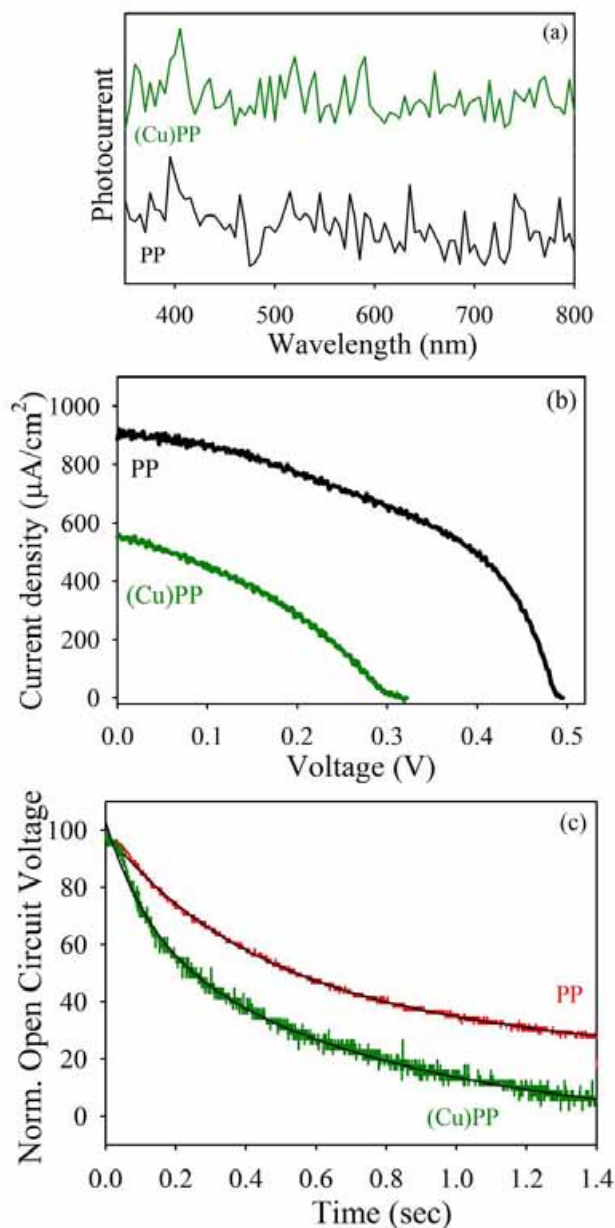
Figure 5.12. *(a) Wavelength dependent photocurrent response curves of different DSSCs (b) Current density–voltage curves under 100 mW cm^{-2} simulated AM 1.5G solar light irradiation. (c) Open circuit voltage decay profiles of different DSSCs.*

spectra of PP. The observation demonstrated that PP sensitizers on the photoanode surface are indeed responsible for photocurrent generation. In order to investigate the photovoltaic performance, we have fabricated DSSCs based on the porphyrin sensitizers. The J–V characteristics of the PP–TiO$_2$ DSSC with Cu (II) as central metal are shown in Figure 5.12b. The solar cell parameters are shown in Table 5.4. The results demonstrated that presence of

Table 5.4. Photovoltaic performance of DSSCs in presence and absence of copper ion within the Protoporphyrin macrocycle.

Cell	J_{SC} (μA/cm^2)	V_{OC} (V)	FF (%)	Efficiency (%)
PP	885.94	0.50	47.19	0.21
(Cu)PP	550.55	0.32	34.17	0.05

copper within the porphyrin moiety decreases overall photovoltaic efficiency. Different photovoltaic efficiency in presence of Cu (II) metal ion within the porphyrin moiety have been investigated by monitoring the temporal decay of the open circuit voltage which has been monitored for different cells in the dark following a brief period of illumination as shown in Figure 5.12c. The open circuit voltage decay reflects the timescales (as shown in Table 5.5) for the recombination processes of the electrons at the conduction band of the semiconductor with the oxidized electrolytes. Thus inclusion of copper within the porphyrin moiety eventually increase the back electron transfer, thus can substantially affect the photovoltaic performance i.e. reduces its efficiency [54, 131, 132].

**Table 5.5. Dynamics of photovoltage transients of DSSCs fabricated using different active and counter electrodes. The values in parentheses represent the relative weight percentages of the time components.**

Active electrode	τ_1 (ms)	τ_2 (ms)	τ_{avg} (s)
PP-TiO$_2$	0.42 (63.1 %)	3.0 (36.9 %)	1.37
(Cu)PP-TiO$_2$	0.13 (36.4 %)	0.76 (63.6 %)	0.53

There are several reports which indicate that a promising light harvesting nanohybrid is very much efficient for photocatalysis and photovoltaic applications due to synergetic effect of many factors like hierarchical structure, surface area, rapid photoinduced charge separation and a relatively slow charge recombination [133-136]. In our present study, the developed PP-TiO$_2$ light harvesting nanohybrid is very much efficient for MB degradation in presence of Cu (II) metal ion within the core of porphyrin moiety. A tentative photocatalytic mechanism of (Cu)PP-TiO$_2$ was deduced and a schematic illustration shown in Scheme 5.2. Under visible light
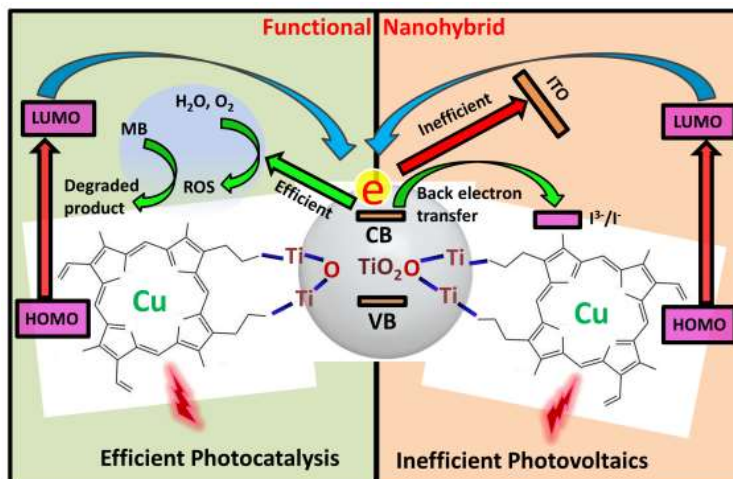
Scheme 5.2. Schematic representation of the overall mechanistic pathways for photocatalytic and photovoltaic efficiency by (Cu)PP-TiO₂.

illumination, excitation of electron from HOMO to LUMO takes place by PP molecule attached on TiO_2 surface. Then transfer of electron to the CB of TiO_2 takes place which eventually reacts with dissolve oxygen and water to produce ROS. However, presence of Cu (II) metal ion within porphyrin moiety increases stability of (Cu)PP-TiO_2 nanohybrid against photo bleaching and thus promote generation of ROS that are responsible for enhancement in photocatalytic activity. To further study the effect on photovoltaics by (Cu)PP-TiO_2 nanohybrid, we observed that light harvesting nanohybrid is inefficient for DSSC application. We note that although nanohybrid is sufficiently stable against photobleaching, the enhanced back electron transfer due to the recombination of photoinjected electrons at the CB of TiO_2 with redox electrolyte contribute significantly. The enhancement in back electron transfer is therefore responsible for poor photovoltaic device as it diminish the charge carriers to be collected into their respective contacts. Based on the above observation a schematic illustration is proposed as shown in Scheme 5.2.

5.2.3. Facile Synthesis of Reduced Graphene Oxide-Gold Nanohybrid for Potential Use in Industrial Waste-Water Treatment [137]:

The formation of Au-RGO nanohybrids has been confirmed by TEM. From Figure 5.13a, the nanosheet like morphology of RGO is clearly visible along with uniformly high coverage of Au NPs. The average particle size of Au NPs anchored on the RGO nanosheet is found to be 25.62±0.35 nm. The HRTEM image and fast Fourier transform (FFT) pattern of Au-RGO

nanohybrid (Figure 5.13b) demonstrate high crystallinity of the Au NPs as well as the RGO nanosheet. The inter-planar distance between the fringes is found to 0.235 nm which correspond to the (111) plane of Au NPs [138]. However, lattice spacing of 0.356 nm for RGO corresponds to (002) planes [139]. Formation of nanohybrid was further confirmed by SEM. Figure 5.13c
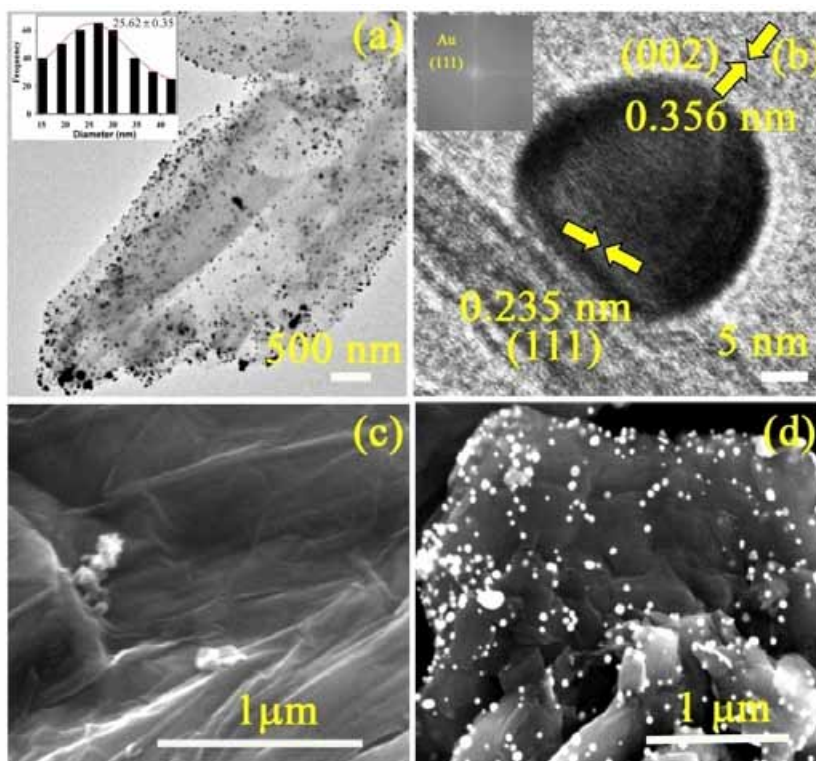
Figure 5.13. *(a) TEM image of the as synthesized Au-RGO nanohybrids (inset shows size distribution of Au NPs). (b) HRTEM image of a Au NP attached to the RGO (Inset shows FFT pattern of Au-RGO). SEM images of (c) RGO and (d) Au-RGO.*

shows an SEM image of RGO having typical wrinkled and paper-like sheet morphology. Figure 5.13d illustrates an SEM image of Au-RGO nanohybrid, reveals that the nanoparticles are well dispersed on graphene nanosheets which is consistent with TEM image.

The presence of Au NPs on RGO nanosheets was further characterized by X-ray diffraction (XRD). From Figure 5.14a the diffraction peaks can be indexed as the (111), (200), (220), (311) and (222) reflections of the face-centered cubic (fcc) structure of Au (JCPDS 04-0784) [140]. Additionally, exfoliation behavior of RGO in presence of Au NPs can be explained by XRD analysis [141]. After photochemical reduction of GO, the broad diffraction peak at 24° arises due to partial restacking of some graphene oxide layer [141]. However broad peak at 24º

disappear in Au-RGO due to Au NPs effectivelly prevented the restacking of GO layer. Thus the
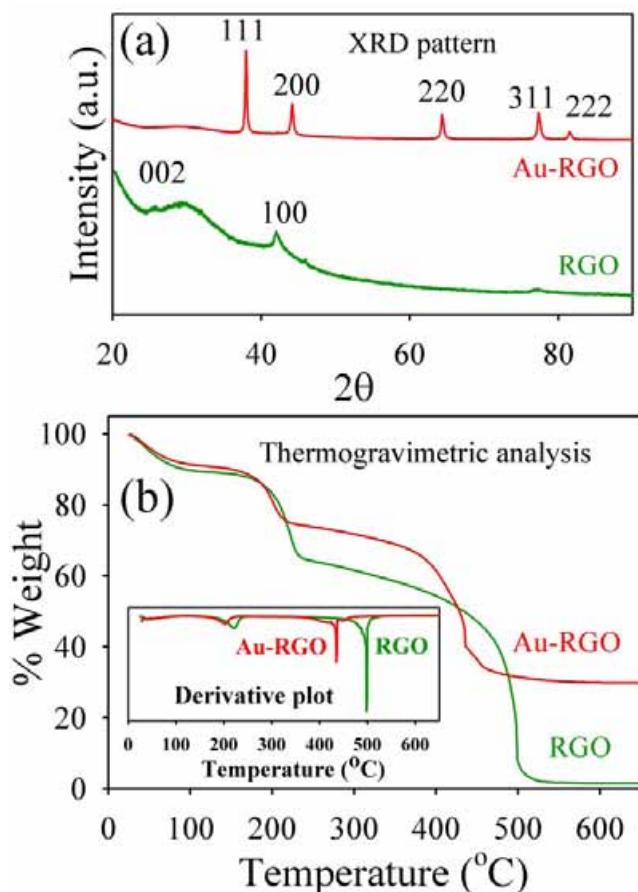
Figure 5.14. *(a) XRD patterns of Au-RGO and RGO. (b) TGA curves of Au-RGO and RGO.*

XRD pattern indicates that Au NPs successfully incorporated between RGO layers and act as a spacer between two layers to prevent restacking. Thermogravimetry analysis (TGA) curves of both RGO and Au-RGO shows an obvious weight loss between 160 and 220 °C which is attributed to pyrolysis of the labile oxygen-containing functional groups, yielding CO, CO_2 and steam [142] as shown in Figure 5.14b. RGO shows a complete decomposition of carbon at about 500°C. In contrast, the Au-RGO nanohybrid shows a lower temperature about 420°C, to fully decompose the carbon of Au-RGO. A residual mass of about 30% indicates loading of Au NPs in the Au-RGO nanohybrid. A lower the thermal decomposition temperature for Au-RGO in compare to RGO due to presence of Au NPs help RGO in exfoliation, thereby increasing the interlayer spacing and porosity of the hybrid.
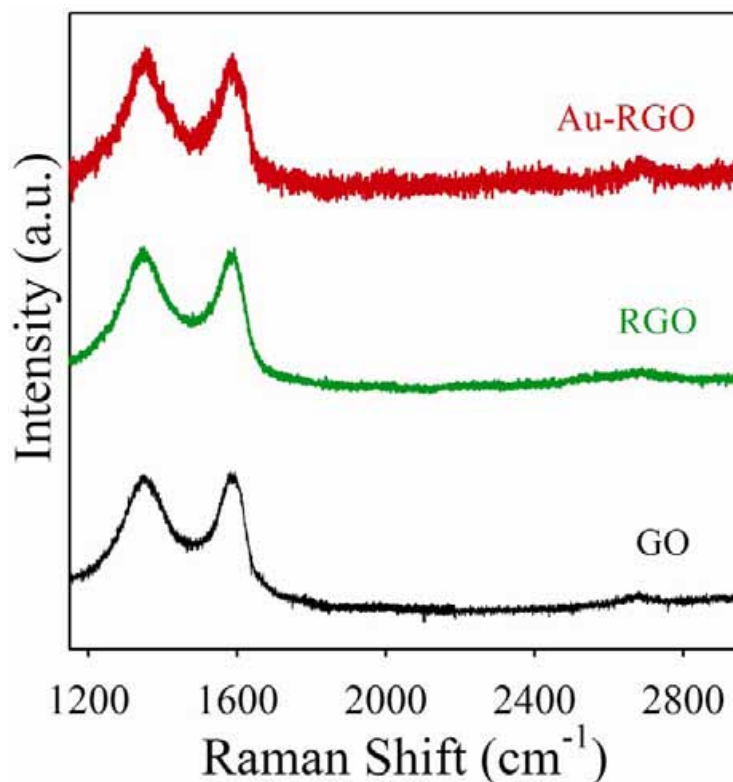
Figure 5.15. *Raman spectra of graphene oxide (GO) and Au decorated graphene oxide (Au-RGO) nanohybrids. The baselines of the spectra are shifted for clarity.*

In order to further investigate the structural and electronic properties of Au-RGO nanohybrid, Raman spectroscopy has been used as a tool. Raman spectra of GO, RGO and Au-RGO are shown in Figure 5.15. The GO exhibit two characteristic peaks located at 1340 cm^{-1} and 1580 cm^{-1}, which can be attributed to D and G bands, respectively, from GO. The D bands correspond to a defect induced in plane A$_{1g}$ zone-edge mode and G band is attributed to E$_{2g}$ mode [93]. After photoirradiation, RGO and Au-RGO show an increased intensity ratio (I$_D$/I$_G$) of 1.01 and 1.12, respectively, in comparison to GO (0.98), indicating a decrease in size of the sp^2 domains [143]. Here after photoirradiation, a broad 2D band for Au-RGO nanohybrid located at 2632 cm^{-1} indicating the formation of layer graphene nanosheet, is present in the nanohybrid [93].

XPS technique becomes useful in order to further investigate the structural evolution of the as-synthesized Au-RGO nanohybrid. Survey-scan XPS spectra obtained from RGO and Au-

RGO are shown in Figure 5.16a. Due to the deposition of a thin layer of the materials on the Si
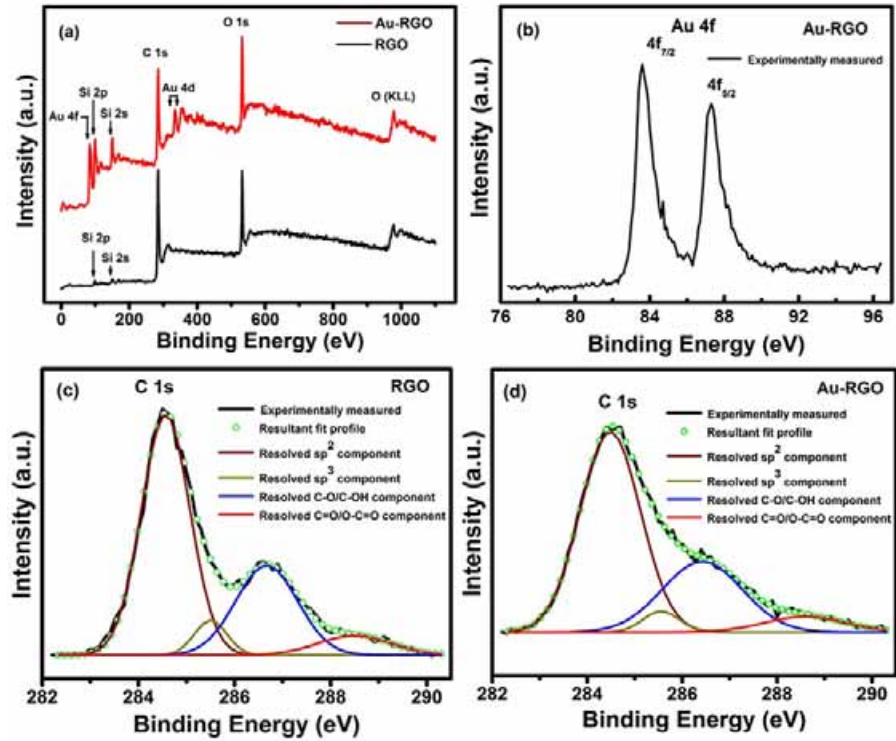
Figure 5.16. *Survey and high resolution XPS spectra of RGO and Au-RGO (a) Survey scans of RGO and Au-RGO (b) High resolution Au 4f spectrum of Au-RGO (c) High resolution C 1s spectrum and resolved components of RGO (d) High resolution C 1s spectrum and resolved components of Au-RGO.*

substrate and the take off angles used for XPS analysis, signature of silicon (Si) signal arising from Si-substrate underneath can be detected in the survey scans of both the samples. It is evident from Figure 5.16a that carbon (C) and oxygen (O) are the primary constituents of RGO while Au-RGO is composed with C, O and gold (Au). Figure 5.16b shows the high resolution Au 4f spectrum recorded from Au-RGO sample where Au $4f_{7/2}$ and Au $4f_{5/2}$ spin-orbit doublets are observed to be located at ~83.6 and 87.3 eV respectively in binding energy scale. Herein, the chemical nature of gold within Au-RGO has been attributed as metallic-Au (Au^0) which is consistent with previous literature [47, 144, 145]. Observed small negative shift (~0.4 eV) in the position of Au 4f spin-orbit doublet with respect to that of the standard referencing positions of metallic-Au (Au^0: Au $4f_{7/2}$ ~ 84.0 eV and Au $4f_{5/2}$ ~87.7 eV) suggests that a strong interaction exists between Au and RGO framework [47, 145]. High resolution C 1s spectra of RGO and Au-RGO can be resolved into four Gaussian components. Peaks centered at binding energy positions

of ~284.5, 285.5, 286.6 and 288.5 eV have been assigned to sp^2 (C=C), sp^3 (C-C, C-H), epoxy and/or hydroxyl (C-O/C-OH) and carbonyl and/or carboxyl (C=O/O-C=O) functional groups respectively (Figures 5.16c and 5.16d) [146, 147]. As shown in Figures 5.16c and 5.16d, excellent match between the experimentally measured C 1s profile (represented by solid black line) and the resultant fit profile (represented by green colored hollow circles) signifies the merit of the peak fitting protocol undertaken to resolve the C 1s profiles into their respective components. However, the concentrations of these functional groups are found to vary depending on the reduction protocol employed to reduce the graphene oxide. Compositions of RGO and Au-RGO as obtained from XPS analysis are listed in Table 5.6. Degree of reduction of RGO can be determined by the abundance of sp^2 hybridized carbon relative to other oxygenated carbon groups (e.g., epoxy, hydroxyl, carboxyl, carbonyl etc) in it. In this regard, degree of reduction of Au-RGO is found to be slightly higher than that of RGO sample (Table 5.6). Also, the concentration of sp^3-C in RGO is estimated to be higher than Au-RGO (Table 5.6).

Table 5.6. Compositions of RGO and Au-RGO as obtained from XPS analysis.

Sample	Atomic ratio	Concentration (%)			
	(Au/C)	sp^2 -C (C=C)	sp^3 -C (C-C/C-H)	C-O/C-OH (epoxy/hydroxyl)	C=O/O-C=O
Au-RGO	0.03	61.3	3.8	28.6	6.3
RGO	-	59.2	5.7	28.1	7.0

Adsorption behaviors of Au-RGO nanohybrid was studied with different dyes at varied pH and temperature as shown in Figure 5.17. From Figure 5.17a, it is observed that adsorption capacity of Au-RGO is higher compared to the RGO nanosheet. This observation could indicate that the presence of Au NPs decorated on RGO sheet enhances the exfoliation of RGO by acting as a spacer. Thus increase in effective surface area facilitates enhanced dye adsorption. Adsorption capacities of the dyes by Au-RGO nanohybrid are shown in Figure 5.17b. It is observed that the Au-RGO nanohybrid is highly efficient for removal of cationic dyes in comparison to anionic and neutral dyes. The results indicates that adsorption capacity for crystal violet, methylene blue, Rh123, eosin and coumarin were 31, 19, 17, 7 and 5 μmol g^{-1} respectively at pH 6. The adsorption capacity of the Au-RGO nanohybrid is comparatively higher than other graphene derivatives [84, 148-150] as shown in Table 5.7. The higher

adsorption capacity of Au-RGO nanohybrid towards cationic dyes suggests strong π-π and electronic interaction between Au-RGO and cationic dyes. This is in conformity to that observed in case of the negative surface charge (-35 mV) of Au-RGO nanohybrid.
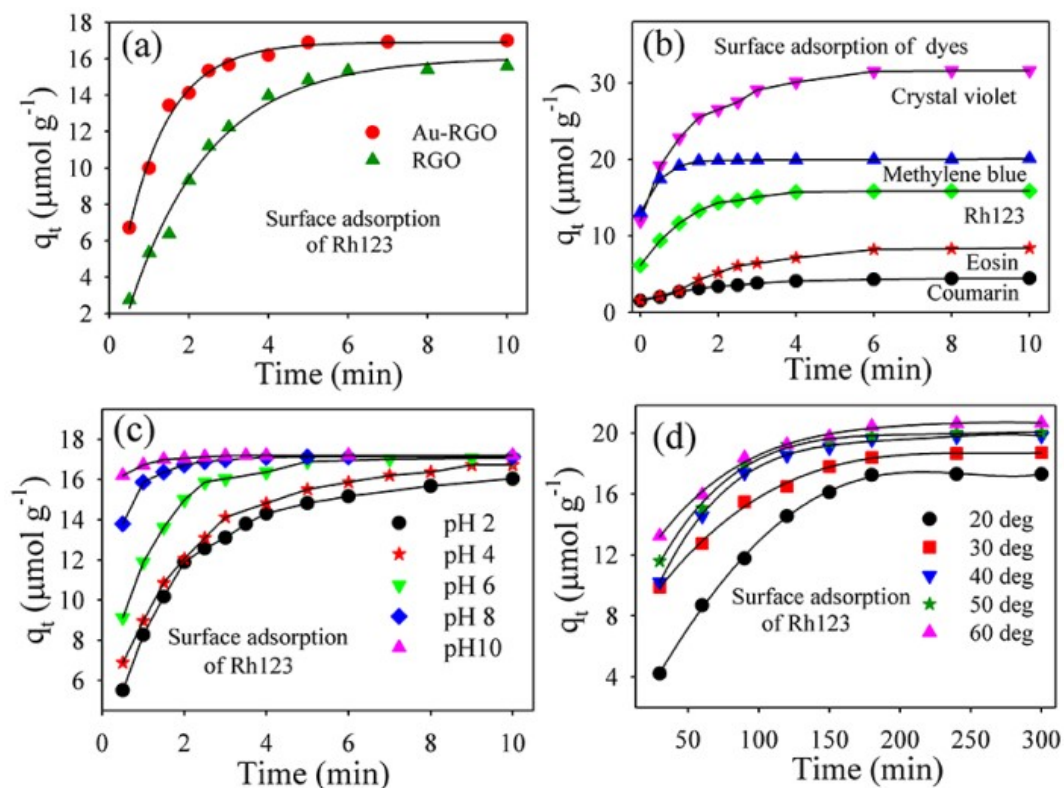
Figure 5.17. *Effect of adsorption rate (a) Au-RGO vs RGO, (b) different dyes, (c) different pH and (d) different temperatures conditions (Solid lines are guide to the eyes).*

Table 5.7. Comparison of the maximum adsorption capability of various adsorbents for Rhodamine.

Adsorbents	Capacity (mg/g)	Contact time (min)	Ref.
Graphene oxide	29	180	49
Graphitic N-doped carbon nanoparticles-decorated carbon flake	13.7	60	48
Hybrid of reduced graphene oxide-Fe_3O_4 nanoparticles	50	720	22
Magnetic-reduced graphene oxide nanocomposite	13.5	120	47
Au-RGO nanohybrid	34.3	10	Present work

The effect of pH on adsorption has been studied over a wide range as shown in Figure 5.17c. It is observed that an increase in adsorption efficiency from 15.3 to 17.2 μmol g^{-1} occurs with increase in pH from 2 to 10. The higher adsorption capacity of Rh123 at high pH may be due to increase negative charge at the surface of adsorbents which may facilitates more Rh123 dye coming into the contact of Au-RGO surface. The reason for cationic dye adsorption with increase in pH is due to increase in ionic interaction in addition to π-π stacking between more negatively charged graphene oxide surface and cationic dye [151]. In order to find out the effect of temperature on adsorption rate, the adsorption experiments were conducted at five different temperatures (20, 30, 40, 50 and 60ºC) at pH 6. It is observed that adsorption capacity of Rh123 on Au-RGO nanohybrid increases from 17.36 to 20.60 μmol g^{-1} as the temperature increased from 293 to 333 K. The higher adsorption capacity of Au-RGO nanohybrid with increase in temperature indicates that the thermal energy allows the dye molecules to come into contact with the internal pores of RGO nanosheet, thereby increasing the adsorption capacity.

Adsorption kinetics is an important tool in order to investigate the adsorption process. The adsorption kinetics of Rh123 on Au-RGO nanohybrid has been studied by pseudo first-order and pseudo second-order models as shown in Figures 5.18a and 5.18b. The Lagergren pseudo first-order kinetic model can be expressed as,

$$\log(q_e - q_t) = \log q_e - k_1 t / 2.303 \tag{5.4}$$

where, k_1 is the pseudo first-order rate constant, q_e and q_t denote the adsorption capacity of Rh123 onto RGO sheet at equilibrium and at time t, respectively.

The pseudo second order kinetic model can be expressed as,

$$t / q_t = 1 / k_2 q_e^2 + 1 / q_e t \tag{5.5}$$

where, k_2 is the pseudo second-order rate constant.

For pseudo first-order model and pseudo second-order model, the values of rate constant and adsorption efficiency are presented in Table 5.8. From the table, it is evident that correlation coefficients (R^2) for pseudo second order are better than that of pseudo first-order model. Therefore, adsorption of Rh123 on Au-RGO nanohybrid follows pseudo second-order model more correctly than pseudo first-order model [152, 153].

In order to investigate the distribution behavior of adsorbate over adsorbent Langmuir and Freundlich adsorption isotherm model are useful. Langmuir adsorption isotherm is based on

the assumption that monolayer coverage of adsorbate over the adsorbent, which is assumed to be homogeneous. The Langmuir adsorption isotherm can be represented as

$$C_e / q_e = 1/Q_0 K_L + (1/Q_0) C_e \qquad (5.6)$$

where, K_L denotes the Langmuir constant related to the energy of adsorption and Q_0 is the Langmuir adsorption capacity. The Freundlich adsorption isotherm can be expressed as,

$$\log q_e = \log K_f + (1/n) \log C_e \qquad (5.7)$$

where, q_e is the amount adsorbed, C_e is the concentration of the adsorbate, K_F and n are the Freundlich constants related to adsorbate and adsorbent respectively.
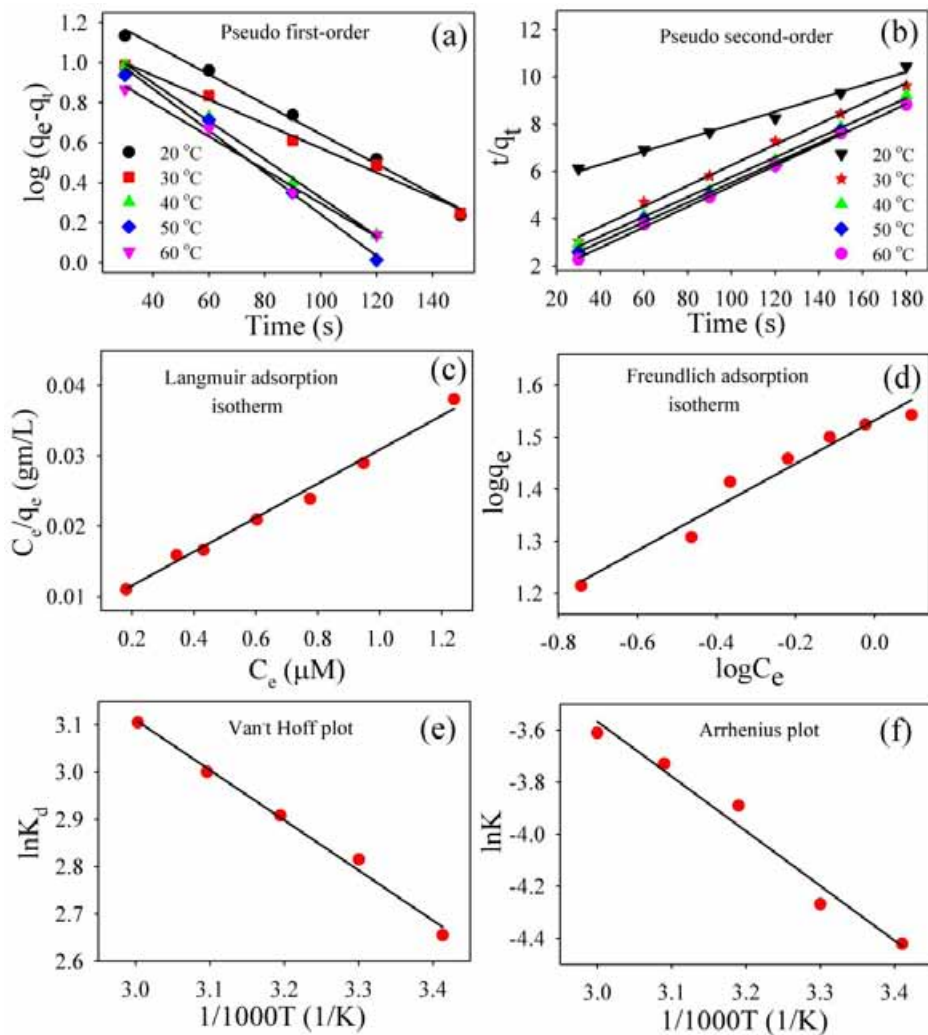

Figure 5.18. *Plot of (a) pseudo first-order model, (b) pseudo second-order model, (c) Langmuir adsorption isotherm and (d) Freundlich adsorption isotherm for Rh123 adsorption. (e) Van't Hoff plot and (f) Arrhenius plot for Rh123 adsorption.*

Plot of C_e/q_e vs C_e gives a straight line indicating that adsorption of dye follows Langmuir adsorption isotherm model as shown in Figure 5.18c. The values of Q_0 and K_L calculated from the slope and intercept are shown in Table 5.9. Plot of $\log q_e$ vs $\log C_e$ gives a straight line indicating that adsorption of dye follows Freundlich adsorption isotherm model as shown in Figure 5.18d. The values of n and K_f calculated from the slope and intercept are shown in Table 5.9. The R^2 value for Langmuir adsorption isotherm is high compared to the Freundlich adsorption isotherm, which indicates adsorption of Rh123 on Au-RGO nanohybrid preferably follow the Langmuir adsorption isotherm. These results are in good agreement with reported results [88, 154].

Table 5.8. Kinetic model parameters for the adsorption of Rh123 onto Au-RGO nanohybrid.

Model	Parameters	Temperature(°C)				
		20	30	40	50	60
Pseudofirst-order	K_1 (s^{-1})	0.017	0.014	0.022	0.024	0.019
	R^2	0.990	0.989	0.996	0.986	0.987
Pseudosecond-order	K_2 (μM^{-1}s^{-1})	1.52×10^{-4}	9.78×10^{-4}	1.10×10^{-3}	1.30×10^{-3}	1.81×10^{-3}
	R^2	0.985	0.995	0.997	0.995	0.998

Table 5.9. Langmuir and Freundlich constants for adsorption of Rh123 onto Au-RGO nanohybrids.

Temperature (K)	pH	Langmuir constants	
303	6	Q_o (μmol gm^{-1})	K_L (μmol g^{-1})
		38.71	0.227
		Freundlich constants	
		n	K_F (μmol g^{-1})
		2.39	34.1

Furthermore, the various thermodynamic parameters associated with the adsorption process can be calculated using following equations,

$$K_d = \frac{q_e}{C_e} \qquad (5.8)$$

$$\Delta G^o = -RT \ln K_d \qquad (5.9)$$

$$\ln K_d = \Delta S^o / R - \Delta H^o / RT \qquad (5.10)$$

where, K_d is the distribution coefficient, T is the temperature, R is the gas constant, ΔG^0 is the change in free energy, ΔH^0 is the change in enthalpy and ΔS^0 is the change in entropy.

The calculated thermodynamic parameters are summarized in Table 5.10. The negative free

Table 5.10. Thermodynamic parameters for adsorption of Rhodamine123 onto Au-RGO nanohybrids.

Temperature (°C)	ΔG° (kJ mol^{-1})	ΔH° (kJ mol^{-1})	ΔS° (kJ mol^{-1} K^{-1})
20	-6.46	8.33	0.05
30	-7.07		
40	-7.54		
50	-8.05		
60	-8.58		

energy values at different temperatures suggest the feasibility of the process for the adsorption of Rh123 onto Au-RGO nanohybrid. The calculated positive ΔH^0 value (8.72 kJ mol^{-1}) indicates the endothermic nature of the process, where as positive entropy change (0.05 kJ mol^{-1} K^{-1}) indicates the good affinity of Rh123 toward the Au-RGO nanohybrid and the increased randomness at the Au-RGO nanohybrid−water interface during the adsorption process [155-157]. The activation energy (E_a) gives an idea about the nature of the adsorption process. Therefore the value of activation energy (E_a) for the adsorption of Rh123 onto Au-RGO nanohybrid can be calculated by using the Arrhenius equation,

$$\ln K = \ln A - E_a / RT \qquad (5.11)$$

where, A is the Arrhenius pre-exponential factor, R is the gas constant and E_a denote the energy of activation during adsorption process. From the plot of ln K *vs* 1/T (as shown in Figure 5.18f), the activation energy was found to be 17.45 KJ mol^{-1}. A low activation energy (< 40 kJ mol^{-1}) implies physical adsorption process whereas a relatively high activation energy (> 40 kJ mol^{-1}) corresponds the chemical adsorption process [153]. Hence, low activation energy indicates that the adsorption of Rh123 on Au-RGO nanosheet occurs by physical adsorption process which is consistent with previous literature [153, 154].

Figure 5.19a shows the UV-Vis absorption spectra of RGO and Au-RGO. The absorption spectrum of RGO shows a peak at 306 nm indicating incomplete reduction of GO [158]. On the other hand, the absorption spectrum of Au-RGO shows an additional peak at 540 nm due to surface plasmon resonance of gold NPs, indicating decoration of Au NPs on the RGO nanosheet as shown in Figure 5.13. A monotonous decrease of the fluorescence intensity of Rh123 upon adsorption at the Au-RGO nanohybrid is shown in Figure 5.19b. Plot of relative intensity (F_0/F;

where F_0 and F are the fluorescence intensity of Rh123 without and with Au-RGO respectively) with various Au-RGO concentrations is shown in the inset of Figure 5.19b. A deviation from linearity in the increase of F_0/F with gradual increase in the Au-RGO concentration indicates that both static and dynamic quenching is associated in the quenching process [159]. The quenching
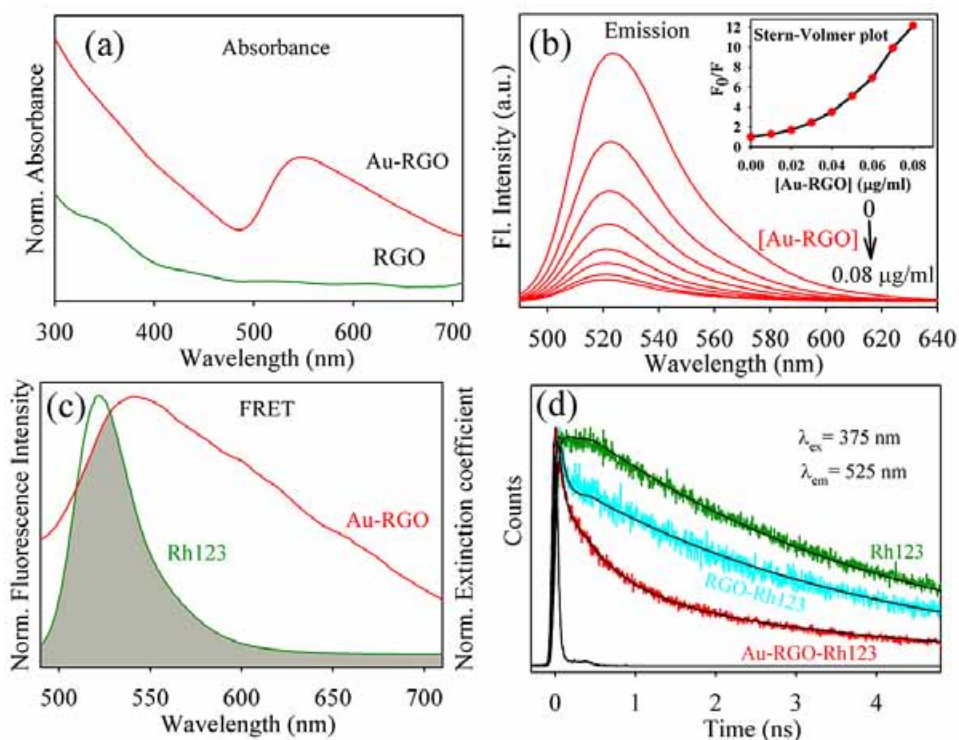
Figure 5.19. *(a) UV-Vis absorption plot for Au-RGO and RGO. (b) The effect of Au-RGO hybrid on the fluorescence intensity of Rh123 (inset shows Stern-Volmer plot). (c) The overlap integral of Au-RGO absorbance and Rh123 emission. (d) Fluorescence decay profiles of Rh123, RGO-Rh123 and Au-RGO-Rh123.*

Table 5.11. Lifetimes of picosecond time-resolved fluorescence transients of Rh123, Rh123-RGO and Rh123-Au-RGO, detected at various fluorescence maxima upon excitation at different wavelengths. The values in parentheses represent the relative weight percentages of the time components.

System	λ_{ex} (nm)	λ_{em} (nm)	τ_1 (ps)	τ_2 (ps)	τ_3 (ps)	τ_{avg} (ps)
Rh123	375	525	3850 (100%)			3850
Rh123-RGO	375	525	60 (52%)	3850 (48%)		1874
Rh123-Au-RGO	375	525	60 (53%)	546 (27%)	3850 (20%)	825

of Rh123 followed by surface adsorption at the Au-RGO surface can be rationalized in the following ways. Firstly, the remarkable spectral overlap (J(λ)=2.04X10^{20} M^{-1}cm^{-1}nm^4) of the Au-RGO absorption spectrum with that of the emission spectrum of Rh123 reveals possibility of (FRET) or (NSET) from Rh123 to the surface of Au-decorated RGO. A significant shortening of fluorescence lifetime of Rh123 on the Au-NP decorated RGO compared to that in bulk water is shown in figure 5.19d and Table 5.11. Following FRET strategy [160]. We have estimated the donor (Rh123) acceptor (surface of Au NPs) distance is found to be 36.3 nm, which is beyond the probing limit of FRET (~10 nm) and much higher than the diameter of the Au NPs as revealed from the TEM micrograph (Figure 5.13). Thus the FRET is not expected to be quenching mechanism of the probe Rh123 at the surface of the Au NPs in the nanosheet of RGO. The donor-acceptor distance following NSET strategy is 7.4 nm, which indicates proximity of the dye Rh123 at the Au-NPs (average diameter of ~25 nm). It should be noted that the fluorescence quenching of Rh123 could be associated with the photoinduced electron transfer from the dye to the RGO surface [161]. As shown in figure 5.19d and Table 5.11, a faster time component in the fluorescence decay of Rh123 at the RGO surface in absence of Au-NPs is eminent and consistent with photoinduced electron transfer [162].

The interaction between Rh123 and Au-RGO nanohybrid was studied by Fourier transform infrared (FTIR) absorption spectroscopy. The FTIR spectra of Rh123 before and after adsorption onto Au-RGO nanohybrid are shown in Figure 5.20. FTIR spectra of RGO exhibit a band at 1725 cm^{-1} corresponding to C=O stretching frequency of the –COOH group. The peak at 1228 cm^{-1} is attributed to C-OH (epoxy functional group) and the peak at 1065 cm^{-1} originates from the C-O band of alkoxy functional group [163]. For free Rh123, the peaks at 1651, 1594, 1541, 1476, 1411 cm^{-1} correspond to xanthene ring stretching frequencies while peaks at 1081, 1130, 1187 and 1287 cm^{-1} are attributed to the C-H bending modes of the xanthene ring [159]. After adsorption of Rh123 onto Au-RGO nanohybrid, the peaks corresponding to xanthene ring and –COOH, C-OH, C-O bands of alkoxy group present in Au-RGO nanohybrid are perturbed, which indicates interaction of these groups during adsorption process. So, -OH group of Au-RGO undergoes electrostatic interaction with =NH$_2$$^+$ of Rh123, which may facilitate adsorption of Rh123 onto Au-RGO surface. Here π-π electrostatic interaction between π electrons of Rh123 and π electrons of Au-RGO nanohybrid may facilitate the adsorption of Rh123 onto Au-RGO surface, which is consistent with the reported literature [154, 164].
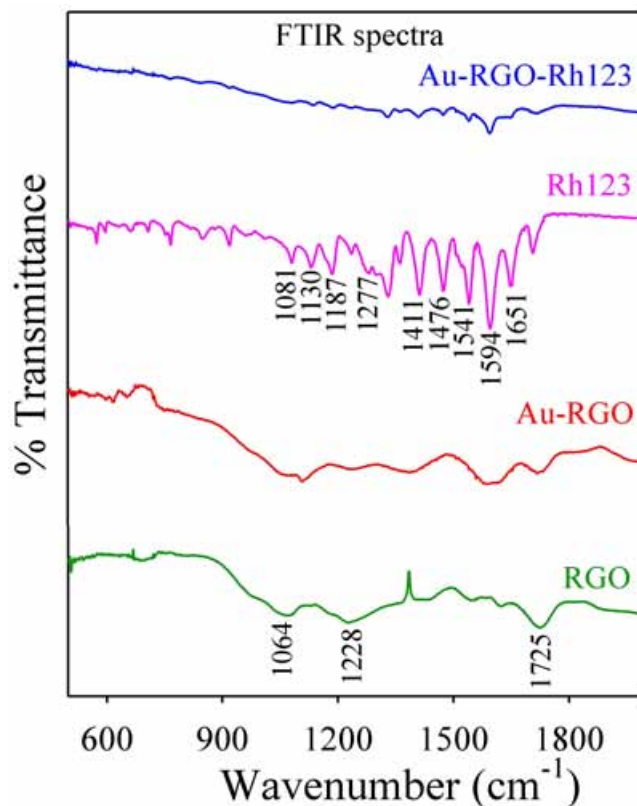
Figure 5.20. *FTIR spectra of Rh123 before and after adsorption on Au-RGO.*

For potential application of Au-RGO nanohybrid in dye removal, we first developed a prototype device as shown in Figure 5.21a. The developed device consists of 0.22 μm filter paper that is directly attached with a syringe pump. At first we loaded Au-RGO nanohybrid (10 mg) over 0.22 μm filter paper so that water can transport through the pores of the filter paper. SEM images of the filter paper shown in Figure 5.21a (inset shows the distance between pores is approximately 227 nm). The dyes used in adsorption process are Rh123 and crystal violet. During the adsorption process flow rate is maintained at 1mL/min and each cycle consists of 10 mL of dye solution. From Figures 5.21b and 5.21c, it is clear that Au-RGO nanohybrid is very much efficient for removal of Rh123 and crystal violet, whereas under controlled condition (absence of Au-RGO loading onto filter) adsorption of Rh123 and crystal violet is negligibly small. The results clearly demonstrate that nanohybrid is very much efficient for dye adsorption. After the 10th cycle of re-adsorption, nanohybrid is not likely further affect the adsorption capacity, which is almost same as the 1st cycle. Such a device has advantage of easy and rapid extraction of dyes from waste water along with recyclable feature with almost no compromise on the adsorption capacity.
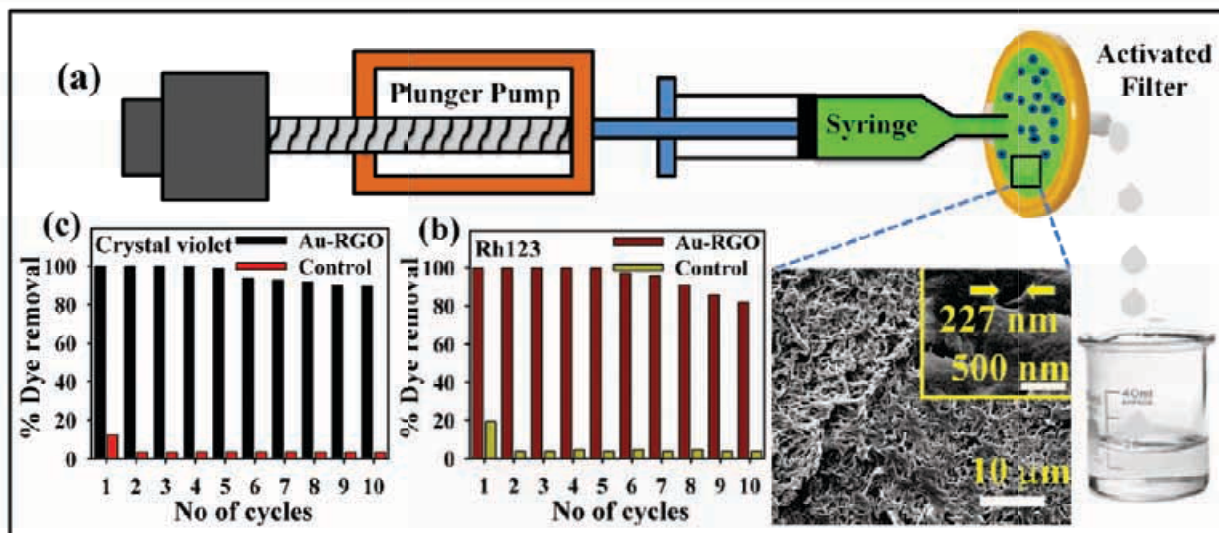
Figure 5.21. *(a) Schematic representation of flow device developed for adsorption (Inset shows the SEM image of filter), (b) and (c) shows recyclability study of Rh123 and crystal violet respectively.*

5.3. Conclusion:

We have synthesized and characterized a protoporphyrin IX-ZnO nanohybrid (PP-ZnO) for potential applications in a prototype photo-device for decontamination of test water with a model hazardous organic waste product from the textiles industry. We have investigated the role of dissolved iron (III) and copper (II) ions in the test water based on their natural abundance (WHO prescribed). A number of microscopic and spectroscopic studies involving HRTEM, XRD, UV-Vis absorption, fluorescence and FTIR have confirmed the structural integrity of nanohybrid and the mode of attachment of the "green" PP to the ZnO host. Steady-state IR spectroscopy has provided conclusive experimental evidence for covalent attachment of PP to the host ZnO nanoparticles. On the other hand, our femtosecond resolved transient absorption followed by picosecond resolved fluorescence studies have clearly demonstrate that the residence of photoexcited electron transfer from the PP sensitizer in the centrally located iron moiety hinders ground-state bleach recovery of the sensitizer, affecting the overall photocatalytic efficiency of the nanohybrid. A schematic description of the mechanistic pathway in the nanohybrid upon UV and visible light irradiation has also been presented. We envisage that this detailed spectroscopic study will potentially find relevance in the large-scale use of non-toxic and less expensive porphyrin-based nanohybrids for decontamination of waste water.

In another study, PP-TiO$_2$ has been used as a light harvesting nanohybrid for photocatalysis and DSSCs application. The picosecond resolved fluorescence quenching successfully explains the excited state electron transfer dynamics in the nanohybrid. In the Protoporphyrin sensitizers, the presence of centrally located Cu (II) metal ion can substantially affect the photovoltaic and photocatalytic performance. Presence of copper metal ion within the porphyrin moiety increases the photocatalytic activity but decreases the DSSC efficiency. The outstanding photocatalytic activity of the (Cu)PP-TiO$_2$ nanohybrid is concluded to be structural stability, whereas faster back electron transfer is found to be responsible for poor photovoltaic performance. These results highlight that different ultrafast processes are equally crucial in light harvesting nanohybrid upon photoinduced charge separation. The present work also demonstrates that exciting potential light harvesting nanohybrid may not always simultaneously be used in visible-light photocatalysis and photovoltaics.

In summary, we have developed a facile approach for the synthesis of Au-RGO nanohybrids where reduced graphene oxide nanosheets are decorated by a uniform distribution of Au NPs. Due to the high surface area and negative surface charge, Au-RGO nanohybrids are highly efficient for dye removal through electrostatic and π-π interactions. The efficiency of dye can be tuned up by changing pH value and the temperature of the medium. A Langmuir model has been successfully applied to show that the adsorption takes place *via* surface monolayer coverage. The kinetics of dye removal process indicates that the pseudo-second order kinetics are preferably followed, while thermodynamic parameters suggest that the adsorption process is spontaneous and endothermic in nature. Time-resolved fluorescence spectroscopy clarified the excited state electron and energy transfer processes associated with adsorption process. A shortening of average lifetime after adsorption of Rh123 on an Au-RGO surface leads to NSET process because of close proximity between dye and Au NPs. Development of an engineered prototype device shows rapid efficiency as well as recyclability for dye removal from waste water. Therefore, we believe that such kind of nanohybrids will be suitable for water purification and treatment.

References

[1]   B. O'Regan, M. Gratzel, A Low-Cost, High-Efficiency Solar Cell Based on Dye-Sensitized Colloidal TiO$_2$ Films, *Nature* 353 (1991) 737-740.

[2]   A. Fujishima, K. Honda, Electrochemical Photolysis of Water at a Semiconductor Electrode, *Nature* 238 (1972) 37-38.

[3]   H. Zhou, T. Fan, D. Zhang, Biotemplated Materials for Sustainable Energy and Environment: Current Status and Challenges, *ChemSusChem* 4 (2011) 1344-1387.

[4]   Y. Sun, Q. Wu, G. Shi, Graphene Based New Energy Materials, *Energy Environ. Sci.* 4 (2011) 1113-1132.

[5]   L. M. Peter, The Grätzel Cell: Where Next?, *J. Phys. Chem. Lett.* 2 (2011) 1861-1867.

[6]   J. N. Demas, D. Diemente, E. W. Harris, Oxygen Quenching of Charge-Transfer Excited States of Ruthenium(II) Complexes. Evidence for Singlet Oxygen Production, *J. Am. Chem. Soc.* 95 (1973) 6864-6865.

[7]   S. L. Buell, J. N. Demas, Heterogeneous Preparation of Singlet Oxygen using an Ion-Exchange-Resin-Bound Tris(2,2'-bipyridine)ruthenium(II) Photosensitizer, *J. Phys. Chem.* 87 (1983) 4675-4681.

[8]   J. W. Dobrucki, Interaction of Oxygen-Sensitive Luminescent Probes Ru(phen)$_3^{2+}$ and Ru(bipy)$_3^{2+}$ with Animal and Plant Cells in Vitro: Mechanism of Phototoxicity and Conditions for Non-Invasive Oxygen Measurements, *J. Photochem. Photobiol. B* 65 (2001) 136-144.

[9]   N. Robertson, Optimizing Dyes for Dye-Sensitized Solar Cells, *Angew. Chem. Int. Ed.* 45 (2006) 2338-2345.

[10]   H. Hayashi, I. V. Lightcap, M. Tsujimoto, M. Takano, T. Umeyama, P. V. Kamat, H. Imahori, Electron Transfer Cascade by Organic/Inorganic Ternary Composites of Porphyrin, Zinc Oxide Nanoparticles, and Reduced Graphene Oxide on a Tin Oxide Electrode that Exhibits Efficient Photocurrent Generation, *J. Am. Chem. Soc.* 133 (2011) 7684-7687.

[11]   A. Yella, H.-W. Lee, H. N. Tsao, C. Yi, A. K. Chandiran, M. K. Nazeeruddin, E. W.-G. Diau, C.-Y. Yeh, S. M. Zakeeruddin, M. Grätzel, Porphyrin-Sensitized Solar Cells with

Cobalt (II/III)–Based Redox Electrolyte Exceed 12 Percent Efficiency, *Science* 334 (2011) 629-634.

[12] L.-L. Li, E. W.-G. Diau, Porphyrin-Sensitized Solar Cells, *Chem. Soc. Rev.* 42 (2013) 291-304.

[13] M.-y. Duan, J. Li, G. Mele, C. Wang, X.-f. Lü, G. Vasapollo, F.-x. Zhang, Photocatalytic Activity of Novel Tin Porphyrin/TiO$_2$ Based Composites, *J. Phys. Chem. C* 114 (2010) 7857-7862.

[14] Y. Chen, Z.-H. Huang, M. Yue, F. Kang, Integrating Porphyrin Nanoparticles into a 2D Graphene Matrix for Free-Standing Nanohybrid Films with Enhanced Visible-Light Photocatalytic Activity, *Nanoscale* 6 (2014) 978-985.

[15] S. M. Reda, Stability and Photodegradation of Phthalocyanines and Hematoporphyrin Doped PMMA as Solar Concentrators, *Sol. Energy* 81 (2007) 755-760.

[16] J. A. Anta, E. Guillén, R. Tena-Zaera, ZnO-Based Dye-Sensitized Solar Cells, *J. Phys. Chem. C* 116 (2012) 11413-11425.

[17] G. Granados-Oliveros, E. A. Páez-Mozo, F. M. Ortega, C. Ferronato, J.-M. Chovelon, Degradation of Atrazine using Metalloporphyrins Supported on TiO$_2$ Under Visible Light Irradiation, *Appl. Catal. B Environ.* 89 (2009) 448-454.

[18] S. Sarkar, A. Makhal, T. Bora, K. Lakhsman, A. Singha, J. Dutta, S. K. Pal, Hematoporphyrin–ZnO Nanohybrids: Twin Applications in Efficient Visible-Light Photocatalysis and Dye-Sensitized Solar Cells, *ACS Appl. Mater. Interfaces* 4 (2012) 7027-7035.

[19] J. Zhou, N. S. Xu, Z. L. Wang, Dissolving Behavior and Stability of ZnO Wires in Biofluids: A Study on Biodegradability and Biocompatibility of ZnO Nanostructures, *Adv. Mater.* 18 (2006) 2432-2435.

[20] W.-j. Sun, J. Li, G.-p. Yao, M. Jiang, F.-x. Zhang, Efficient Photo-Degradation of 4-Nitrophenol by using New CuPp-TiO$_2$ Photocatalyst under Visible Light Irradiation, *Catal. Comm.* 16 (2011) 90-93.

[21] T. Shiragami, J. Matsumoto, H. Inoue, M. Yasuda, Antimony Porphyrin Complexes as Visible-Light Driven Photocatalyst, *J. Photochem. Photobiol. C* 6 (2005) 227-248.

[22] W.-j. Sun, J. Li, G.-p. Yao, F.-x. Zhang, J.-L. Wang, Surface-Modification of TiO$_2$ with New Metalloporphyrins and their Photocatalytic Activity in the Degradation of 4-Notrophenol, *Appl. Surf. Sci.* 258 (2011) 940-945.

[23] H.-P. Lu, C.-Y. Tsai, W.-N. Yen, C.-P. Hsieh, C.-W. Lee, C.-Y. Yeh, E. W.-G. Diau, Control of Dye Aggregation and Electron Injection for Highly Efficient Porphyrin Sensitizers Adsorbed on Semiconductor Films with Varying Ratios of Coadsorbate, *J. Phys. Chem. C* 113 (2009) 20990-20997.

[24] E. M. Barea, V. Gónzalez-Pedro, T. Ripollés-Sanchis, H.-P. Wu, L.-L. Li, C.-Y. Yeh, E. W.-G. Diau, J. Bisquert, Porphyrin Dyes with High Injection and Low Recombination for Highly Efficient Mesoscopic Dye-Sensitized Solar Cells, *J. Phys. Chem. C* 115 (2011) 10898-10902.

[25] S. Afzal, W. A. Daoud, S. J. Langford, Photostable Self-Cleaning Cotton by a Copper(II) Porphyrin/TiO$_2$ Visible-Light Photocatalytic System, *ACS Appl. Mater. Interfaces* 5 (2013) 4753-4759.

[26] M. K. Panda, K. Ladomenou, A. G. Coutsolelos, Porphyrins in Bio-Inspired Transformations: Light-Harvesting to Solar Cell, *Coord. Chem. Rev.* 256 (2012) 2601-2627.

[27] S. Sardar, S. Sarkar, M. T. Z. Myint, S. Al-Harthi, J. Dutta, S. K. Pal, Role of Central Metal Ions in Hematoporphyrin-Functionalized Titania in Solar Energy Conversion Dynamics, *Phys. Chem. Chem. Phys.* 15 (2013) 18562-18570.

[28] N. Nasuha, B. H. Hameed, A. T. M. Din, Rejected Tea as a Potential Low-Cost Adsorbent for the Removal of Methylene Blue, *J. Hazard. Mater.* 175 (2010) 126-132.

[29] Z. Abdin, M. A. Alim, R. Saidur, M. R. Islam, W. Rashmi, S. Mekhilef, A. Wadi, Solar Energy Harvesting with the Application of Nanotechnology, *Renew. Sustainable Energy Rev.* 26 (2013) 837-852.

[30] Z. L. Wang, W. Wu, Nanotechnology-Enabled Energy Harvesting for Self-Powered Micro-/Nanosystems, *Angew. Chem. Int. Ed.* 51 (2012) 11700-11721.

[31] Y. Bai, I. Mora-Seró, F. De Angelis, J. Bisquert, P. Wang, Titanium Dioxide Nanomaterials for Photovoltaic Applications, *Chem. Rev.* 114 (2014) 10095-10130.

[32] R. Yu, Q. Lin, S.-F. Leung, Z. Fan, Nanomaterials and Nanostructures for Efficient Light Absorption and Photovoltaics, *Nano Energy* 1 (2012) 57-72.

[33] R. Slota, G. Dyrda, K. Szczegot, G. Mele, I. Pio, Photocatalytic Activity of Nano and Microcrystalline TiO$_2$ Hybrid Systems Involving Phthalocyanine or Porphyrin Sensitizers, *Photochem. Photobiol. Sci.* 10 (2011) 361-366.

[34] Y. Shen, X. Yu, W. Lin, Y. Zhu, Y. Zhang, A Facile Preparation of Immobilized BiOCl Nanosheets/TiO$_2$ Arrays on FTO with Enhanced Photocatalytic Activity and Reusability, *Appl. Surf. Sci.* 399 (2017) 67-76.

[35] C.-K. Huang, T. Wu, C.-W. Huang, C.-Y. Lai, M.-Y. Wu, Y.-W. Lin, Enhanced Photocatalytic Performance of BiVO$_4$ in Aqueous AgNO$_3$ Solution under Visible Light Irradiation, *Appl. Surf. Sci.* 399 (2017) 10-19.

[36] J. Lv, D. Li, K. Dai, C. Liang, D. Jiang, L. Lu, G. Zhu, Multi-walled Carbon Nanotube Supported CdS-DETA Nanocomposite for Efficient Visible Light Photocatalysis, *Mater. Chem. Phys.* 186 (2017) 372-381.

[37] J. Z. Zhang, Interfacial Charge Carrier Dynamics of Colloidal Semiconductor Nanoparticles, *J. Phys. Chem. B* 104 (2000) 7239-7253.

[38] A. Listorti, B. O'Regan, J. R. Durrant, Electron Transfer Dynamics in Dye-Sensitized Solar Cells, *Chem. Mater.* 23 (2011) 3381-3399.

[39] P. Tiwana, P. Docampo, M. B. Johnston, H. J. Snaith, L. M. Herz, Electron Mobility and Injection Dynamics in Mesoporous ZnO, SnO$_2$, and TiO$_2$ Films Used in Dye-Sensitized Solar Cells, *ACS Nano* 5 (2011) 5158-5166.

[40] T. K. Maji, D. Bagchi, P. Kar, D. Karmakar, S. K. Pal, Enhanced Charge Separation through Modulation of Defect-State in Wide Band-Gap Semiconductor for Potential Photocatalysis Application: Ultrafast Spectroscopy and Computational Studies, *J. Photochem. Photobiol. A* 332 (2017) 391-398.

[41] S. Meng, E. Kaxiras, Electron and Hole Dynamics in Dye-Sensitized Solar Cells: Influencing Factors and Systematic Trends, *Nano Lett.* 10 (2010) 1238-1247.

[42] J. Z. Zhang, Ultrafast Studies of Electron Dynamics in Semiconductor and Metal Colloidal Nanoparticles: Effects of Size and Surface, *Acc. Chem. Res.* 30 (1997) 423-429.

[43] R. L. Milot, C. A. Schmuttenmaer, Electron Injection Dynamics in High-Potential Porphyrin Photoanodes, *Acc. Chem. Res.* 48 (2015) 1423-1431.

[44] S. Sarkar, A. Makhal, T. Bora, S. Baruah, J. Dutta, S. K. Pal, Photoselective Excited State Dynamics in ZnO-Au Nanocomposites and their Implications in Photocatalysis and Dye-sensitized Solar Cells, *Phys. Chem. Chem. Phys.* 13 (2011) 12488-12496.

[45] S. A. Haque, E. Palomares, B. M. Cho, A. N. M. Green, N. Hirata, D. R. Klug, J. R. Durrant, Charge Separation versus Recombination in Dye-Sensitized Nanocrystalline Solar Cells: the Minimization of Kinetic Redundancy, *J. Am. Chem. Soc.* 127 (2005) 3456-3462.

[46] P. Lei, F. Wang, S. Zhang, Y. Ding, J. Zhao, M. Yang, Conjugation-Grafted-TiO_2 Nanohybrid for High Photocatalytic Efficiency under Visible Light, *ACS Appl. Mater. Interfaces* 6 (2014) 2370-2376.

[47] H. Li, Z. Bian, J. Zhu, Y. Huo, H. Li, Y. Lu, Mesoporous Au/TiO_2 Nanocomposites with Enhanced Photocatalytic Activity, *J. Am. Chem. Soc.* 129 (2007) 4538-4539.

[48] J. C. Yu, Jiaguo, Wingkei, Zitao, Lizhi, Effects of F^- Doping on the Photocatalytic Activity and Microstructures of Nanocrystalline TiO_2 Powders, *Chem. Mater.* 14 (2002) 3808-3816.

[49] K. Selvam, M. Swaminathan, Au-doped TiO_2 Nanoparticles for Selective Photocatalytic Synthesis of Quinaldines from Anilines in Ethanol, *Tetrahedron Lett.* 51 (2010) 4911-4914.

[50] P. Kar, S. Sardar, E. Alarousu, J. Sun, Z. S. Seddigi, S. A. Ahmed, E. Y. Danish, O. F. Mohammed, S. K. Pal, Impact of Metal Ions in Porphyrin-Based Applied Materials for Visible-Light Photocatalysis: Key Information from Ultrafast Electronic Spectroscopy, *Chem. Eur. J.* 20 (2014) 10475-10483.

[51] R. Qiu, D. Zhang, Z. Diao, X. Huang, C. He, J.-L. Morel, Y. Xiong, Visible Light Induced Photocatalytic Reduction of Cr(VI) over Polymer-Sensitized TiO_2 and its Synergism with Phenol Oxidation, *Water Res.* 46 (2012) 2299-2306.

[52] N. Liang, M. Wang, L. Jin, S. Huang, W. Chen, M. Xu, Q. He, J. Zai, N. Fang, X. Qian, Highly Efficient $Ag_2O/Bi_2O_2CO_3$ p-n Heterojunction Photocatalysts with Improved Visible-Light Responsive Activity, *ACS Appl. Mater. Interfaces* 6 (2014) 11698-11705.

[53] S. Sardar, P. Kar, H. Remita, B. Liu, P. Lemmens, S. K. Pal, S. Ghosh, Enhanced Charge Separation and FRET at Heterojunctions between Semiconductor Nanoparticles and

Conducting Polymer Nanofibers for Efficient Solar Light Harvesting, *Sci. Rep.* 5 (2015) 17313.

[54] P. Kar, T. K. Maji, P. K. Sarkar, S. Sardar, S. K. Pal, Direct Observation of Electronic Transition-Plasmon Coupling for Enhanced Electron Injection in Dye-Sensitized Solar Cells, *RSC Adv.* 6 (2016) 98753-98760.

[55] L. M. Peter, The Grätzel Cell: Where Next?, *J. Phys. Chem. Lett.* 2 (2011) 1861-1867.

[56] R. Bonnett, Photosensitizers of the Porphyrin and Phthalocyanine Series for Photodynamic Therapy, *Chem. Soc. Rev.* 24 (1995) 19-33.

[57] M. Silva, M. E. Azenha, M. M. Pereira, H. D. Burrows, M. Sarakha, C. Forano, M. F. Ribeiro, A. Fernandes, Immobilization of Halogenated Porphyrins and their Copper Complexes in MCM-41: Environmentally Friendly Photocatalysts for the Degradation of Pesticides, *Appl. Catal. B* 100 (2010) 1-9.

[58] A. Suzuki, K. Kobayashi, T. Oku, K. Kikuchi, Fabrication and Characterization of Porphyrin Dye-Sensitized Solar Cells, *Mater. Chem. Phys.* 129 (2011) 236-241.

[59] S. Sardar, S. Chaudhuri, P. Kar, S. Sarkar, P. Lemmens, S. K. Pal, Direct Observation of Key Photoinduced Dynamics in a Potential Nano-Delivery Vehicle of Cancer Drugs, *Phys. Chem. Chem. Phys.* 17 (2015) 166-177.

[60] S. Sardar, P. Kar, S. K. Pal, The Impact of Central Metal Ions in Porphyrin Functionalized ZnO/TiO_2 for Enhanced Solar Energy Conversion, *J. Mat. NanoSci.* 1 (2014) 12-30.

[61] D. Chen, D. Yang, J. Geng, J. Zhu, Z. Jiang, Improving Visible-Light Photocatalytic Activity of N-doped TiO_2 Nanoparticles via Sensitization by Zn Porphyrin, *Appl. Surf. Sci.* 255 (2008) 2879-2884.

[62] S. Murphy, C. Saurel, A. Morrissey, J. Tobin, M. Oelgemöller, K. Nolan, Photocatalytic Activity of a Porphyrin/TiO_2 Composite in the Degradation of Pharmaceuticals, *Appl. Catal. B* 119–120 (2012) 156-165.

[63] M. A. Shannon, P. W. Bohn, M. Elimelech, J. G. Georgiadis, B. J. Marinas, A. M. Mayes, Science and Technology for Water Purification in the Coming Decades, *Nature* 452 (2008) 301-310.

[64] M. T. Yagub, T. K. Sen, S. Afroze, H. M. Ang, Dye and Its Removal from Aqueous Solution by Adsorption: A Review, *Adv. Colloid Interface Sci.* 209 (2014) 172-184.

[65] P. R. Chang, P. Zheng, B. Liu, D. P. Anderson, J. Yu, X. Ma, Characterization of Magnetic Soluble Starch-Functionalized Carbon Nanotubes and its Application for the Adsorption of the Dyes, *J. Hazard. Mater.* 186 (2011) 2144-2150.

[66] T. Madrakian, A. Afkhami, M. Ahmadi, H. Bagheri, Removal of Some Cationic Dyes from Aqueous Solutions using Magnetic-Modified Multi-Walled Carbon Nanotubes, *J. Hazard. Mater.* 196 (2011) 109-114.

[67] W. Wang, Y. Cheng, T. Kong, G. Cheng, Iron Nanoparticles Decoration onto Three-Dimensional Graphene for Rapid and Efficient Degradation of Azo Dye, *J. Hazard. Mater.* 299 (2015) 50-58.

[68] I. Ali, New Generation Adsorbents for Water Treatment, *Chem. Rev.* 112 (2012) 5073-5091.

[69] W. Lei, D. Portehault, D. Liu, S. Qin, Y. Chen, Porous Boron Nitride Nanosheets for Effective Water Cleaning, *Nat. Commun.* 4 (2013) 1777.

[70] M. Qiu, C. Qian, J. Xu, J. Wu, G. Wang, Studies on the Adsorption of Dyes into Clinoptilolite, *Desalination* 243 (2009) 286-292.

[71] V. K. Gupta, R. Kumar, A. Nayak, T. A. Saleh, M. A. Barakat, Adsorptive Removal of Dyes from Aqueous Solution onto Carbon Nanotubes: A Review, *Adv. Colloid Interface Sci.* 193–194 (2013) 24-34.

[72] H. Sun, A. Li, Z. Zhu, W. Liang, X. Zhao, P. La, W. Deng, Superhydrophobic Activated Carbon-Coated Sponges for Separation and Absorption, *ChemSusChem* 6 (2013) 1057-1062.

[73] Y. Liu, Y. Zhao, B. Sun, C. Chen, Understanding the Toxicity of Carbon Nanotubes, *Acc. Chem. Res.* 46 (2013) 702-713.

[74] K. S. Novoselov, A. K. Geim, S. V. Morozov, D. Jiang, Y. Zhang, S. V. Dubonos, I. V. Grigorieva, A. A. Firsov, Electric Field Effect in Atomically Thin Carbon Films, *Science* 306 (2004) 666-669.

[75] A. K. Geim, K. S. Novoselov, The Rise of Graphene, *Nat. Mater.* 6 (2007) 183-191.

[76] D. Chen, H. Feng, J. Li, Graphene Oxide: Preparation, Functionalization, and Electrochemical Applications, *Chem. Rev.* 112 (2012) 6027-6053.

[77]   X.-H. Li, J.-S. Chen, X. Wang, M. E. Schuster, R. Schlögl, M. Antonietti, A Green Chemistry of Graphene: Photochemical Reduction towards Monolayer Graphene Sheets and the Role of Water Adlayers, *ChemSusChem* 5 (2012) 642-646.

[78]   H. Zhang, X. Lv, Y. Li, Y. Wang, J. Li, P25-Graphene Composite as a High Performance Photocatalyst, *ACS Nano* 4 (2010) 380-386.

[79]   A. C. Balazs, T. Emrick, T. P. Russell, Nanoparticle Polymer Composites: Where Two Small Worlds Meet, *Science* 314 (2006) 1107-1110.

[80]   S. Ghosh, A. H. Khan, S. Acharya, Fabrication of Highly Stable, Hybrid PbS Nanocomposites in PAMAM Dendrimer Matrix for Photodetection, *J. Phys. Chem. C* 116 (2012) 6022-6030.

[81]   S. Ghosh, A.-L. Teillout, D. Floresyona, P. de Oliveira, A. Hagège, H. Remita, Conducting Polymer-Supported Palladium Nanoplates for Applications in Direct Alcohol Oxidation, *Int. J. Hydrogen Energy* 40 (2015) 4951-4959.

[82]   S. Ghosh, D. Ghosh, P. K. Bag, S. C. Bhattacharya, A. Saha, Aqueous Synthesis of ZnTe/Dendrimer Nanocomposites and their Antimicrobial Activity: Implications in Therapeutics, *Nanoscale* 3 (2011) 1139-1148.

[83]   G. Palui, F. Aldeek, W. Wang, H. Mattoussi, Strategies for Interfacing Inorganic Nanocrystals with Biological Systems Based on Polymer-Coating, *Chem. Soc. Rev.* 44 (2015) 193-227.

[84]   Z. Geng, Y. Lin, X. Yu, Q. Shen, L. Ma, Z. Li, N. Pan, X. Wang, Highly Efficient Dye Adsorption and Removal: A Functional Hybrid of Reduced Graphene Oxide-Fe_3O_4 Nanoparticles as an Easily Regenerative Adsorbent, *J. Mater. Chem.* 22 (2012) 3527-3535.

[85]   T. Zeng, X.-l. Zhang, Y.-r. Ma, H.-y. Niu, Y.-q. Cai, A Novel Fe_3O_4-Graphene-Au Multifunctional Nanocomposite: Green Synthesis and Catalytic Application, *J. Mater. Chem.* 22 (2012) 18658-18663.

[86]   V. Chabot, D. Higgins, A. Yu, X. Xiao, Z. Chen, J. Zhang, A Review of Graphene and Graphene Oxide Sponge: Material Synthesis and Applications to Energy and the Environment, *Energy Environ. Sci.* 7 (2014) 1564-1596.

[87]   N. Hussain, A. Gogoi, R. K. Sarma, P. Sharma, A. Barras, R. Boukherroub, R. Saikia, P. Sengupta, M. R. Das, Reduced Graphene Oxide Nanosheets Decorated with Au

Nanoparticles as an Effective Bactericide: Investigation of Biocompatibility and Leakage of Sugars and Proteins, *ChemPlusChem* 79 (2014) 1774-1784.

[88] W. Fan, W. Gao, C. Zhang, W. W. Tjiu, J. Pan, T. Liu, Hybridization of Graphene Sheets and Carbon-Coated Fe_3O_4 Nanoparticles as a Synergistic Adsorbent of Organic Dyes, *J. Mater. Chem.* 22 (2012) 25108-25115.

[89] S. Zhang, Y. Shao, H.-g. Liao, J. Liu, I. A. Aksay, G. Yin, Y. Lin, Graphene Decorated with PtAu Alloy Nanoparticles: Facile Synthesis and Promising Application for Formic Acid Oxidation, *Chem. Mater.* 23 (2011) 1079-1081.

[90] B. Adhikari, A. Biswas, A. Banerjee, Graphene Oxide-Based Supramolecular Hydrogels for Making Nanohybrid Systems with Au Nanoparticles, *Langmuir* 28 (2012) 1460-1469.

[91] B.-S. Kong, J. Geng, H.-T. Jung, Layer-By-Layer Assembly of Graphene and Gold Nanoparticles by Vacuum Filtration and Spontaneous Reduction of Gold Ions, *Chem. Commun.*, (2009) 2174-2176.

[92] H. Zhou, C. Qiu, Z. Liu, H. Yang, L. Hu, J. Liu, H. Yang, C. Gu, L. Sun, Thickness-Dependent Morphologies of Gold on N-Layer Graphenes, *J. Am. Chem. Soc.* 132 (2010) 944-946.

[93] P. Wang, Z.-G. Liu, X. Chen, F.-L. Meng, J.-H. Liu, X.-J. Huang, UV Irradiation Synthesis of an Au-Graphene Nanocomposite with Enhanced Electrochemical Sensing Properties, *J. Mater. Chem. A* 1 (2013) 9189-9195.

[94] S. Fujihara, H. Naito, T. Kimura, Visible Photoluminescence of ZnO Nanoparticles Dispersed in Highly Transparent MgF_2 Thin-Films via Sol–Gel Process, *Thin Solid Films* 389 (2001) 227-232.

[95] A. McLaren, T. Valdes-Solis, G. Li, S. C. Tsang, Shape and Size Effects of ZnO Nanocrystals on Photocatalytic Activity, *J. Am. Chem. Soc.* 131 (2009) 12540-12541.

[96] G. B. Deacon, R. J. Phillips, Relationships Between the Carbon-Oxygen Stretching Frequencies of Carboxylato Complexes and the Type of Carboxylate Coordination, *Coord. Chem. Rev.* 33 (1980) 227-250.

[97] W. Tu, J. Lei, P. Wang, H. Ju, Photoelectrochemistry of Free-Base-Porphyrin-Functionalized Zinc Oxide Nanoparticles and Their Applications in Biosensing, *Chem. Eur. J.* 17 (2011) 9440-9447.

[98] P. Jiang, J. J. Zhou, H. F. Fang, C. Y. Wang, Z. L. Wang, S. S. Xie, Hierarchical Shelled ZnO Structures Made of Bunched Nanowire Arrays, *Adv. Funct. Mater.* 17 (2007) 1303-1310.

[99] E. Collini, C. Ferrante, R. Bozio, Strong Enhancement of the Two-Photon Absorption of Tetrakis(4-sulfonatophenyl)porphyrin Diacid in Water upon Aggregation, *J. Phys. Chem. B* 109 (2004) 2-5.

[100] S. Verma, A. Ghosh, A. Das, H. N. Ghosh, Ultrafast Exciton Dynamics of J- and H-Aggregates of the Porphyrin-Catechol in Aqueous Solution, *J. Phys. Chem. B* 114 (2010) 8327-8334.

[101] G. Mele, R. del Sole, G. Vasapollo, E. García-López, L. Palmisano, L. Jun, R. Słota, G. Dyrda, TiO_2-Based Photocatalysts Impregnated with Metallo-Porphyrins Employed for Degradation of 4-Nitrophenol in Aqueous Solutions: Role of Metal and Macrocycle, *Res. Chem. Intermed.* 33 (2007) 433-448.

[102] S. G. Kruglik, P. A. Apanasevich, V. S. Chirvony, V. V. Kvach, V. A. Orlovich, Resonance Raman, CARS, and Picosecond Absorption Spectroscopy of Copper Porphyrins: The Evidence for the Exciplex Formation with Oxygen-Containing Solvent Molecules, *J. Phys. Chem.* 99 (1995) 2978-2995.

[103] D. Kim, D. Holten, M. Gouterman, Evidence From Picosecond Transient Absorption and Kinetic Studies of Charge-Transfer States in Copper(II) Porphyrins, *J. Am. Chem. Soc.* 106 (1984) 2793-2798.

[104] S. Sarkar, A. Makhal, S. Baruah, M. A. Mahmood, J. Dutta, S. K. Pal, Nanoparticle-Sensitized Photodegradation of Bilirubin and Potential Therapeutic Application, *J. Phys. Chem. C* 116 (2012) 9608-9615.

[105] C. Yogi, K. Kojima, N. Wada, H. Tokumoto, T. Takai, T. Mizoguchi, H. Tamiaki, Photocatalytic Degradation of Methylene Blue by TiO_2 Film and Au Particles-TiO_2 Composite Film, *Thin Solid Films* 516 (2008) 5881-5884.

[106] A. Mills, J. Wang, Photobleaching of Methylene Blue Sensitised by TiO_2: An Ambiguous System?, *J. Photochem. Photobiol. A* 127 (1999) 123-134.

[107] E. B. Fleischer, E. I. Choi, P. Hambright, A. Stone, Porphyrin Studies: Kinetics of Metalloporphyrin Formation, *Inorg. Chem.* 3 (1964) 1284-1287.

[108] P. Castillero, J. R. Sánchez-Valencia, M. Cano, J. M. Pedrosa, J. Roales, A. Barranco, A. R. González-Elipe, Active and Optically Transparent Tetracationic Porphyrin/TiO_2 Composite Thin Films, *ACS Appl. Mater. Interfaces* 2 (2010) 712-721.

[109] H. Huang, X. Gu, J. Zhou, K. Ji, H. Liu, Y. Feng, Photocatalytic Degradation of Rhodamine B on TiO_2 Nanoparticles Modified with Porphyrin and Iron-Porphyrin, *Catal. Comm.* 11 (2009) 58-61.

[110] A. Kongkanand, K. Tvrdy, K. Takechi, M. Kuno, P. V. Kamat, Quantum Dot Solar Cells. Tuning Photoresponse through Size and Shape Control of CdSe−TiO_2 Architecture, *J. Am. Chem. Soc.* 130 (2008) 4007-4015.

[111] A. Kathiravan, P. S. Kumar, R. Renganathan, S. Anandan, Photoinduced Electron Transfer Reactions Between Meso-tetrakis(4-sulfonatophenyl)porphyrin and Colloidal Metal-Semiconductor Nanoparticles, *Colloids Surf., A* 333 (2009) 175-181.

[112] D. Li, W. Dong, S. Sun, Z. Shi, S. Feng, Photocatalytic Degradation of Acid Chrome Blue K with Porphyrin-Sensitized TiO_2 under Visible Light, *J. Phys. Chem. C* 112 (2008) 14878-14882.

[113] M. R. Hoffmann, S. T. Martin, W. Choi, D. W. Bahnemann, Environmental Applications of Semiconductor Photocatalysis, *Chem. Rev.* 95 (1995) 69-96.

[114] P. Kar, T. K. Maji, J. Patwari, S. K. Pal, Can a Light Harvesting Material be Always Common in Photocatalytic and Photovoltaic Applications?, *Mater. Chem. Phys.*, 200 (2017) 70-77.

[115] W.-K. Wang, J.-J. Chen, X. Zhang, Y.-X. Huang, W.-W. Li, H.-Q. Yu, Self-induced Synthesis of Phase-Junction TiO_2 with a Tailored Rutile to Anatase Ratio Below Phase Transition Temperature, *Sci. Rep.* 6 (2016) 20491.

[116] T. D. Schladt, K. Schneider, M. I. Shukoor, F. Natalio, H. Bauer, M. N. Tahir, S. Weber, L. M. Schreiber, H. C. Schroder, W. E. G. Muller, W. Tremel, Highly Soluble Multifunctional MnO Nanoparticles for Simultaneous Optical and MRI Imaging and Cancer Treatment using Photodynamic Therapy, *J. Mater. Chem.* 20 (2010) 8297-8304.

[117] A. Marcelli, I. Jelovica Badovinac, N. Orlic, P. R. Salvi, C. Gellini, Excited-State Absorption and Ultrafast Relaxation Dynamics of Protoporphyrin IX and Hemin, *Photochem. Photobiol. Sci.* 12 (2013) 348-355.

[118] P. Kar, S. Sardar, S. Ghosh, M. R. Parida, B. Liu, O. F. Mohammed, P. Lemmens, S. K. Pal, Nano Surface Engineering of Mn_2O_3 for Potential Light-Harvesting Application, *J. Mater. Chem. C* 3 (2015) 8200-8211.

[119] X.-q. Su, J. Li, Z.-q. Zhang, M.-m. Yu, L. Yuan, Cu(II) Porphyrins Modified TiO_2 Photocatalysts: Accumulated Patterns of Cu(II) Porphyrin Molecules on the Surface of TiO_2 and Influence on Photocatalytic Activity, *J. Alloys Compd.* 626 (2015) 252-259.

[120] C. Wang, J. Li, G. Mele, M.-y. Duan, X.-f. Lü, L. Palmisano, G. Vasapollo, F.-x. Zhang, The Photocatalytic Activity of Novel, Substituted Porphyrin/TiO_2-based Composites, *Dyes Pigm.* 84 (2010) 183-189.

[121] Y. Luo, J. Li, G.-p. Yao, F.-x. Zhang, Influence of Polarity of the Peripheral Substituents of Porphyrin Molecules on the Photocatalytic Activity of Cu(ii) Porphyrin Modified TiO_2 Composites, *Catal. Sci. Tech.* 2 (2012) 841-846.

[122] P. Kar, T. K. Maji, R. Nandi, P. Lemmens, S. K. Pal, In-Situ Hydrothermal Synthesis of Bi–$Bi_2O_2CO_3$ Heterojunction Photocatalyst with Enhanced Visible Light Photocatalytic Activity, *Nano-Micro Lett.* 9 (2016) 18.

[123] Y. Park, S.-H. Lee, S. O. Kang, W. Choi, Organic Dye-Sensitized TiO_2 for the Redox Conversion of Water Pollutants Under Visible Light, *Chem. Commun.* 46 (2010) 2477-2479.

[124] Q. Lu, Y. Zhang, S. Liu, Graphene Quantum Dots Enhanced Photocatalytic Activity of Zinc Porphyrin toward the Degradation of Methylene Blue under Visible-Light Irradiation, *J. Mater. Chem. A* 3 (2015) 8552-8558.

[125] F. A. Harraz, A. A. Ismail, S. A. Al-Sayari, A. Al-Hajry, Novel α-Fe_2O_3/Polypyrrole Nanocomposite with Enhanced Photocatalytic Performance, *J. Photochem. Photobiol. A* 299 (2015) 18-24.

[126] S. Li, L. Zhang, H. Wang, Z. Chen, J. Hu, K. Xu, J. Liu, Ta_3N_5-Pt Nonwoven Cloth with Hierarchical Nanopores as Efficient and Easily Recyclable Macroscale Photocatalysts, *Sci. Rep.* 4 (2014) 3978.

[127] M.-M. Yu, C. Wang, J. Li, L. Yuan, W.-J. Sun, Facile Fabrication of CuPp–TiO_2 Mesoporous Composite: An Excellent and Robust Heterostructure Photocatalyst for 4-Nitrophenol Degradation, *Appl. Surf. Sci.* 342 (2015) 47-54.

[128] X. Zhao, X. Liu, M. Yu, C. Wang, J. Li, The Highly Efficient and Stable Cu, Co, Zn-Porphyrin–TiO$_2$ Photocatalysts with Heterojunction by using Fashioned One-step Method, *Dyes Pigm.* 136 (2017) 648-656.

[129] A. Kathiravan, V. Raghavendra, R. Ashok Kumar, P. Ramamurthy, Protoporphyrin IX on TiO$_2$ electrode: A spectroscopic and photovoltaic investigation, *Dyes Pigm.* 96 (2013) 196-203.

[130] R. L. Milot, G. F. Moore, R. H. Crabtree, G. W. Brudvig, C. A. Schmuttenmaer, Electron Injection Dynamics from Photoexcited Porphyrin Dyes into SnO$_2$ and TiO$_2$ Nanoparticles, *J. Phys. Chem. C* 117 (2013) 21662-21670.

[131] H. Choi, Y.-S. Chen, K. G. Stamplecoskie, P. V. Kamat, Boosting the Photovoltage of Dye-Sensitized Solar Cells with Thiolated Gold Nanoclusters, *J. Phys. Chem. Lett.* 6 (2015) 217-223.

[132] E. Palomares, J. N. Clifford, S. A. Haque, T. Lutz, J. R. Durrant, Slow Charge Recombination in Dye-Sensitised Solar Cells (DSSC) using Al$_2$O$_3$ Coated Nanoporous TiO$_2$ Films, *Chem. Commun.*, (2002) 1464-1465.

[133] T. Zhao, J. Zai, M. Xu, Q. Zou, Y. Su, K. Wang, X. Qian, Hierarchical Bi$_2$O$_2$CO$_3$ Microspheres with Improved Visible-Light-Driven Photocatalytic Activity, *CrystEngComm* 13 (2011) 4010-4017.

[134] Y. Zhou, Z. Zhao, F. Wang, K. Cao, D. E. Doronkin, F. Dong, J.-D. Grunwaldt, Facile Synthesis of Surface N-doped Bi$_2$O$_2$CO$_3$: Origin of Visible Light Photocatalytic Activity and In situ DRIFTS Studies, *J. Hazard. Mater.* 307 (2016) 163-172.

[135] R. Jiang, B. Li, C. Fang, J. Wang, Metal/Semiconductor Hybrid Nanostructures for Plasmon-Enhanced Applications, *Adv. Mater.* 26 (2014) 5274-5309.

[136] D. M. Fragua, R. Abargues, P. J. Rodriguez-Canto, J. F. Sanchez-Royo, S. Agouram, J. P. Martinez-Pastor, Au–ZnO Nanocomposite Films for Plasmonic Photocatalysis, *Adv. Mater. Interf.* 2 (2015) 1500156.

[137] P. Kar, S. Sardar, B. Liu, M. Sreemany, P. Lemmens, S. Ghosh, S. K. Pal, Facile Synthesis of Reduced Graphene Oxide–Gold Nanohybrid for Potential Use in Industrial Waste-Water Treatment, *Sci. Technol. Adv. Mater.* 17 (2016) 375-386.

[138] Y. Wang, W. Liang, C. Geng, Coalescence Behavior of Gold Nanoparticles, *Nanoscale Res. Lett.* 4 (2009) 684 - 688.

[139] C. H. Kiang, M. Endo, P. M. Ajayan, G. Dresselhaus, M. S. Dresselhaus, Size Effects in Carbon Nanotubes, *Phys. Rev. Lett.* 81 (1998) 1869-1872.

[140] B. K. Barman, K. K. Nanda, The Dual Role of Zn-Acid Medium for One-Step Rapid Synthesis of M@rGO (M = Au, Pt, Pd and Ag) Hybrid Nanostructures at Room Temperature, *Chem. Commun.* 49 (2013) 8949-8951.

[141] K. Zhang, Y. Zhang, S. Wang, Enhancing Thermoelectric Properties of Organic Composites through Hierarchical Nanostructures, *Sci. Rep.* 3 (2013) 8328.

[142] S. Sardar, S. Ghosh, H. Remita, P. Kar, B. Liu, C. Bhattacharya, P. Lemmens, S. K. Pal, Enhanced Photovoltage in DSSCs: Synergistic Combination of a Silver Modified TiO_2 Photoanode and a Low Cost Counter Electrode, *RSC Adv.* 6 (2016) 33433-33442.

[143] V. Singh, D. Joung, L. Zhai, S. Das, S. I. Khondaker, S. Seal, Graphene Based Materials: Past, Present and Future, *Prog. Mater Sci.* 56 (2011) 1178-1271.

[144] F. Ren, C. Wang, C. Zhai, F. Jiang, R. Yue, Y. Du, P. Yang, J. Xu, One-pot Synthesis of a RGO-Supported Ultrafine Ternary PtAuRu Catalyst with High Electrocatalytic Activity towards Methanol Oxidation in Alkaline Medium, *J. Mater. Chem. A* 1 (2013) 7255-7261.

[145] J. Li, C.-y. Liu, Y. Liu, Au/Graphene Hydrogel: Synthesis, Characterization and its Use for Catalytic Reduction of 4-Nitrophenol, *J. Mater. Chem.* 22 (2012) 8426-8430.

[146] T. Fan, W. Zeng, W. Tang, C. Yuan, S. Tong, K. Cai, Y. Liu, W. Huang, Y. Min, A. Epstein, Controllable Size-Selective Method to Prepare Graphene Quantum Dots from Graphene Oxide, *Nanoscale Res. Lett.* 10 (2015) 55.

[147] C. K. Chua, M. Pumera, Renewal of sp^2 Bonds in Graphene Oxides via Dehydrobromination, *J. Mater. Chem.* 22 (2012) 23227-23231.

[148] H. Sun, L. Cao, L. Lu, Magnetite/Reduced Graphene Oxide Nanocomposites: One Step Solvothermal Synthesis and Use as a Novel Platform for Removal of Dye Pollutants, *Nano Research* 4 (2011) 550-562.

[149] G. K. Ramesha, A. Vijaya Kumara, H. B. Muralidhara, S. Sampath, Graphene and Graphene Oxide as Effective Adsorbents toward Anionic and Cationic Dyes, *J. Colloid Interface Sci.* 361 (2011) 270-277.

[150] S. Liu, J. Tian, L. Wang, Y. Zhang, Y. Luo, A. M. Asiri, A. O. Al-Youbi, X. Sun, A Novel Acid-driven, Microwave-assisted, One-pot Strategy Toward Rapid Production of Graphitic N-doped Carbon Nanoparticles-Decorated Carbon Flakes from N,N-

Dimethylformamide and their Application in Removal of Dye from Water, *RSC Adv.* 2 (2012) 4632-4635.

[151] Y. Li, Q. Du, T. Liu, X. Peng, J. Wang, J. Sun, Y. Wang, S. Wu, Z. Wang, Y. Xia, L. Xia, Comparative Study of Methylene Blue Dye Adsorption onto Activated Carbon, Graphene Oxide, and Carbon Nanotubes, *Chem. Eng. Res. Des.* 91 (2013) 361-368.

[152] R. Sitko, E. Turek, B. Zawisza, E. Malicka, E. Talik, J. Heimann, A. Gagor, B. Feist, R. Wrzalik, Adsorption of Divalent Metal Ions from Aqueous Solutions using Graphene Oxide, *Dalton Trans.* 42 (2013) 5682-5689.

[153] F. Liu, S. Chung, G. Oh, T. S. Seo, Three-Dimensional Graphene Oxide Nanostructure for Fast and Efficient Water-Soluble Dye Removal, *ACS Appl. Mater. Interfaces* 4 (2012) 922-927.

[154] P. Sharma, M. R. Das, Removal of a Cationic Dye from Aqueous Solution Using Graphene Oxide Nanosheets: Investigation of Adsorption Parameters, *J. Chem. Eng. Data* 58 (2013) 151-158.

[155] L. Ai, M. Li, L. Li, Adsorption of Methylene Blue from Aqueous Solution with Activated Carbon/Cobalt Ferrite/Alginate Composite Beads: Kinetics, Isotherms, and Thermodynamics, *J. Chem. Eng. Data* 56 (2011) 3475-3483.

[156] P. Sharma, N. Hussain, D. J. Borah, M. R. Das, Kinetics and Adsorption Behavior of the Methyl Blue at the Graphene Oxide/Reduced Graphene Oxide Nanosheet–Water Interface: A Comparative Study, *J. Chem. Eng. Data* 58 (2013) 3477-3488.

[157] T. Liu, Y. Li, Q. Du, J. Sun, Y. Jiao, G. Yang, Z. Wang, Y. Xia, W. Zhang, K. Wang, H. Zhu, D. Wu, Adsorption of Methylene Blue from Aqueous Solution by Graphene, *Colloids Surf., B* 90 (2012) 197-203.

[158] S. Yang, W. Yue, D. Huang, C. Chen, H. Lin, X. Yang, A Facile Green Strategy for Rapid Reduction of Graphene Oxide by Metallic Zinc, *RSC Adv.* 2 (2012) 8827-8832.

[159] J. Sarkar, J. Chowdhury, P. Pal, G. B. Talapatra, Ab Initio, DFT Vibrational Calculations and SERRS Study of Rhodamine 123 Adsorbed on Colloidal Silver Particles, *Vib. Spectrosc.* 41 (2006) 90-96.

[160] N. Goswami, S. Chaudhuri, A. Giri, P. Lemmens, S. K. Pal, Surface Engineering for Controlled Nanocatalysis: Key Dynamical Events from Ultrafast Electronic Spectroscopy, *J. Phys. Chem. C* 118 (2014) 23434-23442.

[161] T. Tachikawa, S.-C. Cui, M. Fujitsuka, T. Majima, Interfacial Electron Transfer Dynamics in Dye-Modified Graphene Oxide Nanosheets Studied by Single-Molecule Fluorescence Spectroscopy, *Phys. Chem. Chem. Phys.* 14 (2012) 4244-4249.

[162] S. Choudhury, S. Batabyal, T. Mondol, D. Sao, P. Lemmens, S. K. Pal, Ultrafast Dynamics of Solvation and Charge Transfer in a DNA-Based Biomaterial, *Chem. Asian J.* 9 (2014) 1395-1402.

[163] S. Thakur, N. Karak, Green Reduction of Graphene Oxide by Aqueous Phytoextracts, *Carbon* 50 (2012) 5331-5339.

[164] G. Z. Kyzas, E. A. Deliyanni, K. A. Matis, Graphene Oxide and its Application as an Adsorbent for Wastewater Treatment, *J. Chem. Technol. Biotechnol.* 89 (2014) 196-205.

Chapter 6

Spectroscopic Studies on Light Harvesting Nanomaterials for Solar Light Photocatalysis Application

6.1. Introduction:

Photocatalysis technology has attracted enormous interest because of its potential to soften and release the global energy crisis and environmental pollution [1-6]. Although various types of semiconductor photocatalyst have been developed, their applications are impeded by a high recombination rate of electron-hole pairs and low efficiency of solar light absorption in the photocatalysis [7, 8]. A tremendous effort has been made to optimize the electronic band structure allowing an efficient electron-hole separation, which has been acknowledged to be a key factor in enhancing solar energy conversion [9-14]. The development of heterojunction systems has also been understood since it is beneficial for electron transfer to improved electron-hole pair separation and therefore resulting in an excellent photocatalytic activity under solar light illumination [15, 16].

Recently, economic and abundant bismuth-containing semiconductors have been attracted large attention for diverse applications, especially in the area of energy conversion and environmental treatment [17-20]. The bismuth subcarbonate ($Bi_2O_2CO_3$) is one of the most interesting semiconductor having a large bang gap (3.3 eV). It belongs to the layered Aurivillius-related oxide family, consisting of $Bi_2O_2^{2+}$ layers sandwiched between two slabs of CO_3^{2-} layers [21]. However, the use of $Bi_2O_2CO_3$ in light harvesting applications is very limited because it can absorb only UV light. To overcome this drawback several 3D hierarchical $Bi_2O_2CO_3$ architectures composed of nanosheets, nanoplate and microsphere have been developed [22, 23]. The coupling of $Bi_2O_2CO_3$ with other materials to construct heterojunctions has also been shown as an advantages approach to improve the visible light responsive activity and to facilitate the separation of photogenerated electron−hole pairs. Different low band gap semiconductors and polymers have been used to improve the photocatalytic activity of $Bi_2O_2CO_3$. Liu et al. constructed hierarchical graphene–$Bi_2O_2CO_3$ composites which exhibit a significantly enhanced visible light photocatalytic performance [24]. Good visible light photocatalytic activity toward the degradation of Rhodamine B was reported by Zhang et al. for n-n heterostructured

$Bi_2O_2CO_3$/ Bi_2WO_6 [25]. Zhou's group reported that PANI decorated $Bi_2O_2CO_3$ nanosheets exhibit a four to half times better photocatalytic activity for degradation of Rhodamine B in comparison to $Bi_2O_2CO_3$ nanosheets under visible light illumination [26]. Recently, p-n heterojunction Ag_2O/$Bi_2O_2CO_3$ photocatalysts was shown to manifest an excellent visible light activity for degradation of MB and methyl orange [27].

Recently, surface plasmon resonance (SPR) of noble metal nanoparticles (Ag or Au) was reported for improving the activity of semiconductor photocatalysts [28, 29]. In comparison with the high cost of noble-metals, Bi nanoparticles are inexpensive and show comparable surface plasmon resonances (SPR) [30]. Recently, two reports on Bi nanoparticles demonstrate that they are useful for catalysis and sensing applications [31, 32]. Dong et al. show that plasmonic Bi nanoparticles can be used for NO removal [33]. Several Bi nanoparticles based nanocomposites like Bi/BiOCl, Bi/Bi_2O_3 and Bi/BiOI exhibit enhanced photocatalytic activity comparing to their counterpart [34-36]. Recently, Bi nanoparticles based heterojunctions with semiconductor have been an intense research area due to their enhanced charge separation and improved photocatalytic efficacies [37-39]. However, Bi nanoparticles decorated $Bi_2O_2CO_3$ nanosheets have not been considered up to date.

Firstly, we developed an in-situ decoration of Bi nanoparticles on $Bi_2O_2CO_3$ nanosheets *via* a one-pot hydrothermal method. From time-resolved fluorescence spectroscopy we observed that an ultrafast electron transfer process in the Bi-$Bi_2O_2CO_3$ heterojunction reveals an excited state electron transfer from $Bi_2O_2CO_3$ to Bi. The novel Bi-decorated $Bi_2O_2CO_3$ nanosheets exhibited a dramatically enhanced photocatalytic activity towards MB degradation comparing to pure $Bi_2O_2CO_3$ nanosheets because of the SPR effect of Bi nanoparticles and an efficient separation of electron–hole pairs in the Bi-$Bi_2O_2CO_3$ heterojunction. We also observed that Bi-$Bi_2O_2CO_3$ exhibits a good recyclability with respect to degradation of MB, which is significant for real world applications.

The beauty of nanomaterials lies in their higher surface to volume ratio compared to that of bulk material with the same chemical composition. Therefore, for tailor made applications, nanomaterials are more promising compared to their bulk counterpart. In addition, to be used in several practical applications further surface modifications of nanomaterials are essential [40-44]. Attaching suitable organic ligand to their surface atoms is one of the most facile route for modifications of metal oxide nanomaterials [45]. This leads, e.g. to protection of nanoparticles

(NPs) from agglomeration and makes them available for an interaction with other molecules. Frequent reports on functionalization of NPs with biocompatible ligand for catalysis, cancer therapy and biomedical applications exist [46-50]. Previously, our group functionalized various NPs with biologically important ligands to allow potential biomedical and environmental applications [51-54]. Our recent attention towards manganese oxide NPs is due to their emerging use in biomedical, photocatalysis, supercapacitor applications and also because this material is relatively inexpensive, non toxic, naturally abundant [55-59]. It has been reported that different varieties of manganese oxide NPs (MnO, Mn_2O_3, Mn_3O_4) with tunable morphologies can be easily synthesized via different routes [60-64]. By varying the dripping speed of NaOH in presence of $MnCl_2$ and H_2O_2, different Mn_3O_4 morphologies, like nanoparticles, nanorod and nanofractals can be obtained [65, 66]. While hollow and core shell type Mn_2O_3 nanostructures are applied in CO reduction, [67] the former are reported to be useful in pollutant adsorption [68]. Recently, Chen et al. have shown that hierarchical mesoporous manganese dioxide (MnO_2) synthesized by soft interface method is a much efficient catalyst for degradation of organic pollutants like methylene blue [69]. To make the low band gap material Mn_2O_3 photocatalytically active a contact between graphene sheets and Mn_2O_3 nanoparticles has been made to facilitate easy electron transfer from the metal oxide to the graphene sheet [70]. Functionalized manganese oxide NPs are also reported to have novel optical and catalytic properties [42]. In recent reports from our group we have shown that the interaction of Mn_3O_4 NPs with various hydroxyl and carboxylate containing ligands changes the optical and magnetic properties of the NPs [71]. While α-hydroxy-carboxylate is found to have an impact on optical properties of the NPs though ligand to metal charge transfer (LMCT) and Jahn-Teller effects, interaction with carboxyl containing ligands is efficient in controlling the magnetic properties of Mn_3O_4 NPs [71]. Citrate functionalized Mn_3O_4 NPs containing multiple oxidation states (+2,+3 and +4) have been recently found to be useful for the treatment of hyperbilirubinemia [52]. The balance of different oxidation states in functionalized NPs is critical to achieve novel optical and catalytic properties. In this context, the functionalization of Mn_2O_3 having only one oxidation state (+3) and inducing interesting optical properties would be important, however, is only sparsely reported in the literature. This is one of the motives of the present work. Another important aspect is doping of Mn_2O_3 with metal ions in order to improve the functionality of the native oxide. Patoux et al. have shown that nickel doped spinel manganese oxides are attractive materials for Li ion

batteries [72]. Zinc doped manganese oxides are efficient coal gas absorbers for desulfurization [73]. Recently, Fe-loaded mesoporous manganese dioxide with urchin-like superstructures have been successfully used for dye degradation [74]. Therefore, we have also investigated the optical and catalytic properties of doped Mn_2O_3 upon functionalization with organic ligands.

Secondly, we have synthesized Mn_2O_3 microsphere by a hydrothermal process and duly functionalized them with the model organic ligand citrate. High resolution transmission electron microscopy (HRTEM) reveals the formation of Mn_2O_3 nanoparticles (NPs) from the microsphere as a result of ligand etching [75, 76]. We further confirmed the nature of citrate binding to the NPs by a series of characterization techniques such as Raman scattering, Fourier transformed infrared (FTIR) spectroscopy, cyclic voltametry (CV) and X-ray photo-emission spectroscopy (XPS). We also demonstrated that citrate functionalized NPs induce multiple photoluminescence (PL) processes. We further investigated the photocatalytic activity of citrate functionalized NPs using Methylene Blue (MB) as a model organic pollutant. The effect of doping metal ions (Cu^{2+} and Fe^{3+}) on the photoluminescence and catalytic activity of the NPs has also been investigated. In order to fabricate prototypes for potential applications, we have immobilized citrate functionalized Mn_2O_3 microspheres on stainless steel mesh and confirmed the filtering activity of the mesh to suspended particulates and catalytic degradation of a model contaminant in the presence of light.

6.2. Results and Discussion:

6.2.1. In-situ Hydrothermal Synthesis of Bi-Bi$_2$O$_2$CO$_3$ Heterojunction Photocatalyst with Enhanced Visible Light Photocatalytic Activity [77]:

Figure 6.1a shows XRD patterns of the as-synthesized $Bi_2O_2CO_3$ and $Bi-Bi_2O_2CO_3$. The diffraction pattern of $Bi_2O_2CO_3$ is perfectly indicated as a tetragonal $Bi_2O_2CO_3$ phase. After the addition of ethanol, the XRD pattern of the $Bi-Bi_2O_2CO_3$ sample is also indexed to the $Bi_2O_2CO_3$ phase (JCPDS card no. 41-1488) [78]. No characteristic peak for Bi nanoparticles in $Bi-Bi_2O_2CO_3$ was observed, probably due to low content of Bi. Similar results were reported in previously literatures based on metal/semiconductor photocatalyst [34, 79, 80]. As shown in Figure 6.1b-c the SEM images of $Bi_2O_2CO_3$ and $Bi-Bi_2O_2CO_3$ reveal a large sheet-like morphology with a width from 50-600 nm. After decoration of Bi on the $Bi_2O_2CO_3$ nanosheets
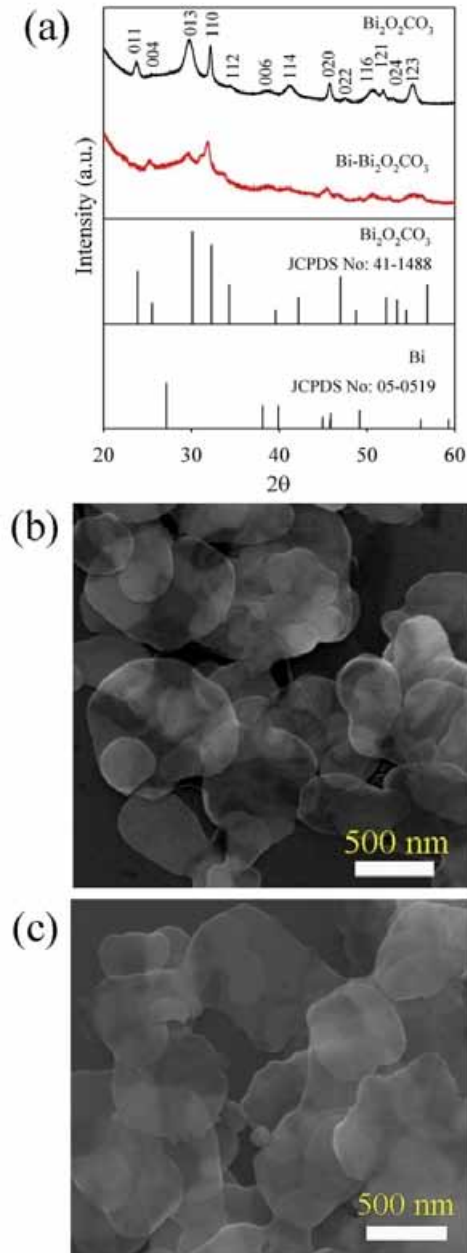
Figure 6.1. *(a) XRD patterns of $Bi_2O_2CO_3$ and Bi-$Bi_2O_2CO_3$. SEM images of (b) $Bi_2O_2CO_3$ and (c) Bi-$Bi_2O_2CO_3$.*

no significant structural and morphological change was observed. The smooth sheet-like morphology of Bi-$Bi_2O_2CO_3$ indicates a uniform distribution of Bi nanoparticles on the surface of $Bi_2O_2CO_3$. Morphology and crystallinity of $Bi_2O_2CO_3$ and Bi-$Bi_2O_2CO_3$ were further examined *via* TEM and HRTEM as shown in Figure 6.2a-d. The TEM images of Bi-$Bi_2O_2CO_3$ show a uniform distribution of Bi nanoparticles on the surface of the $Bi_2O_2CO_3$ nanosheets. The
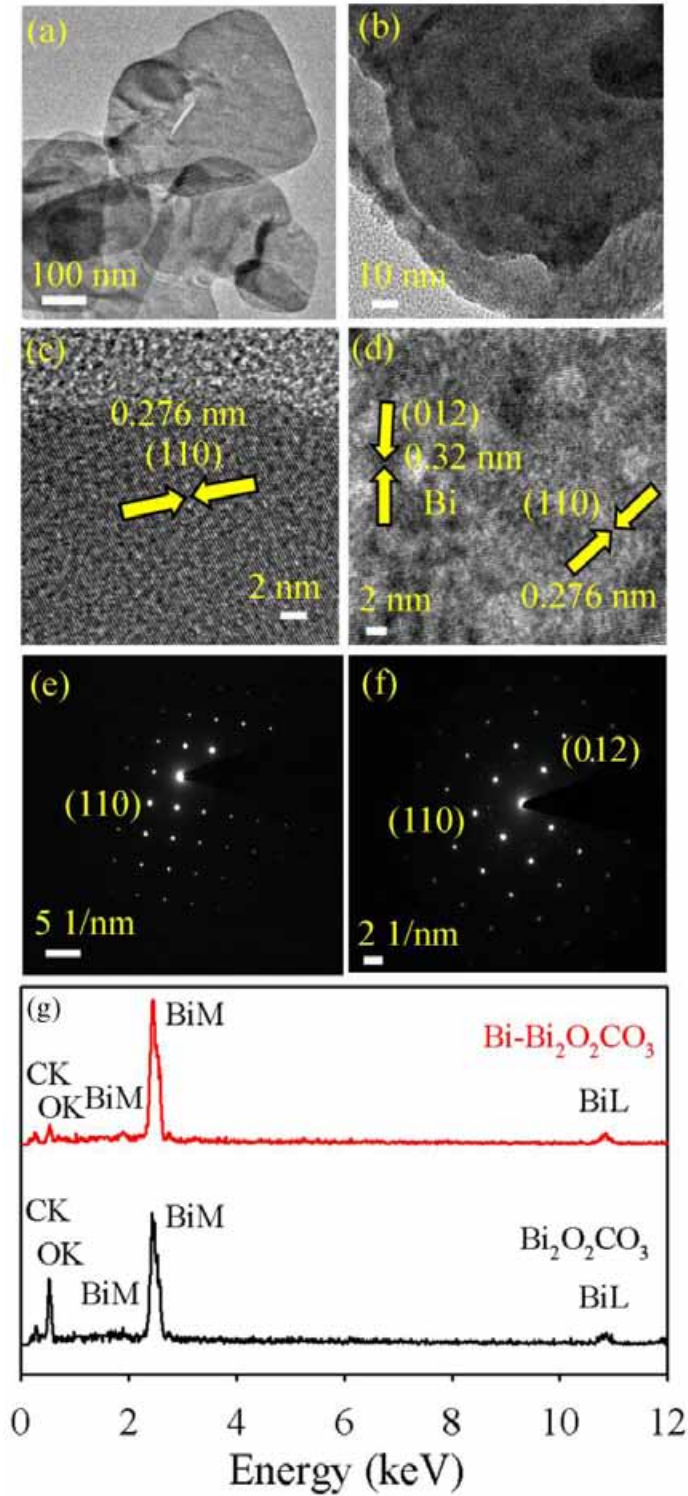
Figure 6.2. *TEM images of (a) $Bi_2O_2CO_3$ and (b) $Bi-Bi_2O_2CO_3$. HRTEM images of (c) $Bi_2O_2CO_3$ and (d) $Bi-Bi_2O_2CO_3$. SAED patterns of (e) $Bi_2O_2CO_3$ and (f) $Bi-Bi_2O_2CO_3$. (g) EDAX spectrum of $Bi_2O_2CO_3$ and $Bi-Bi_2O_2CO_3$.*

HRTEM images of $Bi_2O_2CO_3$ and $Bi-Bi_2O_2CO_3$ exhibit a high crystallinity of $Bi_2O_2CO_3$ nanosheet and Bi nanoparticles as given in Figure 6.2c-d. The inter-planar distance between the fringes are about 0.276 nm and 0.32 nm, which correspond to the (110) crystal plane of $Bi_2O_2CO_3$ and (012) crystal plane of Bi nanoparticles, respectively [37, 81]. The selected area electron diffraction (SAED) pattern obtained from the HRTEM images Figure 6.2e-f demonstrates further the well-crystallinity. From the EDAX measurement shown in Fig. 6.2g the at% ratio of Bi and O is 1:5 for $Bi_2O_2CO_3$ whereas 2:3 for $Bi-Bi_2O_2CO_3$. The XPS study of $Bi_2O_2CO_3$ and $Bi-Bi_2O_2CO_3$ were well documented in earlier studies [18, 26, 30, 82]. In those studies they concluded that the O 1s peak centered at 530.5 eV ascribed to Bi-O bonds in $Bi_2O_2CO_3$, while peaks at 284.8 eV and 288.7 eV were the characteristic peaks of adventitious carbon species and CO_3^{2-} in $Bi_2O_2CO_3$. Peaks around 157.0 eV and 162.3 eV were assigned to the formation of Bi metal present in the heterostructure. The other characterization on $Bi_2O_2CO_3$ and $Bi-Bi_2O_2CO_3$ related materials [18, 26, 30, 82] including HRTEM and EDAX are consistent with our experimental observations.

Figure 6.3a shows UV-Vis absorption spectra of $Bi_2O_2CO_3$ and $Bi-Bi_2O_2CO_3$. The $Bi_2O_2CO_3$ shows absorption peak at 360 nm and long tail over 800 nm due to scattering of the nanoparticles presented in the solution, which consists with earlier reports [83, 84]. After formation of heterojunction $Bi-Bi_2O_2CO_3$, an enhancement of absorption in the visible region was observed due to the presence of Bi nanoparticles and surface plasmon absorption around 500 nm as shown in Figure 6.3b. The SPR of non-noble metal Bi in the near ultraviolet and visible region were reported by different groups [85, 86]. Notably, such absorption enhancement in the visible region is also according to the color change of the samples as shown in the inset of Figure 6.3a-b. Thus, formation of Bi nanoparticles on the surface of $Bi_2O_2CO_3$ nanosheets results in an enhancement of absorption over the entire UV-Vis region. The photoluminescence of $Bi_2O_2CO_3$ and $Bi-Bi_2O_2CO_3$ exhibit emission around 400-550 nm upon excitation at 365 nm as shown in Figure 6.3c, e. Picosecond-resolved fluorescence was studied to investigate the detailed photophysical properties of the heterostructure after decoration of Bi nanoparticles on the $Bi_2O_2CO_3$ nanosheets. The fluorescence decay of $Bi_2O_2CO_3$ and $Bi-Bi_2O_2CO_3$ was determined at 460 nm upon excitation by 375 nm laser source (Figure 6.4) and tabulated in Table 6.1.

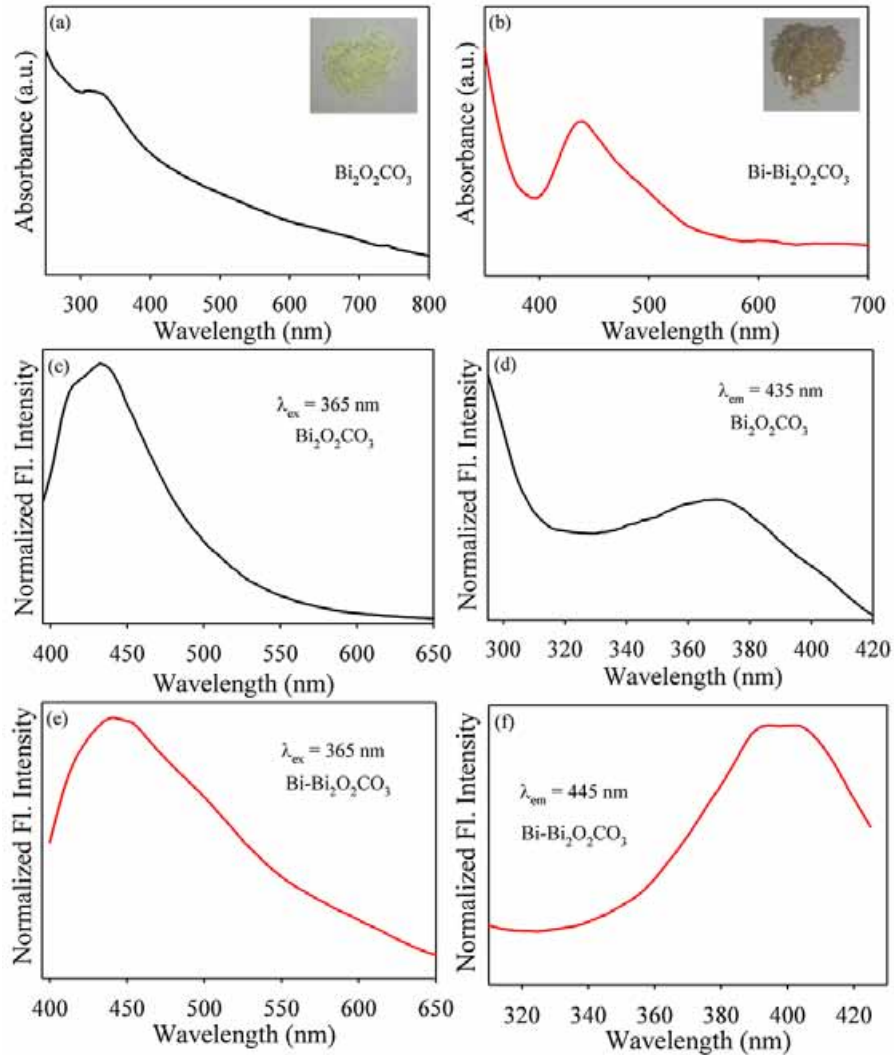**Figure 6.3.** *UV-Vis absorption spectrum of (a) Bi₂O₂CO₃ and (b) Bi-Bi₂O₂CO₃ (Inset shows the image of Bi₂O₂CO₃ and Bi-Bi₂O₂CO₃). Normalized steady-steady PL spectra of (c) Bi₂O₂CO₃ and (e) Bi-Bi₂O₂CO₃. The excitation spectra of Bi₂O₂CO₃ (d) and Bi-Bi₂O₂CO₃ (f) at different PL maxima.*

The fluorescence decay of $Bi_2O_2CO_3$ shows two components of 343 ps and 3.5 ns along with an average time of 1.25 ns. After decoration of Bi nanoparticles, the average time of Bi-$Bi_2O_2CO_3$ decreases to 0.70 ns. Thus, the faster component of 50 ps is attributed to the excited state electron transfer from $Bi_2O_2CO_3$ to Bi. The obvious decrease in fluorescence lifetime of the heterostructures suggests that the decoration of Bi nanoparticles on the $Bi_2O_2CO_3$ nanosheets can act as electron sink and therefore contribute to electron-hole separation. Such kind of metal-semiconductor heterojunctions facilitates in a remarkable way of the decline in the recombination of electron-hole pairs and is useful to enhanced solar energy utilization.
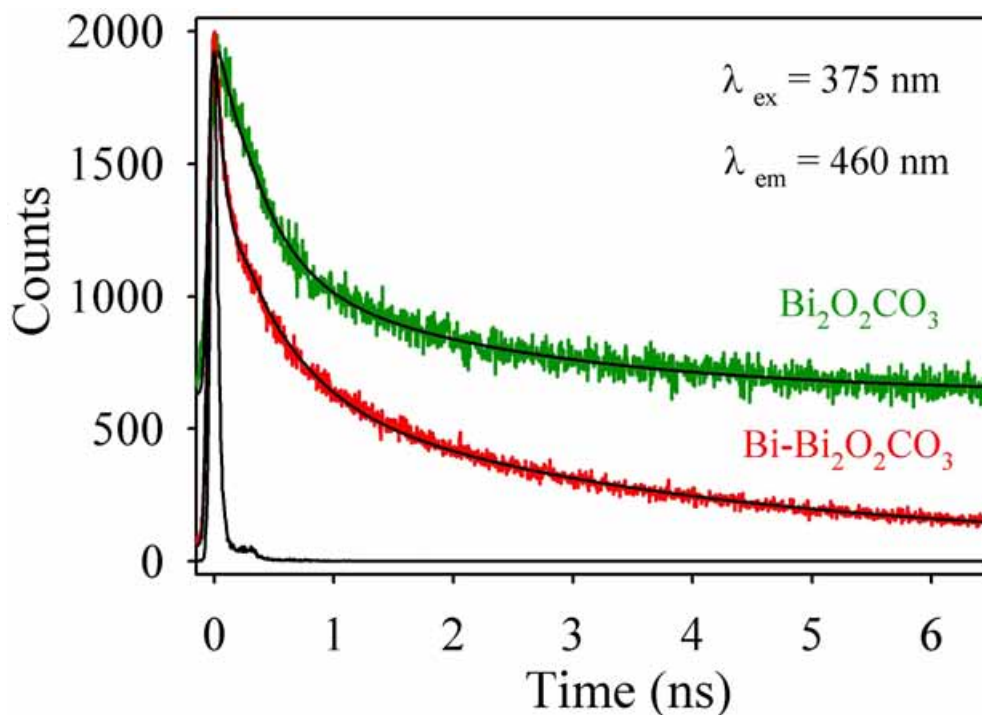
Figure 6.4. *Picosecond-resolved PL transients of $Bi_2O_2CO_3$ and Bi-$Bi_2O_2CO_3$ measured at $\lambda_{em} = 460$ nm upon $\lambda_{ex} = 375$ nm.*

Table 6.1. Lifetimes of picosecond time-resolved PL transients of $Bi_2O_2CO_3$ and Bi-$Bi_2O_2CO_3$ detected at 460 nm PL maxima upon excitation at 375 nm wavelength. The values in parentheses represent the relative weight percentages of the time components.

System	τ_1 (ps)	τ_2 (ps)	τ_3 (ps)	τ_{avg} (ns)
$Bi_2O_2CO_3$	343 (71%)	3500 (29%)		1.25
Bi-$Bi_2O_2CO_3$	50 (58%)	394 (25%)	3400 (17%)	0.70

The photocatalytic activities of $Bi_2O_2CO_3$ and Bi-$Bi_2O_2CO_3$ were evaluated by photodegradation of the model organic contaminant MB under visible light illumination. However, in our case the as-prepared $Bi_2O_2CO_3$ and Bi-$Bi_2O_2CO_3$ have insignificant photocatalytic activity in dark (Figure 6.5a). During the photocatalytic reaction, MB forms a well-known colorless product leucomethylene blue (LMB) [87, 88] as expressed in equation (6.1).

$$2MB + 2e^- + H^+ = MB + LMB \qquad (6.1)$$

Figure 6.5a shows changes in MB concentration as a function of time in presence and absence of photocatalysts. With our experimental time window, MB has less than 10% degradation under light illumination in the absence of photocatalysts. In contrast, $Bi_2O_2CO_3$ nanosheets show an

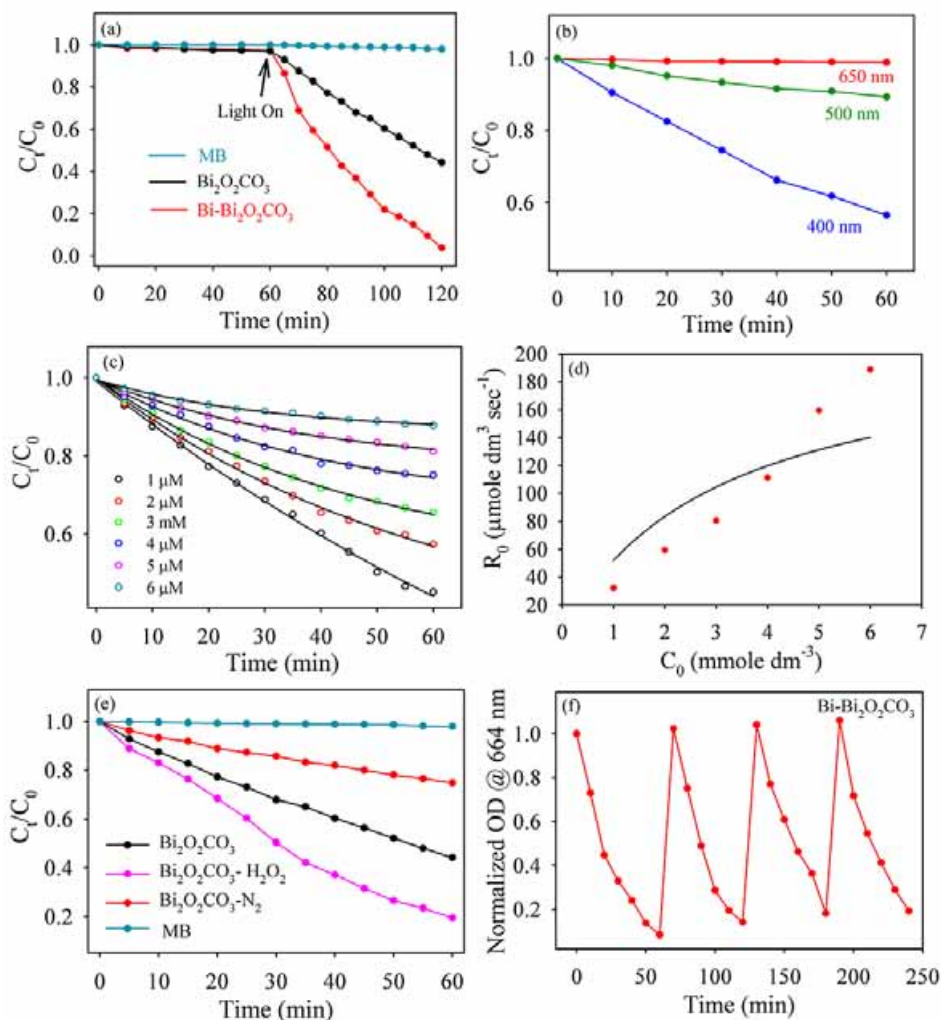***Figure 6.5.*** *(a) Photocatalytic degradation of MB under visible light illumination. (b) Photocatalytic degradation of MB by $Bi_2O_2CO_3$ at different wavelength. (c) C_t/C_0 versus time with various concentrations of methylene blue by $Bi_2O_2CO_3$. (d) Langmuir–Hinshelwood plot (L–H) for photocatalytic degradation of methylene blue using $Bi_2O_2CO_3$ (solid line is the model fitting and solid circles are experimental data). (e) Photodegradation of MB over $Bi_2O_2CO_3$ and Bi-$Bi_2O_2CO_3$ under conventional condition, presence of H_2O_2 and N_2 into the solution. (f) A recyclability study of Bi-$Bi_2O_2CO_3$ under visible light illumination.*

enhanced photocatalytic activity: 60% of MB degraded after 60 min illumination. One can see that presence of Bi nanoparticles on the $Bi_2O_2CO_3$ nanosheets further enhanced photocatalytic activity (100%) compared to $Bi_2O_2CO_3$ nanosheets (60%). Figure 6.5b shows photocatalysis of methylene blue (MB) at different wavelength by $Bi_2O_2CO_3$. Insignificant photocatalysis at 650 nm (MB absorbance maxima 660 nm) indicates that MB is unable to photosensitize $Bi_2O_2CO_3$. Thus photocatalysis predominately takes place via sensitization of $Bi_2O_2CO_3$. In order to find out the effect of the surface on photocatalysis, the Langmuir–Hinshelwood (L–H) kinetics was

studied using different concentrations of MB (Figure 6.5c). As shown in Figure 6.5d a significant deviation of the model (solid line) from experimental data is evident. The observation indicates that surface adsorption of the model pollutant play insignificant role in the photodegradation. In order to investigate the catalytic pathway, we further studied the photocatalytic activity of $Bi_2O_2CO_3$ in the presence of a radical initiator (H_2O_2) and radical quencher (N_2 bubbling) separately (Figure 6.5e). In fact, in the presence of H_2O_2 under solar light illumination increases generation of OH· which eventually increases the photocatalytic activity of $Bi_2O_2CO_3$ for degradation of MB. This demonstrated the role of reactive oxygen species (ROS) in the degradation of MB [71]. The photodegradation efficiency of $Bi_2O_2CO_3$ decreases with N_2 bubbling in the solution, so O_2 primarily acts as an efficient electron trap, leading to the generation of $O_2^{\cdot-}$ radicals during photocatalytic reaction [89]. From the application point of view, photochemical stability and durability of photocatalysts are significant during photocatalytic reaction [90]. To further test photocatalytic performance of the as-prepared
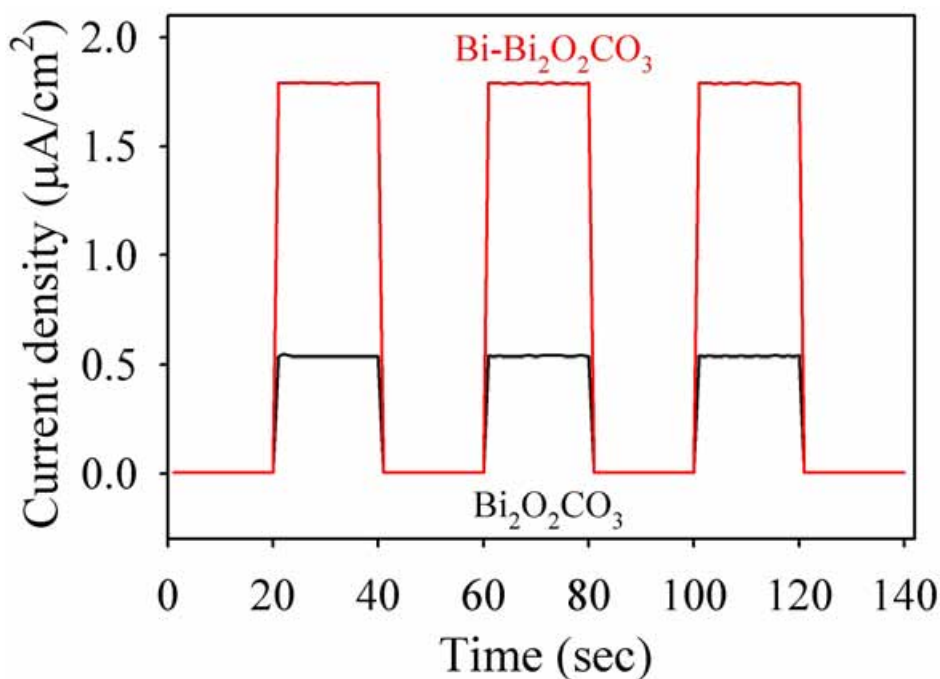
Figure 6.6. *Current−time curves of electrodes made of pure Bi$_2$O$_2$CO$_3$ and Bi-Bi$_2$O$_2$CO$_3$ heterojunction.*

heterojunction Bi-$Bi_2O_2CO_3$ photocatalyst, recycling experiment was carried out under repeated irradiation. Figure 6.5f shows the repeated photocatalytic activity of Bi-$Bi_2O_2CO_3$. The results indicate that the rate remains similar after four consecutive cycles, implying that the obtained Bi-

Bi$_2$O$_2$CO$_3$ heterojunction photocatalyst has high stability and no photocorrosion occurs during the photodegradation of MB. Photocurrent measurement was carried out under solar light illumination to investigate the efficient electron-hole separation. The photocurrent of Bi-Bi$_2$O$_2$CO$_3$ heterostructures is much higher than that of Bi$_2$O$_2$CO$_3$ (Figure 6.6). This implies that the heterojunction shows an improved separation of photogenerated electron−hole pairs and can greatly facilitate its photocatalytic activity.
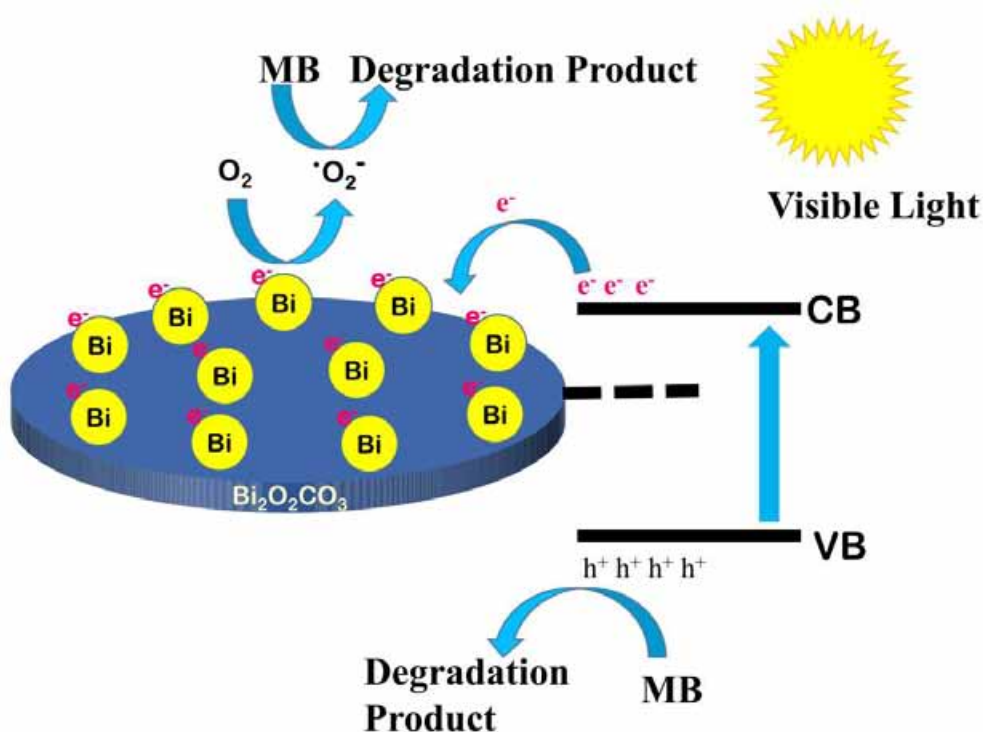
Scheme 6.1. *Schematic illustration of enhanced photocatalytic activity by Bi-Bi$_2$O$_2$CO$_3$ heterojunction under visible light illumination.*

There are several reports which indicate that the enhancement in photocatalytic performance can be ascribed to the synergetic effects of many factors, such as hierarchical structure, surface area, interfacial charge transfer and efficient separation of photoinduced electrons and holes [91-95]. In the present study, the enhanced photocatalytic performance for the Bi-Bi$_2$O$_2$CO$_3$ photocatalyst can be ascribed to the formation of heterojunction between Bi nanoparticles and the surface of Bi$_2$O$_2$CO$_3$ nanosheets. Furthermore, the Fermi level of Bi nanoparticles which act as electron acceptors can be estimated to be about -0.17 eV as calculated by the work function of metallic bismuth of 4.22 eV [96-98]. Since the Fermi level of metallic Bi

(-0.17 eV) is lower than the conduction band of $Bi_2O_2CO_3$ (-1.40 eV) [26], the photogenerated electrons would probably transfer from $Bi_2O_2CO_3$ to the deposited Bi nanoparticles and therefore promote the separation of photo-generated electrons and holes, effectively. After the separation of electrons and holes, these two kinds of photogenerated charge carriers would be transformed into reactive species that are responsible for promoting photocatalytic activity. Based on the above investigations, a schematic illustration is proposed as shown in Scheme 6.1.

6.2.2. Nano Surface Engineering of Mn_2O_3 for Potential Light-Harvesting Application [5]:

Figure 6.7a-c show the morphology of the as-synthesized Mn_2O_3 microspheres without and with Fe^{+3}/Cu^{+2} doping as revealed from FESEM. The average sizes of the native, Fe (Fe-Mn_2O_3) and Cu (Cu-Mn_2O_3) doped Mn_2O_3 microspheres are found to be 6-8 μm, 4-6 μm and 5-7 μm, respectively. Figure 6.7d shows XRD patterns of native Mn_2O_3, Fe-Mn_2O_3 and Cu-Mn_2O_3, respectively. XRD patterns of Fe-Mn_2O_3 and Cu-Mn_2O_3 are similar to that of native bare Mn_2O_3
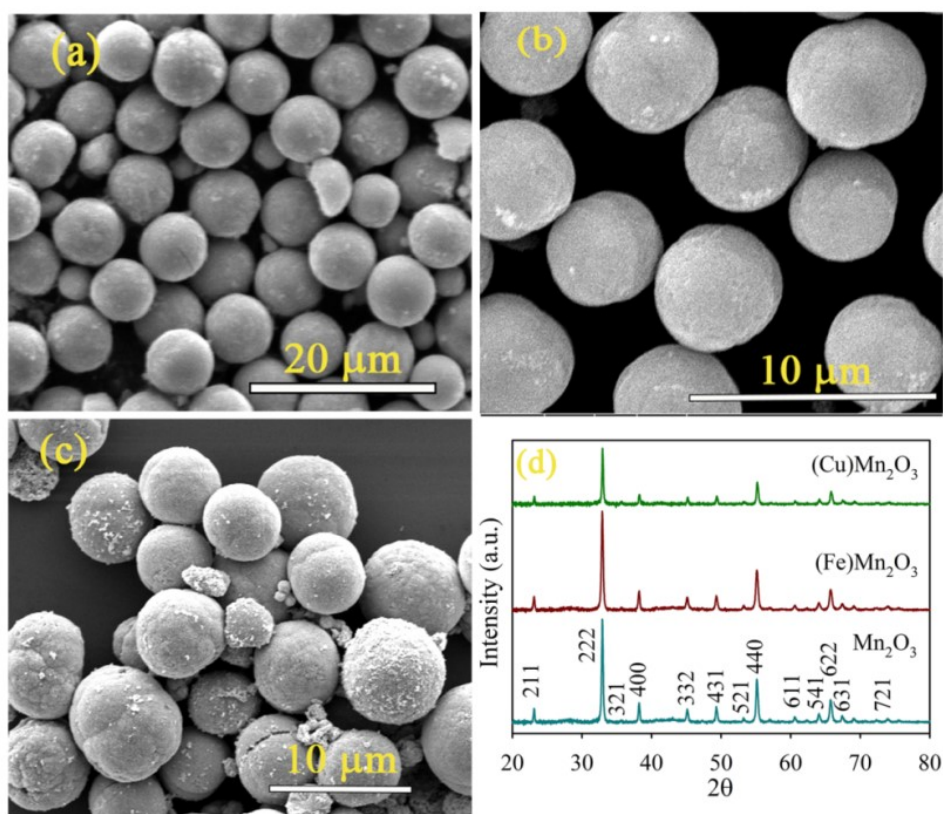
Figure 6.7. *FESEM images of (a) Mn_2O_3, (b) Fe doped Mn_2O_3 and (c) Cu doped Mn_2O_3 microsphere samples. (d) XRD pattern of Mn_2O_3, Fe doped Mn_2O_3 and Cu doped Mn_2O_3.*

and consistent with the diffraction pattern of pristine bulk Mn_2O_3 reported in the literature [99]. During doping of bulk Mn_2O_3, Cu^{2+} ion can easily replace Mn^{3+} in the crystal lattice due to the smaller radius of the Cu^{2+} ion (0.057 nm) compared to that of Mn^{3+} (0.066). Similarly the substitution of Mn^{3+} ion by Fe^{3+} occurs due to the smaller radius of the Fe^{3+} ion (0.063) [100, 101].

In order to confirm the uniform distribution of Fe and Cu atoms in the $Fe-Mn_2O_3$ and $Cu-Mn_2O_3$ microspheres we have performed elemental EDAX mapping as shown in Figure 6.8. From the EDAX measurement, it is observed that 2.5 wt % of Fe is doped into the Mn_2O_3 crystal and 1.96 wt % of Cu is doped into Mn_2O_3 crystal lattice. TEM was used in order to investigate
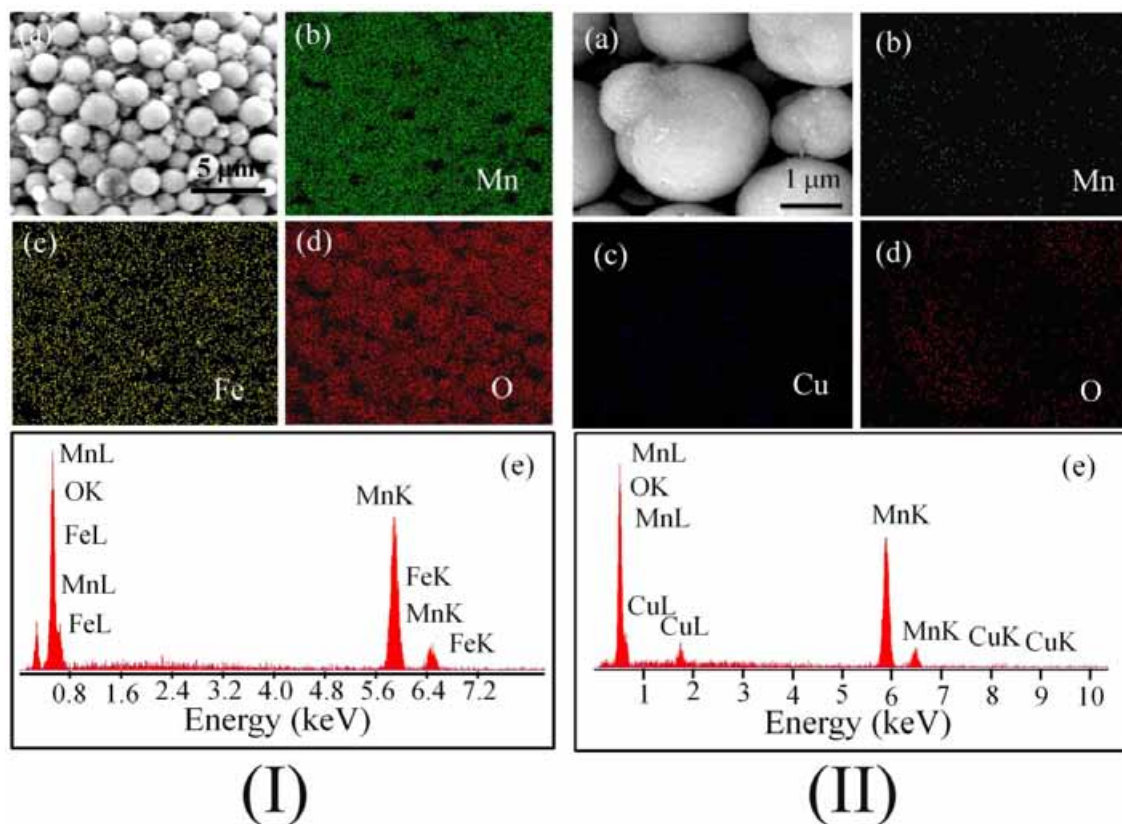
Figure 6.8. *(I) (a) SEM image, (b) Mn, (c) Fe, and (d) O elemental mapping images of Fe doped Mn_2O_3 microsphere.(e) EDAX spectrum of Fe doped Mn_2O_3 microsphere (II) (a) SEM image, (b) Mn, (c) Cu, and (d) O elemental mapping images of Cu doped Mn_2O_3 microsphere.(e) EDAX spectrum of Cu doped Mn_2O_3 microsphere.*

the microscopic structure of as synthesized Mn_2O_3 microspheres (Figure 6.9a). Upon interaction with citrate ligands the Mn_2O_3 microspheres become water soluble and smaller in size as evident from the HRTEM image (Figure 6.9b). The citrate functionalized Mn_2O_3 nanoparticles (C-

Mn_2O_3 NPs) are found to have a size distribution with an average diameter of 29.01 ± 0.27 nm (inset of Figure 6.9b). The HRTEM images of $C-Mn_2O_3$ NPs also show the high crystallinity of the NPs. The inter planar distance between the fringes is found to be about 0.268 nm consistent with (222) planes of bulk Mn_2O_3 [102]. The citrate functionalized Fe doped Mn_2O_3 and Cu doped Mn_2O_3 NPs are found to have an average size of 43 ± 0.16 and 40.38 ± 0.45 nm respectively. HRTEM images also indicate the highly crystalline nature of citrate functionalized Fe doped Mn_2O_3 and Cu doped Mn_2O_3 NPs.
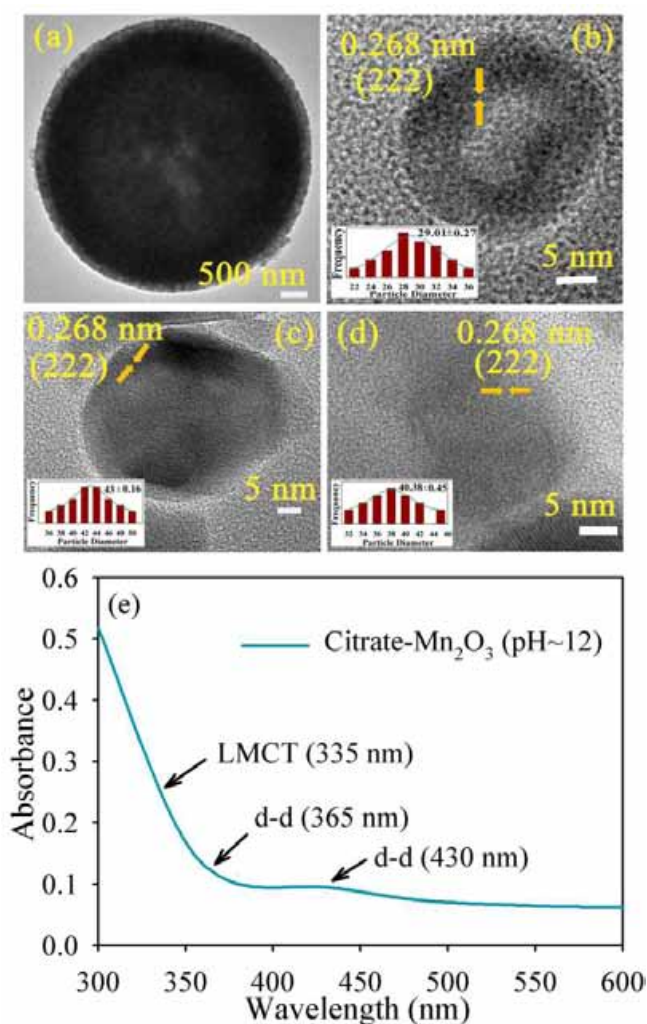
Figure 6.9. *TEM image of Mn_2O_3 microsphere (a) $C-Mn_2O_3$ (b) Fe doped $C-Mn_2O_3$ (c) and Cu doped $C-Mn_2O_3$ (d) NPs. (inset shows size distribution of NPs) (e) UV-vis absorption spectrum of $C-Mn_2O_3$ NPs (at pH ~12 and $70^\circ C$ for 12 h).*

The effect of citrate functionalization of the NPs is evident in UV-Vis absorbance spectra of the NPs at room temperature. While the citrate ligand and native Mn_2O_3 do not show any characteristic peak in the wavelength range of 300-600 nm, functionalized NPs show several absorption peaks (at 335, 365 and 430 nm) in the wavelength window (as shown in Figure 6.9e) [42, 103]. The observed peak at 335 nm may be assigned to high energy ligand to metal charge transfer (LMCT) processes involving citrate-Mn^{3+} interactions. The other peaks at 365 and 430 nm correspond to the d-d transitions of Mn^{3+} in Mn_2O_3 NPs since Mn^{3+} (d^4) forms a high spin
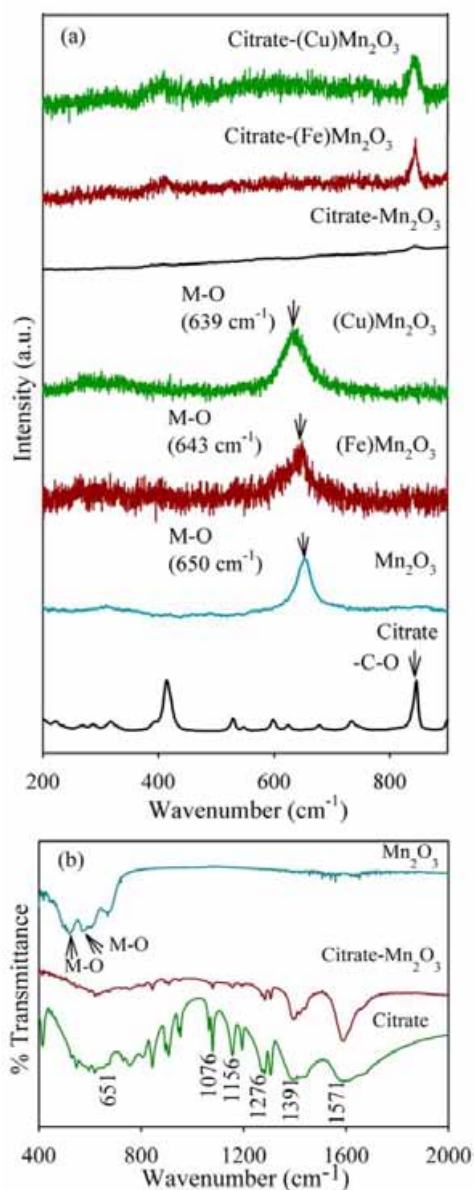
Figure 6.10. *(a) Raman spectra of the citrate, Mn_2O_3, Fe doped Mn_2O_3, Cu doped Mn_2O_3, C-Mn_2O_3, Fe doped C-Mn_2O_3 and Cu doped C-Mn_2O_3. (b) FTIR spectra of citrate, C-Mn_2O_3 and Mn_2O_3 respectively.*

229

complex. The ground state term of $Mn^{3+}(d^4)$ is 5E in Mn_2O_3 from the high spin complex which undergoes a Jahn-Teller distortion due to functionalization with citrate. This leads to band transitions of $5B_1$-5E, $5B_1$-$5B_2$ and $5B_1$-$5A_1$ [104, 105]. Figure 6.10a shows Raman spectra of the ligand, bare Mn_2O_3 and C-Mn_2O_3 revealing the structural modification of Mn_2O_3 NPs upon functionalization with the citrate ligand. The main characteristic peak observed at 650 cm^{-1} of Mn_2O_3 NPs corresponds to M-O stretching vibrations, [106] and C-O stretching vibration of the citrate ligand located at 843 cm^{-1} are perturbed upon functionalization with citrate. This indicates the covalent binding of citrate ligand with the NPs surface. Similar changes are observed for Fe-Mn_2O_3 and Cu-Mn_2O_3 after citrate functionalization as shown in Figure 6.10a. A strong electronic coupling of the ligand with Mn_2O_3 NPs is also evident from FTIR spectra as shown in Figure 6.10b. Bare Mn_2O_3 shows two characteristic bands at 576 and 521 cm^{-1} corresponding to M-O stretching vibrations of Mn_2O_3 NPs [107]. After functionalization with citrate ligands, the bands are distinctly diminished indicating strong interaction between Mn_2O_3 NPs and citrate ligand. It is also observed that two sharp bands at 1156 and 1076 cm^{-1} responsible for the C-O stretching modes of citrate [108] are broadened in C-Mn_2O_3 NPs. This observation is consistent with the fact that the carboxylate functional group in the citrate makes covalent binding with the NPs surface.

Figure 6.11. *Cyclic voltammogram of bare Mn_2O_3 (cyan line) and Mn_2O_3 after functionalization with citrate (green line) recorded at a scan rate 50 mVS^{-1} in the range of 0 to 3 V using Ag/AgCl as a reference electrode.*

A clear change in the redox property of bare Mn_2O_3 upon citrate functionalization is evident from CV measurements as shown in Figure 6.11. It is known that for bare Mn_2O_3, the first reduction process at ~1.1 V corresponds to th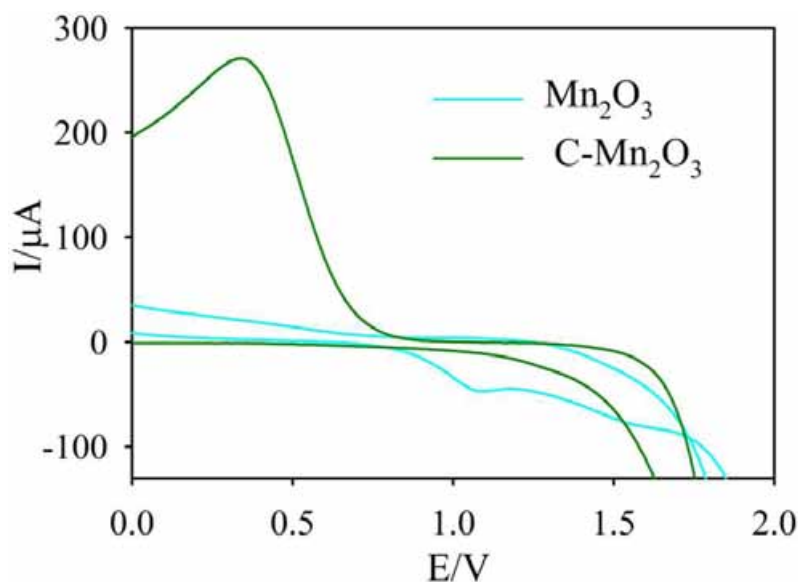e reduction of Mn^{3+} to Mn^{2+} [109]. As evident from Figure 6.11, the reduction peak at 1.06 V for bare Mn_2O_3 is significantly perturbed upon functionalization and a new peak at ~0.35 V appears for Mn_2O_3 NPs. This peak can be attributed to the oxidation of Mn^{+3}/Mn^{+4} species [110]. This implies that after functionalization in Mn_2O_3 the charge state of Mn^{3+} disproportionates and is generate dominantly by the +4 charge state. It has to be noted that the formation of the +2 state as a result of disproportionation is not clear from these CV studies, however, evident in the XPS spectrum. Figure 6.12 shows XPS spectra of Mn_2O_3, $Fe-Mn_2O_3$ and $Cu-Mn_2O_3$ after citrate functionalization. As reported in the earlier studies Mn_2O_3 shows two Mn 2p peaks at 642.40 and 654.13 eV, which are attributed to Mn $2p_{3/2}$ and Mn $2p_{1/2}$, respectively [111]. A spin energy gap of 11.73 eV is reported to be a significant signature of Mn^{3+} in Mn_2O_3 [112]. As shown in Figure 6.12a the XPS spectrum (Mn 2p) for C-Mn_2O_3 can be deconvoluted into four peaks at 640.27, 640.46, 642.23 and 653.18 eV. While 640.27 eV can be attributed to Mn^{2+}, 640.46 and 642.23 eV are corresponds to Mn^{3+} and Mn^{4+} respectively [61, 113]. The Mn $2p_{1/2}$ at 653.18 eV indicates a +3 oxidation state of Mn assuming the peak at 646.09 eV to be a shake-up satellite [71]. The deconvoluted O 1s line spectra are composed of three peaks. The O 1s line at 530.72 eV corresponds to the surface hydroxyl groups and the peaks at 531.54 and 535.25 eV indicate the presence of adsorbed water molecules [114]. Again, the deconvoluted C 1s line spectra were recorded with three peaks to analyze the interactions between the citrate ligand and NPs. The C 1s peak at 284.56, 286.50 and 288.10 eV can be assigned to carbon present in citrate in the form of C-C, C-OH and COO, respectively [115]. Therefore, functionalization with citrate suppresses the +3 oxidation state of Mn and generates +4 and +2 states via a disproportionation mechanism [116]. As shown in Figure 6.12, similar changes in the oxidation state of Mn for $Fe-Mn_2O_3$ and $Cu-Mn_2O_3$ NPs after citrate functionalization are evident. The XPS spectrum of Fe doped Mn_2O_3 shows two Fe 2p peaks at 710.19 and 724.51 eV which can be attributed to Fe $2p_{3/2}$ and Fe $2p_{1/2}$ respectively [117, 118]. This indicates incorporation of Fe into the lattice of Mn_2O_3. The XPS spectrum of Cu doped Mn_2O_3 illustrates two Cu 2p peaks at 932.9 and 952.8 eV, which can be attributed to Cu $2p_{3/2}$ and Cu $2p_{1/2}$, respectively [99, 119, 120]. The observation confirms the incorporation of Cu into the lattice of Mn_2O_3.
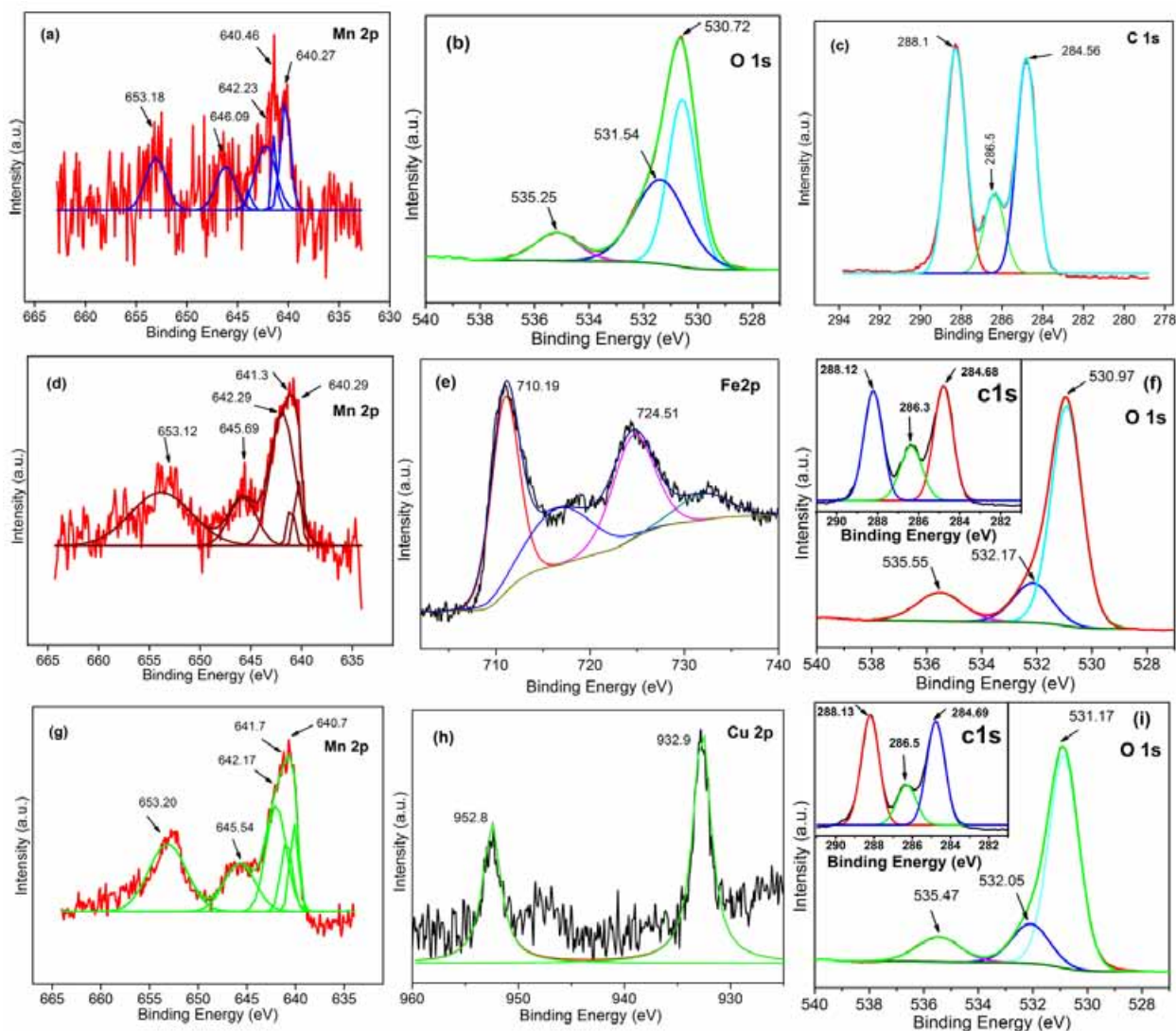
Figure 6.12. *XPS spectra of C-Mn$_2$O$_3$ NPs (a) Mn 2p, (b) O 1s, and (c) C 1s. XPS spectra of Fe doped C-Mn$_2$O$_3$ NPs (d) Mn 2p, (e) Fe2p, and (f) O 1s (inset shows C 1s). XPS spectra of Cu doped C-Mn$_2$O$_3$ NPs (g) Mn 2p, (h) Cu2p, and (i) O 1s (inset shows C 1s).*

Figure 6.13a shows normalized fluorescence spectra of C-Mn$_2$O$_3$ NPs at room temperature at pH 12. C-Mn$_2$O$_3$ NPs show multiple photoluminescence (PL maxima at 392, 462 and 491 nm) upon excitation at different wavelengths (335, 365 and 430 nm, respectively). Figure 6.13b shows excitation spectra of C-Mn$_2$O$_3$ NPs with different emission wavelengths. The ligand field theory can be useful in order to understand the multiple PL of the C-Mn$_2$O$_3$ NPs [121, 122]. Multiple PL of the C-Mn$_2$O$_3$ NPs arise mainly due to the LMCT (citrate-Mn^{3+})
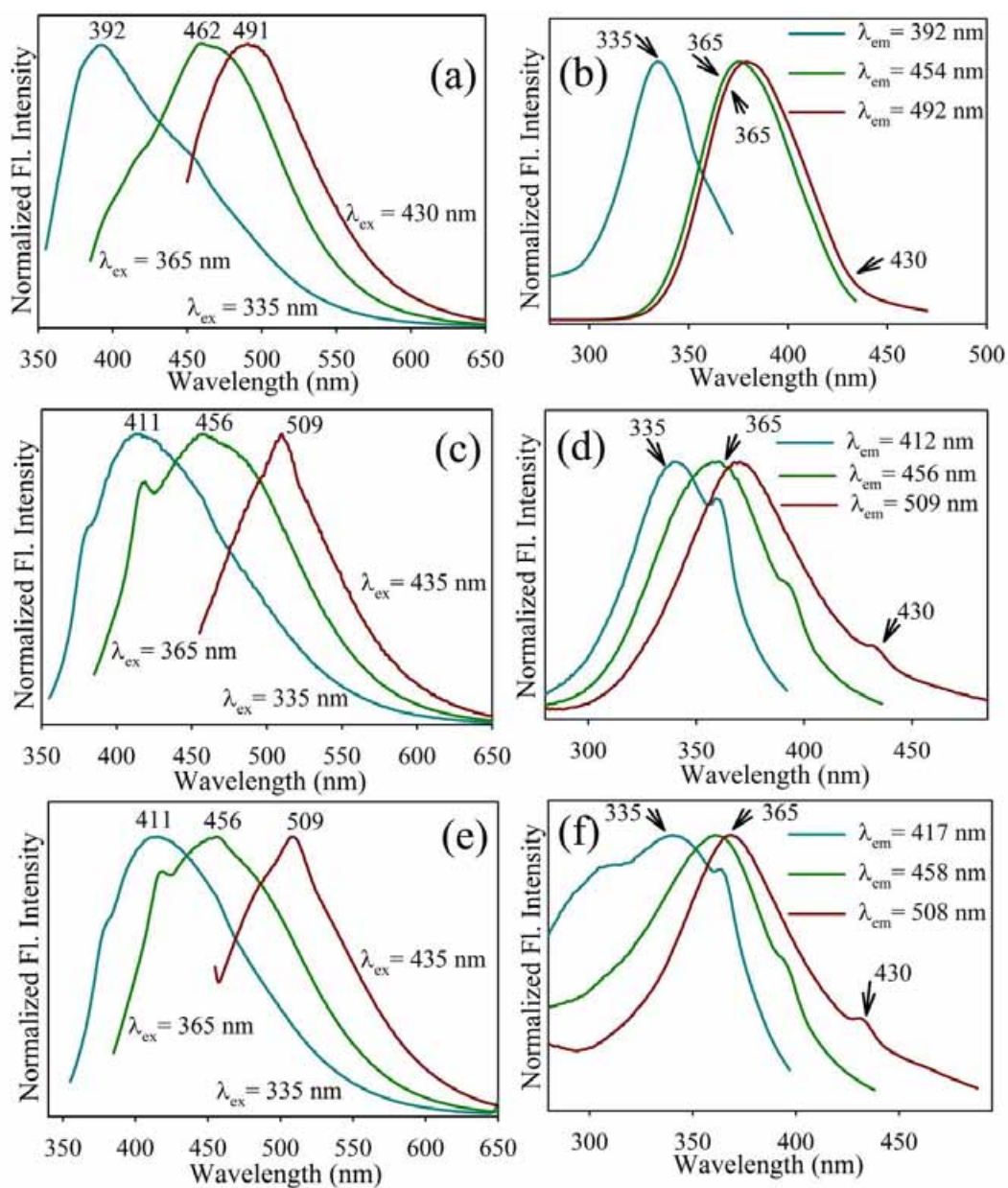
Figure 6.13. *(a), (c) and (e) are normalized steady-steady PL spectra collected from C-Mn₂O₃, Fe doped C-Mn₂O₃ and Cu doped C-Mn₂O₃ NPs respectively at three different excitation wavelengths at pH ~ 12. Figure b,d and f are the excitation spectra of C-Mn₂O₃, Fe doped C-Mn₂O₃ and Cu doped C-Mn₂O₃ NPs respectively at different PL maxima.*

excited states and the ligand field excited states of the metal (Mn^{3+}) d-orbitals. Thus the PL peak at 392 nm arises due to LMCT from HOMO (Highest occupied molecular orbital, centered in the ligand) to LUMO (Lowest unoccupied molecular orbital, centered in the metal centre). On the other hand, PL peaks at 462 and 492 nm arise due to d-d transition of Mn^{3+} ion, in presence of the citrate ligand. Similarly, the multiple PL (maxima at 411, 456 and 509 nm) arises in C-Fe-

Mn$_2$O$_3$ NPs and C-Cu-Mn$_2$O$_3$ NPs upon excitation at different wavelengths (335, 365 and 435 nm, see Figure 6.13c, 6.13e). Figure 6.13d and 6.13f shows excitation spectra of C-Fe-Mn$_2$O$_3$ NPs and C-Cu-Mn$_2$O$_3$ NPs detected at different PL maxima. It is observed that unfunctionalized Mn$_2$O$_3$, Fe-Mn$_2$O$_3$ and Cu-Mn$_2$O$_3$ have no such PL properties due to absence of LMCT and J-T phenomenon. The multiple PL of the citrate functionalized NPs is further recorded under a fluorescence microscope, see Figure 6.14. Figure 6.14a-c shows bright field images and two fluorescence images of C-Mn$_2$O$_3$ NPs (excitation at 365 and 436 nm) respectively. C-Mn$_2$O$_3$ NPs upon 365 nm excitation shows cyan emission and 436 nm excitation shows green emission. Figure 6.14d-f shows similar PL of functionalized Mn$_2$O$_3$ microspheres on the stainless steel mesh.
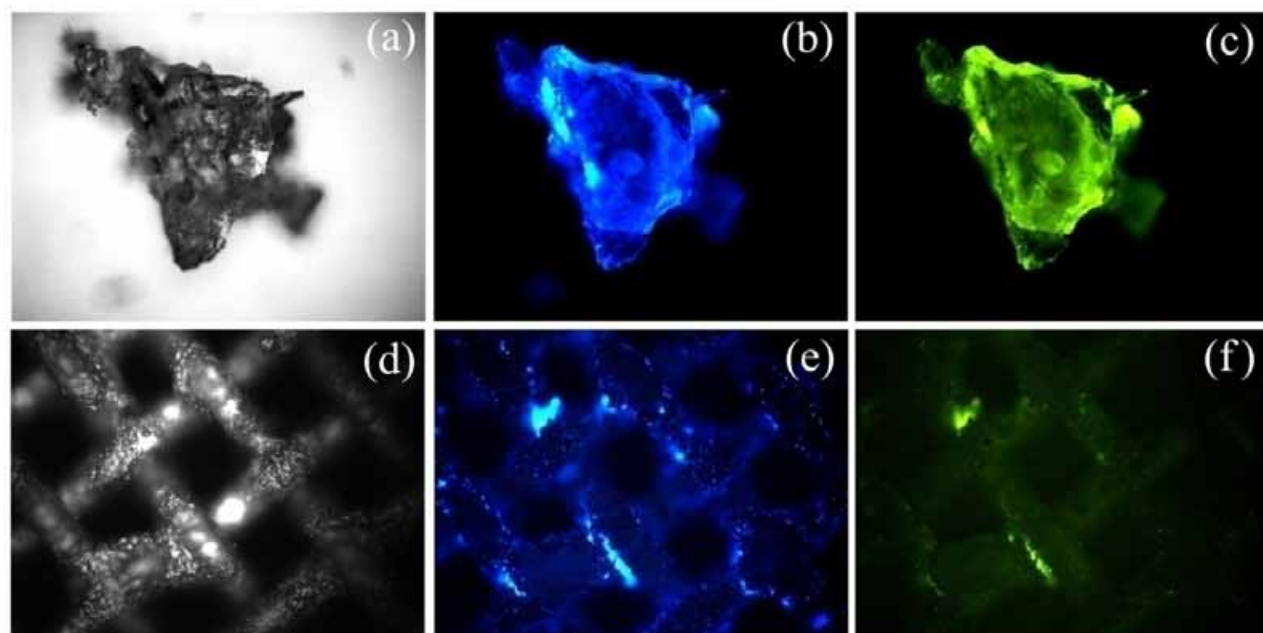
Figure 6.14. *Fluorescence microscopic images of the C-Mn$_2$O$_3$ NPs and mesh-C-Mn$_2$O$_3$ under white light (a and d) and light of two different wavelengths 365 nm (b and e) and 436 nm (c and f), respectively.*

In order to investigate a detailed mechanistic insight into the origin of the multiple PL of the functionalized NPs, we have performed picosecond-resolved fluorescence studies. From Figure 6.15, the fluorescence decay of the C-Mn$_2$O$_3$, C-Fe-Mn$_2$O$_3$ and C-Cu-Mn$_2$O$_3$ NPs was determined at different PL maxima of 456 and 507 nm using lasers as an excitation source at 375
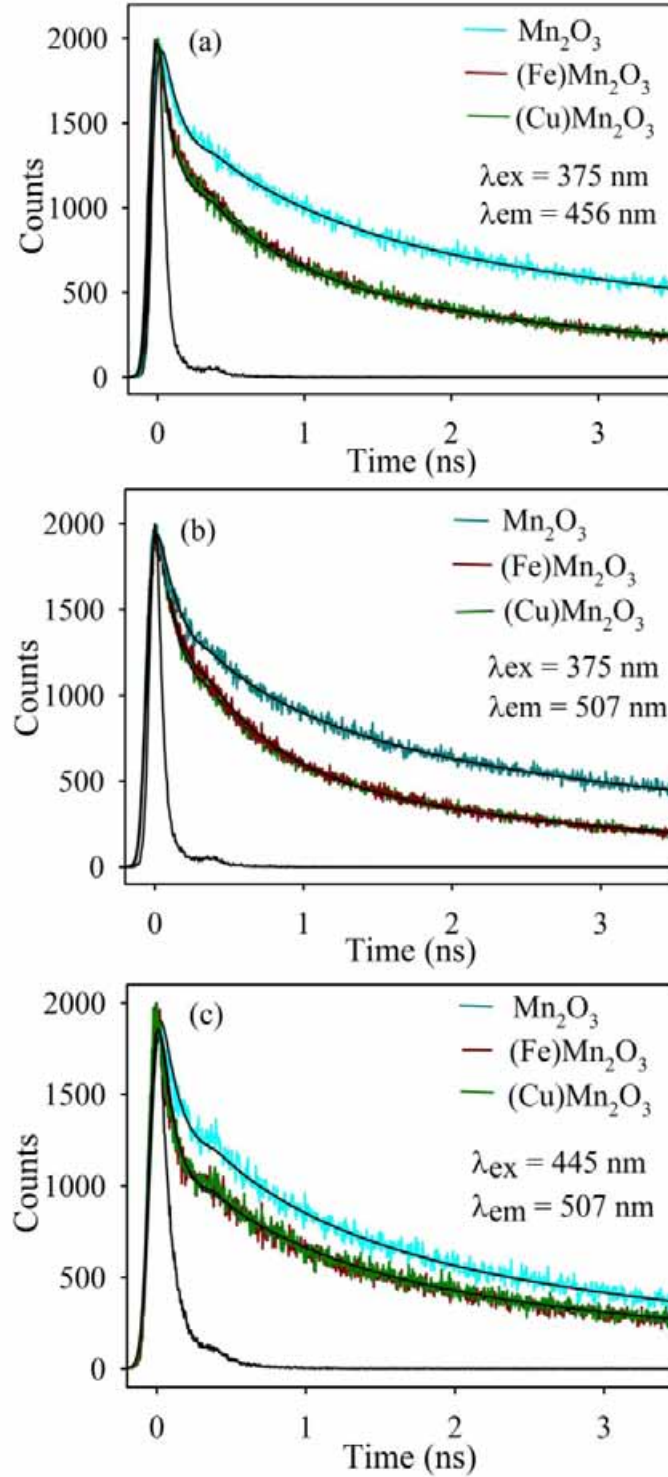
Figure 6.15. *(a) and (b) are the picosecond-resolved PL transients of C-Mn$_2$O$_3$ NPs, Fe doped C-Mn$_2$O$_3$ NPs and Cu doped C-Mn$_2$O$_3$ NPs measured at emission wavelenghts 456 nm and 507 nm upon excitation at a wavelength 375 nm. (c) Picosecond-resolved PL transients of C-Mn$_2$O$_3$ NPs, Fe doped C-Mn$_2$O$_3$ NPs and Cu doped C-Mn$_2$O$_3$ NPs measured at emission wavelenght of 507 nm upon excitation at wavelength of 445 nm.*

235

and 445 nm, respectively. The lifetime values for 456 and 507 nm emission (upon excitation by 375 and 445 nm laser sources) decays are shown in Table 6.2. From this table it is shown that the average life time of C-Mn_2O_3 are 2.01 and 1.95 ns when the PL is measured at 456 and 507 nm, respectively, upon 375 nm laser excitation, while it is 0.59 ns when PL is taken at 507 nm upon 445 nm laser excitation. The lifetime data clearly suggest that the Jahn-Teller distortion leads to PL maxima at 456 and 507 nm upon excitation at 375 and 445 nm, respectively. Here, it is observed that after doping the J-T distorted d-d transition leads to PL maxima at 456 and 507 nm. The average lifetime of C-Fe-Mn_2O_3 are 0.76 and 0.94 ns, respectively, upon 375 laser excitation, while it is 0.34 ns when PL is measured at 507 nm upon 445 nm laser excitation. The decrease in average lifetime after iron doping may be attributed to the faster electron transfer from C-Mn_2O_3 to Fe^{+3}. The average lifetime of C-Cu-Mn_2O_3 are 0.74 and 0.91 ns upon 375 nm laser excitation while it is 0.33 ns when PL is measured at 507 nm upon 445 nm laser excitation. The decrease in average lifetimes indicate an additional nonradiative time scale in the excited

Table 6.2. Lifetimes of picosecond time-resolved PL transients of C-Mn_2O_3 , Fe doped C-Mn_2O_3 and Cu doped C-Mn_2O_3 NPs, detected at various PL maxima upon excitation at different wavelengths. The values in parentheses represent the relative weight percentages of the time components.

System	λ_{ex} (nm)	λ_{em} (nm)	τ_1 (ns)	τ_2 (ns)	τ_3 (ns)	τ_{avg} (ns)	k_{nr} (10^{10} s^{-1})
C-Mn_2O_3	375	456	0.08(58)	1.5(23)	8.6(19)	2.01	
		507	0.14(58)	1.65(26)	9.04(14)	1.95	
	445	507	0.04(80)	0.85(10)	4.59(10)	0.59	
Fe doped C-Mn_2O_3	375	456	0.06(69)	1.1(22)	5.35(9)	0.76	8.14
		507	0.15(62)	1.17(10)	5.4(10)	0.94	5.51
	445	507	0.03(88)	0.99(7)	5.26(5)	0.34	12.46
Cu doped C-Mn_2O_3	375	456	0.06(71)	1.13(20)	5.54(9)	0.74	8.53
		507	0.14(65)	1.2(26)	5.53(9)	0.91	5.86
	445	507	0.11(88)	0.9(6)	4.63(6)	0.33	13.35

state which can altered the fluorescence lifetimes. The apparent rate constant (k_{nr}) is determined for the nonradiative processes by comparing the lifetimes of citrate functionalized Mn_2O_3 NPs in the absence (τ_0) and the presence (τ) of doping metal ion, using the equation.

$$\kappa_{nr} = \frac{1}{\tau} - \frac{1}{\tau_0} \qquad (6.2)$$

The apparent rate constant values for Fe doped C-Mn_2O_3 and Cu doped C-Mn_2O_3 are shown in Table 6.2 which indicates the excited state electron transfer from C-Mn_2O_3 to Fe and Cu.

It has been reported that adsorption play an important role in the removal of pollutants [123-126]. However, in our case the as prepared microsphere has insignificant ability for methylene blue adsorption (data not shown). During photocatalytic reaction, MB form a well-known colorless product leucomethylene blue (LMB) [87, 88] as shown in equation 6.3.

$$2\ MB + 2\ e^- + H^+ = MB + LMB \qquad\qquad (6.3)$$

In order to confirm the formation of the leucomethylene blue, the degradation of methylene blue was performed in the presence of citrate capped Mn_2O_3 NPs under UV light irradiation and the absorption spectra were monitored at different time interval. As shown in Figure 6.16a, the methylene blue peak at 664 nm is decreases with time whereas another peak at 246 nm corresponding to the leucomethylene blue formation increases during photocatalysis. As shown in Figure 6.16b, no degradation of MB is observed in the absence of light. With our experimental time window, MB shows <10 % degradation under light illumination in the absence of NPs. Under UV light illumination, C-Mn_2O_3 NPs show a 50% MB degradation after 80 minutes. It is important to be noted that with our experimental conditions (pH 3), Mn^{3+} ions easily disproportionate into Mn^{2+} and Mn^{4+}. So there is a possibility of d-d transitions involving $Mn^{2+/4+}$ ions on the C-Mn_2O_3 NPs surface. According to the selection rules of fundamental electronic spectroscopy, LMCT bands (involving the interaction between the highest occupied molecular orbital of citrate and the lowest unoccupied molecular orbital $Mn^{2+/4+}$) are mainly responsible for photocatalytic degradation of the model pollutant, MB. After doping with Fe, the photocatalytic activity of C-Fe-Mn_2O_3 NPs shows 65% MB degradation under UV light illumination. However, in C-Cu-Mn_2O_3 NPs the photocatalytic activity decreases to 20%. As compared to other catalysts reported in the literatures, the photocatalytic activity of citrate functionalized Fe doped Mn_2O_3 NPs used in this work shows better catalytic activity [59, 60, 70, 127-129]. In order to find out the effect of surface on photocatalysis, the Langmuir-Hinshelwood (L-H) kinetics has been studied using different concentration of MB. From Figure 6.16c-d it is observed that surface do not play any role in photocatalysis since a huge deviation of the model from experimental data is evident. In order to investigate the catalytic pathway, we further studied the photocatalytic activity of citrate functionalized NPs in presence of a radical initiator (H_2O_2) and radical quencher (sodium azide) separately. The photocatalytic activity of citrate functionalized NPs
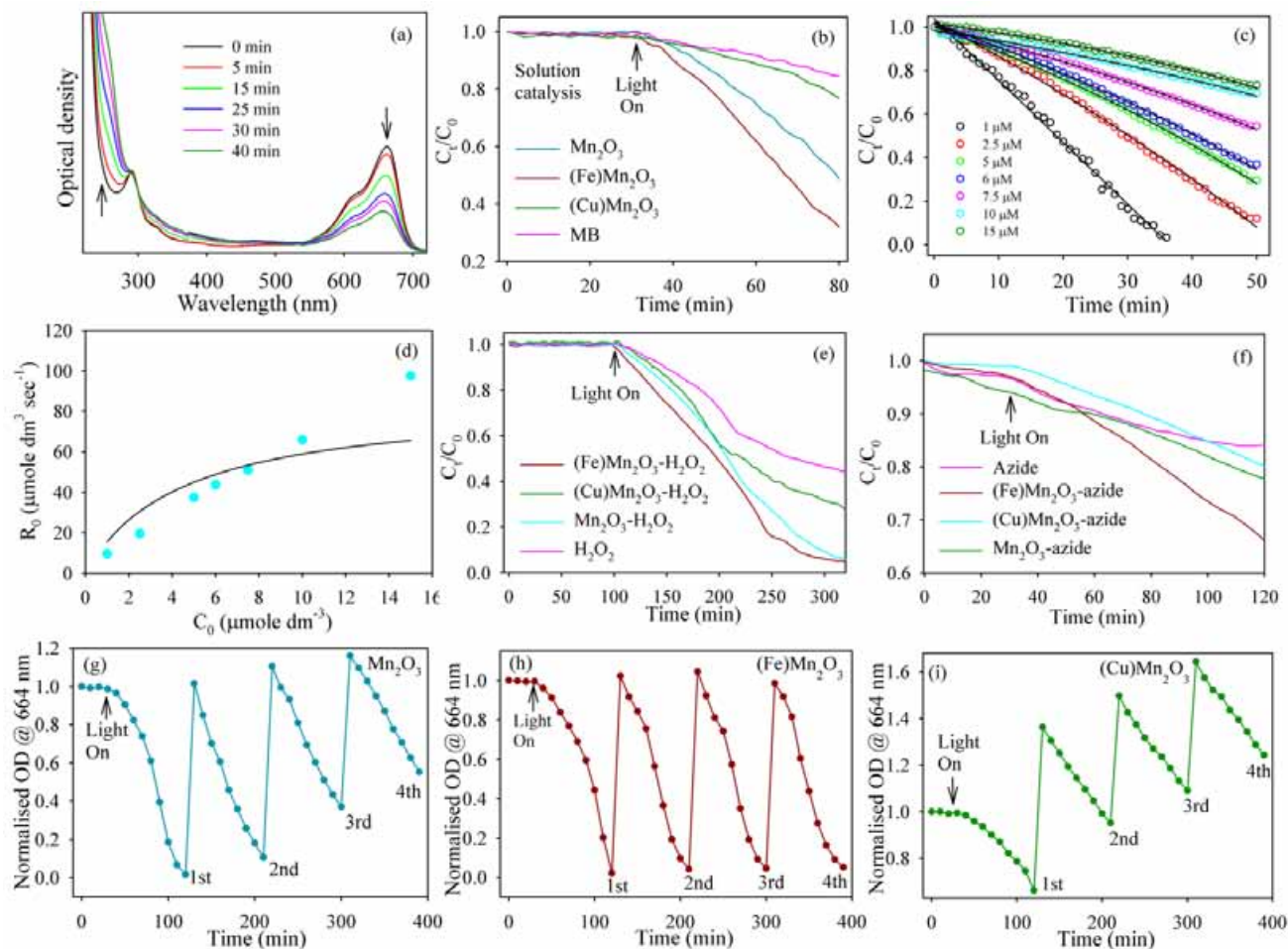
Figure 6.16. *Photocatalytic degradation of MB in the presence of (a) C-Mn$_2$O$_3$ (b) C-Mn$_2$O$_3$, Fe doped C-Mn$_2$O$_3$ and Cu doped C-Mn$_2$O$_3$ NPs in solution under UV light illumination. (c) C$_t$/C$_0$ versus time with various concentrations of methylene blue. (d) Langmuir-Hinshelwood plot (L-H) for photocatalytic degradation of methylene blue using citrate functionalized Mn$_2$O$_3$ nanoparticles (solid line is the model fitting and solid circles are experimental data). (e) Photocatalytic degradation of MB in the presence of hydrogen peroxide under UV light illumination. (f) Photocatalytic degradation of MB in the presence of sodium azide under UV light illumination. The recyclability study of C-Mn$_2$O$_3$ (g) Fe doped C-Mn$_2$O$_3$ (h) and Cu doped C-Mn$_2$O$_3$ (i) NPs under UV light illumination.*

increases in presence of H$_2$O$_2$ indicating a role of reactive oxygen species (ROS) in the degradation of MB [71]. Actually, in presence of H$_2$O$_2$ and under UV light illumination, the generation of $^\bullet$OH increases the enhanced photocatalytic activity. We further studied the effect of sodium azide (a ROS quencher) on the degradation of MB by citrate functionalized NPs under UV light illumination. Figure 6.16f clearly shows that in the presence of sodium azide the degradation rate of MB become slower. This indirectly confirms that the reaction proceeds via a ROS mechanism. The increase in the photocatalytic activity of C-Fe-Mn$_2$O$_3$ NPs compare to C-

Mn_2O_3 NPs may be due to the excited state electron transfer from Mn_2O_3 to Fe^{3+}. This excited state electron transfer may facilitates the charge separation. The regeneration of Fe^{3+} takes places via ROS generation in an aqueous medium that eventually enhances the photocatalytic activity of Fe-C-Mn_2O_3 NPs [130, 131]. However, in case of C-Cu-Mn_2O_3 an excited electron transfer from Mn_2O_3 to Cu^{2+} takes place which is evident from the TCSPC data. The regeneration of Cu^{2+} may takes place efficiently through the ground state recovery of C-Mn_2O_3 and not via a ROS generation. To examine the stability of citrate functionalized nanoparticles, we examined the photocatalytic degradation of MB upto four cycles under UV light illumination at room temperature. The recyclability of C-Mn_2O_3, C-Fe-Mn_2O_3 and C-Cu-Mn_2O_3 NPs is shown in Figure 6.16g-i. This data suggests that C-Fe-Mn_2O_3 NPs shows good recyclability up to the fourth cycle, whereas the C-Mn_2O_3 and C-Cu-Mn_2O_3 degradation efficiency decreases with each cycle.

In order to explore possible applications of citrate functionalized NPs for waste water treatment a stainless steel mesh has been used as a template. Figure 6.17a-b show pure Mn_2O_3 microspheres on the stainless steel mesh at low and high magnification, respectively. While the low magnification FESEM image of the mesh confirms an attachment of Mn_2O_3 microspheres, the high magnification image shows the uniform size distribution of the microspheres ranging from 2.5-3.5 μm. Upon doping with Fe^{3+} and Cu^{2+} the average size distributions of the synthesized microsphere are 3.5-4.5 μm and 1.5-2 μm, respectively. We have successfully functionalized the microspheres in the mesh with the citrate ligand. Here, the photocatalytic activity of C-Mn_2O_3, C-Fe-Mn_2O_3 and C-Cu-Mn_2O_3 has been studied on the mesh using MB as a model contaminant under solar light illumination. The pH of the solution is maintained at 6. The area of the mesh used in the photocatalytic study was 2 cm × 1.5 cm. From Figure 6.17e it is evident that in absence of light the citrate functionalized microspheres show no photocatalytic activity. However, under solar light illumination C-Mn_2O_3 exhibits 25% degradation, while the photocatalytic activity of C-Fe-Mn_2O_3 on the mesh increases to 34%. In the case of copper doping the photocatalytic activity of the sensitized C-Cu-Mn_2O_3 on the mesh decreases down to 12%. Under the same experimental conditions, MB in the absence of functionalized Mn_2O_3 microspheres shows no such degradation (7%). To our understanding such type of system is
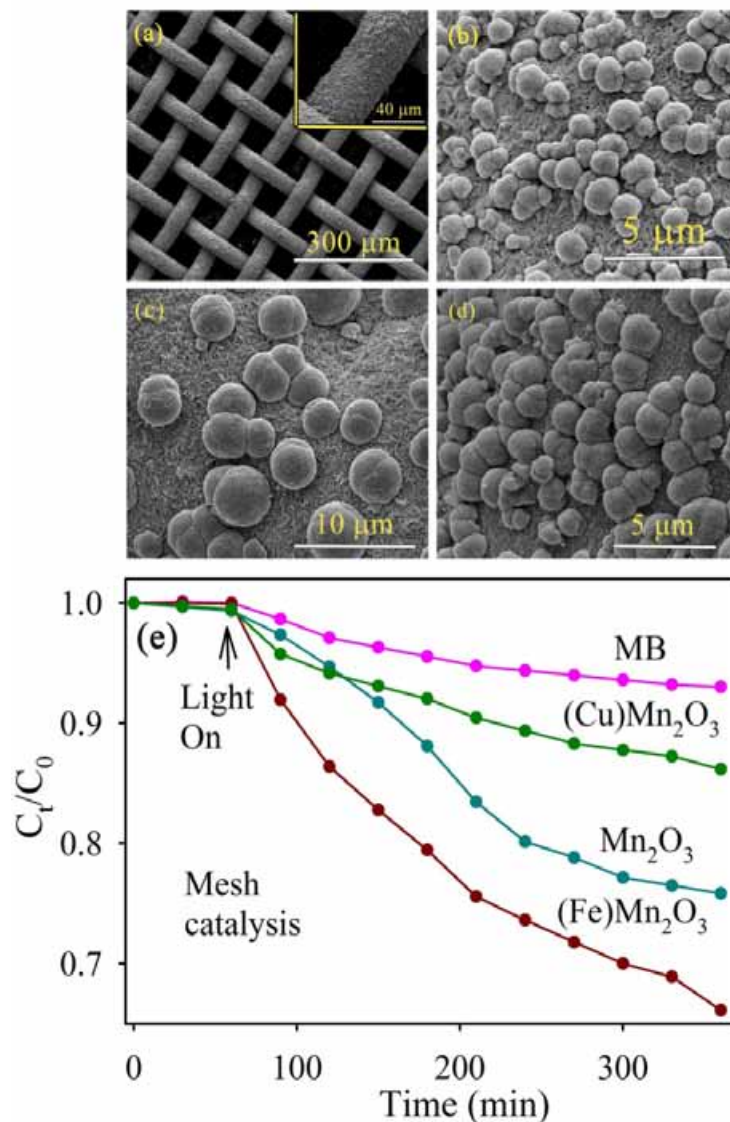
Figure 6.17. *(a) SEM images of Mn_2O_3 on the stainless steel mesh (inset shows high magnification). (b) SEM images of Mn_2O_3 on mesh in high magnification. (c) SEM images of Fe doped Mn_2O_3 on mesh in high magnification. (d) SEM images of Cu doped Mn_2O_3 on mesh in high magnification. (e) Photocatalytic degradation of MB by C-Mn_2O_3, Fe doped C-Mn_2O_3 and Cu doped C-Mn_2O_3 on the mesh under solar light illumination.*

promising for water purification both by physical (filtration) and chemical (photocatalysis) processes. Earlier Ochiai et al. showed that a TiO_2 enhanced Ti mesh filter is very much useful in water purification [132]. Li et al. showed that a Ti/TiO_2 mesh photoelectrode is an excellent system for photocatalytic degradation of humic acid in aqueous solution [133]. In comparison with these earlier reports, our system is more cost effective if large scale water purification systems are concerned (Scheme 6.2).
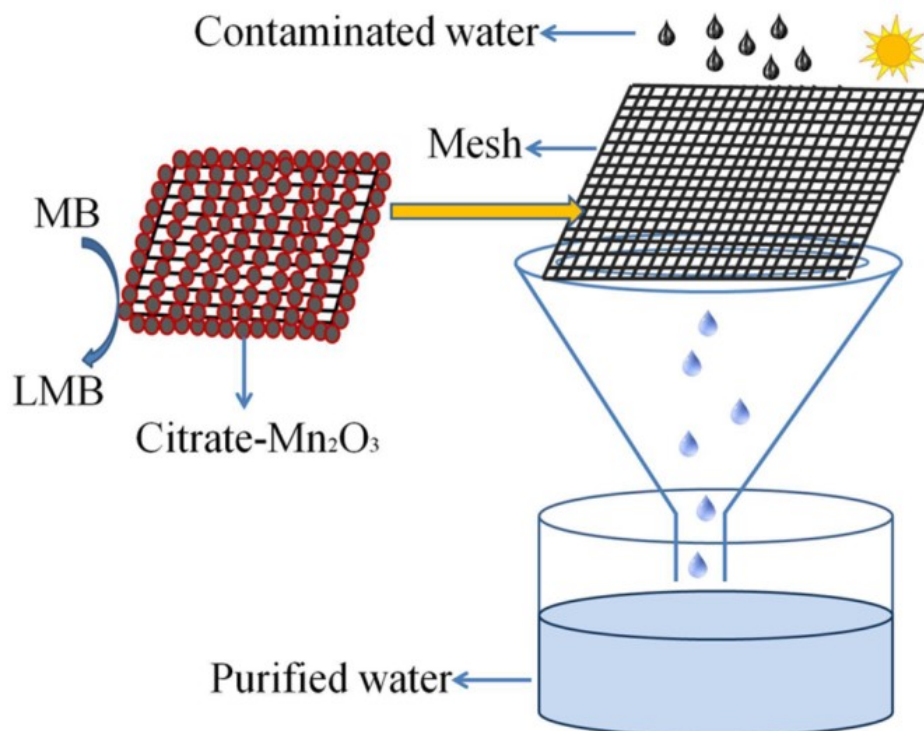
Scheme 6.2. *Schematic representation of water purification by citrate functionalized Mn$_2$O$_3$ under solar light illumination.*

6.3. Conclusion:

In summary, we have successfully synthesized Bi-Bi$_2$O$_2$CO$_3$ heterojunction by a one-step hydrothermal method. Detailed spectroscopic investigations reveal that ultrafast photo-induced charge separation in the Bi-Bi$_2$O$_2$CO$_3$ heterojunction is conducive for enhanced solar energy conversion. As a potential prototype application, we found enhanced photocatalytic activity of the heterostructure using MB as a model organic contaminant under visible light illumination. The efficient separation of photoinduced electron-hole pairs in the heterojunction was further proved by photocurrent measurement. Moreover, this work not only provides cost effective procedure to prepare efficient photocatalyst with high stability but also opens up a new field for bismuth containing heterostructures with several future applications.

Additionally, we have successfully synthesized Mn$_2$O$_3$ microspheres via a hydrothermal route. The surface modification of the synthesized microspheres with citrate leads to new optical and functional properties. A detail spectroscopic investigation leads to the conclusion that J-T splitting of the Mn^{3+} ions and the LMCT bands are mainly responsible for the origin of such optical properties. The photocatalytic activity under solar light illumination of the citrate

functionalized microspheres embedded on a mesh has also been studied using Methylene Blue as a model contaminant. Tuning of the photocatalytic activity of the microspheres upon doping with metal ions (Fe^{3+} and Cu^{2+}) has been demonstrated and correlated with intra-particle electron transfer. We have also realized a prototype for a larger scale water purification system using an "active filter", where the citrate functionalized Mn_2O_3 microspheres are attached on a stainless steel mesh. The system is supposed to filter suspended particulates and decontaminates water soluble pollutants in the presence of solar light.

References

[1]   M. N. Chong, B. Jin, C. W. K. Chow, C. Saint, Recent Developments in Photocatalytic Water Treatment Technology: A Review, *Water Res.* 44 (2010) 2997-3027.

[2]   M. R. Hoffmann, S. T. Martin, W. Choi, D. W. Bahnemann, Environmental Applications of Semiconductor Photocatalysis, *Chem. Rev.* 95 (1995) 69-96.

[3]   S. Dong, J. Feng, M. Fan, Y. Pi, L. Hu, X. Han, M. Liu, J. Sun, J. Sun, Recent Developments in Heterogeneous Photocatalytic Water Treatment using Visible Light-Responsive Photocatalysts: A Review, *RSC Adv.* 5 (2015) 14610-14630.

[4]   P. Kar, S. Sardar, E. Alarousu, J. Sun, Z. S. Seddigi, S. A. Ahmed, E. Y. Danish, O. F. Mohammed, S. K. Pal, Impact of Metal Ions in Porphyrin-Based Applied Materials for Visible-Light Photocatalysis: Key Information from Ultrafast Electronic Spectroscopy, *Chem. Eur. J.* 20 (2014) 10475-10483.

[5]   P. Kar, S. Sardar, S. Ghosh, M. R. Parida, B. Liu, O. F. Mohammed, P. Lemmens, S. K. Pal, Nano Surface Engineering of Mn_2O_3 for Potential Light-Harvesting Application, *J. Mater. Chem. C* 3 (2015) 8200-8211.

[6]   T. K. Maji, D. Bagchi, P. Kar, D. Karmakar, S. K. Pal, Enhanced Charge Separation through Modulation of Defect-State in Wide Band-Gap Semiconductor for Potential Photocatalysis Application: Ultrafast Spectroscopy and Computational Studies, *J. Photochem. Photobiol. A* 332 (2017) 391-398.

[7]   Y. Wang, Q. Wang, X. Zhan, F. Wang, M. Safdar, J. He, Visible Light Driven type II Heterostructures and their Enhanced Photocatalysis Properties: A Review, *Nanoscale* 5 (2013) 8326-8339.

[8]   J. Liqiang, S. Xiaojun, S. Jing, C. Weimin, X. Zili, D. Yaoguo, F. Honggang, Review of Surface Photovoltage Spectra of Nano-Sized Semiconductor and its Applications in Heterogeneous Photocatalysis, *Sol. Energ. Mat. Sol. Cells* 79 (2003) 133-151.

[9]   H. Huang, X. Li, J. Wang, F. Dong, P. K. Chu, T. Zhang, Y. Zhang, Anionic Group Self-Doping as a Promising Strategy: Band-Gap Engineering and Multi-Functional Applications of High-Performance CO_3^{2-}-Doped $Bi_2O_2CO_3$, *ACS Catal.* 5 (2015) 4094-4103.

[10]   H. Huang, X. Han, X. Li, S. Wang, P. K. Chu, Y. Zhang, Fabrication of Multiple Heterojunctions with Tunable Visible-Light-Active Photocatalytic Reactivity in BiOBr–

BiOI Full-Range Composites Based on Microstructure Modulation and Band Structures, *ACS Appl. Mater. Interfaces* 7 (2015) 482-492.

[11]   H. Huang, K. Xiao, Y. He, T. Zhang, F. Dong, X. Du, Y. Zhang, In Situ Assembly of $BiOI@Bi_{12}O_{17}Cl_2$ p-n Junction: Charge Induced Unique Front-Lateral Surfaces Coupling Heterostructure with High Exposure of BiOI {001} Active Facets for Robust and Nonselective Photocatalysis, *Appl. Catal. B* 199 (2016) 75-86.

[12]   H. Huang, K. Liu, K. Chen, Y. Zhang, Y. Zhang, S. Wang, Ce and F Comodification on the Crystal Structure and Enhanced Photocatalytic Activity of Bi_2WO_6 Photocatalyst under Visible Light Irradiation, *J. Phys. Chem. C* 118 (2014) 14379-14387.

[13]   Q. He, S. Huang, C. Wang, Q. Qiao, N. Liang, M. Xu, W. Chen, J. Zai, X. Qian, The Role of Mott–Schottky Heterojunctions in $Ag–Ag_8SnS_6$ as Counter Electrodes in Dye-Sensitized Solar Cells, *ChemSusChem* 8 (2015) 817-820.

[14]   S. Huang, Q. He, J. Zai, M. Wang, X. Li, B. Li, X. Qian, The Role of Mott-Schottky Heterojunctions in $PtCo-Cu_2ZnGeS_4$ as Counter Electrodes in Dye-Sensitized Solar Cells, *Chem. Commun.* 51 (2015) 8950-8953.

[15]   L. Jin, G. Zhu, M. Hojamberdiev, X. Luo, C. Tan, J. Peng, X. Wei, J. Li, P. Liu, A Plasmonic $Ag–AgBr/Bi_2O_2CO_3$ Composite Photocatalyst with Enhanced Visible-Light Photocatalytic Activity, *Ind. Eng. Chem. Res.* 53 (2014) 13718-13727.

[16]   G. Zhu, M. Hojamberdiev, K.-i. Katsumata, X. Cai, N. Matsushita, K. Okada, P. Liu, J. Zhou, Heterostructured $Fe_3O_4/Bi_2O_2CO_3$ Photocatalyst: Synthesis, Characterization and Application in Recyclable Photodegradation of Organic Dyes under Visible Light Irradiation, *Mater. Chem. Phys.* 142 (2013) 95-105.

[17]   A. Hameed, T. Montini, V. Gombac, P. Fornasiero, Surface Phases and Photocatalytic Activity Correlation of Bi_2O_3/Bi_2O_{4-x} Nanocomposite, *J. Am. Chem. Soc.* 130 (2008) 9658-9659.

[18]   S. Xiao, Y. Li, J. Hu, H. Li, X. Zhang, L. Liu, J. Lian, One-Step Synthesis of Nanostructured $Bi-Bi_2O_2CO_3-ZnO$ Composites with Enhanced Photocatalytic Performance, *CrystEngComm* 17 (2015) 3809-3819.

[19]   W. Wang, J. Wang, Z. Wang, X. Wei, L. Liu, Q. Ren, W. Gao, Y. Liang, H. Shi, p-n Junction $CuO/BiVO_4$ Heterogeneous Nanostructures: Synthesis and Highly Efficient Visible-Light Photocatalytic Performance, *Dalton Trans.* 43 (2014) 6735-6743.

[20] Y. Zhang, G. Zhu, M. Hojamberdiev, J. Gao, J. Hao, J. Zhou, P. Liu, Synergistic Effect of Oxygen Vacancy and Nitrogen Doping on Enhancing the Photocatalytic Activity of $Bi_2O_2CO_3$ Nanosheets with Exposed {0 0 1} Facets for the Degradation of Organic Pollutants, *Appl. Surf. Sci.* 371 (2016) 231-241.

[21] C. Greaves, S. K. Blower, Structural Relationships Between $Bi_2O_2CO_3$ and β-Bi_2O_3, *Mater. Res. Bull.* 23 (1988) 1001-1008.

[22] P. Madhusudan, J. Zhang, B. Cheng, G. Liu, Photocatalytic Degradation of Organic Dyes with Hierarchical $Bi_2O_2CO_3$ Microstructures Under Visible-Light, *CrystEngComm* 15 (2013) 231-240.

[23] T. Zhao, J. Zai, M. Xu, Q. Zou, Y. Su, K. Wang, X. Qian, Hierarchical $Bi_2O_2CO_3$ Microspheres with Improved Visible-Light-Driven Photocatalytic Activity, *CrystEngComm* 13 (2011) 4010-4017.

[24] P. Madhusudan, J. Yu, W. Wang, B. Cheng, G. Liu, Facile Synthesis of Novel Hierarchical Graphene-$Bi_2O_2CO_3$ Composites with Enhanced Photocatalytic Performance under Visible Light, *Dalton Trans.* 41 (2012) 14345-14353.

[25] Y.-S. Xu, W.-D. Zhang, Anion Exchange Strategy for Construction of Sesame-Biscuit-Like $Bi_2O_2CO_3$/Bi_2MoO_6 Nanocomposites with Enhanced Photocatalytic Activity, *Appl. Catal. B* 140–141 (2013) 306-316.

[26] Z. Zhao, Y. Zhou, F. Wang, K. Zhang, S. Yu, K. Cao, Polyaniline-Decorated {001} Facets of $Bi_2O_2CO_3$ Nanosheets: In Situ Oxygen Vacancy Formation and Enhanced Visible Light Photocatalytic Activity, *ACS Appl. Mater. Interfaces* 7 (2015) 730-737.

[27] N. Liang, M. Wang, L. Jin, S. Huang, W. Chen, M. Xu, Q. He, J. Zai, N. Fang, X. Qian, Highly Efficient Ag_2O/$Bi_2O_2CO_3$ p-n Heterojunction Photocatalysts with Improved Visible-Light Responsive Activity, *ACS Appl. Mater. Interfaces* 6 (2014) 11698-11705.

[28] S. Peng, L. Li, H. Tan, Y. Wu, R. Cai, H. Yu, X. Huang, P. Zhu, S. Ramakrishna, M. Srinivasan, Q. Yan, Monodispersed Ag Nanoparticles Loaded on the PVP-Assisted Synthetic $Bi_2O_2CO_3$ Microspheres with Enhanced Photocatalytic and Supercapacitive Performances, *J. Mater. Chem. A* 1 (2013) 7630-7638.

[29] R. Wang, X. Li, W. Cui, Y. Zhang, F. Dong, In Situ Growth of Au Nanoparticles on 3D $Bi_2O_2CO_3$ for Surface Plasmon Enhanced Visible Light Photocatalysis, *New J. Chem.* 39 (2015) 8446-8453.

[30] F. Dong, Q. Li, Y. Sun, W.-K. Ho, Noble Metal-Like Behavior of Plasmonic Bi Particles as a Cocatalyst Deposited on $(BiO)_2CO_3$ Microspheres for Efficient Visible Light Photocatalysis, *ACS Catal.* 4 (2014) 4341-4350.

[31] H. Safardoust-Hojaghan, M. Salavati-Niasari, M. H. Motaghedifard, S. M. Hosseinpour-Mashkani, Synthesis of Micro Sphere-like Bismuth Nanoparticles by Microwave Assisted Polyol Method; Designing a Novel Electrochemical Nanosensor for Ultra-trace Measurement of Pb^{2+} Ions, *New J. Chem.* 39 (2015) 4676-4684.

[32] Z. Wang, C. Jiang, R. Huang, H. Peng, X. Tang, Investigation of Optical and Photocatalytic Properties of Bismuth Nanospheres Prepared by a Facile Thermolysis Method, *J. Phys. Chem. C* 118 (2014) 1155-1160.

[33] F. Dong, T. Xiong, Y. Sun, Z. Zhao, Y. Zhou, X. Feng, Z. Wu, A Semimetal Bismuth Element as a Direct Plasmonic Photocatalyst, *Chem. Commun.* 50 (2014) 10386-10389.

[34] D. Chen, M. Zhang, Q. Lu, J. Chen, B. Liu, Z. Wang, Facile Synthesis of Bi/BiOCl Composite with Selective Photocatalytic Properties, *J. Alloys Compd.* 646 (2015) 647-654.

[35] Y. Huang, W. Wang, Q. Zhang, J.-j. Cao, R.-j. Huang, W. Ho, S. C. Lee, In Situ Fabrication of α-Bi_2O_3/$(BiO)_2CO_3$ Nanoplate Heterojunctions with Tunable Optical Property and Photocatalytic Activity, *Sci. Rep.* 6 (2016) 23435.

[36] C. Chang, L. Zhu, Y. Fu, X. Chu, Highly Active Bi/BiOI Composite Synthesized by One-Step Reaction and its Capacity to Degrade Bisphenol A Under Simulated Solar Light Irradiation, *Chem. Eng. J.* 233 (2013) 305-314.

[37] M. Gao, D. Zhang, X. Pu, H. Li, D. Lv, B. Zhang, X. Shao, Facile Hydrothermal Synthesis of Bi/BiOBr Composites with Enhanced Visible-Light Photocatalytic Activities for the Degradation of Rhodamine B, *Sep. Purif. Technol.* 154 (2015) 211-216.

[38] Y. Chen, D. Chen, J. Chen, Q. Lu, M. Zhang, B. Liu, Q. Wang, Z. Wang, Facile Synthesis of Bi Nanoparticle Modified TiO_2 with Enhanced Visible Light Photocatalytic Activity, *J. Alloys Compd.* 651 (2015) 114-120.

[39] X. Liu, H. Cao, J. Yin, Generation and Photocatalytic Activities of $Bi@Bi_2O_3$ Microspheres, *Nano Res.* 4 (2011) 470-482.

[40] R. Hu, X.-B. Zhang, R.-M. Kong, X.-H. Zhao, J. Jiang, W. Tan, Nucleic Acid-Functionalized Nanomaterials for Bioimaging Applications, *J. Mater. Chem.* 21 (2011) 16323-16334.

[41] Y.-P. Sun, K. Fu, Y. Lin, W. Huang, Functionalized Carbon Nanotubes: Properties and Applications, *Acc. Chem. Res.* 35 (2002) 1096-1104.

[42] A. Giri, A. Makhal, B. Ghosh, A. K. Raychaudhuri, S. K. Pal, Functionalization of Manganite Nanoparticles and their Interaction with Biologically Relevant Small Ligands: Picosecond Time-Resolved FRET Studies, *Nanoscale* 2 (2010) 2704-2709.

[43] P. Sahu, B. L. V. Prasad, Time and Temperature Effects on the Digestive Ripening of Gold Nanoparticles: Is There a Crossover from Digestive Ripening to Ostwald Ripening?, *Langmuir* 30 (2014) 10143-10150.

[44] G. Palui, F. Aldeek, W. Wang, H. Mattoussi, Strategies for Interfacing Inorganic Nanocrystals with Biological Systems Based on Polymer-Coating, *Chem. Soc. Rev.* 44 (2015) 193-227.

[45] M. A. H. Muhammed, F. Aldeek, G. Palui, L. Trapiella-Alfonso, H. Mattoussi, Growth of In Situ Functionalized Luminescent Silver Nanoclusters by Direct Reduction and Size Focusing, *ACS Nano* 6 (2012) 8950-8961.

[46] C. S. S. R. Kumar, F. Mohammad, Magnetic Nanomaterials for Hyperthermia-Based Therapy and Controlled Drug Delivery, *Adv. Drug Deliv. Rev.* 63 (2011) 789-808.

[47] V. Polshettiwar, R. Luque, A. Fihri, H. Zhu, M. Bouhrara, J.-M. Basset, Magnetically Recoverable Nanocatalysts, *Chem. Rev.* 111 (2011) 3036-3075.

[48] A. Ito, M. Shinkai, H. Honda, T. Kobayashi, Medical Application of Functionalized Magnetic Nanoparticles, *J. Biosci. Bioeng.* 100 (2005) 1-11.

[49] R. Hao, R. Xing, Z. Xu, Y. Hou, S. Gao, S. Sun, Synthesis, Functionalization, and Biomedical Applications of Multifunctional Magnetic Nanoparticles, *Adv. Mater.* 22 (2010) 2729-2742.

[50] S. Dhar, P. Murawala, A. Shiras, V. Pokharkar, B. L. V. Prasad, Gellan Gum Capped Silver Nanoparticle Dispersions and Hydrogels: Cytotoxicity and In Vitro Diffusion Studies, *Nanoscale* 4 (2012) 563-567.

[51] S. Sardar, S. Chaudhuri, P. Kar, S. Sarkar, P. Lemmens, S. K. Pal, Direct Observation of Key Photoinduced Dynamics in a Potential Nano-Delivery Vehicle of Cancer Drugs, *Phys. Chem. Chem. Phys.* 17 (2015) 166-177.

[52] A. Giri, N. Goswami, C. Sasmal, N. Polley, D. Majumdar, S. Sarkar, S. N. Bandyopadhyay, A. Singha, S. K. Pal, Unprecedented Catalytic Activity of Mn_3O_4 Nanoparticles: Potential Lead of a Sustainable Therapeutic Agent for Hyperbilirubinemia, *RSC Adv.* 4 (2014) 5075-5079.

[53] S. Ghosh, D. Ghosh, P. K. Bag, S. C. Bhattacharya, A. Saha, Aqueous Synthesis of ZnTe/Dendrimer Nanocomposites and their Antimicrobial Activity: Implications in Therapeutics, *Nanoscale* 3 (2011) 1139-1148.

[54] S. Sardar, P. Kar, S. K. Pal, The Impact of Central Metal Ions in Porphyrin Functionalized ZnO/TiO_2 for Enhanced Solar Energy Conversion, *J. Mat. NanoSci.* 1 (2014) 12-30.

[55] K. T. Nguyen, Y. Zhao, Integrated Graphene/Nanoparticle Hybrids for Biological and Electronic Applications, *Nanoscale* 6 (2014) 6245-6266.

[56] P. Li, C. Nan, Z. Wei, J. Lu, Q. Peng, Y. Li, Mn3O4 Nanocrystals: Facile Synthesis, Controlled Assembly, and Application, *Chem. Mater.* 22 (2010) 4232-4236.

[57] J. Xiao, X. M. Tian, C. Yang, P. Liu, N. Q. Luo, Y. Liang, H. B. Li, D. H. Chen, C. X. Wang, L. Li, G. W. Yang, Ultrahigh Relaxivity and Safe Probes of Manganese Oxide Nanoparticles for in Vivo Imaging, *Sci. Rep.* 3 (2013) 3424.

[58] G.-J. Lee, A. Manivel, V. Batalova, G. Mokrousov, S. Masten, J. Wu, Mesoporous Microsphere of ZnS Photocatalysts Loaded with CuO or Mn_3O_4 for the Visible-Light-Assisted Photocatalytic Degradation of Orange II Dye, *Ind. Eng. Chem. Res.* 52 (2013) 11904-11912.

[59] R. Saravanan, V. K. Gupta, V. Narayanan, A. Stephen, Visible Light Degradation of Textile Effluent using Novel Catalyst ZnO/γ-Mn_2O_3, *J. Taiwan Inst. Chem. Eng.* 45 (2014) 1910-1917.

[60] X. Hong-Yu, H. Lin, Y. Qi-Zhi, Preparation and Photocatalytic Activity of Mn_2O_3 Microspheres, *J. Inorg. Mater.* 26 (2011) 317-320.

[61]   T. Ahmad, K. V. Ramanujachary, S. E. Lofland, A. K. Ganguli, Nanorods of Manganese Oxalate: A Single Source Precursor to Different Manganese Oxide Nanoparticles (MnO, Mn_2O_3, Mn_3O_4), *J. Mater. Chem.* 14 (2004) 3406-3410.

[62]   F. Cheng, J. Zhao, W. Song, C. Li, H. Ma, J. Chen, P. Shen, Facile Controlled Synthesis of MnO_2 Nanostructures of Novel Shapes and Their Application in Batteries, *Inorg Chem* 45 (2006) 2038-2044.

[63]   Z. Chen, Z. Jiao, D. Pan, Z. Li, M. Wu, C.-H. Shek, C. M. L. Wu, J. K. L. Lai, Recent Advances in Manganese Oxide Nanocrystals: Fabrication, Characterization, and Microstructure, *Chem. Rev.* 112 (2012) 3833-3855.

[64]   G. Salazar-Alvarez, J. Sort, S. Suriñach, M. D. Baró, J. Nogués, Synthesis and Size-Dependent Exchange Bias in Inverted Core−Shell MnO|Mn_3O_4 Nanoparticles, *J. Am. Chem. Soc.* 129 (2007) 9102-9108.

[65]   Z. W. Chen, Z. Jiao, M. H. Wu, C. H. Shek, C. M. L. Wu, J. K. L. Lai, Microstructural Evolution of Oxides and Semiconductor Thin Films, *Prog. Mater. Sci.* 56 (2011) 901-1029.

[66]   C. Chen, G. Ding, D. Zhang, Z. Jiao, M. Wu, C.-H. Shek, C. M. L. Wu, J. K. L. Lai, Z. Chen, Microstructure Evolution and Advanced Performance of Mn_3O_4 Nanomorphologies, *Nanoscale* 4 (2012) 2590-2596.

[67]   L. Liu, X. Zhang, R. Wang, J. Liu, Facile Synthesis of Mn_2O_3 Hollow and Core–Shell Cube-Like Nanostructures and their Catalytic Properties, *Superlattices Microstruct.* 72 (2014) 219-229.

[68]   J. Cao, Y. Zhu, L. Shi, L. Zhu, K. Bao, S. Liu, Y. Qian, Double-Shelled Mn_2O_3 Hollow Spheres and Their Application in Water Treatment, *Eur. J. Inorg. Chem.* 2010 (2010) 1172-1176.

[69]   Y. Liu, Z. Chen, C.-H. Shek, C. M. L. Wu, J. K. L. Lai, Hierarchical Mesoporous MnO_2 Superstructures Synthesized by Soft-Interface Method and Their Catalytic Performances, *ACS Appl. Mater. Interfaces* 6 (2014) 9776-9784.

[70]   S. Chandra, P. Das, S. Bag, R. Bhar, P. Pramanik, Mn_2O_3 Decorated Graphene Nanosheet: An Advanced Material for the Photocatalytic Degradation of Organic Dyes, *Mater. Sci. Eng., B* 177 (2012) 855-861.

[71] A. Giri, N. Goswami, M. Pal, M. T. Zar Myint, S. Al-Harthi, A. Singha, B. Ghosh, J. Dutta, S. K. Pal, Rational Surface Modification of Mn_3O_4 Nanoparticles to Induce Multiple Photoluminescence and Room Temperature Ferromagnetism, *J. Mater. Chem. C* 1 (2013) 1885-1895.

[72] S. Patoux, L. Sannier, H. Lignier, Y. Reynier, C. Bourbon, S. Jouanneau, F. Le Cras, S. Martinet, High Voltage Nickel Manganese Spinel Oxides for Li-Ion Batteries, *Electrochim. Acta* 53 (2008) 4137-4145.

[73] L. Alonso, J. M. Palacios, Performance and Recovering of a Zn-Doped Manganese Oxide as a Regenerable Sorbent for Hot Coal Gas Desulfurization, *Energy Fuels* 16 (2002) 1550-1556.

[74] R. Huang, Y. Liu, Z. Chen, D. Pan, Z. Li, M. Wu, C.-H. Shek, C. M. L. Wu, J. K. L. Lai, Fe-Species-Loaded Mesoporous MnO_2 Superstructural Requirements for Enhanced Catalysis, *ACS Appl. Mater. Interfaces* 7 (2015) 3949-3959.

[75] N. Goswami, A. Baksi, A. Giri, P. L. Xavier, G. Basu, T. Pradeep, S. K. Pal, Luminescent Iron Clusters in Solution, *Nanoscale* 6 (2014) 1848-1854.

[76] M. Habeeb Muhammed, S. Ramesh, S. Sinha, S. K. Pal, T. Pradeep, Two Distinct Fluorescent Quantum Clusters of Gold Starting from Metallic Nanoparticles by pH-Dependent Ligand Etching, *Nano Res.* 1 (2008) 333-340.

[77] P. Kar, T. K. Maji, R. Nandi, P. Lemmens, S. K. Pal, In-situ Hydrothermal Synthesis of Bi-$Bi_2O_2CO_3$ Heterojunction Photocatalyst with Enhanced Visible Light Photocatalytic Activity, *Nano-Micro Lett.* 9 (2017) 18.

[78] Y. Sun, Z. Zhao, F. Dong, W. Zhang, Mechanism of Visible Light Photocatalytic NO_x Oxidation with Plasmonic Bi Cocatalyst-Enhanced $(BiO)_2CO_3$ Hierarchical Microspheres, *Phys. Chem. Chem. Phys.* 17 (2015) 10383-10390.

[79] J. L. T. Chen, V. Nalla, G. Kannaiyan, V. Mamidala, W. Ji, J. J. Vittal, Synthesis and Nonlinear Optical Switching of Bi_2S_3 Nanorods and Enhancement in the NLO Response of Bi_2S_3@Au Nanorod-Composites, *New J. Chem.* 38 (2014) 985-992.

[80] S. P. Lim, A. Pandikumar, N. M. Huang, H. N. Lim, Facile Synthesis of Au@TiO_2 Nanocomposite and its Application as a Photoanode in Dye-Sensitized Solar Cells, *RSC Adv.* 5 (2015) 44398-44407.

[81]   G. Cheng, H. Yang, K. Rong, Z. Lu, X. Yu, R. Chen, Shape-Controlled Solvothermal Synthesis of Bismuth Subcarbonate Nanomaterials, *J. Solid State Chem.* 183 (2010) 1878-1883.

[82]   G. Zhu, Y. Liu, M. Hojamberdiev, J. Han, J. Rodriguez, S. A. Bilmes, P. Liu, Thermodecomposition Synthesis of Porous [small beta]-Bi_2O_3/$Bi_2O_2CO_3$ Heterostructured Photocatalysts with Improved Visible Light Photocatalytic Activity, *New J. Chem.* 39 (2015) 9557-9568.

[83]   S. Lin, L. Liu, Y. Liang, W. Cui, Z. Zhang, Oil-in-Water Self-Assembled Synthesis of Ag@AgCl Nano-Particles on Flower-like $Bi_2O_2CO_3$ with Enhanced Visible-Light-Driven Photocatalytic Activity, *Materials* 9 (2016) 486.

[84]   J. Siegel, O. Kvítek, P. Ulbrich, Z. Kolská, P. Slepička, V. Švorčík, Progressive Approach for Metal Nanoparticle Synthesis, *Mater. Lett.* 89 (2012) 47-50.

[85]   S. Weng, B. Chen, L. Xie, Z. Zheng, P. Liu, Facile In Situ Synthesis of a Bi/BiOCl Nanocomposite with High Photocatalytic Activity, *J. Mater. Chem. A* 1 (2013) 3068-3075.

[86]   J. Toudert, R. Serna, M. Jiménez de Castro, Exploring the Optical Potential of Nano-Bismuth: Tunable Surface Plasmon Resonances in the Near Ultraviolet-to-Near Infrared Range, *J. Phys. Chem. C* 116 (2012) 20530-20539.

[87]   C. Yogi, K. Kojima, N. Wada, H. Tokumoto, T. Takai, T. Mizoguchi, H. Tamiaki, Photocatalytic Degradation of Methylene Blue by TiO_2 Film and Au Particles-TiO_2 Composite Film, *Thin Solid Films* 516 (2008) 5881-5884.

[88]   A. Mills, J. Wang, Photobleaching of Methylene Blue Sensitised by TiO_2: An Ambiguous System?, *J. Photochem. Photobiol., A* 127 (1999) 123-134.

[89]   Y. Park, S.-H. Lee, S. O. Kang, W. Choi, Organic Dye-Sensitized TiO_2 for the Redox Conversion of Water Pollutants under Visible Light, *Chem. Commun.* 46 (2010) 2477-2479.

[90]   Z. Ai, W. Ho, S. Lee, L. Zhang, Efficient Photocatalytic Removal of NO in Indoor Air with Hierarchical Bismuth Oxybromide Nanoplate Microspheres under Visible Light, *Environ. Sci. Technol.* 43 (2009) 4143-4150.

[91] F. Dong, Y. Sun, M. Fu, Z. Wu, S. C. Lee, Room Temperature Synthesis and Highly Enhanced Visible Light Photocatalytic Activity of Porous BiOI/BiOCl Composites Nanoplates Microflowers, *J. Hazard. Mater.* 219–220 (2012) 26-34.

[92] Q. Xiang, J. Yu, M. Jaroniec, Graphene-Based Semiconductor Photocatalysts, *Chem. Soc. Rev.* 41 (2012) 782-796.

[93] Q. Li, H. Liu, F. Dong, M. Fu, Hydrothermal Formation of N-doped $(BiO)_2CO_3$ Honeycomb-Like Microspheres Photocatalysts with Bismuth Citrate and Dicyandiamide as Precursors, *J. Colloid Interface Sci.* 408 (2013) 33-42.

[94] S. Yu, H. Huang, F. Dong, M. Li, N. Tian, T. Zhang, Y. Zhang, Synchronously Achieving Plasmonic Bi Metal Deposition and I– Doping by Utilizing $BiOIO_3$ as the Self-Sacrificing Template for High-Performance Multifunctional Applications, *ACS Appl. Mater. Interfaces* 7 (2015) 27925-27933.

[95] Y. Guo, Y. Zhang, N. Tian, H. Huang, Homogeneous {001}-BiOBr/Bi Heterojunctions: Facile Controllable Synthesis and Morphology-Dependent Photocatalytic Activity, *ACS Sustainable Chem. Eng.* 4 (2016) 4003-4012.

[96] V. Subramanian, E. E. Wolf, P. V. Kamat, Catalysis with TiO_2/Gold Nanocomposites. Effect of Metal Particle Size on the Fermi Level Equilibration, *J. Am. Chem. Soc.* 126 (2004) 4943-4950.

[97] S. Trasatti, Electronegativity, Work Function, and Heat of Adsorption of Hydrogen on Metals, *J. Chem. Soc. Faraday Trans. 1* 68 (1972) 229-236.

[98] Y. Yu, C. Cao, H. Liu, P. Li, F. Wei, Y. Jiang, W. Song, A Bi/BiOCl Heterojunction Photocatalyst with Enhanced Electron-Hole Separation and Excellent Visible Light Photodegrading Activity, *J. Mater. Chem. A* 2 (2014) 1677-1681.

[99] Q. Li, L. Yin, Z. Li, X. Wang, Y. Qi, J. Ma, Copper Doped Hollow Structured Manganese Oxide Mesocrystals with Controlled Phase Structure and Morphology as Anode Materials for Lithium Ion Battery with Improved Electrochemical Performance, *ACS Appl. Mater. Interfaces* 5 (2013) 10975-10984.

[100] G. Z. Xing, J. B. Yi, J. G. Tao, T. Liu, L. M. Wong, Z. Zhang, G. P. Li, S. J. Wang, J. Ding, T. C. Sum, C. H. A. Huan, T. Wu, Comparative Study of Room-Temperature Ferromagnetism in Cu-Doped ZnO Nanowires Enhanced by Structural Inhomogeneity, *Adv. Mater.* 20 (2008) 3521-3527.

[101] D. Bravo, F. J. Lopez, Superposition Model Analysis on the Site Symmetry of Fe $^{3+}$ Ions Doping Spinel Crystals, *J. Phys. Condens. Matter* 4 (1992) 10335.

[102] G. Yang, W. Yan, J. Wang, H. Yang, Fabrication and Formation Mechanism of Mn_2O_3 Hollow Nanofibers by Single-Spinneret Electrospinning, *CrystEngComm* 16 (2014) 6907-6913.

[103] J. Cao, Y. Zhu, K. Bao, L. Shi, S. Liu, Y. Qian, Microscale Mn_2O_3 Hollow Structures: Sphere, Cube, Ellipsoid, Dumbbell, and Their Phenol Adsorption Properties, *J. Phys. Chem. C* 113 (2009) 17755-17760.

[104] M. Matzapetakis, N. Karligiano, A. Bino, M. Dakanali, C. P. Raptopoulou, V. Tangoulis, A. Terzis, J. Giapintzakis, A. Salifoglou, Manganese Citrate Chemistry: Syntheses, Spectroscopic Studies, and Structural Characterizations of Novel Mononuclear, Water-Soluble Manganese Citrate Complexes, *Inorg. Chem.* 39 (2000) 4044-4051.

[105] F. Aguado, F. Rodriguez, P. Núñez, Pressure-Induced Jahn-Teller Suppression and Simultaneous High-Spin to Low-Spin Transition in the Layered Perovskite *Phys. Rev. B* 76 (2007) 094417.

[106] C. Zhiwen, T. Shun, Z. Shuyuan, W. Jian, J. Sizhao, Z. Yuheng, S. Hisashi, Size Dependence of Phonon Raman Spectra in Mn_2O_3 Nanocrystals, *Jpn. J. Appl. Phys.* 39 (2000) 6293.

[107] R. Manigandan, R. Suresh, K. Giribabu, L. Vijayalakshmi, A. Stephen, V. Narayanan, Synthesis, Characterization, Optical and Sensing Property of Manganese Oxide Nanoparticles, *AIP Conf. Proc.* 1576 (2014) 125-127.

[108] A. K. Thottoli, A. K. A. Unni, Effect of Trisodium Citrate Concentration on the Particle Growth of ZnS Nanoparticles, *J. Nanostruct. chem.* 3 (2013) 56.

[109] F. M. Courtel, H. Duncan, Y. Abu-Lebdeh, I. J. Davidson, High Capacity Anode Materials for Li-Ion Batteries Based on Spinel Metal Oxides AMn_2O_4 (A = Co, Ni, and Zn), *J. Mater. Chem.* 21 (2011) 10206-10218.

[110] T. Nathan, M. Cloke, S. Prabaharan, Electrode Properties of Mn_2O_3 Nanospheres Synthesized by Combined Sonochemical/Solvothermal Method for Use in Electrochemical Capacitors, *J.Nano Mat.* 2008 (2008) 81.

[111] P. Pal, A. K. Giri, S. Mahanty, A. B. Panda, Morphology-Mediated Tailoring of the Performance of Porous Nanostructured Mn_2O_3 as an Anode Material, *CrystEngComm* 16 (2014) 10560-10568.

[112] J. W. Lee, A. S. Hall, J.-D. Kim, T. E. Mallouk, A Facile and Template-Free Hydrothermal Synthesis of Mn_3O_4 Nanorods on Graphene Sheets for Supercapacitor Electrodes with Long Cycle Stability, *Chem. Mater.* 24 (2012) 1158-1164.

[113] H. Nesbitt, D. Banerjee, Interpretation of XPS Mn (2p) Spectra of Mn Oxyhydroxides and Constraints on the Mechanism of MnO_2 Precipitation, *Am. Mineral.* 83 (1998) 305-315.

[114] F. Xiao, Y. Xu, Pulse Electrodeposition of Manganese Oxide for High-Rate Capability Supercapacitors, *Int. J. Electrochem. Sci.* 7 (2012) 7440-7450.

[115] A. S. Tselesh, Anodic Behaviour of Tin in Citrate Solutions: The IR and XPS Study on the Composition of the Passive Layer, *Thin Solid Films* 516 (2008) 6253-6260.

[116] L. L. Zhang, T. Wei, W. Wang, X. S. Zhao, Manganese Oxide–Carbon Composite as Supercapacitor Electrode Materials, *Microporous Mesoporous Mater.* 123 (2009) 260-267.

[117] Y. Dai, L. Yin, Low Fe-Doped Bi_2O_3 Photocatalyst with Long Wavelength Response: Crystalline Transition and Mechanisms by First-Principles Calculation, *J. Alloys Compd.* 563 (2013) 80-84.

[118] T. Yamashita, P. Hayes, Analysis of XPS Spectra of Fe^{2+} and Fe^{3+} Ions in Oxide Materials, *Appl. Surf. Sci* 254 (2008) 2441-2449.

[119] S. Gao, S. Yang, J. Shu, S. Zhang, Z. Li, K. Jiang, Green Fabrication of Hierarchical CuO Hollow Micro/Nanostructures and Enhanced Performance as Electrode Materials for Lithium-ion Batteries, *J. Phys. Chem. C* 112 (2008) 19324-19328.

[120] D. H. Xu, W. Z. Shen, Cu-Doped ZnO Hemispherical Shell Structures: Synthesis and Room-Temperature Ferromagnetism Properties, *J. Phys. Chem. C* 116 (2012) 13368-13373.

[121] C. R. Vestal, Z. J. Zhang, Effects of Surface Coordination Chemistry on the Magnetic Properties of $MnFe_2O_4$ Spinel Ferrite Nanoparticles, *J. Am. Chem. Soc.* 125 (2003) 9828-9833.

[122] A.-H. Lu, E. L. Salabas, F. Schüth, Magnetic Nanoparticles: Synthesis, Protection, Functionalization, and Application, *Angew. Chem. Int. Ed.* 46 (2007) 1222-1244.

[123] X. Li, K. Lv, K. Deng, J. Tang, R. Su, J. Sun, L. Chen, Synthesis and Characterization of ZnO and TiO_2 Hollow Spheres with Enhanced Photoreactivity, *Mater. Sci. Eng., B* 158 (2009) 40-47.

[124] K. Lv, Y. Xu, Effects of Polyoxometalate and Fluoride on Adsorption and Photocatalytic Degradation of Organic Dye X3B on TiO_2: The Difference in the Production of Reactive Species, *J. Phys. Chem. B* 110 (2006) 6204-6212.

[125] Y. Xu, C. H. Langford, UV- or Visible-Light-Induced Degradation of X3B on TiO_2 Nanoparticles: The Influence of Adsorption, *Langmuir* 17 (2001) 897-902.

[126] Y. Xu, K. Lv, Z. Xiong, W. Leng, W. Du, D. Liu, X. Xue, Rate Enhancement and Rate Inhibition of Phenol Degradation over Irradiated Anatase and Rutile TiO_2 on the Addition of NaF: New Insight into the Mechanism, *J. Phys. Chem. C* 111 (2007) 19024-19032.

[127] G. Panthi, A. Yousef, N. A. M. Barakat, K. Abdelrazek Khalil, S. Akhter, Y. Ri Choi, H. Y. Kim, Mn_2O_3/TiO_2 Nanofibers with Broad-Spectrum Antibiotics Effect and Photocatalytic Activity for Preliminary Stage of Water Desalination, *Ceram. Int.* 39 (2013) 2239-2246.

[128] S. Gnanam, V. Rajendran, Facile Hydrothermal Synthesis of Alpha Manganese Sesquioxide (α-Mn_2O_3) Nanodumb-Bells: Structural, Magnetic, Optical and Photocatalytic Properties, *J. Alloys Compd.* 550 (2013) 463-470.

[129] M. M. Mohamed, I. Othman, R. M. Mohamed, Synthesis and Characterization of MnOx/TiO_2 Nanoparticles for Photocatalytic Oxidation of Indigo Carmine Dye, *J. Photochem. Photobiol., A* 191 (2007) 153-161.

[130] D. Spuhler, J. Andrés Rengifo-Herrera, C. Pulgarin, The Effect of Fe^{2+}, Fe^{3+}, H_2O_2 and the Photo-Fenton Reagent at Near Neutral pH on the Solar Disinfection (SODIS) at Low Temperatures of Water Containing Escherichia Coli K12, *Appl. Catal. B* 96 (2010) 126-141.

[131] I. Yamazaki, L. H. Piette, ESR Spin-Trapping Studies on the Reaction of Fe^{2+} Ions with H_2O_2-Reactive Species in Oxygen Toxicity in Biology, *J. Biol. Chem.* 265 (1990) 13589-13594.

[132] T. Ochiai, H. Nanba, T. Nakagawa, K. Masuko, K. Nakata, T. Murakami, R. Nakano, M. Hara, Y. Koide, T. Suzuki, M. Ikekita, Y. Morito, A. Fujishima, Development of an O_3-Assisted Photocatalytic Water-Purification Unit by Using a TiO_2 modified Titanium Mesh Filter, *Catal. Sci. Tech.* 2 (2012) 76-78.

[133] X. Z. Li, F. B. Li, C. M. Fan, Y. P. Sun, Photoelectrocatalytic Degradation of Humic Acid in Aqueous Solution Using a Ti/TiO_2 Mesh Photoelectrode, *Water Res.* 36 (2002) 2215-2224.

Chapter 7

Spectroscopic Studies on Light Harvesting Nanomaterials for Enhanced Solar Photovoltaic Application

7.1. Introduction:

The mechanistic pathways for the enhancement of the efficiency of a dye sensitized solar cell (DSSC) using plasmonic nanoparticles have attracted lots of attention in contemporary literature [1-8]. The specific role of plasmon in the nanoparticles over the nonspecific scattering of incident radiation leading to the 'light trapping' has been addressed in recent studies [9-13]. In a theoretical investigation on a model DSSC, the magnitude of dipole-dipole coupling between the plasmon resonance of metallic nanoparticles and the electronic transition in the sensitizing dye has been carefully varied and an optimum coupling strength for which the electron population injected into the host semiconductor is maximized [14]. The delocalization of plasmonic state in the proximity of wide band gap semiconductor in a DSSC, leading to conversion of photon to charge carriers has been predicted in another computational study [9]. The role of spacing between the semiconductor surface and plasmonic metal structure on the rate of electron injection from metal to semiconductor has also been demonstrated experimentally [15, 16]. However, the direct experimental evidence of dipolar coupling between electronic transition of a dye in a DSSC and plasmonic resonance of a metal nanoparticle in active electrode on the overall efficiency of the DSSC is sparse in the existing literature, and is the motive of the present work.

Here we have studied Protoporphyrin IX (PP) sensitized TiO_2 as photoanode in DSSC as model solar cell. The semiconductor (TiO_2) is decorated with Au nanoparticles having absorption maxima at 530 nm due to surface plasmon resonance (SPR) band, which has spectral overlap with the fluorescence of the model dye in the DSSC. We have utilized steady state and picosecond resolved photoluminescence of the dye PP in order to confirm dipolar coupling with the Au nanoparticles. The manifestation of the dipolar coupling in the photocurrent and photovoltage of the DSSC have also been investigated. In order to decouple the interference of non-specific light scattering by the Au nanoparticles on the enhancement of the DSSC efficiency, we have used synthesized aluminum nanoparticles (SPR at 370 nm) as scattering layer in the DSSC and compared enhancement of efficiency. A clear difference in the electron injection due

to the SPR in the Al nanoparticles decorated DSSC is evident in our studies. We have fabricated DSSCs with plasmonic nanoparticles (Al and Au) which exhibit much higher power conversation efficiencies in compared to their counterparts. In order to validate the proposed mechanism of dipolar coupling for conventional dyes, we have used non-emissive N719 as sensitizing dye to fabricate DSSCs and found that it is following the similar trend as that of the PP with higher solar cell efficiencies.

7.2. Results and Discussion:

Direct Observation of Electronic Transition-Plasmon Coupling for Enhanced Electron Injection in Dye-Sensitized Solar Cells [17]:

The powder X-ray diffraction pattern of as synthesized Al nanoparticles is shown in Figure 7.1a which is compared with the JCPDS data (#04–0787) and found to be in good agreement with the face-centered cubic (fcc) form of aluminum. Figure 7.1b shows the morphology of the synthesized Al nanoparticles as revealed from FESEM. The size of the Al nanoparticles is observed by HRTEM as shown in Figure 7.1c. The Al nanoparticles are found to have a size distribution with an average diameter of 150-250 nm. The inter-planar distance between the fringes is found to be about 0.230 nm (as shown in Figure 7.1d) which is consistent with (111) planes of fcc Al nanoparticles [18]. Figure 7.1e shows the X-ray diffraction patterns of TiO_2 and $(Au)TiO_2$ nanohybrid. This indicates that the mixture is composed of mixed anatase and rutile phases, which was in good agreement with the reference patterns of JCPDS card no. 83-2243 and 21-1276, respectively. The tiny peaks at 38.1° (111) (overlapping with the TiO_2) and 77.6° (311) in the Figure 7.1e are attributed to metallic gold in the $(Au)TiO_2$ nanohybrid. Figure 7.1f shows the FESEM image of the $(Au)TiO_2$ nanohybrid, which appeared to be spherical and uniform in size. Since the distribution of Au cannot be clearly shown by the FESEM image, TEM images for $(Au)TiO_2$ nanohybrid were also recorded, and are shown in Figure 7.1g. From the Figure 7.1g it can be observed that the TiO_2 nanoparticles are spherical in shape, with a particle size range of 20–25 nm and the Au nanoparticles size range is 20 nm. The HRTEM images (as shown in Figure 7.1h) of $(Au)TiO_2$ nanohybrid show the high crystallinity of the nanoparticles. The inter-planar distance between the fringes is found to be about 0.327 nm and 0.233 nm which is consistent with (110) planes of bulk TiO_2 and (111) planes of Au nanoparticles, respectively [19].
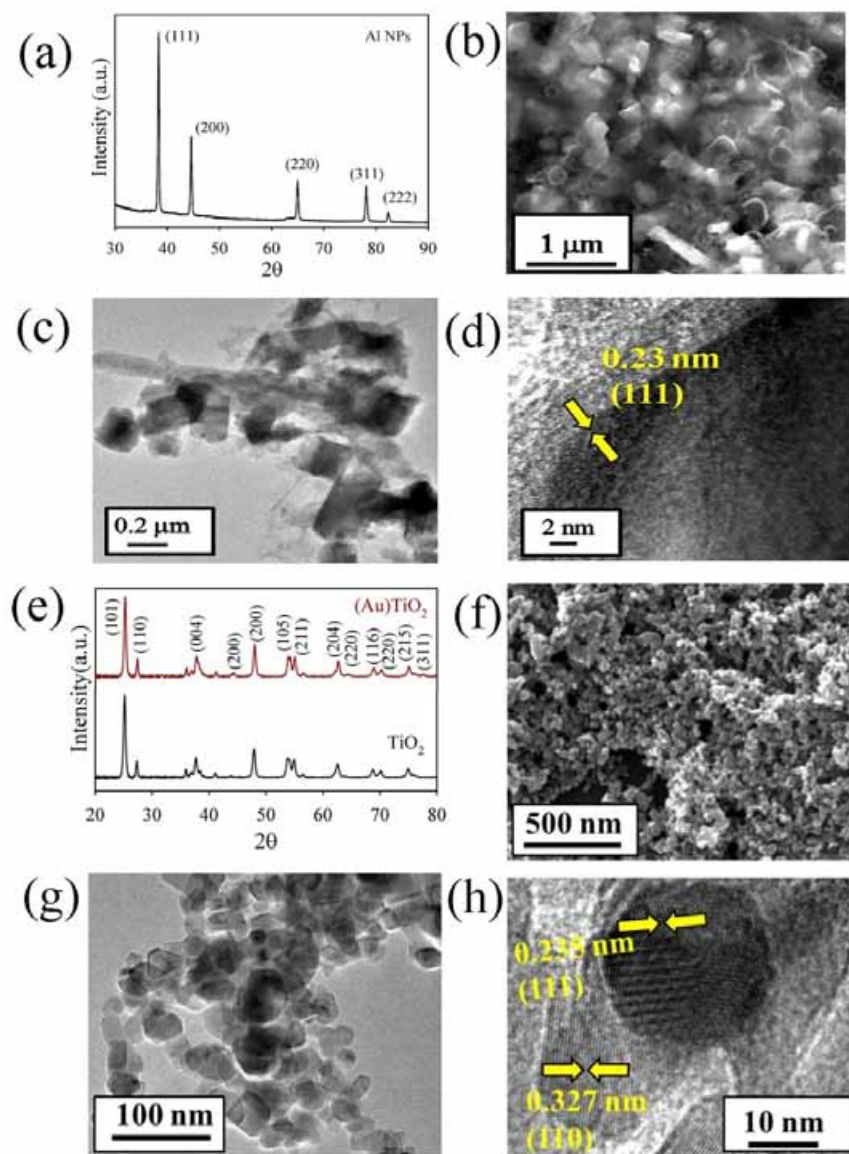
Figure 7.1. *(a) XRD pattern of Al nanoparticles. (b) FESEM image of Al nanoparticles. (c) TEM image of Al nanoparticles. (d) HRTEM image of Al nanoparticles. (e) XRD pattern of TiO₂ and (Au)TiO₂ nanohybrid. (f) FESEM image of (Au)TiO₂ nanohybrid. (g) TEM image of (Au)TiO₂ nanohybrid. (h) HRTEM image of (Au)TiO₂ nanohybrid.*

Figure 7.2a shows the UV-visible absorption spectra of TiO_2 and $(Au)TiO_2$ nanohybrid. The bare TiO_2 nanoparticles show absorption in the UV region at around ~350 nm (band gap 3.2 eV). Decoration of Au nanoparticles on the surface of the TiO_2 significantly influenced the visible light absorption, and an additional peak was also observed at 560 nm due to surface plasmon resonance (SPR) of Au nanoparticles [20]. The spectral overlap ($J(\lambda)$=3.91X10^{16} M^{-1}cm^{-1}nm^4) of the SPR band with the emission spectrum of the dye PP is shown in Figure 7.2b

revealing the possibility of significant dipolar coupling [21]. In Figure 7.2c the picosecond resolved emission transients of PP with various nanoparticles are shown. A significant faster component in the case of PP-TiO$_2$ compared to both PP and PP-Al$_2$O$_3$ is clearly evident showing
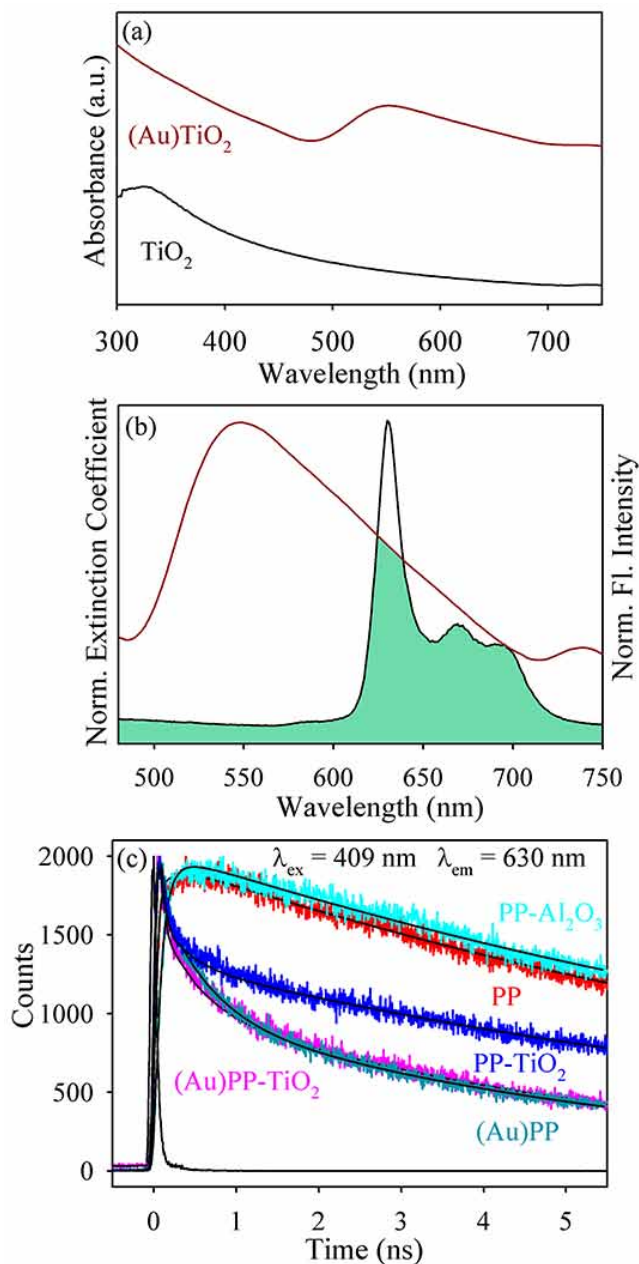

Figure 7.2. (a) Absorption spectra of TiO$_2$ and (Au)TiO$_2$ nanohybrid. (b) The overlap integral of PP-TiO$_2$ emission and Au absorbance. (c) Fluorescence decay profiles of PP, PP-Al$_2$O$_3$, PP-TiO$_2$, (Au)PP and (Au)PP-TiO$_2$ nanohybrid.

260

Table 7.1. Lifetimes of picosecond-resolved PL transients of PP, PP-Al$_2$O$_3$, PP-TiO$_2$, (Au)PP, (Au)PP-TiO$_2$, (Al)PP and (Al)PP-TiO$_2$ detected at 630 nm PL maxima uopn excitation at 409 nm wavelength. The values in parentheses represent the relative weight percentages of the time components.

System	τ_1 (ps)	τ_2 (ps)	τ_3 (ps)	τ_{avg} (ns)
PP	11400 (100%)			11.4
PP-Al$_2$O$_3$	10900 (100%)			10.9
PP-TiO$_2$	300 (59%)	10000 (41%)		4.2
(Au)PP	86 (51%)	9710 (49%)		4.7
(Au)PP-TiO$_2$	86 (57%)	300 (22%)	7120 (21%)	1.6
(Al) PP	11400 (100%)			11.4
(Al)PP-TiO$_2$	300 (59%)	9712 (41%)		4.1

the PET from PP to the host TiO$_2$, which is further enhanced in the presence of Au nanoparticle. The associated time constants are tabulated in Table 7.1. It has to be noted that the faster fluorescence transient of (Au)PP-TiO$_2$ could be manifestation of FRET from PP to Au nanoparticle in TiO$_2$ matrix. Our control experiment on Au-PP sample shows similar time scales compared to (Au)PP-TiO$_2$. The observation is not confirmatory that the faster fluorescence transient in the latter sample is exclusively for the enhanced electron transfer due to the presence of Au nanoparticles with SPR band rather include the possibility of ground state recovery (recombination) of PP through FRET. However, enhanced photocurrent measurement (see below) concludes the faster fluorescence transient to be due to efficient PET from PP to the host TiO$_2$ in presence of Au Nanoparticles. We have calculated the donor-acceptor distances by following both FRET and NSET mechanisms. Following FRET strategy, we have estimated the donor (PP)-acceptor (surface of Au nanoparticles) distance and it is found to be 8.6 nm, which is within the probing limit of FRET (1-10 nm). Whereas, the donor–acceptor distance following NSET strategy is found to be 3.8 nm which is less than the probing limit of NSET (>10 nm). The calculated FRET distance (8.6 nm) is more close to the radius of the Au nanoparticles (~10 nm as observed from the HRTEM image) than that of the NSET distance. Thus, FRET over NSET is

found to be the prevailing mechanism in this case. The observed PP-Au nanoparticle distance is consistent with the fact that PP would be under the strong influence of Au-SPR for the enhanced electron injection to the TiO_2 matrix as evident from other reported literature [21-24].

A comparative study with the Al instead of Au nanoparticles is shown in Figure 7.3. The SPR band of the synthesized Al nanoparticles in UV region (~360 nm) is consistent with reported literature as shown in Figure 7.3a [25]. A significant fluorescence quenching of PP upon TiO_2 and its insignificant change in the proximity of Al nanoparticles are shown in Figure 7.3b.
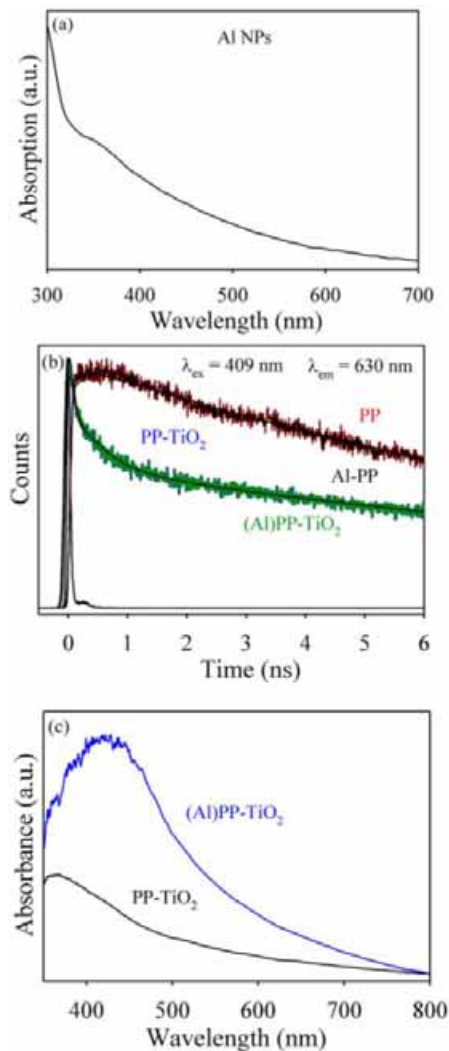

Figure 7.3. (a) Absorption spectra of Al nanoparticles. (b) Fluorescence decay profiles of PP, (Al)PP, (PP)TiO₂ and (Al)PP-TiO₂. (c) Optical absorption of dye-sensitized TiO₂ anodes incorporated with/without Al nanoparticles.

The observation demonstrates that Al nanoparticles have insignificant influence in the PET from PP to host TiO_2 matrix. At this juncture it has to be noted that enhanced PET in the case of (Au)PP-TiO_2 compared to (Al)PP-TiO_2 may not be due to the Schottky barrier for the following reason. Following simplified model of White and Catchpole (WC), [26] one can estimate the barrier in the case of Al-TiO_2 to be lower than that of the Au-TiO_2 on taking Al & Au work functions are -4.28 eV & -5.1 eV, respectively and the position of the conduction band of TiO_2 is -4.14 eV [27, 28]. In the above context the rate of PET in the case of (Al)PP-TiO_2 is expected to be higher than (Au)PP-TiO_2, which is not consistent with our experimental observation (Figures 7.2 and 7.3). However, the light trapping as evident from higher absorption due to the scattering of the Al nanoparticles are evident in Figure 7.3c. We have found that 4.6×10^{-7}, 5.0×10^{-7}, 4.8×10^{-7} and 5.2×10^{-7} mole of dye loading for TiO_2, (Al)TiO_2, (Au)TiO_2 and (Al)(Au)TiO_2 electrode with PP whereas 6.0×10^{-7}, 6.2×10^{-7}, 6.2×10^{-7} and 6.4×10^{-7} mole of dye loading for TiO_2, (Al)TiO_2, (Au)TiO_2 and (Al)(Au)TiO_2 electrode with N719.
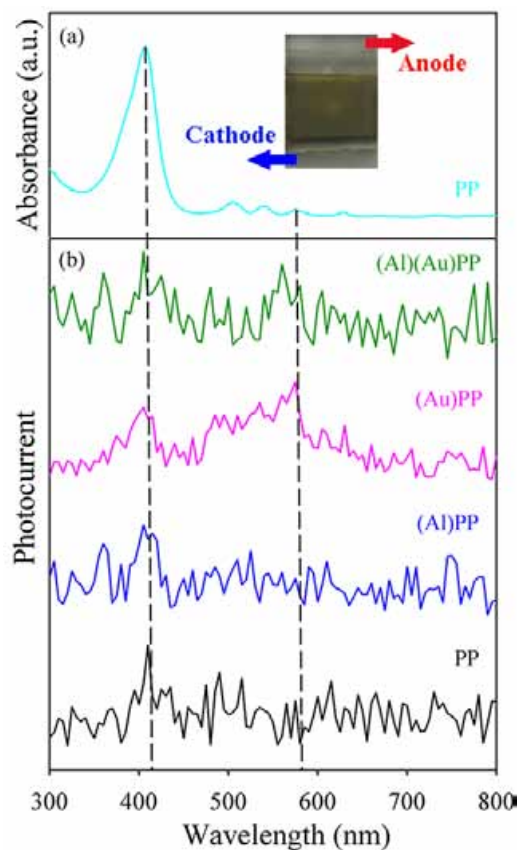

Figure 7.4. *(a) Absorption spectra of PP (The inset shows photo of DSSC). (b) Wavelength dependent photocurrent response curves of different DSSCs (Base lines were shifted for clarity).*

The photocurrent measurements on the fabricated PP-TiO$_2$ DSSC with Au and Al nanoparticles are shown in Figure 7.4. The absorption spectrum of the sensitizing dye is also shown for the comparison. The enhancement of the photocurrent around ~560 nm in presence of Au compared to Al nanoparticles is evident from the Figure. The observation is consistent with the Au-SPR induced electron injection from PP to TiO$_2$ matrix [21, 23]. The J-V characteristics of the PP-TiO$_2$ DSSC with Au and Al nanoparticles are shown in Figure 7.5a. The solar cell parameters are shown in Table 7.2. From the Figure and the Table a significant enhancement of efficiency in the Au and Al containing solar cell compared to that of the cell without the metal nanoparticles is evident. The comparable DSSC efficiency in the presence of Al and Au nanoparticles could be rationalized in the following manner. While the SPR in the case of Au nanoparticles in the DSSC
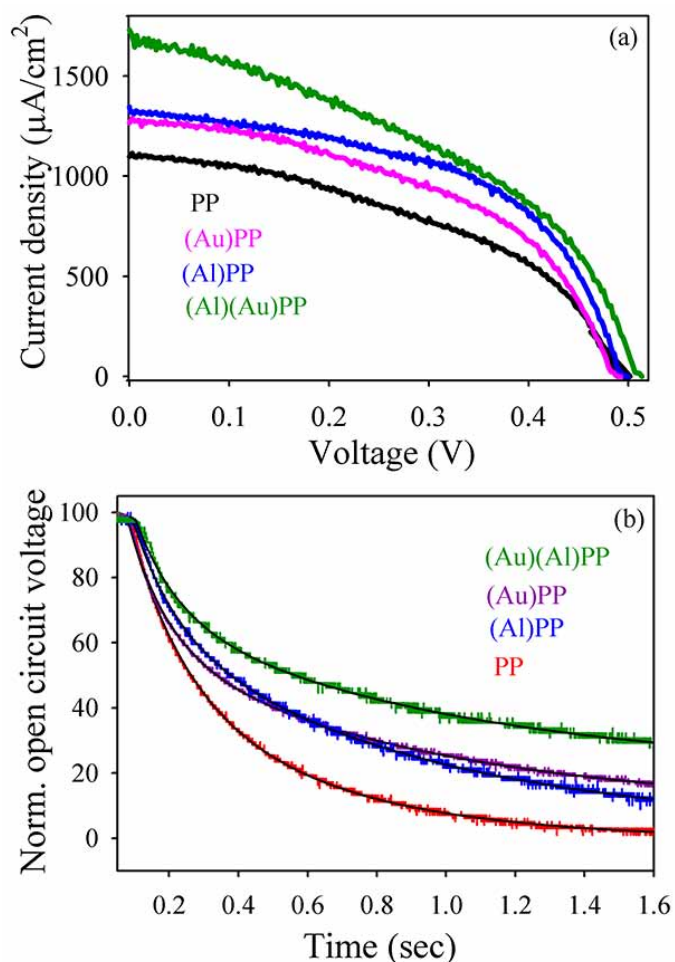

Figure 7.5. *(a) Current density–voltage curves under 100 mW cm^{-2} simulated AM 1.5G solar light irradiation. (b) Open circuit voltage decay profiles of different DSSCs.*

Table 7.2. Photovoltaic performance of DSSCs fabricated using different active electrodes sensitized with PP.

Cell	J_{SC} (μA/cm^2)	V_{OC} (V)	FF (%)	Efficiency (%)
TiO$_2$	1098.09	0.490	44.56	0.22 ± 0.02
(Al)TiO$_2$	1345.90	0.500	51.32	0.30 ± 0.01
(Au)TiO$_2$	1265.05	0.492	47.86	0.29 ± 0.01
(Au)(Al)TiO$_2$	1730.80	0.513	41.34	0.34 ± 0.01

helps in the enhanced PET, other factors including light trapping and reduced back electron transfer in the case of Al nanoparticle containing DSSC are responsible for the betterment of efficiency in latter one. As shown in Figure 7.5b, the photovoltaic decay in the case of Al nanoparticle containing DSSC is similar to that of the Au nanoparticle containing DSSC, revealing similar less back-electron transfer in the former case [29, 30]. Thus the scattering of the Al-nanoparticles leading to better light trapping makes the efficiency of the corresponding DSSC comparable to that of the Au-nanoparticle containing DSSC which is consistent with the recent reports [25, 31]. We have also attempted to fabricate a hybrid PP-TiO$_2$ DSSC containing both Au and Al nanoparticles, where Au and Al nanoparticles are supposed to take care better electron injection and light trapping, respectively. The enhanced solar cell efficiency of the hybrid DSSC is shown in Figure 7.5a. Figure 7.5b shows slower photovoltage decay in the hybrid solar cell revealing reduced back electron transfer as shown in Table 7.3. The actual reason for the observation is not clear and needs further investigation which is under way in our laboratory.

Table 7.3. Dynamics of photovoltage transients of DSSCs fabricated using different active electrodes. The values in parentheses represent the relative weight percentages of the time components.

Active electrode	τ_1 (sec)	τ_2 (sec)	τ_{avg} (sec)
PP-TiO$_2$	0.16 (78.5 %)	0.50 (21.5 %)	0.23
(Al)PP-TiO$_2$	0.11 (75.5 %)	0.80 (24.5 %)	0.28
(Au)PP-TiO$_2$	0.12 (68 %)	0.77 (32 %)	0.33
(Au)(Al)PP-TiO$_2$	0.12 (66%)	0.89 (34 %)	0.38

Figure 7.6a shows absorption spectra of N719 adsorbed TiO$_2$, (Al)TiO$_2$, (Au)TiO$_2$ and (Al)(Au)TiO$_2$ films. Higher light trapping ability of Al nanoparticles in compare to Au nanoparticles is evident from Figure 7.6a. After detail spectroscopic investigation using PP as
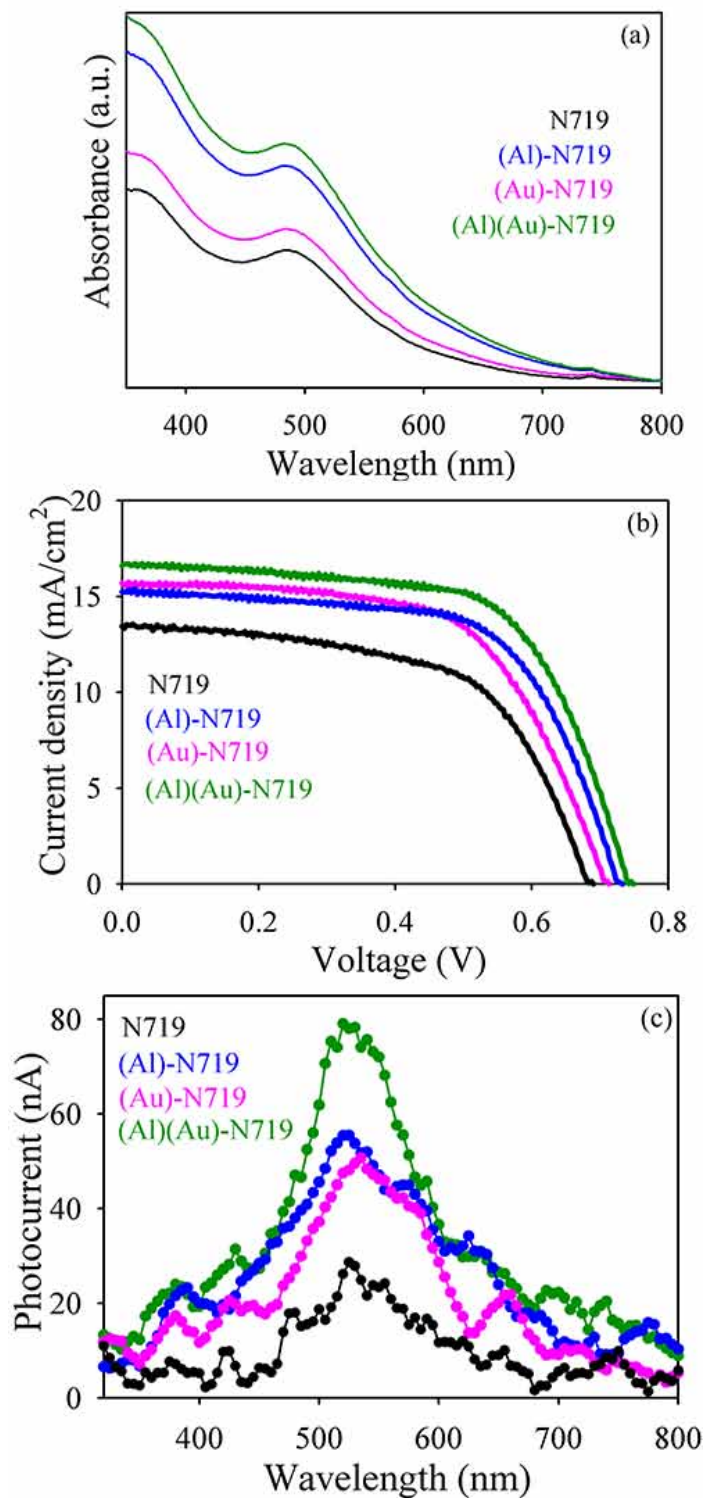
Figure 7.6. *(a) Optical absorption spectra of N-719 adsorbed on the TiO_2, $(Al)TiO_2$, $(Au)TiO_2$ and $(Al)(Au)TiO_2$ electrode. (b) Current density–voltage curves under 100 mW cm^{-2} simulated AM 1.5G solar light irradiation. (c) Wavelength dependent photocurrent response curves of different DSSCs.*

Table 7.4. Photovoltaic performance of DSSCs fabricated using different active electrodes sensitized with N719.

Cell	J_{SC} (mA/cm^2)	V_{OC} (V)	FF (%)	Efficiency (%)
TiO$_2$	13.45	0.68	58.64	5.63 ± 0.13
(Al)TiO$_2$	15.23	0.73	63.23	6.25 ± 0.1
(Au)TiO$_2$	15.68	0.71	60.47	6.05 ± 0.12
(Au)(Al)TiO$_2$	16.6	0.74	63.70	7.10 ± 0.1

sensitizer, we developed model prototype device using N719 dye in order to improve efficiencies of DSSCs. The J–V curves obtained for the TiO$_2$ with Au and Al nanoparticles are shown in Figure 7.6b. The detailed photovoltaic parameters, including the open-circuit voltage (V_{OC}), short-circuit current density (J_{SC}), fill factor (FF), and PEC are listed in Table 7.4. The larger
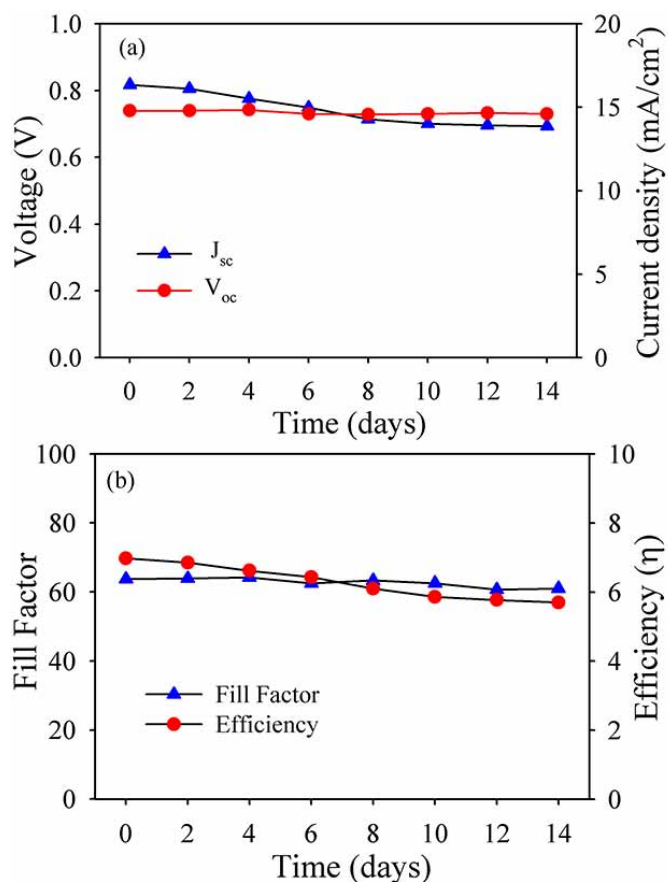

Figure 7.7. *Stability of the device. Plot of (a) J_{SC} and V_{OC}, (b) fill factor and efficiency of the DSSC fabricated using (Au)(Al)TiO$_2$ photoanode with time.*

PCE of (7.1 ± 0.1) % for DSSC with Au and Al nanoparticles compared to that with TiO$_2$ alone (5.63 ± 0.13) % can be attributed to the fact that plasmonic band and scattering effect are

responsible for enhanced electron injection behavior. From Figure 7.6c, it is clear that the plasmonic nanoparticles based DSSC exhibits higher photocurrent in the wavelength range of 400–800 nm. Due to dipolar coupling between PP and Au nanoparticles, energy transfer from PP to Au nanoparticles takes place. This leads to transfer of electron from Au nanoparticles to conduction band of TiO_2, which increases photocurrent for $(Au)TiO_2$. The light scattering ability by Al nanoparticles enhanced photocurrent for $(Al)TiO_2$. Thus, the improved photocurrent for $(Al)(Au)TiO_2$ may be attributed to the superior light harvesting ability induced by plasmonic and light scattering effect of the Au and Al nanoparticles, respectively. Figure 7.7 shows the stability of the dye sensitized solar cells which were kept in an ambient atmosphere. The V_{OC} is very stable during the experimental time window but the efficiency of dye sensitized solar cells began to decrease initially because of the decrease in short circuit current density. This could be due to the instability of the plasmonic nanoparticles in the I^-/I^{3-} redox electrolyte or further exposure to the ambient environment [32, 33]. The overall mechanistic pathways for the enhanced electron
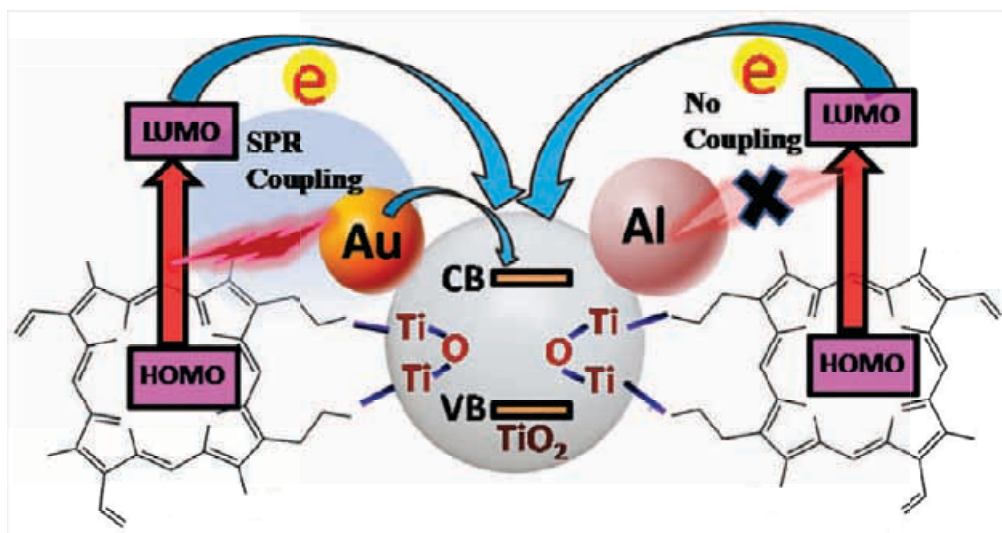

Figure 7.8. *Schematic representation of the overall mechanistic pathways for DSSC efficiency in presence of plasmonic nanoparticles (for Au nanoparticles dipolar coupling between Au and PP responsible for higher DSSC efficiency whereas scattering ability for Al nanoparticles responsible for higher DSSC efficiency).*

injection in DSSC with Au nanoparticles compared to that of Al nanoparticles are schematically shown in Figure 7.8. The enhancement in DSSC efficiency in the presence of Au nanoparticles is due to higher light trapping ability by dipolar coupling along with insignificant scattering ability.

On the other hand light trapping ability by Al nanoparticles by its significant scattering ability increases the DSSC efficiencies.

7.3. Conclusion:

In summary, we have experimentally demonstrated that plasmonic nanoparticles influence electron injection from a sensitizing dye to the host semiconductor of a model DSSC. While the SPR of Au nanoparticles contribute to enhance the solar cell efficiency through better PET, Al nanoparticles, which have a plasmonic absorption at the UV region essentially, improve solar energy harvesting ability by their better light scattering efficacy. Time-resolved fluorescence technique has been successfully demonstrated that ultrafast electron transfer dynamics are keys for overall electron injection efficiencies. Finally, we have also fabricated and characterized the prototype dye sensitized solar cell in which Au and Al nanoparticles have been employed to engineer the photoanode layer, resulting an increase of power conversion efficiency compared to values achieved in reference devices without Au and Al nanoparticles, respectively. The results highlight the crucial role played by the plasmonic nanoparticles is the plasmonic dipolar coupling as well as scattering effect which are responsible for enhanced solar energy conversation.

References

[1]   X. Dang, J. Qi, M. T. Klug, P.-Y. Chen, D. S. Yun, N. X. Fang, P. T. Hammond, A. M. Belcher, Tunable Localized Surface Plasmon-Enabled Broadband Light-Harvesting Enhancement for High-Efficiency Panchromatic Dye-Sensitized Solar Cells, *Nano Lett.* 13 (2013) 637-642.

[2]   W. Hou, P. Pavaskar, Z. Liu, J. Theiss, M. Aykol, S. B. Cronin, Plasmon Resonant Enhancement of Dye Sensitized Solar Cells, *Energy Environ. Sci.* 4 (2011) 4650-4655.

[3]   Y. Bai, T. Butburee, H. Yu, Z. Li, R. Amal, G. Q. Lu, L. Wang, Controllable Synthesis of Concave Cubic Gold Core–Shell Nanoparticles for Plasmon-Enhanced Photon Harvesting, *J. Colloid Interface Sci.* 449 (2015) 246-251.

[4]   Q. Xu, F. Liu, Y. Liu, K. Cui, X. Feng, W. Zhang, Y. Huang, Broadband Light Absorption Enhancement in Dye-Sensitized Solar Cells with Au-Ag Alloy Popcorn Nanoparticles, *Sci. Rep.* 3 (2013) 2112.

[5]   J. Yun, S. H. Hwang, J. Jang, Fabrication of Au@Ag Core/Shell Nanoparticles Decorated TiO_2 Hollow Structure for Efficient Light-Harvesting in Dye-Sensitized Solar Cells, *ACS Appl. Mater. Interfaces* 7 (2015) 2055-2063.

[6]   P. Reineck, G. P. Lee, D. Brick, M. Karg, P. Mulvaney, U. Bach, A Solid-State Plasmonic Solar Cell via Metal Nanoparticle Self-Assembly, *Adv. Mater.* 24 (2012) 4750-4755.

[7]   H. F. Zarick, W. R. Erwin, A. Boulesbaa, O. K. Hurd, J. A. Webb, A. A. Puretzky, D. B. Geohegan, R. Bardhan, Improving Light Harvesting in Dye-Sensitized Solar Cells Using Hybrid Bimetallic Nanostructures, *ACS Photonics* 3 (2016) 385-394.

[8]   R. Milan, G. S. Selopal, M. Epifani, M. M. Natile, G. Sberveglieri, A. Vomiero, I. Concina, $ZnO@SnO_2$ Engineered Composite Photoanodes for Dye Sensitized Solar Cells, *Sci. Rep.* 5 (2015) 14523.

[9]   R. Long, O. V. Prezhdo, Instantaneous Generation of Charge-Separated State on TiO_2 Surface Sensitized with Plasmonic Nanoparticles, *J. Am. Chem. Soc.* 136 (2014) 4343-4354.

[10]   S. Linic, P. Christopher, D. B. Ingram, Plasmonic-Metal Nanostructures for Efficient Conversion of Solar to Chemical Energy, *Nat. Mater.* 10 (2011) 911-921.

[11]   S. W. Sheehan, H. Noh, G. W. Brudvig, H. Cao, C. A. Schmuttenmaer, Plasmonic Enhancement of Dye-Sensitized Solar Cells Using Core–Shell–Shell Nanostructures, *J. Phys. Chem. C* 117 (2013) 927-934.

[12]   Y. H. Jang, Y. J. Jang, S. T. Kochuveedu, M. Byun, Z. Lin, D. H. Kim, Plasmonic Dye-Sensitized Solar Cells Incorporated with Au-TiO$_2$ Nanostructures with Tailored Configurations, *Nanoscale* 6 (2014) 1823-1832.

[13]   M.-k. Song, P. Rai, K.-J. Ko, S.-H. Jeon, B.-S. Chon, C.-H. Lee, Y.-T. Yu, Synthesis of TiO$_2$ Hollow Spheres by Selective Etching of Au@TiO$_2$ Core-Shell Nanoparticles for Dye Sensitized Solar Cell Applications, *RSC Adv.* 4 (2014) 3529-3535.

[14]   S. Ramakrishna, M. Pelton, S. K. Gray, T. Seideman, Plasmon-Enhanced Electron Injection in Dye-Sensitized Solar Cells, *J. Phys. Chem. C* 119 (2015) 22640-22645.

[15]   P. V. Kamat, Photophysical, Photochemical and Photocatalytic Aspects of Metal Nanoparticles, *J. Phys. Chem. B* 106 (2002) 7729-7744.

[16]   S. D. Standridge, G. C. Schatz, J. T. Hupp, Distance Dependence of Plasmon-Enhanced Photocurrent in Dye-Sensitized Solar Cells, *J. Am. Chem. Soc.* 131 (2009) 8407-8409.

[17]   P. Kar, T. K. Maji, P. K. Sarkar, S. Sardar, S. K. Pal, Direct Observation of Electronic Transition-Plasmon Coupling for Enhanced Electron Injection in Dye-Sensitized Solar Cells, *RSC Adv.* 6 (2016) 98753-98760.

[18]   E. Stratakis, M. Barberoglou, C. Fotakis, G. Viau, C. Garcia, G. A. Shafeev, Generation of Al Nanoparticles via Ablation of Bulk Al in Liquids with Short Laser Pulses, *Opt. Express* 17 (2009) 12650-12659.

[19]   M. Hussain, M. Ahmad, A. Nisar, H. Sun, S. Karim, M. Khan, S. D. Khan, M. Iqbal, S. Z. Hussain, Enhanced Photocatalytic and Electrochemical Properties of Au Nanoparticles Supported TiO$_2$ Microspheres, *New J. Chem.* 38 (2014) 1424-1432.

[20]   C. Andrei, E. Lestini, S. Crosbie, C. de Frein, T. O'Reilly, D. Zerulla, Plasmonic Enhancement of Dye Sensitized Solar Cells via a Tailored Size-Distribution of Chemically Functionalized Gold Nanoparticles, *PLOS ONE* 9 (2014) e109836.

[21]   P. Reineck, D. Gómez, S. H. Ng, M. Karg, T. Bell, P. Mulvaney, U. Bach, Distance and Wavelength Dependent Quenching of Molecular Fluorescence by Au@SiO$_2$ Core–Shell Nanoparticles, *ACS Nano* 7 (2013) 6636-6648.

[22] W. R. Erwin, H. F. Zarick, E. M. Talbert, R. Bardhan, Light Trapping in Mesoporous Solar Cells with Plasmonic Nanostructures, *Energy Environ. Sci.* 9 (2016) 1577-1601.

[23] S. T. Kochuveedu, T. Son, Y. Lee, M. Lee, D. Kim, D. Kim, Revolutionizing the FRET-Based Light Emission in Core-Shell Nanostructures via Comprehensive Activity of Surface Plasmons, *Sci. Rep.* 4 (2014) 4735.

[24] K. A. Kang, J. Wang, J. B. Jasinski, S. Achilefu, Fluorescence Manipulation by Gold Nanoparticles: From Complete Quenching to Extensive Enhancement, *J. Nanobiotechnol.* 9 (2011) 16.

[25] X. Chen, B. Jia, Y. Zhang, M. Gu, Exceeding the Limit of Plasmonic Light Trapping in Textured Screen-Printed Solar Cells using Al Nanoparticles and Wrinkle-Like Graphene Sheets, *Light: Sci. Appl.* 2 (2013) e92.

[26] T. P. White, K. R. Catchpole, Plasmon-Enhanced Internal Photoemission for Photovoltaics: Theoretical Efficiency Limits, *Appl. Phys. Lett.* 101 (2012) 073905.

[27] H. B. Michaelson, The Work Function of the Elements and its Periodicity, *J. Appl. Phys.* 48 (1977) 4729-4733.

[28] Z. Xuming, C. Yu Lim, L. Ru-Shi, T. Din Ping, Plasmonic Photocatalysis, *Rep. Prog. Phys.* 76 (2013) 046401.

[29] H. Choi, Y.-S. Chen, K. G. Stamplecoskie, P. V. Kamat, Boosting the Photovoltage of Dye-Sensitized Solar Cells with Thiolated Gold Nanoclusters, *J. Phys. Chem. Lett.* 6 (2015) 217-223.

[30] S. Sardar, S. Ghosh, H. Remita, P. Kar, B. Liu, C. Bhattacharya, P. Lemmens, S. K. Pal, Enhanced Photovoltage in DSSCs: Synergistic Combination of a Silver Modified TiO_2 Photoanode and a Low Cost Counter Electrode, *RSC Adv.* 6 (2016) 33433-33442.

[31] Q. Xu, F. Liu, Y. Liu, W. Meng, K. Cui, X. Feng, W. Zhang, Y. Huang, Aluminum Plasmonic Nanoparticles Enhanced Dye Sensitized Solar Cells, *Opt. Express* 22 (2014) A301-A310.

[32] C. Wen, K. Ishikawa, M. Kishima, K. Yamada, Effects of Silver Particles on the Photovoltaic Properties of Dye-Sensitized TiO_2 Thin Films, *Sol. Energ. Mat. Sol. Cells* 61 (2000) 339-351.

[33] J. You, L. Meng, T.-B. Song, T.-F. Guo, Y. Yang, W.-H. Chang, Z. Hong, H. Chen, H. Zhou, Q. Chen, Y. Liu, N. De Marco, Y. Yang, Improved Air Stability of Perovskite

Solar Cells via Solution-Processed Metal Oxide Transport Layers, *Nat. Nanotechnol.* 11 (2016) 75-81.

List of Publications

(Peer-Reviewed Journals)

1. **P. Kar**, S. Sardar, E. Alarousu, J. Sun, Z. S. Seddigi, S. A. Ahmed, E. Y. Danish, O. F. Mohammed and S. K. Pal "The Impact of the Metal Ions in the Porphyrin-based Applied Materials for Visible Light Photocatalysis: Key Information from Ultrafast Electronic Spectroscopy", Chem. Eur. J. 20 (2014) 10475-10483.

2. **P. Kar**, S. Sardar, S. Ghosh, M. R. Parida, B. Liu, O. F. Mohammed, P. Lemmens and S. K. Pal "Nano Surface Engineering of Mn_2O_3 for Potential Light-Harvesting Application", J. Mat. Chem. C 3 (2015) 8200-8211.

3. **P. Kar**, T. K. Maji, P. K. Sarkar, S. Sardar and S. K. Pal "Direct Observation of Electronic "Transition-Plasmon Coupling for Enhanced Electron Injection in Dye-sensitized Solar Cells", RSC Adv. 6 (2016) 98753-98760.

4. **P. Kar**, S. Sardar, B. Liu, M. Sreemany, P. Lemmens, Srabanti Ghosh and S. K. Pal "Facile Synthesis of Reduced Graphene Oxide-gold Nanohybrid for Potential Use in Industrial Waste-water Treatment", Sci. Tech. Adv. Mat. 17 (2016) 375-386.

5. **P. Kar**, T. K. Maji, R. Nandi, P. Lemmens and S. K. Pal "In-situ Hydrothermal Synthesis of $Bi-Bi_2O_2CO_3$ Heterojunction Photocatalyst with Enhanced Visible Light Photocatalytic Activity", Nano-Micro Lett. 9 (2017) 18.

6. **P. Kar**, T. K. Maji, J. Patwari and S. K. Pal "Can a Light Harvesting Material be Always Common in Photocatalytic and Photovoltaic Applications?" Mater. Chem. Phys. 200 (2017) 70-77.

7. S. Ghosh, **P. Kar**, N. Bhandary, S. Basu, S. Sardar, T. Maiyalagan, D. Majumdar, S. K. Bhattacharya, A. Bhaumik, P. Lemmens and S. K. Pal "Microwave-Assisted Synthesis of Mn_2O_3 Porous Balls as Bifunctional Electrocatalyst for Oxygen Reduction and Evolution Reaction", Catal. Sci. Tech. 6 (2016) 1417-1429.

8. S. Ghosh, **P. Kar**, N. Bhandary, S. Basu, T. Maiyalagan, S. Sardar and S. K. Pal "Reduced Graphene Oxide Supported Hierarchical Flower like Manganese Oxide as Efficient Electrocatalysts Toward Reduction and Evolution of Oxygen", Int. J. Hydrogen Energy 42 (2017) 4111-4122.

9. S. Ghosh, H. Remita, **P. Kar**, S. Choudhury, S. Sardar, P. Beaunier, P. S. Roy, S. K. Bhattacharya and S. K. Pal "Facile Synthesis of Pd Nanostructures in Hexagonal Mesophases as Promising Electrocatalyst for Ethanol Oxidation", J. Mat. Chem. A 3 (2015) 9517-9527.

10*. S. Sardar, **P. Kar** and S. K. Pal "The Impact of Central Metal Ions in Porphyrin Functionalized ZnO/TiO_2 for Enhanced Solar Energy Conversion", J. Mat. NanoSci. 1 (2014) 12-30.

11*. S. Sardar, **P. Kar**, S. Sarkar, P. Lemmens and S. K. Pal "Interfacial Carrier Dynamics in PbS-ZnO Light Harvesting Assemblies and their Potential Implication in Photovoltaic/ Photocatalysis Application", Sol. Energ. Mat. Sol. Cells. 134 (2015) 400-406.

12*. S. Sardar, **P. Kar**, H. Remita, B. Liu, P. Lemmens, S. K. Pal and S. Ghosh "Enhanced Charge Separation and FRET at Heterojunctions between Semiconductor Nanoparticles and Conducting Polymer Nanofibers for Efficient Solar Light Harvesting", Sci. Rep. 5 (2015) 17313.

13*. S. Sardar, S. Chaudhuri, **P. Kar**, S. Sarkar, P. Lemmens and S. K. Pal "Direct Observation of Key Photoinduced Dynamics in a Potential Nano-delivery Vehicle of Cancer Drugs", Phys. Chem. Chem. Phys. 17 (2015) 166-177.

14*. S. Sardar, S. Ghosh, H. Remita, **P. Kar**, B. Liu, C. Bhattacharya, P. Lemmens and S. K. Pal "Enhanced Photovoltage in DSSC: Synergistic Combination of Silver Modified TiO_2 Photoanode and Low Cost Counter Electrode", RSC Adv. 6 (2016) 33433-33442.

15*. T. K. Maji, D. Bagchi, **P. Kar**, D. Karmakar and S. K. Pal "Enhanced Charge Separation through Modulation of Defect-state in Wide Band-gap Semiconductor for Potential Photocatalysis Application: Ultrafast Spectroscopy and Computational Studies'', J. Photochem. Photobiol. A 332 (2017) 391-398.

16*. R. Nandi, S. Mishra, T. K. Maji, K. Manna, **P. Kar**, S. Banerjee, S. Dutta, S. K Sharma, P. Lemmens, K. Das Saha, S. K. Pal "A Novel Nanohybrid for Cancer Theranostics: Folate Sensitized Fe_2O_3 Nanoparticle for Colorectal Cancer Diagnosis and Photodynamic Therapy", J. Mater. Chem. B 5 (2017) 3927-3939.

* Not included in the thesis.